

Newcastle University

Characterisation and application of low temperature $\text{YBaCo}_4\text{O}_{7+\delta}$ for oxygen enrichment processes by redox cycling

A thesis submitted to the school of Engineering, in partial fulfilment of requirement for the award of a doctorate in philosophy in chemical engineering

Stephen Johnston

September 2019

Primary supervisor – Professor Ian Metcalfe

Secondary supervisor – Dr. Wenting Hu

Abstract

Oxygen enrichment is of growing importance in industry, with processes ranging from oxy-fuel combustion to the Claus process relying upon this technology. The major limiting factor of the technology is the cost of oxygen. Oxygen production is most often performed by cryogenic distillation, however redox cycling of oxygen non-stoichiometric materials is an attractive and potentially cheaper alternative. Metal oxides such as copper or cobalt oxide, can be used to produce oxygen by redox cycling however, low stability over redox cycling make them unattractive. Non-stoichiometric materials, such as perovskites, have greater cycling stability, however, three main issues prevent widespread implementation, namely:

Issues with characterisation techniques – oxygen diffusion rates are often so high that mass transfer limitations mask the true rates of oxygen diffusion in a material using traditional diffusion characterisation techniques such as electrochemical relaxation making accurate modelling of the materials difficult

High temperature operation – The materials often studied operate at temperatures of approximately 800°C. For oxygen enrichment processes, air is typically the feed gas for the oxidation step, requiring air to be heated by approximately 750°C. Some of this heat can be recovered, however it is more efficient to have a material that does not require such a large temperature increase.

Low oxygen capacity – Many perovskite and non-stoichiometric materials have a cyclable oxygen capacity two orders of magnitude lower than that of the metal oxides. This requires fast cycling which can lead to particle degradation as well as large pressure drops and unwanted gas mixing, depending upon the size and type of reactor bed.

In this work, a new characterisation technique to avoid mass transfer limitations is explored. Additionally, the thermodynamics and crystal structure of a low temperature and high oxygen capacity non-stoichiometric material, namely $\text{YBaCo}_4\text{O}_{7+\delta}$, is studied, before a feasibility study of the material for oxygen enrichment is performed.

Acknowledgements

There are several people I would like to thank for their continued help and assistance throughout my PhD, without their support I would not have pushed through to the end.

Firstly, I would like to thank my family and my parents for always supporting me through every step of the way. Their unconditional love, in this and everything else in my life, has been so important to me throughout this journey. There has never been a worry too great or too small for them to take the time to help me when I needed it, and I can only hope to be as kind and generous as them.

Thanks to my lab mates Liam, Chris and Maria – the wildcard. You made each day fun, and I hope I made each of yours slightly nerdier. Also, to the large crowd of marine biologists I somehow infiltrated, particularly Josh for putting up and coping so well with my panicking these last few months before submission, I've never had a better and more supportive group of friends around me.

I would also like to mention four people by name who helped immensely throughout my work. Thanks to Maggie White, for performing countless XRD scans and always managing to get my samples to the front of the queue, and constantly willing to listen to me. Thanks to Evangelos, for constantly being there when things were not going my way, and always having a kind word for me. Thanks to Mike Gaultious, for performing many hours of in-situ XRD scans for me in Cambridge and helping me make sense of everything. And finally, to Brian Ray, who constantly challenged me, and never stopped supporting me, even after returning home.

Thanks to Wenting Hu, Brian Ray and Mike Gaultious for their valuable advice and comments on my thesis. Acknowledgements must also go to Mike Gaultious for performing the *in-situ* XRD work in Chapter 6. Additionally, the pressure relaxation technique described in Chapter 5 was introduced by Henny Bouwmeester, Ian Metcalfe and Wei Chen.

And finally, thanks to Ian Metcalfe, for giving me the opportunity to pursue my dream of doing a PhD.

Contents page

List of Figures	8
Chapter 1 – Application and production method of oxygen	16
1.1 The uses of oxygen	16
1.1.1 Oxy-fuel combustion	19
1.1.2 Claus process.....	23
1.1.3 Oxygen enriched combustion	25
1.1.4 Conclusions on the use of oxygen within industrial processes	26
1.2 Methods of oxygen production	26
1.2.1 Cryogenic distillation	26
1.2.2 Pressure swing absorption (PSA).....	28
1.2.3 Membrane separation of air	29
1.2.4 Chemical separation of air through redox cycling	31
1.3 Conclusion	34
1.4 References.....	35
Chapter 2 – Review of oxygen carriers for CLAS.....	46
2.1 Metal oxide oxygen carriers.....	46
2.2 Non-stoichiometric oxygen carriers	49
2.3 Oxygen carriers with hysteresis behaviour in the oxygen capacity	56
2.3.1 Hexagonal rare-earth manganites.....	58
2.3.2 $\text{Ca}_2\text{AlMnO}_{5+\delta}$	59
2.3.3 Rare earth cobaltites	61
2.3.4 Summary of material literature review	65
2.4 Characterisation techniques for non-stoichiometric materials	66
2.4.1 Techniques to determine oxygen non-stoichiometry	66
2.4.2 Techniques to determine oxygen diffusion co-efficients	68
2.5 References.....	72
Chapter 3 Aims and objectives.....	82
3.2 Objectives	83
3.3 References.....	85

Chapter 4 – Methods of creating and characterising non-stoichiometric materials	86
4.1 X-ray diffraction.....	86
4.2 Thermogravimetric analysis (TGA)	87
4.2.1 TGA heat pre-treatment.....	90
4.3 Synthesis of $\text{YBaCo}_4\text{O}_{7+\delta}$	91
4.4 Chapter 5 experiments.....	92
4.4.1 Preparation of LSCF pellet	93
4.4.2 Pressure relaxation rig.....	93
4.4.3 Pressure relaxation experiments.....	94
4.5 Chapter 6 experiments.....	95
4.5.1 Chapter 6 oxygen measurement experiments	95
4.5.2 <i>In-situ</i> XRD studies	97
4.5.3 Thermodynamic calculations	98
4.6 Chapter 7 experiments.....	99
4.7 References	103
Chapter 5 – Development of novel pressure relaxation technique for characterisation of non-stoichiometric materials.....	104
5.1 Introduction	105
5.1.1 Method of calculating oxygen diffusion rates using pressure relaxation..	107
5.2 Results.....	110
5.2.1 Leak rates of the pressure relaxation system	110
5.3.2 Thermal profiling of the reactor.....	112
5.2.3 Blank runs of the pressure relaxation system	115
5.2.4 Determination of oxygen non-stoichiometry using pressure relaxation ...	119
5.2.5 Oxygen relaxation studies using pressure relaxation	121
5.2.6 Upgrading the measurement system	122
5.2.7 - Further investigations of the pressure change	123
5.3 Discussion	127
5.5 References	130
Chapter 6 -An investigation into the thermodynamic and structural changes of $\text{YBaCo}_4\text{O}_{7+\delta}$.....	133

6.1	Introduction.....	133
6.2	Results	134
6.2.1	Oxygen release of $\text{YBaCo}_4\text{O}_{7+\delta}$	134
6.2.2	Isothermal oxygen incorporation of $\text{YBaCo}_4\text{O}_{7+\delta}$	137
6.2.3	Stepwise heating and cooling of $\text{YBaCo}_4\text{O}_{7+\delta}$	143
6.2.4	Equilibria plot of $\text{YBaCo}_4\text{O}_{7+\delta}$	145
6.2.5	<i>In-situ</i> XRD study of $\text{YBaCo}_4\text{O}_{7+\delta}$	147
6.2.6	<i>Ex-situ</i> XRD study of $\text{YBaCo}_4\text{O}_{7+\delta}$	153
6.2.7	Thermodynamic study of $\text{YBaCo}_4\text{O}_{7+\delta}$	156
6.4	Oxygen release and incorporation of YBaCo_4O_7 compared to other oxygen carriers.....	166
6.4.1	Amount of oxygen released per °C of a temperature swing compared to other oxygen carriers	166
6.4.2	The use of oxygen from an air stream	168
6.5	Discussion	169
6.6	Conclusions and future work.....	173
Chapter 7 – An investigation into the stability and use of non-stoichiometric $\text{YBaCo}_4\text{O}_{7+\delta}$ for oxygen enrichment processes.....		
7.1	Introduction.....	179
7.2	Results and discussion	179
7.2.1	Material stability	179
7.2.2	Isothermal oxygen incorporation/release experiments	181
7.2.3	Investigation into the effect of $p\text{O}_2$ on the useful oxygen release of $\text{YBaCo}_4\text{O}_{7+\delta}$	183
7.2.4	Method of using YBaCo_4O_7 for oxygen enrichment processes.....	184
7.2.5	Reducing the temperature swing required for redox cycling.....	186
7.2.6	Stability of $\text{YBaCo}_4\text{O}_{7+\delta}$ over multiple redox cycles.....	190
7.2.7	Effect of reducing the oxygen incorporation time during cycling upon sample stability	193
7.4	- Model of oxygen enrichment using $\text{YBaCo}_4\text{O}_{7+\delta}$	198
7.4.1	– Kinetics of oxygen release from $\text{YBaCo}_4\text{O}_{7+\delta}$	198
7.4.2	– Size of exhaust gas stream	199
7.4.3	- Sizing of the reactor dimensions.....	200

7.4.4 – Model results	200
7.4.5– Required bed length for oxy-fuel combustion.....	202
7.4.6 – Operational time of the material	203
7.4 Discussion	204
7.5 Conclusions and further work	207
7.6 References	209
Chapter 8 - Conclusions	214
8.1 Review of the initial objectives	214
8.1.1 Creation of a useful technique to characterise oxygen diffusion coefficients and non-stoichiometry	214
8.1.2 Detailed investigation into the thermodynamics of selected oxygen carrier	214
8.1.3 Investigation into the stability of the non-stoichiometric material.....	215
8.1.4 Investigation into the kinetics of the oxygen incorporation and release of the selected material	215
8.2 Further work.....	215
8.3 References	217

List of Figures

Figure 2.1 – Diagram showing (a) Schottky vacancy and (b) an interstitial oxygen position in a perovskite material, where the blue spheres represent the oxygen ions in the closest three planes, the white spheres in the furthest three planes, and the red spheres the metallic cations.....	50
Figure 2.2 - Van der Walls plot representing phase transition between a state A and B as a function of temperature	57
Figure 4.1 – Diagram showing simplified workings of an XRD unit	86
Figure 4.2 – Schematic of TGA used for experiments.....	88
Figure 4.5 – Schematic of preparation of YBaCo ₄ O ₇ powders undergoing, (A) grinding of precursors, (B) 1000 °C sintering for 12 hours, (C) intermittent grinding of intermediate phases, (D) final 1200 °C sintering for 12 hours	91
Figure 4.7 – Schematic of the pressure relaxation system	94

Figure 5.1 – Plot of pressure in the sealed pressure relaxation reactor vessel versus time at a starting pressure of 1 mbar and a room temperature of 22°C	110
Figure 5.3 – A plot of recorded pressure versus time of a sealed reactor heated to 800°C, with the reservoir left open to the atmosphere.....	112
Figure 5.4 – Scatter plot of recorded pressure in the reactor versus temperature for the pressure relaxation system heated from room temperature to 800°C with V1 either open (red) or closed (blue).....	113
Figure 5.5 – Scatterplot showing average system temperature for the pressure relaxation system as a function of reactor temperature	114
Figure 5.6 – Plot of normalised pressure change of the reactor vessel, when V1 is opened, with the reactor pressure between 15 and 60 mbar, and the reservoir pressure equal to half the reactor vessel pressure, versus time at 800°C	115
Figure 5.7 – Plot of normalised pressure change of the reactor vessel, when V1 is opened, with the reactor vessel pressure between 15 and 60 mbar, and the reservoir pressure equal to half the reactor vessel pressure, versus time at 500°C.....	116
Figure 5.8 – Plot of pressure in the reactor vessel versus time for a blank run after V1 was opened, with the reactor vessel temperature at 800°C.....	117
Figure 5.9 – Plot of the reactor pressure versus time showing the pressure re-equilibration of the system after V1 vessel was opened (blue lines) or opened and quickly closed (red lines) with, (A) reactor at room temperature, starting pressure of 30 mbar, (B) reactor at room temperature, starting pressure of 60 mbar, (C) reactor at 800 °C, starting pressure of 30 mbar, (D) reactor at 800°C, starting pressure of 60 mbar. The reservoir pressure for each run was half the starting pressure of the reactor and data sampling occurred at a rate of 10 samples a second.....	118
Figure 5.10 – Plot showing oxygen non-stoichiometry versus pO_2 at temperatures between 700 and 900°C obtained from the literature (open symbols) or experimentally using the pressure relaxation rig (closed symbols).....	119
Figure 5.11 – Plot showing oxygen non-stoichiometry versus pO_2 at 900°C obtained experimentally using the pressure relaxation rig (closed symbols) with different conditions to show the sensitivity of calculations. The parameter changed in each graph was, (A) - reactor volume, (B) – reservoir volume, (C) – reactor temperature, and (D) – reservoir temperature.....	120

Figure 5.12 (A-D)– Plots showing pressure in the reactor vessel versus time, highlighting the pressure change as the non-stoichiometric LSCF re-equilibrates to the new pO_2 after the opening of V1. The starting pressures of the reactor vessel during the experiment were approximately, (A) – 210 mbar, (B) – 60 mbar, (C) – 30 mbar and (D) – 15 mbar. The reservoir pressure was set at $\frac{1}{4}$ of the starting reactor vessel pressure, and sampling was performed at a rate of 10 points per second..... 122

Figure 5.13 – Plot showing pressure in the reactor vessel versus time, showing the pressure change as the non-stoichiometric LSCF re-equilibrates to the new pO_2 after the opening of V3. The starting pressures of the reactor vessel during the experiment were approximately 80 mbar and the temperature $700^\circ C$. The reservoir pressure was set at $\frac{1}{4}$ of the starting reactor vessel pressure, and sampling was performed at a rate of 10 points per second using the Picologger, and 100 points per second using the DMM..... 123

Figure 5.14– Plot showing pressure in the reactor vessel versus time, highlighting the pressure change as the non-stoichiometric LSCF re-equilibrates to the new pO_2 after the opening of V3. The starting pressures of the reactor vessel during the experiment were approximately 60 mbar and the temperatures between 700 and $850^\circ C$. The reservoir pressure was set at $\frac{1}{4}$ of the starting reactor vessel pressure, and sampling was performed at a rate of 10 points per second..... 124

Figure 5.15 (a)– Plot showing the change in the non-stoichiometry of the dense LSCF pellet versus time, calculated from the change in pressure of the reactor vessel. The starting pressures of the reactor vessel during the experiment were approximately 60 mbar and the temperatures between 700 and $850^\circ C$. The reservoir pressure was set at $\frac{1}{4}$ of the starting reactor vessel pressure, and sampling was performed at a rate of 10 points per second. **(b)** – Plot showing the data shown in Figure 5.16 (a) for $700^\circ C$ (blue line) compared to the estimated change in oxygen non-stoichiometry from thermodynamic data. The blue star refers to the expected change in non-stoichiometry from calculations 125

Figure 6.1 – Plot showing δ versus temperature of $YBaCo_4O_{7+\delta}$ heated between $50^\circ C$ to $500^\circ C$, with a heating rate of $1^\circ C/min$, in pO_2 s between 0.05 and 0.42 bar with gas flow rates of 200. ml/min (S.T.P). 135

Figures 6.3 – Plotted data points showing the amount of oxygen incorporated (δ) into a sample of $YBaCo_4O_{7+\delta}$ after different lengths of time for samples held isothermally in a pO_2 of **(A)** 0.05 bar, **(B)** 0.25 bar, **(C)** 0.42 bar versus temperature,

after the helium pre-treatment. Figure 6.3 (D) compares the δ achieved upon heating during the dynamic heating ramp in Figure 6.1 and isothermally in Figure 6.3, for a pO_2 of 0.21 bar (B) in a pO_2 of 0.25 bar after 180 minutes. The data points for the oxygen content of the material gained isothermally after 120 and 180 minutes are rendered onto a 3-d graph in Figure 6.3 (E) 138

Figure 6.4 – A plot of δ versus time for a sample of $YBaCo_4O_7$ cooled stepwise between 430 and 280°C in four hour long, 10 °C increments in a pO_2 of 0.25 bar. 140

Figures 6.5 – Plotted data points showing the amount of oxygen incorporated (δ) into a sample of $YBaCo_4O_7$ after different lengths of time for samples held isothermally in a gas flow rate of 200 ml/min at a temperature of 340°C, with the pO_2 changing between 0.05 and 0.42 bar. 141

Figure 6.6 – Stepwise cooling curve showing δ of $YBaCo_4O_{7+\delta}$ after being held at 430°C under He for four hours, followed by stepwise cooling in hour-long 5°C steps to 300°C in pO_2 of between 0.05 and 0.42 bar. 142

Figure 6.7 (a) - Stepwise heating curve showing δ of $YBaCo_4O_7$ after being held at 300°C for ten hours in a pO_2 of 0.21 bar, before being heated in hour long 5°C steps to 430°C at the same pO_2 . **(b)** Stepwise cooling curve showing δ of $YBaCo_4O_{7+\delta}$ after being held at 430°C in a pO_2 of 0.25 bar for two hours before being cooled in hour long 5°C steps to 300°C at the same pO_2 . The red line shows the change in temperature, while the blue line shows the change in δ . The marked lines A, B and C display areas of interest discussed in the text. 143

Figure 6.8 - Hysteresis equilibria plot of $YBaCo_4O_{7+\delta}$ in a pO_2 of 0.42 and 0.25 bar upon different directions of heating and cooling. 144

Figure 6.9–Equilibria plot showing δ versus $\log pO_2$ for $YBaCo_4O_{7+\delta}$ equilibrated at 320, 350, and 380°C..... 146

Figure 6.10 – Scatter plot showing the change in cell parameters of $YBaCo_4O_{7+\delta}$ versus temperature, used to calculate the thermal expansion co-efficient..... 148

Figure 6.11 – XRD waterfall plot of $YBaCo_4O_7$ upon (a) heating and (b) cooling between 430 and 200°C with a rest of two hour at each recorded temperature at a pO_2 of 1 bar with flow rated of 150 ml/min (S.T.P.) The green line marks the peaks of the orthorhombic phase growing in..... 149

Figure 6.12 – Scatterplot showing the weight percentage of $YBaCo_4O_7$ in the hexagonal or orthorhombic phase in a pO_2 of 1 bar upon heating and cooling..... 150

Figure 6.15 – Scatterplot showing temperature at which a sample of YBaCo_4O_7 lost its orthorhombic phase upon heating (red) or grew it upon cooling (blue). A strong correlation between the growth and dissolution of the orthorhombic phase as a function of $p\text{O}_2$ was found, with a notable shift in the temperature of growth and dissolution of 30°C , between 0.05 and 1 bar.....	153
Figure 6.16 – Scatterplot showing wt.% orthorhombic versus δ for $\text{YBaCo}_4\text{O}_{7+\delta}$ annealed at 310°C . It can be seen, that the orthorhombic phase was seen to grow in at a δ of 0.3-0.4.....	154
Figure 6.17 - Plot showing δ versus temperature from TPOs of samples of $\text{YBaCo}_4\text{O}_{7+\delta}$, annealed at 310°C in a $p\text{O}_2$ of 0.21 bar, heated between 50 to 500°C in argon at a heating rate of $1^\circ\text{C}/\text{min}$. Different temperatures of oxygen release are apparent for the different oxygen contents.....	155
Figure 6.18 - Plot showing temperature of oxygen loss versus wt.% of the material in the orthorhombic phase, for the data shown in Figure 6.17.....	156
Figure 6.19 – Arrhenius plot for TG data collected at a $p\text{O}_2$ of 0.21 bar.....	157
Figure 6.21 – Plot of Chemical potential of oxygen relative to a $p\text{O}_2$ 0.21 mol oxygen in $\text{YBaCo}_4\text{O}_{7+\delta}$ versus δ at temperatures between 320 and 380°C	160
Figure 6.22 (a) - plot of $-\ln p_2 p_1$ versus $1/T$ for δ 's of between 0.1 and 0.6, (b) – Plot of the standard partial molar entropy (ΔS°) and enthalpy (ΔH°) versus δ ...	162
Figure 6.23 – plot of $-\ln p_2 p_1$ versus $1/T$ for a $\delta = 1.1$, comparing the data obtained in Figure 6.6? upon heating and cooling in a $p\text{O}_2$ of 0.25 and 0.42 bar...	163
Figure 6.24 – Plot of $\Delta\mu$ versus temperature for $\text{YBaCo}_4\text{O}_{7+\delta}$ calculated using Eq.6.13, using the values of ΔS° and ΔH° shown in Table 6.1.....	165
Figure 7.1 – Dynamic TG curves showing the mass change versus temperature of $\text{YBaCo}_4\text{O}_{7+\delta}$ heated at a ramp rate of $1^\circ\text{C}/\text{min}$ in (a), $p\text{CO} = 0.05$ bar, (b), $p\text{H}_2 = 0.05$ bar, (c), $p\text{CO}_2 = 0.5$ bar (balance He). Inserts show XRD results of fresh powder and powder after each treatment. Peaks corresponding to barium carbonate are identified by a ★	180
Figure 7.2 (a) - TG curves showing δ versus time for isothermal holds of $\text{YBaCo}_4\text{O}_{7+\delta}$ held in a $p\text{O}_2$ of 0.21 bar between 270 and 330°C , (b) – TG curves showing δ change versus time for isothermal holds of $\text{YBaCo}_4\text{O}_{7+\delta}$ held in helium at	

temperatures between 270 and 330 °C after oxygen incorporation shown in Figure 7.2(a).....	182
Figure 7.3 –TG curves showing δ versus time for YBaCo ₄ O _{7+δ} heated in hour-long 5 °C steps from 300°C to 430°C with pO ₂ s ranging from 0.05 to 0.42 bar after an initial 10 hour oxygen annealing in the same pO ₂	184
Figure 7.4 - TG curves showing δ versus time for YBaCo ₄ O _{7+δ} cycling between 120 minutes long holds in a pO ₂ of 0.21 bar at 310 °C (pale green rectangles) before being heated at a rate of 20°C/min to 430°C in a pO ₂ of 0.31 bar (pale blue rectangles).....	185
Figure 7.5 - TG curves showing δ versus time for isothermal holds of YBaCo ₄ O _{7+δ} held in a pO ₂ of 0.21 or 0.42 bar between 340 and 370°C	187
Figure 7.6 – Schematic show idealised methods for oxygen cycling using YBaCo ₄ O ₇	188
Figure 7.7 (a) - TG curves showing δ versus time for YBaCo ₄ O _{7+δ} cycling between 30 minutes long holds in a pO ₂ of 0.21 bar at 310°C (pale green rectangles) before being heated at a rate of 20°C/min to 370°C in an inert (pale blue rectangles), (b) TG curves showing δ versus time for YBaCo ₄ O _{7+δ} cycling between 30 minute long holds in a pO ₂ of 0.42 bar at 350°C (pale green rectangles) before being heated at a rate of 20°C/min to 370°C in inert (pale blue rectangles).....	189
Figure 7.8 – Change in the oxygen non-stoichiometry ($\Delta\delta$) per cycle versus the cycle number, for YBaCo ₄ O _{7+δ} cycling between a pO ₂ of 0.21 bar at 310°C and argon at 430°C The sample was heated from 310°C at a rate of 20°C /min in argon until 430°C, at which point the sample was held isothermally for 54 minutes to remove the incorporated oxygen. The sample was subsequently cooled in a pO ₂ of 0.21 bar to 310°C taking approximately 15 minutes, at which point the sample was held isothermally for 105 minutes	190
Figure 7.9 – Change in the oxygen non-stoichiometry ($\Delta\delta$) per cycle versus the cycle number, for YBaCo ₄ O _{7+δ} cycling between a pO ₂ of 0.21 bar at 310°C and argon at 430°C. The sample was heated from 310°C at a rate of 20°C/min in argon until 430°C, at which point the sample was held isothermally for 54 minutes to remove the incorporated oxygen. The sample was subsequently cooled in argon for 60 minutes until it reached 310°C. The gas environment was then switched from	

argon to a pO₂ of 0.21 bar where the sample was held isothermally for 120 minutes
..... 191

Figure 7.10 - Change in the oxygen non-stoichiometry ($\Delta\delta$) per cycle versus the cycle number, for YBaCo₄O_{7+ δ} cycling between a pO₂ of 0.21 bar at 310°C and argon at 430°C. For the first ten cycles, the sample was heated from 310°C at a rate of 20°C/min in argon until 430°C, at which point the sample was held isothermally for 54 minutes to remove the incorporated oxygen. The sample was subsequently cooled in argon for 60 minutes until it reached 310°C. The gas environment was then switched from argon to a pO₂ of 0.21 bar where the sample was held isothermally for 120 minutes. For the final ten cycles the sample was heated from 310°C at a rate of 20°C /min in argon until 430°C, at which point the sample was held isothermally for 54 minutes to remove the incorporated oxygen. The sample was subsequently cooled in a pO₂ of 0.21 bar to 310°C taking approximately 15 minutes, at which point the sample was held isothermally for 105 minutes. 192

Figure 7.11 – Change in the oxygen non-stoichiometry ($\Delta\delta$) per cycle versus the cycle number, for YBaCo₄O_{7+ δ} cycling between a pO₂ of 0.21 bar at 310°C and argon at 430°C. The sample was heated from 310°C at a rate of 20°C/min in argon until 430°C, at which point the sample was held isothermally for 54 minutes to remove the incorporated oxygen. The sample was subsequently cooled in argon for 60 minutes until it reached 310°C. The gas environment was then switched from argon to a pO₂ of 0.21 bar where the sample was held isothermally for 60 minutes
..... 194

Figure 7.12 – Change in the oxygen non-stoichiometry ($\Delta\delta$) per cycle versus the cycle number, for YBaCo₄O_{7+ δ} cycling between a pO₂ of 0.21 bar at 310°C and argon at 430°C. The sample was heated from 310°C at a rate of 20°C/min in argon until 430°C, at which point the sample was held isothermally for 114 minutes to remove the incorporated oxygen. The sample was subsequently cooled in a pO₂ of 0.21 bar to 310°C taking approximately 15 minutes, at which point the sample was held isothermally for 105 minutes. The black dashed line shows at which point the material underwent the helium pre-treatment. 195

Figure 7.13 – Change in the oxygen non-stoichiometry ($\Delta\delta$) per cycle versus the cycle number, for YBaCo₄O_{7+ δ} cycling between a pO₂ of 0.21 bar at 310°C and argon. During the first 15 cycles the argon reduction step occurred at 500°C, and the

subsequent 14 cycles the reduction step occurred at 430°C. The sample was heated from 310°C at a rate of 20°C/min in argon until the reduction temperature, at which point the sample was held isothermally to remove the incorporated oxygen. The sample was subsequently cooled in a pO₂ of 0.21 bar to 310°C taking approximately 20 or 15 minutes respectively for 500 and 430°C, after which point the sample was held isothermally for a total duration of 120 minutes..... 196

Figure 7.15 – Rate of oxygen release from YBaCo₄O₇ versus pO₂ for temperatures ranging from 370 to 430°C 199

Figure 7.16 – Plot showing pO₂ versus length as calculated using the model using step sizes of 1, 5 and 10 cm.201

Figure 7.18 – Plot of calculated data showing the change in δ versus length of a reactor bed of YBaCo₄O₇ treating a (a) 10 Mw, (b) 100 Mw, and (c) a 600 Mw power plant exhaust stream operating at 430 °C.....203

Chapter 1 – Application and production method of oxygen

1.1 The uses of oxygen

Over the last few decades, oxygen demand has increased significantly worldwide. In Japan alone, between 12.09 and 13.1 billion m³ of oxygen was produced each year between 2012 and 2017 [1]. The uses of oxygen are varied, and applications include medical treatments, the production of rocket fuel, and oxygen enhanced combustion processes to produce steel and glass. Table 1.1 below shows some of the more common uses of oxygen.

Table 1.1 – List of processes in which pure oxygen is used

Process	Reason
Medical applications	Oxygen is widely used in the medical industry to help manage respiratory conditions, by increasing the concentration of oxygen in the lungs, allowing for easier diffusion into the body, with documented uses as early as 1794 [2]. Additional applications such as hyperbaric oxygen therapy are also widespread [3]. With the current Covid-19 pandemic, the need has increased, and many countries are suffering shortages [4].
Welding	Oxy-fuel welding or oxy-fuel cutting, are techniques where fuel is mixed with pure oxygen and ignited to cut or bind metal. The advantage of oxy-fuel welding is a higher oxygen concentration, allowing higher flame temperatures [5].
Gasification	Gasification is a technique where a carbon-based fuel is partially oxidised in a mixture of oxygen and water vapour at high temperatures (approx. 700°C) [6]. This treatment produces syngas (a mixture of CO ₂ , H ₂ , and CO), along with water vapour. This technique is used to convert materials with low energy density (i.e. an organic waste or crop, such as switchgrass [7-8]), or simply a solid fuel such as coal into a high energy density gaseous fuel [9-10]. This is an essential step of pre-combustion CO ₂ capture, where after gasification, the concentrated CO ₂ is sequestered, and the hydrogen-rich fuel is combusted [11].

Ecological use	Oxygen or oxygen-enriched air is used in wastewater treatment, most commonly the activated sludge process [12-13]. The additional oxygen allows micro-organisms to digest waste faster, as the most common bacteria favour aerobic digestion. Higher oxygen concentrations allow for faster mass transfer rates of oxygen. The solubility of oxygen in wastewater also increases with higher partial pressures of oxygen (pO_2 s), described by Henry's Law [14], increasing oxygen concentration.
Regeneration of catalysts	Coke deposition on catalysts has severe impacts on performance for various chemical reactions [15-16], the degree dependent upon whether the carbon is deposited on the material's surface or at the active sites of the material [17]. Oxygen enriched air is used to regenerate the material, by burning the deposited carbon, as higher concentrations allow for faster combustion [18]. Similar results have been seen for H_2S and SO_x poisoning [19].
Chemical production	Oxygen is used as a precursor for many different chemical processes, such as in the production of an important precursor to polyvinyl chloride (PVC) - 1,2 dichloroethane [20]. This precursor is produced using the oxychlorination route, where ethane, hydrogen chloride, and oxygen-enriched air are mixed at 500°C.
Oxygen enriched combustion	Additional oxygen during combustion reduces capital and expenditure costs of multiple processes, by improving the efficiency of combustion. Benefits include improved flame stability with higher oxygen concentrations, increased fuel efficiency, and reduced CO production. The most efficient use of oxygen in these processes involves increasing the concentration of oxygen in the air stream to 30%, with limited benefits for higher concentrations [21-22]. This oxygen can either be added to the gas stream, or nitrogen removed from an air stream, to increase the relative oxygen concentration.
Oxygen enhanced	In the presence of a suitable catalyst, a small amount of O_2 co-fed with the WGS feed can improve the conversion of CO whilst

water gas shift	maintaining a high yield of H ₂ in the product stream [23-24]
Autothermal reforming	Oxygen is used to partially combust methane, providing the heat required for the otherwise endothermic methane reforming [25].
Claus process	Oxygen is used to convert H ₂ S to SO ₂ and water which can be further processed to allow recovery of sulphur and removal of acid gas from exhaust streams [26-28]
Ammonia synthesis	Oxygen enrichment can control the N ₂ to H ₂ ratio during ammonia synthesis, improving the reactor efficiency [29-30]
Oxy-fuel combustion	Combustion of fuel in a stream of CO ₂ and O ₂ instead of air can produce a CO ₂ -rich exhaust that can be easily captured with minimal gas separation and treatment [31]
Glass production	The melting kiln is fed oxygen-enriched air, both improving the fuel efficiency and reducing the NO _x and CO ₂ emissions of the process [32]
Biogas production	Biogas gasification to produce syngas often occurs using a two-stage method, similar to coal gasification. Pilot plant studies show that oxygen-enriched air increases the conversion of biomass to syngas [33] and additional studies have shown this increases the lower heating value of the final product gas and reduces problem char [34].
Oxygen enriched combustion	The use of oxygen-enriched air for fossil fuel combustion has been shown to increase the fuel efficiency for many different fuel types including methane, diesel, and coal [35-37]. Most air/fuel burners can adapt to run to oxygen concentrations of under 28% with no modifications to the system, and this adaptation has significant impacts on the combustion [38-39].

Fluid catalytic cracking (FCC)

FCC is an important industrial process, converting low-value heavy hydrocarbons into higher-value products such as gasoline. During operation, zeolite catalysts used for the process will deactivate due to coking [40]. High reactivity can be restored to these materials by burning off the carbon, and studies have shown oxygen enrichment of the combustion air by 5% is the most efficient concentration for the process [41]

Table 1.1 demonstrates the importance of oxygen for many industries. From the examples shown, oxygen within a process rarely needs to be of high purity. For industrial purposes, high mole fraction oxygen is often produced and transported, to then be blended or mixed with a process gas to achieve a mol fraction of $\approx 30\text{-}40\%$ for most oxygen enrichment or oxygen enhanced combustion processes. Producing gas mol fractions of 30-40% *in-situ* would be preferable, rather than obtaining, storing, and mixing pure oxygen. This is for several reasons namely, reducing required transport, improving site safety, and supply chain considerations.

The next section, reviews in detail three major industrial processes which benefit from oxygen enrichment. These are oxy-fuel combustion, steel and glass production, and the Claus process. The aim is to highlight the potential benefits of the addition of pure oxygen into a process gas stream and the potential factors that must be considered when designing systems.

1.1.1 Oxy-fuel combustion

Over the last 50 years, the amount of CO₂ and other greenhouse gases in the atmosphere has increased substantially. This increase in greenhouse gases has caused a significant rise in global temperatures [42-43], leading to a variety of potential issues, such as rising sea levels and drought. There has been widespread concern from many nations, leading to the forming of several important legislation, limiting greenhouse gases from each country (i.e. The Paris Agreement and The Kyoto Protocol [44-45]).

While there has been much progress in developing low CO₂ technologies, such as solar cells and tidal power [46-47], no technology is currently able to completely replace fossil fuels. Biofuels have been examined to potentially replace fossil fuels, however, several issues such as large variability in water content and energy density make application difficult [48]. Additionally, biofuels raise environmental concerns and require large amounts of water for growing the fuel [49]. Promising results for co-fed furnaces mixing fossil and biofuels, to

lower the carbon footprint of processes are in the early stages of development, but offer potential improvement [50].

Perhaps more importantly, the amount of new infrastructure required to replace fossil fuel is significant, when industrial and societal requirements are examined. Therefore the cost of completely replacing fossil fuels is thought by many to be too large [51]. For this reason, carbon capture and storage is one of the preferred technologies for reducing greenhouse gases.

There are four main branches of carbon capture and storage (CCS), describing multiple technologies. These are:

- Capturing CO₂ released post-combustion – namely separating the products of combustion using membranes or scrubbing technologies (using liquid solvents such as monomethylamine or mineral salts) [52-53]
- Capturing CO₂ released pre-combustion– during gasification, carbon-based fuels are partially combusted to produce a mixture of H₂ and CO (with some CO₂). After this step, the CO is further combusted to CO₂, which is then separated before the combustion process, leaving a high-quality hydrogen gas stream [54-55]
- Chemical looping combustion – This process uses a solid oxygen carrier (such as iron oxide), which reacts with a fuel producing a high purity exhaust stream which can then be captured easily, with the oxygen carrier going from its oxidised state to a reduced state. The oxygen carrier can then be recovered by reacting with air to re-oxidise [56-57].
- Oxy-fuel combustion – this process involves the addition of oxygen into a recycled exhaust gas in which the combustion occurs. This produces a CO₂-rich exhaust stream with no nitrogen present, which can then be easily captured. [58-59].

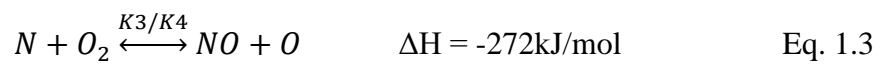
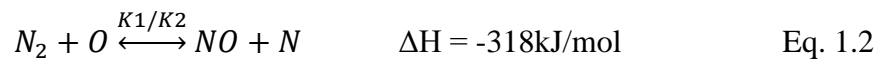
The oxy-fuel combustion process (often known as the O₂/CO₂ recycle process) was first suggested by Abraham et al. to produce large quantities of high purity CO₂ for the facilitation of enhanced oil recovery (EOR) [60]. However, Horn and Steinberg discussed the method with a greater focus on capturing the emissions from fossil fuels [61].

A significant issue with combustion is that the oxidising stream is typically air, which is composed of a mixture of oxygen and nitrogen along with other impurities. As nitrogen is not involved in the oxidation of a hydrocarbon fuel, this unreacted nitrogen exits along with the CO₂ exhaust stream as shown in Eq.1.1, diluting the final product stream.



This reduction in the $p\text{CO}_2$, due to the diluting nitrogen, increases the cost and difficulty of capturing CO_2 with traditional capture techniques [62]. In the oxy-fuel combustion process, as no nitrogen is used in the process significantly easier capture of the exhaust is found.

Air-based combustion may also produce NO_x via the Zeldovich reaction (Eq. 1.2-1.3) due to the large presence of nitrogen in the furnace chamber [63]. NO_x is a harmful gas, causing acid rain and ozone smog if released into the atmosphere. The release of NO_x to the atmosphere is controlled under stringent environmental regulations, requiring additional exhaust cleaning processes to remove.



Oxy-fuel combustion has been shown to reduce the amount of NO_x produced, due to the reduction of nitrogen in the system, as well as the flame temperature of the process [64-67]. Further reductions have been found by staging oxygen addition, to maintain a high $p\text{O}_2$ throughout the reactor [68]. Improvements in SO_x removal during de-sulfurization are also reported, due to sulphates condensing from the flue gas [66]. However, SO_2 remains an issue for the process, and novel systems are still being implemented to mitigate this [69]. Air leaks into the system also cause issues, particularly with older retrofitted furnaces [70]. Leaks increase the nitrogen content of the gas stream, reducing the efficiency [71].

Studies show that a minimum $p\text{O}_2$ of 0.3 bar is required for oxy-fuel combustion [66-67], due to the higher heat capacity of CO_2 . Lower $p\text{O}_2$ s do not facilitate combustion, snuffing the furnace flame, while excess oxygen ratios are seen to give more complete combustions [72]. Water must generally be removed from the system for gaseous fuels, as higher water content shifts the ignition temperature of methane to higher temperatures due to dilution [73]. With solid fuels, this is not seen to be a concern [74]. Some papers promote increasing steam concentration with solid fuels, reporting lower ignition and burnout temperatures of the solid fuel when 20% of the CO_2 is replaced with steam [75]. Water in the stream can also give beneficial impacts on the removal and treatment of SO_2 [76]. It has also been shown that for oxy-fuel combustion, waste minerals such as calcium are also more likely to form carbonates – which are more likely to slag [77].

Heat transfer from a furnace is also less efficient in oxy-fuel combustion. This is due to lower furnace temperatures, caused by a higher specific temperature of the gases [78], as well as the actual mechanical design [79]. Particle temperatures of the fuel are also lower for combustion

in an O₂/CO₂ mixture – although this has been seen to give less sooty flames due to CO₂ promoting a low devolatilization rate of organic material [80]. Burnout time and temperature are lower in an oxy-fuel system, but this can be mitigated by increasing the pO₂ [81].

Several pilot studies of the oxy-fuel combustion process have been conducted by the Argonne National Laboratory [82] as well as The International Flame Research Foundation (IFRF) to examine the potential of the process [83]. The IFRF during their study concluded that the process was feasible and that the radiative and convective heat transfer between an oxy-fuel and traditional air-fed furnace were similar. Flame stability, combustion performance, and gas composition were also found to be similar and a recycle ratio of 0.61 between the recycled gas and new oxygen was found to be the optimum configuration (although this value was found to vary somewhat with different fuel stocks) [83].

A major advantage of oxy-fuel combustion over other CCS technology is the ability to retrofit existing furnaces, allowing easy implementation [84-85]. The major downsides are additional costs and energy penalties. These issues arise from the compression of CO₂ and the cost of producing oxygen to enrich the recycled flue gas. The Institute of Carbon Capture and Storage estimated that oxy-fuel combustion could require up to 25% of the energy produced during a powerplants operation [86]. Oxy-fuel combustion has large capital costs associated with the start-up of a plant, however, several studies have shown that retrofitting existing plants is cheaper than other carbon capture methods [87-88]. In these studies, the costs per tonne of CO₂ captured were estimated to be \$55 for traditional air combustion with post-combustion MEA scrubbing as opposed to \$35 for oxy-fuel combustion. Sensitivity analysis showed the biggest decrease in costs would come from a reduction in the cost of oxygen separation. Recent studies have shown membrane separation of oxygen can be competitive at small scales for this process, however larger air separation units – typically cryogenic processes, are still more cost-effective at a large scale [89]. The energy costs of these processes are large and greatly increase costs.

There are multiple engineering schemes of oxygen enrichment and CO₂ capture for an oxyfuel combustion system [90]. One of particular interest is the Allam cycle. In this scheme, fuel is burned with oxygen and supercritical CO₂. A high-pressure exhaust feeds a turbine expander creating a subcritical CO₂ mixture containing water. This fluid is cooled in a heat exchanger, heating the recycled CO₂ stream. The water is condensed out, leaving high purity CO₂ which can be compressed and recycled, or removed and captured [91].

Further improvements of operating schemes are ongoing, with researchers attempting to utilize the oxy-fuel combustion exhaust gases. Tri reforming of methane is one method researchers are looking to use exhaust CO₂ streams for. This involves simultaneous dry and steam reforming, as well as partial oxidation of methane, producing syngas [92]. The use of the oxy-fuel exhaust stream is suitable for this due to the high concentration of CO₂ and lower concentration of N₂ compared to the traditional air combustion exhaust stream [93]. Additionally, the higher average oxygen content of the oxy-fuel exhaust gases is also seen to prevent coke formation during tri-reforming [94]. It has been shown that using an oxy-fuel combustion exhaust stream for the process converted 3 times more CO₂ per mole of methane [95]. Similarly, gasification of biomass has been examined and found to be a promising use of the exhaust stream [96].

The combustion of “dirtier” fuels such as coal is of particular interest for oxy-fuel combustion. It has been seen that the combustion of coal in an oxy-fuel combustion system is more efficient than that of biomass [97], although due to the environmental issues with coal the desire to use this as a feedstock is decreasing. To mitigate this, dual feed of biomass and coal has been examined in oxy-fuel combustion systems, and biomass addition of 30-50% was found to improve the combustion, due to increased combustion temperatures at the bottom of the bed [98].

1.1.2 Claus process

Hydrogen sulphide is a dangerous gas that in the atmosphere leads to the formation of acid rain, damaging local environments, as well as having toxicity comparable to carbon monoxide. H₂S is often found as an impurity of many fossil fuels, such as natural gas or crude oil, requiring removal. One technique for the removal of this gas is the Claus process. The Claus process oxidises H₂S through a two-stage reaction [99] shown in Eq. 1.4 and 1.5 producing water and sulphur. The Claus process is additionally the most common method to produce sulphur worldwide.



Sulphur is an important precursor for many chemical processes. The most common use is to produce sulphuric acid for fertilisers; however, it is also used for steel and rubber production as well as in cement, explosives and matches. To show the size of the market, Table 1.2 presents the amount of sulphur exported from the top five sulphur producing countries in 2015 [100].

Table 1.2 – List of top five sulphur producing countries and the value of exports in 2015

Country	Sulphur exports in 2015 (U.S.\$)
United Arab Emirates	\$545,797,000
Russia	\$346,775,000
Qatar	\$331,387,000
Canada	\$312,511,000
Kazakhstan	\$286,992,000

The first of these reactions is known as the thermal treatment step [101]. During this step, the H₂S is oxidised, releasing large amounts of heat and creating large amounts of SO₂. Typically, 1/3 of the process gas undergoes this first reaction to maintain the correct gas ratio for the second step of the process, during which SO₂ and H₂S are reacted to produce the elemental sulphur. This process has thermodynamic limitations, so the removal of water from the feed gas is desired [102]. This occurs at high temperatures of approximately 1050°C [103] and any hydrocarbon present in the feed must be effectively removed, as these can have negative impacts on the catalysts [104-105].

After the thermal step, the high-temperature gas is passed into a waste heat boiler [106]. This step is to recover the energy from the thermal step, and high-quality steam of approximately 50 bar is produced. The sulphur produced during this step is then cooled and collected in a condensation unit before passing to the next step.

The second step is the catalytic step, where the reaction shown in Eq1.5 occurs in the presence of a catalyst such as activated aluminium or titanium oxide [107]. This is typically performed three times for higher yields, with each step being cooler than the one previous, the first staying at 330°C, with subsequent steps at 240 and 200°C. The exhaust gases after these steps are cooled, allowing condensation and collection of elemental sulphur.

The above reactions only remove 94-97% of the H₂S in the gas stream [108], meaning additional treatment such as adsorption or absorption towers are required to meet most environmental regulations [109]. Additionally, this process is suitable for a feed gas with an H₂S content of greater than 25%, gas separation and treatment are required for lower H₂S contents.

Additionally, the hydrogen content of the stream is wasted, and the process forms low-grade steam instead of a usable product [110-110]. There have been several other recommendations to improve this process, including the use of oxidative catalysts instead of porous alumina [112-113] which operate at 100 – 300°C, and the thermal decomposition of H₂S to produce hydrogen following Eq. 1.6 below [14].



Reaction 1.6 is endothermic, requiring additional energy to become favourable meaning that high temperatures are needed [15]. To enable this, it has been proposed to couple the thermal decomposition and oxidation reaction of H₂S, balancing the energy requirements of the process.

Oxygen enrichment for the Claus process is commonly used as a method of increasing the furnace temperature during the thermal step [116-117]. Studies have shown that the oxidation rates of H₂S increased with the increasing pO₂'s, with the additional benefit of reducing the number of side products [117]. Additionally, this oxygen is used to prevent more stable hydrocarbons such as benzene from damaging the catalyst, by allowing temperatures above 1050°C to be reached [118].

1.1.3 Oxygen enriched combustion

The thermal efficiencies of many high-temperature combustion processes, such as glass or steel production are low, with studies estimating a thermal efficiency, (i.e. useful heat to produced heat), of 20 – 30% for glass production [119]. There are many reasons for this low efficiency ranging from the start -stopping of the furnace or changing production requirements. Most of this wasted energy originates in the flue gases, which can account for 30 – 50% of the wasted energy [120].

One method to improve the efficiency of a furnace is an increase in the pO₂ of the combustion furnace. Chen et al. found that increasing the oxygen concentration reduced the fuel consumption by 26% in an industrial-style furnace [121]. Increasing oxygen concentration above 25% however, often does not give significant improvements to a process, as the amount of fuel saved does not cover the cost and energy required to produce the pure oxygen [122].

Additionally, oxygen excess in the furnace may decrease the formation of NO_x, a significant issue when using coal as a fuel source [123]. This additional oxygen can give significant improvements to the stability of a flame [124].

Typically, oxygen is added into a flowing gas stream, before it reaches the furnace as this is cheap and easy to retrofit, although higher efficiencies can be achieved by injecting the oxygen directly into the furnace itself [125].

Many processes use oxygen enrichment to allow the furnaces to reach higher temperatures or to reduce fuel consumption in their high-temperature furnaces, most commonly:

- Steel production
- Glass production
- Lime kilns
- Power generation

1.1.4 Conclusions on the use of oxygen within industrial processes

Many processes benefit from oxygen enrichment, and that there is a growing need within industry for oxygen enrichment in the 21 – 30% range to improve efficiencies. It is also clear that the more widespread use of these processes is hampered by the high cost of pure oxygen.

1.2 Methods of oxygen production

At present, there are four main methods used to produce oxygen, dependant on the scale and quality of oxygen required. These methods of oxygen production are;

- Cryogenic distillation
- Pressure swing adsorption
- Membrane separation
- Chemical separation

In this section of work, a review of these methods will be conducted.

1.2.1 Cryogenic distillation

Cryogenic distillation was first conceived by Michael Faraday in the late 1800s. Faraday studied the decomposition of solidified chlorine crystals with large quantities of water present. Upon heating to 100°C, the water and chlorine separated forming two layers upon cooling, which he could easily distill from each other. This occurred at temperatures at which the chlorine should have been in the gas phase. Faraday hypothesised that the pressure caused by the heat and separated water vapour prevented chlorine from becoming gaseous. He confirmed his theory by pressurising chlorine gas within a capped syringe and condensing it [126]. From this simple concept, the technology was derived.

During air separation by cryogenic distillation, air is filtered before compression. This removes most water, with the rest removed through a molecular sieve. This sieve, as well as removing the water, also lowers the amount of CO₂, as both gases would freeze and block the piping during the process. Additionally, hydrocarbons are removed, as during the purification these may reach high concentration, causing potential explosion hazards [127]. The gas is cooled and reheated, giving a nitrogen-rich gas and oxygen-rich liquid (alongside argon and other gases). The boiling temperatures of nitrogen, argon, and oxygen -195, -186 and -183°C respectively, so fine control is needed. For increased purity, secondary or tertiary distillations may be required, with each additional distillation improving purity.

Cryogenic distillation requires large distillation columns, and the process is energy-intensive, making it suitable for large-scale processes [128]. This technology is considered developed, with most current research on reducing losses from the processes and stored gases [129] or improving efficiency. Improvements in process efficiency rely upon integration with other processes such as oxy-fuel combustion [130-131] or recuperation of the heat added [132]. Combining cryogenic distillation with the vaporisation of liquified natural gas (LNG) [133] is one integration method of much interest. LNG is typically stored at ambient pressure, at temperatures of -162°C, and the energy required for refrigeration is often wasted when the gas is vapourised. Combining cryogenic distillation with this vaporisation, recovers the energy, and has been shown to give energy savings of 38% [134]. This is an area of much interest, and work to optimise the combination of processes is ongoing [135]. Another novel idea is to produce pure (>99%) and impure oxygen simultaneously in the system using a single column dual purity plant [136]. This can be performed by drawing oxygen from a few plates above the liquid oxygen and was found to improve oxygen recovery from 91.7 to 99% [137].

Another promising method of reducing losses is the use of a heat-integrated air separation column. This unit has a high-pressure and low-pressure column, with intermediate heat exchangers installed between them acting as side reboilers and condensers [138]. Many fundamental studies on the equipment design of such a unit are ongoing, with significant capital investment savings being found by re-evaluating the position of heat exchangers in the columns [139].

Faheem et al modeled air separation units, separating 500 tons/h of air with 50% relative humidity, to produce 99 mol.% of N₂ and O₂. Their results showed compression was the greatest cause of exergy destruction, and up to 46% of the total exergy destruction occurred here [140]. This conclusion is supported through the literature [141] and novel solutions to improving efficiency are being researched. Waste heat from the compression is a major loss,

and this is often unrecovered. Recovery of this heat is difficult for two main reasons [142]. Firstly, the heat is lost in the form of low-temperature outlet air (approx. 100°C.). With such low-grade heat, finding appropriate ways to recover this is difficult. Some researchers suggest using this energy for heating and other domestic tasks, however finding an appropriate infrastructure to support this would be likely unfeasible in most cases. Secondly, any change of the air compressor design for heat recovery may cause condensation to be generated which can damage the compressor. One promising solution proposed is the use of an organic Rankin vapour compression cycle to recover this low-grade heat as work [143], and the results look promising – however, this does come with an increased initial capital cost for the units.

Compression of the gases is of course not the only area where savings can be achieved. Chowdury et al. examined the impact of changing heat exchangers from a coiled to plate-fin design and found that energy savings of approximately 6% could be theoretically achieved [144]. It should be noted however the authors did clarify that plate-fin units were only commercially available for medium-sized units more suitable to pipeline supply than small plants for cylinder supply.

As cryogenic distillation has so many different simultaneously operating unit steps in the process (i.e., compression, adsorption, cooling, condensation, liquefaction, evaporation, and distillation), modeling and designing these units is difficult and papers examining ways to model the process are still of scientific import today, despite the developed nature of the technology [145]. One major issue with the technology is how small errors in the equations of state, can have a significant impact on the design, with mistakes in calculating the properties of gas mixtures causing significant problems with simulations or operational controls – particularly at conditions near the critical point of gases [146].

1.2.2 Pressure swing absorption (PSA)

PSA was first conceived in the 1960s, by Skarstrom and de Montgareuil [147-148]. Air separation by adsorption uses the natural affinity of materials (most commonly zeolites) to preferentially adsorb nitrogen onto the material's surface, increasing the purity of oxygen in the air stream. This has proved an effective technique for the easy production of oxygen. During this method, an airstream passes through a bed of sorbent material, which preferentially removes nitrogen from the gas stream. The material is regenerated by reducing the pressure or changing the temperature.

Several materials have been used for this process, such as carbon molecular sieves [149] or different zeolites, such as NaX, 5A, Na- Mordenite, CaX, and CaLSX [150] which all have

preferential adsorption of nitrogen over other gases. The main issue with these materials is that the advantageous property that allows for rapid adsorption of nitrogen, prevents the rapid desorption of nitrogen from the material. This means large volumes of material within multiple beds are required for a continuous process, as the time taken for the regeneration of the material, is longer than its operational time. These materials are also vulnerable to contamination and water vapour can have significant detrimental effects on the performance of zeolites [151]. PSA for oxygen production often produces a less pure oxygen stream compared to cryogenic distillation (typically 90%), however, it is generally thought to be cheaper and easier to make site-specific than cryogenic distillation [149]. Typically, PSA is thought to be suitable for small operation units, however a recent study by Ditl et al. questions this. In their study, they found producing oxygen onsite in Germany was 1.33 times more expensive than ordering a liquid oxygen supply, for a small oxy-fuel combustion process [152]. The reason given for this was significantly more expensive electricity prices for smaller consumers. It was also shown in the Czech Republic, the prices for an imported liquid oxygen supply, and operation of a PSA unit were approximately even.

Even with how advanced the technology is, work is still ongoing to optimise the design of PSA systems. Chou et al have examined using two semi-circle-shaped units, with one side desorbing, and the other absorbing at a given time. This was seen to give easier heat compensation between the units, increasing the oxygen purity [153], as the temperature of the gas of a PSA unit is known to have a significant impact on the purity of gases produced [154]. It is also seen higher pressures lead to higher purity of oxygen [155], but also require greater energy requirements from compressors. Some investigators look to recover heat from the compressors to improve efficiency, and one such study examined using this waste heat for several processes and found that it was suitable for dewatering lignite and other biofuels. [156]

1.2.3 Membrane separation of air

Membrane separation of air is an area with the potential to reduce energy costs significantly compared to cryogenic distillation, as no liquefaction of gases is required. There are several different methods of using membranes for this purpose.

Polymeric membranes typically operate by a solution diffusion, where the species to be transported will dissolve into the polymer and be transported across the membrane. The major issue with this technology is that they are not fully selective, and nitrogen can also be transported through the membrane. This is described by the Robeson upper limit, which is an empirical relationship between the selectivity of a membrane, and the permeability [157]. The

membranes are therefore generally only used for oxygen enrichment of air, typically achieving oxygen concentrations of 25 – 40% [158], or for nitrogen production. Some of the more common polymeric membrane materials are polyimide and polysulfone [159]. These membranes have been seen to be cost-effective at smaller scales [160], although suffer upon scaling up. Studies have shown however that oxygen separation using polymeric membranes is not as efficient as other air separation methods, due to the low to moderate purity of the permeate gas. To improve the oxygen concentration of the permeate gas, multiple membrane modules are required in series [161], increasing capital and operating expenditure.

One method of interest for exceeding the Robeson upper limit is the use of pore-flow membranes. These membranes separate based on the size of a molecule, but this is difficult due to the similar size of oxygen and nitrogen (0.346 and 0.364 nm respectively) [162]. The use of a metallic organic framework is one such example of overcoming the Robeson upper limit [163]. These are organic–inorganic materials with specific pore sizes which allow size-sieving. The two ways to use these materials are as a pure film, or as a filler in a polymer matrix to create mixed-matrix membranes [164]. The addition of these materials to polymers has additional impacts bar improving gas separation and has been noted to prevent plasticization of glassy polymers, which lowers performance [165]. Similar results have been found in producing carbon molecular sieve membranes, which have zeolites added to the polymer, and Bae et al found this increased oxygen permeance by 20% [166] Other examples of novel materials with promising results are graphene sheets with nano-windows introduced into the structure, allowing for gas diffusion [167], or carbon membranes, which have been shown to produce oxygen-enriched air with 78% purity, and a nitrogen stream with 99.5% purity by Hagg et al [168].

Ion transport membranes are typically made of inorganic non-stoichiometric materials which can allow selective transport of oxygen ions across themselves by a pO_2 gradient or sometimes an electrical voltage [169]. Ion transport membranes typically transport oxygen at rates, orders of magnitude greater than their polymeric counterparts. Perovskite materials are still considered the best performing material for this, however further studies on other materials such as Ruddlesden-Popper are ongoing [170]. These ion transport membranes also operate at significantly higher temperatures than polymeric membranes, with operating temperatures of approximately 800°C, compared to less than 200°C for polymeric membranes. One material of interest is barium strontium cobalt copper oxide, which was found to perform extremely well in a recent study. It was thought that this was due to the segregation of copper, forming intergranular copper-rich oxide between perovskite grains

[171]. It has been seen however that some of the materials thought to be most suitable for this (i.e. $\text{La}_{0.6}\text{Sr}_{0.4}\text{Co}_{0.2}\text{Fe}_{0.8}\text{O}_{3-\delta}$) can degrade over time when not in use [172].

The ideal morphology of an ion transport membrane is as a hollow fiber, where multiple ceramic tubes carry the gas to be separated within a sweep gas on the other side. The gas to be removed can then permeate from one side of the fiber to the other. Hollow fiber membranes give the largest surface area to volume ratio of ion transport membranes; however, this morphology is prone to cracking which causes leaks in the membrane. Work is ongoing to create self-healing membranes that can repair leaks; however, these are currently in early development. Sealing is a major issue, with leaks reducing the efficiency of the separation step [173]

Molten oxide membranes are another technology of interest. These rely upon intergranular liquid channels which high ionic conductivity. They have also been found to have low risks of leaking/breakage due to the molten liquid plugging any cracks. The molten component is typically Bi_2O_3 or V_2O_5 in these materials [174].

While currently not suitable, increasing natural gas prices or reduction in compressor costs were found to make membrane separation viable for oxygen-enriched combustion [175].

1.2.4 Chemical separation of air through redox cycling

Chemical separation of air typically involves the use of an air-reactive chemical (such as MOLTOX), which can absorb and desorb oxygen by changing the temperature or $p\text{O}_2$. The major advantage of this technique is that oxygen separation can occur at low operating pressures, as only pressure drops through the system need to be accounted for [176]. However, this process has never been fully commercialized due to difficulty in working with molten salts.

Solid metal oxides and non-stoichiometric materials are currently gathering interest for a chemical looping air separation (CLAS) due to the ease and selectivity of the oxygen carriers [177-178]. CLAS allows materials to undergo redox cycling to selectively incorporate oxygen from an oxygen-rich gas stream, before releasing it through changes in the $p\text{O}_2$ or temperature of the system. CLAS using non-stoichiometric materials claims to improve the efficiency of air separation processes by 74% compared to that of cryogenic distillation [179]. It has also been reported that this process can reduce the energy costs for a working oxy-fuel combustion plant by up to 50% [180]. Figure 1.1 shows a schematic of the process.

Chemical separation of air typically involves the use of an air reactive chemical (such as MOLTOX), which can absorb and desorb oxygen by changing the temperature or pO_2 . The major advantage of this technique is that oxygen separation can occur at low operating pressures, as only pressure drops through the system need to be accounted for [176]. However, this process has never been fully commercialized due to difficulty in working with molten salts.

Solid metal oxides and non-stoichiometric materials are currently gathering interest for a chemical looping air separation (CLAS) due to the ease and selectivity of the oxygen carriers [177-178]. CLAS allows the material to undergo redox cycling to selectively incorporate oxygen from an oxygen-rich gas stream, before releasing it through changes in the pO_2 or temperature of the system. CLAS using non-stoichiometric materials claims to improve the efficiency of air separation processes significantly compared to that of cryogenic distillation [179]. It has also been reported that this process can reduce the energy costs for a working oxy-fuel combustion plant by up to 50% [180]. Figure 1.1 shows a schematic of the process.

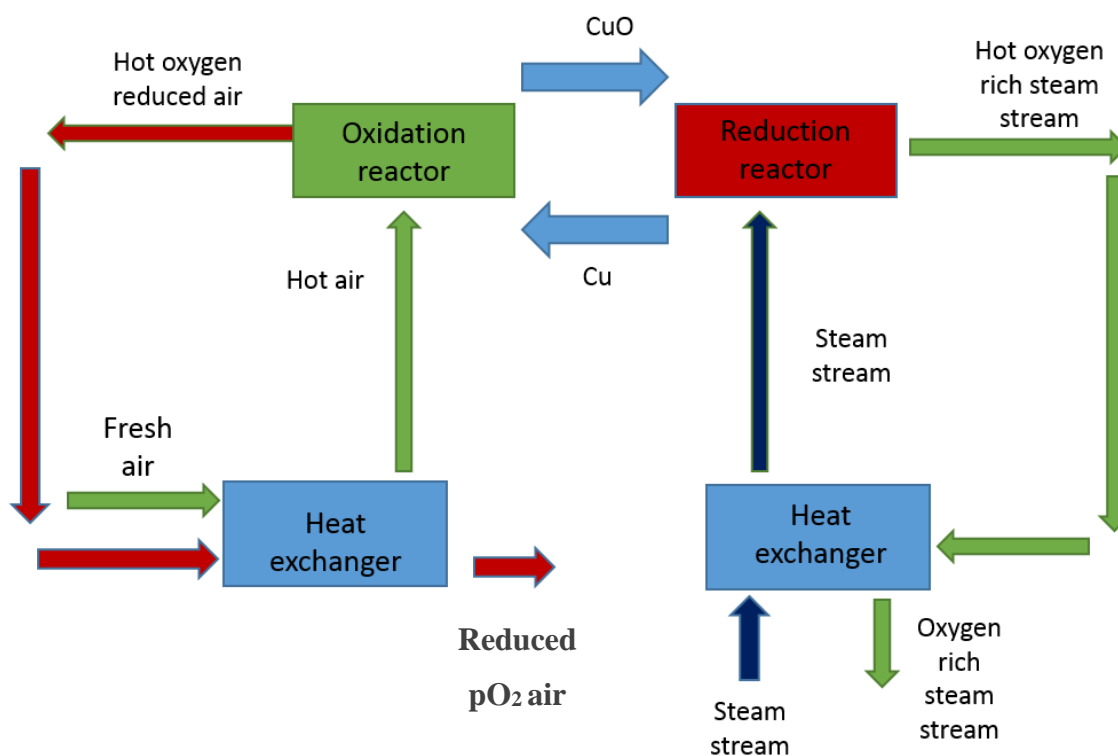


Figure 1.1 -Schematic of the CLAS process

As seen in Figure 1.1, the oxygen carrier is cycled between two connected reactors. In the first reactor, oxygen is incorporated into the material from an air stream, following the reaction shown in Eq.1.7, using copper as an example oxygen carrier.



The oxygen-rich material is then sent to a second reactor where the oxygen is released, due to an increase in the temperature following the reaction shown in Eq. 1.8.



This released oxygen is carried from the reactor using a stream of high-temperature steam. The steam in the steam/oxygen mixture is then condensed to leave a high purity oxygen stream.

The energy required by the process should be balanced, as the energy of the forward and reverse reaction should be recovered and recycled [181]. The major energy requirements come from the pre-heating of the air stream for the oxidation reactor, or by the production of the superheated steam. The energy for both processes can be recovered using a series of heat exchangers, however, this adds to the capital costs and the complexities of the system. Additionally, as oxygen carrier materials will release oxygen to a certain partial pressure of oxygen at different temperatures, it is possible to thermodynamically tune the amount of oxygen in the system by setting the temperature and pressure of the system correctly. This can allow the production of $\approx 30\text{-}40\%$ mol fraction gases *in-situ*, making the process advantageous for producing the mol fractions required for oxygen enrichment processes.

Aims to improve the process focus in two major directions. The first is looking to combine the process with other steps in a power plant. Moghtaderi et al. found that replacing a cryogenic-based air separation unit with a CLAS unit, integrated with heat recovery reduced the average power by 47% [182]. In a more novel approach, Kuo et al. proposed co-generating oxygen, nitrogen, and electricity simultaneously to reduce energy penalties [183]. Although more like a chemical looping combustion process, a method of significant interest in combination with a supercritical CO₂ cycle to produce power [184], and from economic assessments, this has been seen to have potential due to lower capital cost, and energy use [185]

Combinations of CLAS and oxy-fuel combustion have been studied in detail [186-187], and thermodynamic assessments have seen low energy penalties [188]. The integrated process can be quite efficient, with an estimated 90% of CO₂ captured [188]. It was found that in the economics of the process, a high carbon tax and electric price are two of the major factors that impact whether the process is feasible [190].

Currently, work is ongoing to find the most suitable oxygen carrier for the CLAS process, and a range of traditional and novel materials are currently being investigated, which will be discussed in Chapter 2.

1.3 Conclusion

From a review of major industrial processes, reducing the production cost of oxygen would have a significant impact on production costs. Additionally, this reduction would make oxy-fuel combustion, a technology with strong potential to lower greenhouse emissions, significantly more attractive.

Oxygen separation technologies such as cryogenic distillation are well developed, but these processes are often energy-intensive, which increases the cost of oxygen. Technologies such as CLAS and ion transport membranes which have the potential for site-specific and cheaper oxygen production are reaching competitive levels. Work is still ongoing to find the most suitable oxygen carriers for the most promising process, redox cycling of oxygen carriers.

In this work, oxygen carriers for the CLAS process will be examined and reviewed, to enrich an oxy-fuel combustion gas stream. The first step in this will be to find potentially useful materials for further detailed studies. These studies will aim to provide a feasibility study of the material, examining the kinetics, stability, and thermodynamics, and then compare these to other oxygen carriers, to decide if the material has potential.

1.4 References

- [1] Production volume of oxygen in Japan from 2012 to 2017 (in billion cubic meters) – Statista, retrieved from <https://www.statista.com/statistics/737094/japan-oxygen-production-volume/>. Accessed 14/11/2018.
- [2] T.Beddoes, J. Watt - Considerations of the medical use of factitious airs, and on the manner of obtaining them in large quantities, 1794, Bristol: Bulgin and Rossier
- [3] L.K.Weaver - Hyperbaric oxygen therapy indications, 13th edition, 2014, the hyperbaric oxygen therapy committee report
- [4] S.Bikkina, V.K.Manda, U.V.A.Rao - Medical oxygen supply during COVID-19: A study with specific reference to State of Andhra Pradesh, India, Materials Today: Proceedings - 2021,
- [5] A.K.Unni, V.Muthukumaran - Numerical simulation of the influence of oxygen content on the weld pool depth during activated TIG welding, The International Journal of Advanced Manufacturing Technology, 112, 2021, 467–489
- [6] F.J.Dent - The use of oxygen in gasification, Chemical Engineering Science, 3, 1, 1954,126-133
- [7] M.Sarkara, A.Kumara, J.Tumulurub, K.N.Patila, D.D.Bellmera - Gasification performance of switchgrass pre-treated with torrefaction and densification, Applied Energy, 127, 2014, 194-201
- [8] L.Wang, X.Du, J.Chen, Z.Wu - Numerical study on characteristics of biomass oxygen enriched gasification in the new gasifier on an experimental basis, Renewable Energy, 179, 2021, 815-827
- [9] L.Hongtao, C.Feng, P.Xia, Y.Kai, L.Shuqin - Method of oxygen-enriched two stage underground coal gassification, Mining Science and Technology (China), 21, 2011, 191-196
- [10] W.Huang, Z.Wang, T.Duan, L.Xin, -Effect of oxygen and steam on gasification and power generation in industrial tests of underground coal gasification, Fuel, 289, 2021, 119855
- [11] D.Jansen, M.Gazzani, G.Manzolini, E van Dijk, M.Carbo - Pre-combustion CO₂ capture, International Journal of Greenhouse Gas Control, 40, 2015, 167-187
- [12] P.A.Barratt, N.Hannay, A.Michel, A.Smith- The effective use of oxygen in the biological treatment of waste waters, Air products knowledge paper, 2003
- [13] H. Asami, M. Golabi, M. Albaji, -Simulation of the biochemical and chemical oxygen demand and total suspended solids in wastewater treatment plants: Data-mining approach, Journal of Cleaner Production, 296, 2021, 126533
- [14] W.Henry - Experiments on the quantity of gases absorbed by water, at different temperatures, and under different pressures, Phil. Trans. R. Soc. Lond. 93, 1803, 29–274.
- [15] E.Simón, J.M.Rosas, A.Santos, A.Romero - Coke formation in copper catalyst during cyclohexanol dehydrogenation: Kinetic deactivation model and catalyst characterization, Chemical Engineering Journal, 214, 2013, 119-128
- [16] D.J.Moodley, J.van de Loosdrecht, A.M.Saib, M.J.Overett, A.K.Datye, J.W.Niemantsverdriet - Carbon deposition as a deactivation mechanism of cobalt-based Fischer–Tropsch synthesis catalysts under realistic conditions, Applied Catalysis A: General, 354, 1–2, 2009, 102-110
- [17] P.G.Menton - Coke on catalysts-harmful, harmless, invisible and beneficial types, Journal of Molecular Catalysis, 59, 2, 1990, 207-220
- [18] R.K.Meghon, R.Ramachandran, BOC group - Catalyst regeneration process, 2002, European Patent EP0704516,

- [19] P.Wachter, C.Gaber, J.Raic, M.Demuth, C.Hochenauer - Experimental investigation on H₂S and SO₂ sulphur poisoning and regeneration of a commercially available Ni-catalyst during methane tri-reforming, *International Journal of Hydrogen Energy*, 46, 5, 2021, 3437-3452,
- [20] L.Wang, R.Zhang, R.Deng, Y.Luo - Oxygen-Induced Enhancement in Low-Temperature Dechlorination of PVC: An Experimental and DFT Study on the Oxidative Pyrolysis Process, *ACS Sustainable Chemistry and Engineering*, 9, 7, 2021, 2835–2843
- [21] N.Merlo, T.Boushaki, C.Chauveau, S.De.Persis, L.Pillier, B.Sarh, I.Gökalp - Combustion characteristics of methane–oxygen enhanced air turbulent non-premixed swirling flames, *Experimental Thermal and Fluid Science*, 56, 2014, 53-60
- [22] A.O.Said, A.K.Gupta - Oxygen Enriched Air Effects on Combustion, Emission and Distributed Reaction, *Journal of Energy Resources Technology*, 137,4, 2015, 042203
- [23] J. Kugaia, J. T..Miller, N. Guob, C. Song - Oxygen-enhanced water gas shift on ceria-supported Pd–Cu and Pt–Cu bimetallic catalysts, *Journal of Catalysis*, 277, 1, 2011, 46-53
- [24] J. Kugaia, E. B. Fox, C. Song - Kinetic characteristics of oxygen-enhanced water gas shift on CeO₂-supported Pt–Cu and Pd–Cu bimetallic catalysts, *Applied Catalysis A: General*, 497, 2015, 31–41
- [25] R.Horn, K.A.Williams, N.J.Degenstein, A.Bitsch-Larsen, D.Dalle Nogare, S.A. Tupy, L.D.Schmidt - Methane catalytic partial oxidation on autothermal Rh and Pt foam catalysts: Oxidation and reforming zones, transport effects, and approach to thermodynamic equilibrium, *Journal of Catalysis*, 249, 2007, 380–393
- [26] B.M.Khudenko, G.M.Gitman, T.E.P.Wechesler - Oxygen Based Claus Process for Recovery of Sulfur from H₂S Gases, *Journal of Environmental Engineering*, 119, 6, 1993, 1233-1251
- [27] M.Sassi, A.K.Gupta - Sulfur Recovery from Acid Gas Using the Claus Process and High Temperature Air Combustion (HiTAC) Technology, *American Journal of Environmental Sciences* 4, 5, 2008, 502-511
- [28] G.Dezhi, Y.Xinlei, T.Xun, D.Lu, D.Zhenghua, W.Fuchen - Simulation and Optimization of Pure Oxygen Claus Process, *Journal of East China University of Science and Technology*.
- [29] A.Bensakhira, M.Leturia - Natural gas oxy-combustion with flue gas recycling for CO₂ capture *Chemical Engineering Transactions*, 21, 2010, 637-642
- [30] H. Ishaq, I. Dincer - A novel biomass gasification based cascaded hydrogen and ammonia synthesis system using Stoichiometric and Gibbs reactors, *Biomass and Bioenergy*, 145, 2021, 105929
- [31] A.Kontopoulos, J.Koenig - Oxygen and nitrogen injection for increasing ammonia production, U.S. Patent application no WO1998045211 A1
- [32] T. Kato, M. Kubota, N. Kobayashi, Y. Suzuoki - Effective utilization of by-product oxygen from electrolysis hydrogen production, *Energy*, 30, 2005, 2580–2595
- [33] Z. Wang, T. He, J. Qin, J. Wu, J. Li, Z. Zi, G. Liu, J. Wu, L. Sun - Gasification of biomass with oxygen-enriched air in a pilot scale two-stage gasifier, *Fuel*, 150, 2015, 386–393
- [34] G. Cheng, P. He, B. Xiao, Z. Hu, S. Liu, L. Zhang, L. Cai - Gasification of biomass micron fuel with oxygen-enriched air: Thermogravimetric analysis and gasification in a cyclone furnace, *Energy*, 43, 2012, 329-333
- [35] K. Qiu, A.C.S. Hayden, - Increasing the efficiency of radiant burners by using polymer membranes, *Appl Energy*, 86, 2009, 349-354
- [36] P. Baskar, A. Senthilkumar - Effects of oxygen enriched combustion on pollution and performance characteristics of a diesel engine, *Engineering science and technology*, 19, 2016, 438-443

- [37] T. Czakiert, Z. Bis, W. Muskala, W. Nowak -Fuel conversion from oxy-fuel combustion in a circulating fluidized bed, *Fuel Process Technol*, 87, 2006, 531-538, *Engineering Science and Technology, an International Journal*, 19, 2016, 438–443
- [38] A.I.Dalton, DW,Tyndall. - Oxygen enriched air/natural gas burner system development. NTIS report PB91-167510, Springfield, VA; 1989.
- [39] M.M. Abdelaal, M.K. El-Riedy, A.M. El-Nahas- Effect of oxygen enriched air on porous radiant burner performance and NO emissions, *Experimental Thermal and Fluid Science*, 45, 2013, 163-168,
- [40] G. Jimenez-Garc, R. Quintana-Solorzano, R. Aguilar-Lopez, R. Maya-Yescas - Modelling Catalyst Deactivation by External Coke Deposition during Fluid Catalytic Cracking, *International journal of chemical reactor engineering*, 8, 2010, S2
- [41] G.Tang, A.K.Silaen, B.Wu, D.Fu, D.Agnello-Dean, J.Wilson, Q.Meng, S.Khanna , C. Q. Zhou - Numerical simulation and optimization of an industrial fluid catalytic cracking regenerator, *applied Thermal Engineering* 112, 2017, 750–760
- [42] R.M.DeConto, S.Galeotti, M.Pagani, D.Tracy, K.Schaefer, T.Zhang, D.Pollard, D.J. Beerling - Past extreme warming events linked to massive carbon release from thawing permafrost, *Nature*, 484, 2012, 87–91
- [43] D.Qin, G.K.Plattner, M.Tignor , S.K.Allen, J.Boschung, A.Nauels, Y.Xia, V.Bex, P.M.Midgley - *Climate Change 2013: The Physical Science Basis* ed, T Stocker, Cambridge: Cambridge University Press, 2014
- [44] Paris Agreement, United Nations Treaty Collection, 2016
- [45] Kyoto Protocol to the United Nations Framework Convention on Climate Change, United Nations Treaty Collection, 1997
- [46] L.Qiu, L.K.Ono, Y.Qi - Advances and challenges to the commercialization of organic–inorganic halide perovskite solar cell technology, *Materials today Energy*, 7, 2018, 169-189
- [47] S.Md.R.Tousif, S.Md.B.Taslim - Tidal Power: An Effective Method of Generating Power, *International Journal of Scientific & Engineering Research*, 2, 5, 2011, 1-5
- [48] J. Larfeldt, L. Tao, N. Berge - Development of an engineering tool for design and optimisation of biomass combustion in grate-fired boilers. 5th European Conference on Industrial boiler and furnaces, Porto, Portugal, April 2000
- [49] National Research Council; Division on Earth and Life Studies; Water Science and Technology Board; Committee on Water Implications of Biofuels Production in the United States, *Water Implications of Biofuels Production in the United States*, 2008, The National Academies Press, Chapter: 5 Water Issues of Biofuel Production Plants
- [50] W R Livingston Doosan Power Systems - The firing and co-firing of biomass in large pulverised coal boilers, IEA Exco Workshop, Jeju, November 2013
- [51] R.Lyman - Why renewable energy cannot replace fossil fuels by 2050, *Friends of science*, 2016, https://www.friendsofscience.org/assets/documents/Renewable-energy-cannot-replace-FF_Lyman.pdf Accessed 14/11/2018
- [52] R.Idem, T.Supap, H.Shi, D.Gelowitz, M.Ball, C.Campbell, P.Tontiwachwuthikul - Practical experience in post-combustion CO₂ capture using reactive solvents in large pilot and demonstration plants, *International Journal of Greenhouse Gas Control*, 40, 2015, 6-25
- [53] Z.Liang, W.Rongwong, H.Liu, K.Fu, H.Gao, F.Cao, R.Zhang, T.Sema, A.Henni, K.Sumon, D.Nath, D.Gelowitz, W.Srisang, C.Saiwan, A.Benamor, M.Al-Marri, H.Shi, T.Supap C.Chan, Q.Zhou, M.Abu-Zahra, M.Wilson, W.Olson, R.Iidem, P.Tontiwachwuthikul - Recent progress and new developments in post-

- combustion carbon-capture technology with amine based solvents, *International Journal of Greenhouse Gas Control*, 40, 2015, 26-54
- [54] M.Usman, M.Hillestad, L.Deng - Assessment of a membrane contactor process for pre-combustion CO₂ capture by modelling and integrated process simulation, *International Journal of Greenhouse Gas Control*, 71, 2018, 95-103
- [55] J.Peng, D.Iruretagoyena, D.Chadwick, Hydrotalcite/SBA15 composites for pre-combustion CO₂ capture: CO₂ adsorption characteristics, *Journal of CO₂ Utilization*, 24, 2018, 73-80
- [56] J.Adanez, A.Abad, F.Garcia-Labiano, P.Gayan, L.F.de Diego - Progress in Chemical-Looping Combustion and Reforming technologies, *Progress in Energy and Combustion Science*, 38, 2, 2012, 215-282
- [57] Anthony E.J - Chemical Looping Combustion. In: Chen WY., Suzuki T., Lackner M. (eds), *Handbook of Climate Change Mitigation and Adaptation*, Springer, Cham, 2018
- [58] C.Zheng, Z.Liu (eds), *Oxy-Fuel Combustion, Fundamentals, Theory and Practice*, Academic press, 2018
- [59] R.Stanger, T.Wall, R.Spörl, M.Paneru, S.Grathwohl, M.Weidmann, G.Scheffknecht, D.McDonald, K.Myöhänen, J.Ritvanen, S.Rahiala, T.Hyppänen, J.Mletzko, A.Kather, S.Santos - Oxyfuel combustion for CO₂ capture in power plants, *International Journal of Greenhouse Gas Control*, 40, 2015, 55-125
- [60] B. Abraham, J. Asbury, E. Lynch, A. Teotia - Coal-oxygen process provides CO₂ for enhanced recovery, *Oil Gas J* 80, 1982, 68 - 76.
- [61] F. Horn, M. Steinberg M. - Control of carbon dioxide emissions from a power plant (and use in enhanced oil recovery), *Fuel*, 61, 1982, 415 - 422.
- [62] D. Singh, E. Croiset, P.L. Douglas, M.A. Douglas. - Techno-economic study of CO₂ capture from an existing coal-fired power plant: MEA scrubbing Vs. O₂/CO₂ recycle combustion, *Energy Convers Manage*, 44, 2003, 3073–3091.
- [63] J.E. Johnson - Formation and Reduction of Nitrogen Oxides in Fluidized-Bed Combustion, *Fuel*, 73, 1998, 1398–1416.
- [64] K. Kimura , K. Omata , T. Kiga , S. Takano , S. Shikisima - Characteristics of pulverized coal combustion in O₂/CO₂ mixtures for CO₂ recovery. *Energy Convers Manage* 36, 1995, 805–808.
- [65] T. Nozaki, S. Takano, T. Kiga, K. Omata, K. Kimura - Analysis of the flame formed During oxidation of pulverised coal by an O₂- CO₂ mixture. *Energy*, 22, 1997, 199–206.
- [66] T. Kiga, S. Takano, N. Kimura, K. Omata, M. Okawa, T. Mori - Characteristics of Pulverised-coal combustion in the system of oxygen/recycled flue gas combustion, *Energy Conversion and Management*, 38, 1997, 129–134.
- [67] J.C.Chen, J.S.Huang - Combustion Efficiency and CO₂ Emission from O₂/N₂, O₂/CO₂, and O₂/RFG Coal Combustion Processes, *Environmental engineering science*, 24, 3, 2007, 353-362
- [68] M.Vodička, J.Hrdlička, P.Skopec -Experimental study of the NOX reduction through the staged oxygen supply in the oxy-fuel combustion in a 30 kWth bubbling fluidized bed, *Fuel*, 286, 1, 2021, 119343
- [69] M.Xu, H.Wu, Y.Wu, H.Wang, H.Ouyang, Q.Lu - Design and evaluation of a novel system for the flue gas compression and purification from the oxy-fuel combustion process, *Applied Energy*, 285, 2021, 116388
- [70] S.Posch, M.Haider - Optimization of CO₂ compression and purification units (CO₂CPU) for CCS power plants, *Fuel*, 101, 2012, 254-263

- [71] C.Gaber, C.Schluckner, P.Wachter, M.Demuth, C.Hochenauer -Experimental study on the influence of the nitrogen concentration in the oxidizer on NO_x and CO emissions during the oxy-fuel combustion of natural gas, *Energy*, 214, 2021, 118905,
- [72] B.Engin, U.Kayahan, H.Atakül - A comparative study on the air, the oxygen-enriched air and the oxy-fuel combustion of lignites in CFB, *Energy*, 196, 2020, 117021,
- [73] G.Bagheri, E.Ranzi, M.Pelucchi, A.Parente, A.Frassoldati, T.Faravelli - Comprehensive kinetic study of combustion technologies for low environmental impact: MILD and OXY-fuel combustion of methane, *Combustion and Flame*, 212, 2020, 142-155,
- [74] H.Chi, S.Su, H.Li, K.Xu, H.Leong, J.Xu, L.Jiang, Y.Wang, S.Hu, J.Xiang - Effects of CO₂ and H₂O on oxy-fuel combustion characteristics and structural evolutions of Zhundong coal pellet at fast heating rate, *Fuel*, 294, 2021, 120525,
- [75] C.Dueso, M.C.Mayoral, J.M.Andrés, A.I. Escudero, L.I.Díez - Towards oxy-steam combustion: The effect of increasing the steam concentration on coal reactivity, *Fuel*, 239, 2019, 534-546
- [76] H.Wu, M.Xu, Y.Li, J.Wu, J.Shen, H.Liao, Experimental research on the process of compression and purification of CO₂ in oxy-fuel combustion, *Applied Energy*, 259, 2020, 114123
- [77] H.Wu, Yi.Zhang, W.Chen, Z.Liu, T.Zhang, Q.Sun, Z.Zheng - Experimental research on the characteristics of ash in oxy-fuel combustion, *Fuel*, 263, 2020, 116799
- [78] L. Pang, Y. Shao, W. Zhong, H. Liu, P. Jiang - Experimental Investigation of Oxy-coal Combustion in a 15 kW th Pressurized Fluidized Bed Combustor, *Energy Fuels*, 33, 2019, 1694-1703,
- [79] J.Gu, Q.Liu, W.Zhong, A. Yu - Study on scale-up characteristics of oxy-fuel combustion in circulating fluidized bed boiler by 3D CFD simulation, *Advanced Powder Technology*, 31, 5, 2020, 2136-2151
- [80] C.Mock, H.Park, C.Ryu, V.Manovic, S.Choi, Particle temperature and flue gas emission of a burning single pellet in air and oxy-fuel combustion, *Combustion and Flame*, 213, 2020, 156-171
- [81] L.Li, L.Duan, Z.Yang, C.Zhao - Pressurized oxy-fuel combustion characteristics of single coal particle in a visualized fluidized bed combustor, *Combustion and Flame*, 211, 2020, 218-228
- [82] C.S. Wang, G.F. Berry, K.C. Chang, A.M. Wolsky - Combustion of pulverised coal using waste carbon dioxide and oxygen, *Combustion and Flame*, 72, 1988, 301-310.
- [83] D.M. Woycenko, W.L. van de Kamp, P.A. Roberts - Combustion of pulverized coal in a mixture of oxygen and recycled flue gas, in summary of the APG research program, JOU2-CT92-0093, IFRF Doc F98/Y/4, 1995
- [84] S. P. Khare, T. F. Wall, R. P. Gupta, L. K. Elliott, B. J. P. Buhre - Retrofitting of a Conventional Coal Fired Plant to Oxy-Firing: Heat Transfer Impacts for the Furnace and Associated Oxygen Levels, 5th Asia-Pacific Conference on Combustion, 2005, 109-112
- [85] S M Mousavian, M Tajik Mansouri - Conceptual feasibility study of retrofitting coal-fired power plant with oxy-fuel combustion, *Proceedings of the Institution of Mechanical Engineers, Part A: Journal of Power and Energy*, 225, 6, 2011, 689-700
- [86] Global CCS institute, Advantages and disadvantages of major CO₂ capture technologies, <https://hub.globalccsinstitute.com/publications/technology-options-co2-capture/advantages-and-disadvantages-major-co2-capture>, accessed on 14/11/2018
- [87] D. Singh, E. Croiset, P.L. Douglas, M.A. Douglas - Economics of CO₂ capture from a coal-fired power plant — a sensitivity analysis, *Proceedings of the 6th international conference on greenhouse gas control technologies*, Kyoto, Japan, October 1-4, 2002.

- [88] D. Singh, E. Croiset, P.L. Douglas, M.A. Douglas - Techno-economic study of CO₂ capture from an existing coal-fired power plant: MEA scrubbing Vs. O₂/CO₂ recycle combustion, *Energy Convers Manage*, 44, 2003, 3073–3091.
- [89] J.Ahn, T.Kim - Effect of oxygen supply method on the performance of a micro gas turbine-based triple combined cycle with oxy-combustion carbon capture, *Energy*, 211, 2020, 119010,
- [90] H.J. Yang, D.W. Kang, J.H. Ahn, T.S. Kim - Evaluation of design performance of the semi-closed oxy-fuel combustion combined cycle, *J Eng Gas Turbines Power*, 134, 11, 2012, 111702
- [91] R. Allam, S. Martin, B. Forrest, J. Fetvedt, X. Lu, D. Freed, G.W. Brown, T. Sasaki, M. Itoh, J. Manning - Demonstration of the Allam Cycle: an update on the development status of a high efficiency supercritical carbon dioxide power process employing full carbon capture, *Energy Procedia*, 114, 2017, 5948-5966
- [92] C.Song, W.Pan - Tri-reforming of methane: a novel concept for catalytic production of industrially useful synthesis gas with desired H₂/CO ratios, *Catalysis Today*, 98, 4, 2004, 463-484
- [93] A. Dwivedi, R. Gudi, P. Biswas - Oxy-fuel combustion based enhancement of the tri-reforming coupled methanol production process for CO₂ valorization, *Journal of CO₂ Utilization*, 376, 2018, 385
- [94] P.Wachter, C.Gaber, M.Demuth, C.Hochenauer -Experimental investigation of tri-reforming on a stationary, recuperative TCR-reformer applied to an oxy-fuel combustion of natural gas, using a Ni-catalyst, *Energy*, 212, 2020, 118719
- [95] O.Okonkwo, G.Yablonsky, P.Biswas - Thermodynamic analysis of tri-reforming of oxy-fuel combustion exhaust gas, *Journal of CO₂ Utilization*, 39, 2020, 101156
- [96] Y.Xiang, L.Cai, Y.Guan, W.Liu, Z.Cheng, Z.Liu - Study on the effect of gasification agents on the integrated system of biomass gasification combined cycle and oxy-fuel combustion, *Energy*, 206, 2020, 118131
- [97] Y.Shi, Q.Liu, Y.Shao, W.Zhong -Energy and exergy analysis of oxy-fuel combustion based on circulating fluidized bed power plant firing coal, lignite and biomass, *Fuel*, 269, 2020, 117424
- [98] Q.Liu, W.Zhong, R.Tang, H.Yu, Ji.Gu, G.Zhou, A.Yu - Experimental tests on co-firing coal and biomass waste fuels in a fluidised bed under oxy-fuel combustion, *Fuel*, 286, 1, 2021, 119312
- [99] P.D. Clark, N.I. Dowling, M. Huang - Production of H₂ from catalytic partial oxidation of H₂S in a short-contact-time reactor, *Catalyst Communications*, 5, 2004, 743-747
- [100] Worldatlas, top 12 sulphur exporting countries, <https://www.worldatlas.com/articles/top-12-sulphur-exporting-countries.html>, Accessed 15/11/2018
- [101] A.B.Jensen, C.Webb - Treatment of H₂S-containing gases: A review of microbiological alternatives, *Enzyme Microbial Technology*, 17, 1995, 2–10.
- [102] S.Ibrahim, R.KRahman, S.Raj - Effects of H₂O in the Feed of Sulfur Recovery Unit on Sulfur Production and Aromatics Emission from Claus Furnace, *Industrial & Engineering Chemistry Research*, 56, 41, 2017, 11713– 11725
- [103] R.K.Rahman, A.Raj, S.Ibrahim, I.Khan M, N.Omair, A.Muhairi - Reduction in Natural Gas Consumption in Sulfur Recovery Units through Kinetic Simulation Using a Detailed Reaction Mechanism, *Industrial & Engineering Chemistry Research*, 57, 2018, 1417–1428
- [104] P.Crevier, N.Dowling, P.Clark, M.Huang, - Quantifying the Effect of Individual Aromatic Contaminants on Claus Catalyst, *LRGCC Conf*, 2001
- [105] P.D.Clark, N.I.Dowling, M.Huang, W.Y.Svrcek, W.D.Monnerly - Mechanisms of CO and COS Formation in the Claus Furnace, *Industrial & Engineering Chemistry Research*, 40, 2, 2001, 497–508

- [106] L.V.Nasato, K.Karan, A.K.Mehrotra, L.A.Behie - Modeling reaction quench times in the waste heat boiler of a Claus plant, *Industrial & Engineering Chemistry Research*, 33, 1, 1994, 7–13
- [107] A.PiÉPlu, O.Saur, J.C.Lavalley, O.Legendre, C.NÉDez - Claus Catalysis and H₂S Selective Oxidation, *Catalyst reviews: Science and engineering.*, 40,1998, 409–450
- [108] M.Sassi, A.K.Gupta -Sulfur recovery from acid gas using the Claus process and high temperature air combustion (HiTAC) technology, *American journal of environmental science*, 4, 5, 2008, 502-511
- [109] P.D.Clark, R.Sui - Toward zero emission of sulphur species: using alumina nanofiber-based adsorbent for Claus tail gas processing. *ACS National Meeting Book of Abstracts*; 2010.
- [110] F. Manenti, D. Papisidero, E. Ranzi - Revised kinetic scheme for thermal furnace of sulphur recovery units, *Chemical engineering transactions*, 32, 2013, 1185-1290
- [111] J. Zaman, A. Chakma - Production of hydrogen and sulphur from hydrogen sulphide, *Fuel Process Technology*, 41 ,1995, 159-198
- [112] D. Barba, V. Palma , P. Ciambelli - Screening of catalysts for H₂S abatement from biogas to feed molten carbonate fuel cells. *International Journal of Hydrogen Energy* 38, 2013, 328-336.
- [113] T. N. Mashapa, J. D. Rademan, M. J. J Van Vuuren – Catalytic performance and deactivation of precipitated iron catalyst for selective oxidation of hydrogen sulfide to elemental sulfur in the waste gas streams from coal gasification. *Industrial & Engineering Chemistry Research* 46, 2007, 6338-6344.
- [114] V. Palma, V. Vaiano, D. Barba, M. Colozzi, E. Palo, L. Barbato. - H₂ production by thermal decomposition of H₂S in the presence of oxygen, *International journal of Hydrogen Energy*, 40 ,2015, 106-113
- [115] G.Galuszka, P.Iaquaniello, V.Ciambelli, E.Palma - Membrane-assisted catalytic cracking of hydrogen sulphide (H₂S), *Membrane reactors for hydrogen production processes*, Springer, 2011, 161-182
- [116] B.M.Khudenko, G.M.Gitman, T.E.P.Wechsler - Oxygen Based Claus Process for Recovery of Sulfur from H₂S Gases, *Journal of environmental energy*, 119, 6, 1993, 1233–1251.
- [117] S. Ibrahim, H. Selim, A. Al Shoaibi, A. K. Gupta - Effect of Oxygen Enrichment in air on Acid Gas Combustion under Claus Conditions, *11th International Energy Conversion Engineering Conference*, July 14 - 17, 2013
- [118] B.Klint - Hydrocarbon Destruction in the Claus SRU Reaction Furnace, *LRGCC Conf*, 2000
- [119] K.Tapasa, T.Jitwatcharakomol - Thermodynamic calculation of exploited heat used in glass melting furnace, *3rd International Science Social-Science Conference (I-SEEC)*, 2011
- [120] G.Jankes - Energy efficiency improvements and waste heat utilization, *Conference on Industrial Energy*, Yugoslav Thermal Science Society, Belgrade 1994, 70-81
- [121] K.Wu, Y.Chang, C.Chen Y.Chen - High-efficiency combustion of natural gas with 21–30% oxygen-enriched air, *Fuel*, 89, 2010, 2455 – 2462
- [122] I. F. Kurunov, M. P. Beresneva - Effect of enriching the blast with oxygen on the production cost of pig iron, *Metallurgist*, 43, 1999, 217-220
- [123] H.Sarv, Z.Chen, A.N.Sayre, G.J.Maringo - Oxygen-Enriched Combustion of a Powder River Basin Black Thunder Coal for NO_x Reduction In a Cyclone Furnace, *34th International Technical Conference on Clean Coal & Fuel Systems*, 2009
- [124] Y.Kawasoe, K.Harada, H.Hashimoto, O.Moriue, E.Murase -Effects of oxygen enrichment on combustion instability under super lean and high EGR conditions, *9th International Conference on Modeling and Diagnostics for Advanced Engine Systems, COMODIA 2017*

- [125] G.Jankes, Mi.Stanojevi, M.Karan, M.Kuburovi, M.Adzi - The Use of Technical Oxygen for Combustion Processes in Industrial Furnaces, *FME Transactions*, 31, 2003, 31-37
- [126] M.Faraday - *Liquefaction of Gases: Papers*, University of Chicago Press, Chicago, 1906
- [127] V.I.Feinstein - Provision of explosion proof air separation units under contemporary conditions, *Chemical and Petroleum Engineering*, 43, 2007, 96–101
- [128] A.R.Smith, J.Klosek - A review of air separation technologies and their integration with energy conversion processes, *Fuel Processing Technology*, 70, 2, 2001, 115-134
- [129] K.D.Timmerhaus, R.P.Reed - *Cryogenic Engineering: Fifty Years of Progress*, Springer, 2007
- [130] A.R.Smith, J.Klosek, D.W. Woodward - Next-generation integration concepts for air separation units and gas turbines, *Journal of Engineering for Gas Turbines and Power*, 119, 1997, 298-304
- [131] Q.Fu, Y.Kansha, C.Song, Y.Liu, M.Ishizuka, A.Tsutsumi - A cryogenic air separation process based on self-heat recuperation for oxy-combustion plants, *Applied Energy*, 162, 2016, 1114-1121
- [132] Y.Kansha, A.Kishimoto, T.Nakagawa, A.Tsutsumi - A novel cryogenic air separation process based on self-heat recuperation, *Separation and Purification Technology*, 77, 3, 2011, 389-396
- [133] B. Ghorbani, M. Mehrpooya, R. Shirmohammadi, M.H. Hamed - A comprehensive approach toward utilizing mixed refrigerant and absorption refrigeration systems in an integrated cryogenic refrigeration process, *J. Clean. Prod.*, 179, 2018, 495-514
- [134] M. Mehrpooya, M.M.M. Sharifzadeh, M.A. Rosen - Optimum design and exergy analysis of a novel cryogenic air separation process with LNG (liquefied natural gas) cold energy utilization, *Energy*, 90, 2015, 2047-2069
- [135] Y.Wu, Y.Xiang, L.Cai, H.Liu, Y.Liang - Optimization of a novel cryogenic air separation process based on cold energy recovery of LNG with exergoeconomic analysis, *Journal of Cleaner Production*, 275, 2020, 123027
- [136] R.Singla, K.Chowdhury -Enhanced oxygen recovery and energy efficiency in a reconfigured single column air separation unit producing pure and impure oxygen simultaneously, *Chemical Engineering and Processing - Process Intensification*, 162, 2021, 108354
- [137] R. Singla, K. Chowdhury - Saving power by modifying a double column air separation plant to produce high and low purity pressurized gaseous oxygen simultaneously, *Energy*, 210, 118487
- [138] J. Rizk, M. Nemer, D. Clodic - A real column design exergy optimization of a cryogenic air separation unit, *Energy*, 37, 1, 2012, 417-429
- [139] Z.Wang, W.Qin, C.Yang, W.Wang, S.Xu, W.Gui, Y.Sun, D.Xie, Y.Wang, J.Lu, Q.Chen, X.Liu, Heat-transfer distribution optimization for the heat-integrated air separation column, *Separation and Purification Technology*, 248, 2020, 117048
- [140] Hamayun, M.H.; Ramzan, N.; Hussain, M.; Faheem, M. - Evaluation of Two-Column Air Separation Processes Based on Exergy Analysis. *Energies*, 13, 2020, 6361
- [141] K. Matsuda, K. Kawazuishi, Y. Kansha, C. Fushimi, M. Nagao, H. Kunikiyo, F. Masuda, A. Tsutsumi - Advanced energy saving in distillation process with self-heat recuperation technology, *Energy*, 36, 2011, 4640-4645
- [142] Y. Rong, X. Zhi, K. Wang, X. Zhou, X. Cheng, L. Qiu, X. Chi - Thermo-economic analysis on a cascade energy utilization system for compression heat in air separation units, *Energy Conversion and Management*, 213, 2020, 112820

- [143] X.Zhou, Y.Rong, S.Fang, K.Wang, X.Zhi, L.Qiu, X.Chi -Thermodynamic analysis of an organic Rankine–vapor compression cycle (ORVC) assisted air compression system for cryogenic air separation units, *Applied Thermal Engineering*, 189, 2021, 116678,
- [144] R.Singla, K. Chowdhury - Determining design criteria to reduce power and cost in filling high-pressure oxygen cylinders directly from cryogenic air separation plants, *Cryogenics*, 116, 2021, 103299
- [145] Xu, J., Wang, T., Chen, Q.- Performance design of a cryogenic air separation unit for variable working conditions using the lumped parameter model, *Frontiers of Mechanical Engineering*, 15, 2020, 24-42
- [146] F.Bisotti, A.Galeazzi, L.Galatioto, F.Masserdotti, A.Bigi, P.Gritti, F.Manenti -Implementing robust thermodynamic model for reliable bubble/dew problem solution in cryogenic distillation of air separation units, *International Journal of Thermofluids*, 10, 2021, 100083
- [147] C.W.Skarstrom - US Patent, 2, 944, 627, Esso Research and Engineering, 1960
- [148] P. G. de Montgareuil, D.Domine - US Patent, 3, 155, 468, Air Liquide, 1964
- [149] N.O.Lemcoff - Nitrogen separation from air by pressure swing adsorption, *Studies in Surface Science and Catalysis* , 120, 1999, 347-370
- [150] S.Sircar, M.B.Rao, T.C.Golden - Fractionation of air by zeolites, *Studies in Surface Science and Catalysis* 120, 1999, 395-423
- [151] J. C. Santos, F. D. Magalhaes, A. Mende - Contamination of Zeolites Used in Oxygen Production by PSA: Effects of Water and Carbon Dioxide, *Industrial & Engineering Chemistry Research*. 47, 2008, 6197–6203
- [152] R.Šulc, P.Ditl -A technical and economic evaluation of two different oxygen sources for a small oxy-combustion unit, *Journal of Cleaner Production*, 309, 2021, 127427,
- [153] C.Chang, S.Ni, H.Yang, C.Chou -Simulation study of separating oxygen from air by pressure swing adsorption process with semicylindrical adsorber, *Journal of the Taiwan Institute of Chemical Engineers*, 120, 2021, 67-76
- [154] A.Syakdani, Y.Bow, R.S, M.Taufik - Analysis of Cooler Performance in Air Supply Feed for Nitrogen Production Process Using Pressure Swing Adsorption (PSA) Method, *Journal of Physics: Conference Series*, 1167, 2019, 012055
- [155] A.H. Mahdi, S.M.R.Ahmed, S.S.Salih, H.S.Ayuob - Simulation study of two units of pressure swing adsorption for producing oxygen and nitrogen simultaneously, *AIP Conference Proceedings* 2213, 2020, 020166
- [156] Sulc R., Ditl P - The Potential of Energy Savings in Oxygen Production by Pressure Swing Adsorption, *Chemical Engineering Transactions*, 86, 2021, 313-318.
- [157] Z.Yang, W.Guo, S.M.Mahurin, S.Wang, H.Chen, L.Cheng, K.Jie, H.M.Meyer, D.Jiang, G.Liu, W. Jin, I.Popovs, S.Dai - Surpassing Robeson Upper Limit for CO₂/N₂ Separation with Fluorinated Carbon Molecular Sieve Membranes, *Chem*, 6, 2020, 3, 631-645,
- [158] D.F.Sanders, Z.P.Smity, R.Guo, L.M.Robeson, J.E.McGrath, D.R.Paul, B.D.Freeman - Energy-efficient polymeric gas separation membranes for a sustainable future: A review. *Polymer*, 54, 2013 4729-476
- [159] K. C. Chong, S. O. Lai, H. S. Thiam, H. C. Teoh and S. L. Heng- Recent progress of O₂/N₂ separation using membrane technology, *journal of engineering science and technology*, 11 2016, 1016–1030
- [160] B.Adhikari, C.J.Orme, J.R. Klaehn, F.F.Stewart - Technoeconomic analysis of oxygen-nitrogen separation for oxygen enrichment using membranes, *Separation and Purification Technology*, 268, 2021, 118703
- [161] L.Remiroz, G.Wiciack, K.Jansuz-Symanska - Applicability of Polyimide Membranes for Air Separation in Oxy-MILD Power Plants: Semi-Experimental Research. *Journal of Power Technologies*, 101, 2021, 44-53

- [162] A.Jana, D.S.Bergsman, J.C.Grossm - Adsorption-based membranes for air separation using transition metal oxides, *Nanoscale advances*, 3, 2021, 4502-4512
- [163] M. Khdayyer, A. F. Bushell, P. M. Budd, M. P. Atfield, D. Jiang, A. D. Burrows, J. C. Jansen - Mixed matrix membranes based on MIL-101 metal-organic frameworks in polymer of intrinsic microporosity PIM-1, *Separation and purification technology*, 212, 2019, 545-554
- [164] Y.Deng, Y.Wu, G.Chen, X.Zheng, M.Dai, C.Peng - Metal-organic framework membranes: Recent development in the synthesis strategies and their application in oil-water separation, *Chemical Engineering Journal*, 405, 2021, 127004
- [165] Q.Qian, P.A.Asinger, M.J.Lee, G.Han, K.M.Rodriguez, S.Lin, F.M. Benedetti, A.X. Wu, W.S.Chi, Z. P. Smith - MOF-Based Membranes for Gas Separations, *Chemical reviews*, 120,16, 2020, 8161-8266
- [166] C.Y.Chuah, K.Goh, T.HBae - Enhanced Performance of Carbon Molecular Sieve Membranes Incorporating Zeolite Nanocrystals for Air Separation, *Membranes*, 11 2021, 489.
- [167] F. Allejos-Burgos, F.X.Coudert, K.Kaneko - Air separation with graphene mediated by nanowindow-rim concerted motion, *Nature communications*, 9, 2018, 1812
- [168] S.Haider, A.Lindbråthen, J.A.Lie, M.B.Hägg -Carbon membranes for oxygen enriched air – Part II: Techno-economic analysis, *Separation and Purification Technology*, 205,2018, 251-262
- [169] S.S.Hashim, A.R.Mohamed, S.Bhatia - Oxygen separation from air using ceramic-based membrane technology for sustainable fuel production and power generation, *Renewable and Sustainable Energy Reviews*, 15, 2011, 1284-1293
- [170] K.Świerczek, H.Zhao, Z.Zhang, Z.Du - MIEC-type ceramic membranes for the oxygen separation technology, *Energy and Fuels*,108, 2019, 01021
- [171] A.Leo, J.Motuzas, C.Yacou, S.Liu, J.M.Serra, L.Navarrete, J.Drennan, A.Julbe, J.C. Diniz da Costa - Copper oxide - perovskite mixed matrix membranes delivering very high oxygen fluxes, *Journal of Membrane Science*, 526, 2017, 323-333
- [172] N.Han, C.Zhang, X.Tan, Z.Wang, S.Kawi, S.Liu - Re-evaluation of La_{0.6}Sr_{0.4}Co_{0.2}Fe_{0.8}O_{3-δ} hollow fiber membranes for oxygen separation after long-term storage of five and ten years, *Journal of Membrane Science*, 587, 2019, 117180
- [173] Y.Alqaheem, A.AAlomair - Sealing perovskite membranes for long-term oxygen separation from air, *Chemical papers*, 74, 2020, 4159-4168
- [174] A. A. Klimashin, V. V. Belousov - Oxygen Ion Transport in Molten Oxide Membranes for Air Separation and Energy Conversion, *journal of the electrochemical society*, 164, 2017, 5353
- [175] Y.Alqaheem, F.Alswaileh - Oxygen Enrichment Membranes for Kuwait Power Plants: A Case Study. *Membranes*, 11 2021, 211
- [176] B.R. Dunbobbin, W.R. Brown - Air separation by a high temperature molten salt process, *Gas Sep. Purif.* 1, 1987, 23-29
- [177] K.Wang, Q.B.Yu, Q.Qin, Z.L.Zuo - Study of the sorption property of copper oxygen carrier used for chemical looping air separation, *J. Therm. Anal. Calorim.*,120, 2015, 1627-1633
- [178] Z.H.Yang, Y.S.Lin, Y.Zeng – High temperature sorption process for air separation and oxygen removal, *Ind. Eng. Chem. Res.*, 41, 2002, 2775
- [179] B.Moghtaderi, H.Song - Reduction properties of physically mixed metallic oxide oxygen carriers in chemical looping combustion, *Energy Fuels*, 24, 2010, 5359-5368

- [180] D. Acharya, K.R. Krishnamurthy, M. Leison, S. MacAdam, V.K. Sethi, M. Anheden, K. Jordal, J. Yan - Development of a high temperature oxygen generation process and its application to oxycombustion power plants with carbon dioxide capture, 22nd Annual Pittsburgh Coal Conference 2006, Pittsburgh, PA
- [181] B.Moghtaderi - Application of Chemical Looping Concept for Air Separation at High Temperatures, *Energy Fuels*, 24, 2010, 190–198
- [182] C.Zhou, K.Shah, B.Moghtaderi -Techno-Economic Assessment of Integrated Chemical Looping Air Separation for Oxy-Fuel Combustion: An Australian Case Study *Energy Fuels* 29, 4, 2015, 2074–2088
- [183] B.Shi, E.Wu, W.Wu, P.Kuo -Multi-objective optimization and exergoeconomic assessment of a new chemical-looping air separation system, *Energy Conversion and Management*, 157, 2018, 575-586
- [184] S. Chen, A. Soomro, R. Yu, J. Hu, Z. Sun, W. Xiang - Integration of chemical looping combustion and supercritical CO₂ cycle for combined heat and power generation with CO₂ capture, *Energy Conversion Management*, 167, 2018, 113-124,
- [185] N.Khallaghi, D.P. Hanak, V.Manovic - Gas-fired chemical looping combustion with supercritical CO₂ cycle, *Applied Energy*, 249, 2019, 237-244
- [186] Y.Cao, B.He, W.Tong, H.Yao, Z.Duan - On the kinetics of Mn₂O₃/ZrO₂ oxygen carrier for chemical looping air separation, *Chemical Engineering and Processing - Process Intensification*, 136, 2019, 82-91
- [187] S.Chen, J.Hu, W.Xiang -Application of chemical looping air separation for MILD oxy-combustion: Identifying a suitable operational region, *Applied Thermal Engineering*, 132, 2018, 8-17
- [188] R.H. Görke, W. Hu, M.T. Dunstan, J.S. Dennis, S.A. Scott - Exploration of the material property space for chemical looping air separation applied to carbon capture and storage, *Applied Energy*, 212, 2018, 478-488,
- [189] C.C. Cormos, Assessment of copper-based chemical looping air separation system for energy efficiency improvements of oxy-combustion and gasification power plants, *Applied Thermal Engineering*, 130, 2018, 120-126
- [190] C.Zhou, K.Shah, H.Song, J.Zanganeh, E.Doroodchi, B.Moghtaderi - Integration Options and Economic Analysis of an Integrated Chemical Looping Air Separation Process for Oxy-fuel Combustion, *Energy Fuels*, 30, 3,2016, 1741–1755

Chapter 2 – Review of oxygen carriers for CLAS

There are two main materials examined for oxygen production by redox cycling, transition metal oxides, and non-stoichiometric materials. In this Chapter, transition metal oxides and non-stoichiometric materials with variable oxygen capacity will be reviewed, alongside the techniques most often used to characterise them.

2.1 Metal oxide oxygen carriers

2.1.1 Oxygen capacity of metal oxides

A common example of a transition metal used to describe redox cycling is iron oxide. Iron can exist in multiple oxidation states, allowing it to compensate for a change in its oxygen content. Table 2.1 shows the various oxidation states of iron oxide [1].

Table 2.1 – Table showing the different forms of iron oxide found in nature and the oxidation state of the iron

Species	Formula	Average iron oxidation state
Hematite	Fe ₂ O ₃	+3
Magnetite	Fe ₃ O ₄	+8/3
Wüstite	FeO	+2

Transition metal oxides incorporate large weight percentages of oxygen. When iron is reduced from hematite to wustite, a weight loss of up to 10% occurs. This weight loss increases to 30% if hematite is reduced to Fe [2]. This lost oxygen can be re-incorporated into the material, with a decrease in the temperature or an increase in the pO₂. It is this feature that makes transition metal oxides attractive for redox cycling.

Redox cycling of non-stoichiometric materials is a relatively simple chemical process, however, care must be taken in selecting the right oxygen carrier for the right pO₂ range, as the thermodynamics of different processes are more suitable for different materials.

One set of materials of interest are the transition metal oxides have sharp transitions between their oxidation states. This behavior allows for the materials to undergo oxygen cycling over a narrow temperature and range of pO₂s, exchanging significant amounts of oxygen (≈10% wt.) over temperature swings of less than 50°C. For oxygen enrichment processes, the transition metal oxides Mn₂O₃, Co₃O₄, and CuO are of significant interest [3-5]. Mattison et al. [6] identified CuO – CuO₂, CoO – Co₃O₄, and Mn₂O₃ – Mn₃O₄ as potential cycling regimes useful for oxygen enrichment or production processes, due to the temperature and pO₂ range of the phase changes.

For the $\text{CuO} - \text{Cu}_2\text{O}$, $\text{CoO} - \text{Co}_3\text{O}_4$ and $\text{Mn}_2\text{O}_3 - \text{Mn}_3\text{O}_4$ regimes, it is possible to oxidise the material in air ($p\text{O}_2$ of 0.21 bar) and release the oxygen into a higher $p\text{O}_2$ stream of 0.31 bar by a small temperature swing ($<50^\circ\text{C}$). This small temperature swing causes the material to change mass $>5\%$. This large and easily removable oxygen capacity makes transition metal oxides useful for oxygen enrichment processes, such as oxy-fuel combustion. Table 2.2 shows the approximate temperature for oxygen incorporation in a $p\text{O}_2$ of 0.21 bar and the approximate temperatures of oxygen release in a $p\text{O}_2$ of 0.31 bar, alongside the amount of oxygen released per potential cycle for the three metal oxides. The weight change calculated is estimated from the most reduced of the metal oxide species in the cycle.

Table 2.2 – Operating temperatures and potential oxygen cycling capability of transition metal oxides

Material	Approximate temperature of cycling ($^\circ\text{C}$)	Oxygen released per cycle (% wt)
$\text{Cu}-\text{Cu}_2\text{O}$	1300-1350	10%
$\text{Co}_3\text{O}_4 - \text{CoO}$	1150-1200	5%
$\text{Mn}_2\text{O}_3 - \text{Mn}_3\text{O}_4$	650 - 700	9%

The small swings in temperature demonstrated make transition metals attractive for redox cycling. However, high operating temperatures are required for use of the copper and cobalt oxides, making the processes energy-intensive. Redox cycling of manganese is more promising due to the large oxygen capacity and relatively lower.

Many metal oxide systems have been studied for the CLAS process. Qin et al. [7] found $\text{CrO}_2/\text{Cr}_2\text{O}_3$, $\text{PbO}_2/\text{Pb}_3\text{O}_4$, PbO_2/PbO , $\text{Pb}_3\text{O}_4/\text{PbO}$, $\text{MnO}_2/\text{Mn}_2\text{O}_3$, and $\text{Ag}_2\text{O}/\text{Ag}$ suitable for the CLAS process at lower temperatures ($300-500^\circ\text{C}$), while PdO_2/PdO , PdO_2/Pd , PdO/Pd , MnO_2/MnO , and $\text{MnO}_2/\text{Mn}_3\text{O}_4$ were suitable for medium temperatures ($500-800^\circ\text{C}$) applications. The Co systems were found to be useful at higher temperatures ($800-1100^\circ\text{C}$) A thermodynamic study of different metal oxide materials by Wall et al. found that Mn, Co, and Cu were likely to be the most efficient for oxy-fuel combustion [8]. Of these, Cu and Mn are often the most studied [9-12]. Calcium looping has also been examined [13], however due to the stability of calcium in the exhaust gases, it is difficult to use for a combined CLAS/oxy-fuel combustion process.

Using metal oxides, large volumes of oxygen can be produced over small temperature swings, however, this is often not the most efficient process due to the kinetics. Studies have found that while higher temperatures are favourable for reduction, lower temperatures are preferred for oxidation [14-15], so many systems will have larger temperature swings.

2.1.2 Stability of metal oxide carriers over redox cycling

Despite transition metal oxides having large oxygen storage capacities per gram of material, they are well documented to have low stability over redox cycling, and to date, no metal system has the traits of an ideal storage material regarding storage capacity, costs, and cycling stability [16].

Sintering is a significant issue with metal oxides. Sintering reduces oxygen transport capacity, as a reduction in surface area is seen [17]. German et al [18] used the Brunauer, Emmett, and Teller technique (B.E.T) to record the change in surface area of powdered iron oxide held isothermally at 500°C in ambient air. German's results showed that after only 90 minutes there was a decrease in the measured surface area of 18% compared to the fresh sample. This decrease in the surface area makes the use of these materials for multiple redox cycles problematic. This is demonstrated in work performed by Dennis et al. [19] who investigated the stability of untreated iron oxide and modified iron oxide with 1%, 10%, or 30% of a metal additive added (namely Cr, Mg, Al, or Si). These iron oxide samples were then used to produce hydrogen by a chemical looping process, with the iron oxide samples undergoing redox cycling at 900°C between a 10% CO reducing gas feed flown for 10 minutes and a 25% H₂O feed flown for 3 minutes [19]. It was seen that the redox performance of the iron oxide samples tested decreased significantly over just 10 of these redox cycles, with the amount of hydrogen produced decreasing by over 50% compared to the first cycle for most samples tested. A similar study by Cai et al. found manganese ore agglomerated when undergoing redox cycling at high temperature – although the authors believed this may be due to impurities in the sample, as an ore, not pure metals, were used in the experiment [20].

Supports can be used to limit agglomeration [21], however, this is not always effective. Moghdatheri et al [22] found in a test of supported Mn, Cu, and Co, silica-supported copper oxides were the most stable over multiple redox cycles for the CLAS process, however, oxygen transfer still dropped by 10.3% over 41 cycles. Further work was performed by the authors using a bimetallic Cu–Mg-based oxygen carrier, which showed promising results—however, a drop in performance of approximately 5% was noted over 41 cycles [23].

2.2 Non-stoichiometric oxygen carriers

Alternative to the transition metal oxides, non-stoichiometric oxides, primarily perovskites, are more resistant to sintering than the transition metal oxides. These materials, while more stable, unfortunately, exchange much lower quantities of oxygen over redox cycling than the transition metal oxides [24]. These non-stoichiometric materials are often in the form of mixed metal oxide crystals, such as perovskite. Perovskites take the form ABO_3 , with B representing a different transition metal ions and A often being from the lanthanide or rare-earth ion. These materials allow either oxygen excesses or deficits within their structure, depending on the A and B metals. This is due to the transition metal ion compensating for the change in valence with the incorporation and release of the oxygen ions. Perovskites are often represented with the chemical formula, $ABO_{3-\delta}$, where δ is dependent upon the pO_2 and temperature of the environment (although perovskites with hyper stoichiometry do exist, such as the rare earth manganates). This variability in the oxygen non-stoichiometry occurs with often only small changes to the crystal structure, such as slight variations in the cell volume. Due to this changeable oxygen non-stoichiometry, these materials can be used for many of the potential applications of transition metal oxides, such as for chemical looping hydrogen production [25].

2.2.1 Oxygen vacancies

A well-documented example of perovskites in literature is lanthanum strontium ferrite ($La_xSr_{1-x}FeO_{3-\delta}$), where the δ in the chemical formulae is related to the degree of change in non-stoichiometry. Figure 2.1 (a) shows a ball and stick figure of a non-stoichiometric material, with oxygen ions entering or leaving the structure filling or leaving an oxygen vacancy, while still maintaining the overall crystal structure (though the loss of oxygen will slightly change the geometry of a crystal cell, and increase the cell volume [26]).

This type of oxygen vacancy is referred to as a Schottky vacancy, which is a site that oxygen can leave and enter without overly disrupting the crystal lattice and keeping the material relatively stable. A Schottky vacancy occurs when an ion is missing from a lattice. An atom of similar valence and size may enter this space and bond, filling the gap [27]. An example of this vacancy type can be seen in Figure 2.1 (a)

Another potential type of oxygen vacancy is an interstitial site. An interstitial defect occurs when an atom enters a site that is normally empty in the lattice or a site already containing an atom of the same type. It does not join the lattice in a normally occupied atom site, but rather is trapped between ions by weak forces, and this can be seen in Figure 2.1 (b).

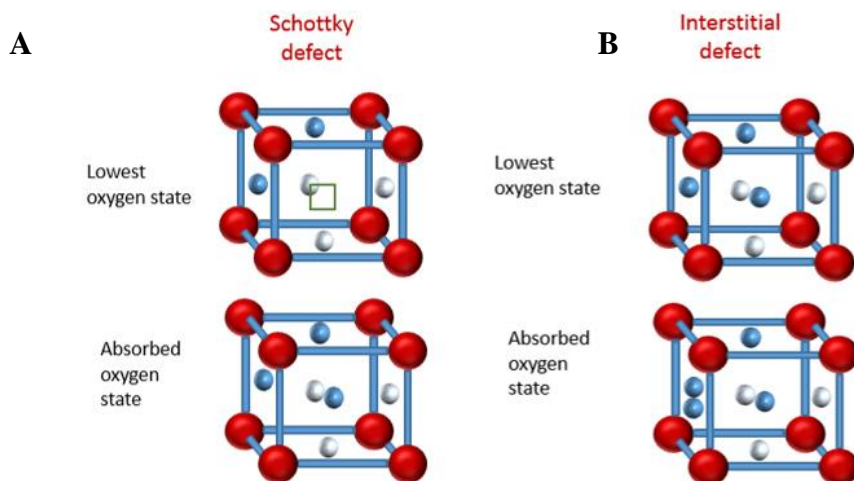


Figure 2.1 – Diagram showing (a) Schottky vacancy and (b) an interstitial oxygen position in a perovskite material, where the blue spheres represent the oxygen ions in the closest three planes, the white spheres in the furthest three planes, and the red spheres the metallic cations.

Oxygen vacancies have the potential to be filled by either oxygen or a hydroxyl ion. This property gives the materials many interesting potential applications such as fuel cells or as mixed ionic conductors due to the ability to carry protons and oxygen ions simultaneously, as both these ions can enter and leave these sites easily [28]. Most non-stoichiometric materials undergo a gradual change in the degree of oxygen non-stoichiometry as the pO_2 and temperature are altered, with increases in the sample temperature and reduction of the pO_2 decreasing the oxygen content of the sample, such as with the $La_xSr_{1-x}FeO_{3-\delta}$ family of materials [29].

2.2.2 Perovskites versus metal oxides for redox cycling

One of the most commonly noted features of perovskites that make the materials attractive for redox cycling is improved stability compared to the transition metal oxides. An example of the improved stability that these materials can offer was shown by Metcalfe et al [15], who compared the cycling performance of powdered iron oxide and the perovskite $La_{0.7}Sr_{0.3}FeO_{3-\delta}$. Metcalfe et al. showed a reduction in the amount of hydrogen produced during redox cycling of iron oxide powders of 80 – 160 microns from approximately 160 to 50 $\mu\text{mol H}_2$ per 50 milligrams of iron oxide powder per cycle when a sample underwent 25 redox cycles between 5% CO and 5% H_2O at 850°C [30]. This data was compared to a $La_{0.7}Sr_{0.3}FeO_{3-\delta}$ sample which underwent the same redox cycling. It was shown that the perovskite sample maintained good stability in its hydrogen production per redox cycle when tested over the same timescale as the iron oxide, which showed significant degradation.

This study, however, also showed the main drawback to the use of perovskites, the low oxygen capacity. During this study, the amount of hydrogen produced by $\text{La}_{0.7}\text{Sr}_{0.3}\text{FeO}_{3-\delta}$ during a redox cycle was approximately half of that produced by the iron oxide at the start of the study. However, the amount of hydrogen produced per redox cycle stayed consistent throughout the 25 cycles for the perovskite, and redox cycling using the perovskite sample produced approximately twice the amount of hydrogen than the redox cycling with the iron oxide sample did over the entirety of the 25 cycles [30]. This study highlights the compromise between the use of a transition metal oxide, and a non-stoichiometric material such as $\text{La}_{0.7}\text{Sr}_{0.3}\text{FeO}_3$, namely the large oxygen capacities but low cycling stability of the transition metal oxides, versus the low oxygen capacities and high cycling stability shown by perovskites and similar on-stoichiometric materials.

2.2.3 Studied perovskites for oxygen production processes

In literature, two perovskites have been identified by Vietena et al [31] as being promising for oxygen cycling processes, $\text{SrFeO}_{3-\delta}$ and $\text{CaMnO}_{3-\delta}$. This is due mainly to the materials exchanging large amounts of oxygen per °C of a temperature swing, and incorporation of large amounts of oxygen even at low $p\text{O}_2$ s.

Upon heating $\text{SrFeO}_{3-\delta}$ in a $p\text{O}_2$ of 0.21 bar, oxygen is released above 300°C, with the oxygen content of the material constant below this temperature [32]. Further heating decreases the oxygen content at a constant rate from a δ of 0.1 to 0.3, between 300 and 750°C [32].

While the properties of the material look promising, work is ongoing to optimise performance. The first method for this is by performing doping to the crystal structure. Muller et al. [37] found that $\text{SrFe}_{0.2}\text{Co}_{0.8}\text{O}_{3-\delta}$ and $\text{Sr}_{0.8}\text{Ca}_{0.2}\text{FeO}_{3-\delta}$ had larger oxygen capacities than the undoped base material. The materials produced by Muller underwent redox cycling, and no drop-in activity was noted after 100 cycles [37]. While cobalt addition has been shown to give improved performance, there are many issues with obtaining ethical cobalt, so the lowest possible cobalt addition is desirable. Examining this, Duan et al suggested that reducing the cobalt doping to $x=0.25$ for $\text{SrFe}_{1-x}\text{Co}_x\text{O}_{3-\delta}$ would give good results, as the reduction in oxygen formation energy from cobalt doping decreases upon doping past $x=0.25$ [38]. Co-doping with calcium on the A site, and cobalt on the B site was found to greatly improve performance by Li et al, and it was seen to lower the activation energy of oxygen diffusion to 26.6 kJ mol^{-1} , and the surface oxygen exchange by $137.9 \text{ kJ mol}^{-1}$ [39]. The preferred ratio found in this study was $\text{Sr}_{0.8}\text{Ca}_{0.2}\text{Fe}_{0.4}\text{Co}_{0.6}\text{O}_3$, and this composition delivered over 6 times the oxygen capacity at 400°C using a pressure swing between $p\text{O}_2$'s of 0.05 and 0.2 bar,

compared to undoped SrFeO_3 or $\text{Sr}_{0.8}\text{Ca}_{0.2}\text{FeO}_3$ [39]. To reduce the cobalt requirements further, Lekse et al investigated co-doping further and claimed the best composition to be $\text{Sr}_{0.7}\text{Ca}_{0.3}\text{Fe}_{0.9}\text{Co}_{0.1}\text{O}_{3-\delta}$ [40]. Steinfeld et al agreed with this assessment, synthesizing $\text{Sr}_{0.93}\text{Ca}_{0.07}\text{Fe}_{0.9}\text{Co}_{0.1}\text{O}_{3-\delta}$, which had a 4 times greater oxidation rate than an undoped material [33]. A recent study [41] showed barium doping improved redox capacities more than calcium doping, which may give further improvements. Studies by Steinfeld et al. have shown the limiting step for oxidation is bulk diffusion, while the limiting step for the reduction is the surface reaction, so surface modification may give good results [33]. To improve upon the oxygen capacity and operation temperatures of $\text{SrFeO}_{3-\delta}$, for oxygen cycling, copper doping has also been attempted. Replacing 15% of the strontium with copper was shown to increase the maximum oxygen content by 20% in a $p\text{O}_2$ of 0.21 bar [42].

Satler et al demonstrated the potential efficiency of the oxygen use of $\text{SrFeO}_{3-\delta}$, removing oxygen at a purity of <1% from a nitrogen gas stream by using pressure and temperature swings [43]. A similar study by Steinfeld et al. showed good stability of $\text{SrFeO}_{3-\delta}$ over 250 redox cycles in a nitrogen purification system [44]. Sintering was seen by Kita et al [45] after 10 redox cycles between 100 and 1000°C in air, however, no loss in performance was noted by the authors. After 1000 redox cycles for thermochemical air separation, a manganese doped sample was shown by Li et al to have a small drop of performance of 3% [46].

Upon oxygen incorporation and release, $\text{SrFeO}_{3-\delta}$ undergoes significant changes to the crystal structure. Upon heating in a $p\text{O}_2$ of 0.21 bar, $\text{SrFeO}_{3-\delta}$ undergoes a phase change from tetragonal to cubic at temperatures greater than 300°C. Four phases of $\text{SrFeO}_{3-\delta}$ have been noted at high temperatures (approx 1400°C), and this has been linked to the oxygen content of the material. The material transforms from cubic to tetragonal to orthorhombic and finally brownmillerite when $\delta \approx 0, 0.125, 0.25,$ and 0.5 respectively [47]. Calculation of the Gibbs energies of formation for these different phases of $\text{SrFeO}_{3-\delta}$ by Maier et al indicated that greater amounts of oxygen vacancies gave a greater range of phase stability at changing temperatures and $p\text{O}_2$'s, and this was explained by the author due to attraction between the vacancies, and spontaneous formation of vacancy clusters in the structure [48]. Scott et al. have shown that further reduction of $\text{SrFeO}_{3-\delta}$ to SrO and Fe is reversible, and XRD images showed a return to the cubic structure after a reoxidation step [49].

$\text{CaMnO}_{3-\delta}$ has also been investigated for oxygen cycling and was reported to release more oxygen per °C of a temperature swing, compared to $\text{SrFeO}_{3-\delta}$ [31,50]. Even at low temperatures, $\text{CaMnO}_{3-\delta}$ incorporated oxygen quickly, reaching its maximum oxygen capacity

at 400°C within 1 minute during isothermal oxygen incorporation [31]. The oxygen content is linked to a phase transition, with samples changing from orthorhombic to tetragonal to cubic upon reduction. The tetragonal phase change occurs at approximately $\delta = 0.035$ and is slightly affected by temperature. The cubic transition ranges between $\delta = 0.08$ and 0.04 in the temperature range of 700 to 950°C [52]. $\text{CaMnO}_{3-\delta}$ decomposes at high temperatures to form $\text{Ca}_2\text{MnO}_{4-\delta}$ and CaMn_2O_4 . Norby et al showed the transition at $T = 1000^\circ\text{C}$ and a $\log p\text{O}_2$ of -1.8 and δ of 0.16 [53]. This decomposition was slow, however, taking a week to complete, and reversible if the $p\text{O}_2$ is increased [53]. These phase changes have been linked to a reduction in the cycling performance of the material, although interestingly the drop in performance was more significant at 750 compared to 900°C [54]. The material has also undergone redox cycling in potential reducing environments, being shown by Amini et al. to perform well in a gas switching combustion of H_2 and CH_4 – although less than 5 cycles were demonstrated [55].

To improve the potential of the material, doping has been performed. Strontium doping was found to reduce the required enthalpy of reduction, making the material more promising for oxygen cycling [31, 56]. Tungsten doping of the B-site was found to improve the reduction kinetics of $\text{CaMnO}_{3-\delta}$ [57]. Most interesting, Fe doping of the B-site by 10-30% decreased the temperature of the beginning of oxygen release temperature from 700 to 400°C upon heating [58]. Fe-doping of 5% was shown to give more efficient combustion at 600°C, although after 15 cycles at 900°C, sintering was observed [59]. This was also seen to increase the temperature at which decomposition to CaMn_2O_4 occurred, increasing the temperature from 1100 to 1200°C at a $p\text{O}_2$ of 0.008 atm. Conversely, lanthanum doping has been seen to increase the temperature at which oxygen is released upon heating [60]. Co-doping was studied by computer simulations performed by Chronos et al. with Ni-Fe and Ga-Al calculated to help improve vacancy diffusion [61]. Doping has also been seen to have the potential to prevent cation segregation, which can lower performance [62].

2.2.4 Oxygen capacities of perovskites for oxygen cycling

From the literature studies of the two perovskites detailed above, $\text{CaMnO}_{3-\delta}$ was identified as the more promising of the materials, due to a reported higher oxygen exchange per °C of a temperature swing. For these reasons, this material will be examined in more detail.

Using thermodynamic data presented in ref [31], the amount of oxygen that could be cycled from $\text{CaMnO}_{3-\delta}$ was calculated by use of a pressure swing or temperature swing of the material. In Table 2.3, the amount of oxygen exchanged during a theoretical temperature

swing was calculated, where the material was considered to have been oxidised in a pO_2 of 0.21 bar at 800°C before the temperature was increased to release the incorporated oxygen into a pO_2 of 0.31 bar. In Table 2.4, data from a similar calculation is presented, however, instead of a temperature swing used for Table 2.3, a pressure swing was considered, with the material incorporating oxygen at a pO_2 of 1 bar, before releasing it into a pO_2 stream of 0.31 bar at the noted temperatures. A pO_2 of 0.31 bar was considered as this is the minimum pO_2 for oxy-fuel combustion.

Table 2.3 - Calculated oxygen released from using $CaMnO_{3.6}$ in a temperature swing oxygen production processes, with oxidation considered at 800°C in a pO_2 of 0.21 bar ($\delta = 0.013$)

The temperature of oxygen release (°C)	Temperature swing (°C)	δ at a pO_2 of 0.31 bar	$\Delta\delta$ from reference of 0.21 bar at 800°C	Change in weight %
900	100	0.03	0.0017	0.19
995	195	0.06	0.0047	0.53
1095	295	0.095	0.082	0.92
1193	393	0.145	0.132	1.48

Table 2.4 – Calculated oxygen released from using $CaMnO_{3.6}$ in a pressure swing oxygen production processes, with oxidation considered at a pO_2 of 1 bar, and reduction considered at a pO_2 of 0.31 bar

Temperature (°C)	δ at a pO_2 of 1 bar	δ at a pO_2 of 0.31 bar	$\Delta\delta$	Change in weight %
900	0.01	0.013	0.003	0.20
995	0.05	0.055	0.005	0.54
1095	0.13	0.145	0.015	0.96

From the values shown in Table 2.3 and 2.4, it is seen that only small amounts of oxygen can be produced per redox cycle using these materials. A pure pressure swing process, alternating between a pO_2 of 1 bar at 1095°C produces less than a 1% weight change of the material, while temperature swings of approximately 400°C between 800 and 1193°C were required to allow the material to undergo a weight change greater than 1%. A combined temperature and pressure swing from a pO_2 of 1 bar at 800°C to 1193°C in a pO_2 of 0.31 bar produced a

weight change of 1.53%. Comparing this performance to the weight changes of the transition metal oxides shown in Table 2.2, the amount of oxygen exchanged per °C of a temperature swing is at least two orders of magnitude lower using perovskites. To use these materials in an industrial process, very fast cycling would be required to produce the necessary volume of oxygen. This will likely require the use of fluidised beds which suffer from large pressure drops and may cause possible damage to the particles as the material is fluidized through the reactor.

2.2.5 Alternative non-stoichiometric materials with a gradual change in non-stoichiometry

Much work has been performed in the literature surrounding the thermodynamics and applications of the perovskites $\text{SrFeO}_{3-\delta}$ and $\text{CaMnO}_{3-\delta}$, but other non-stoichiometric materials such as $\text{Sr}_3\text{Fe}_2\text{O}_{7-\delta}$ are gaining interest for oxygen cycling processes. $\text{Sr}_3\text{Fe}_2\text{O}_{7-\delta}$ is a layered perovskite recently investigated as an oxygen storage material. One of the major reasons for this is that the material has shown improved stability against reduction compared to SrFeO_3 [63]. Oxygen storage in the material is topotactic, however with the oxygen release the crystal structure space group is the same, as oxygen ions at equatorial positions are released when the material is reduced from $\delta = 0.25$ to 1. This is uncommon and allows the material to undergo particularly small changes to the unit cell volume compared to other oxygen storage materials. The belief is that small volume changes can help prevent warping or damage to particles, maintaining their stability [64].

Doping of the material by 20%, in the form of $\text{Sr}_3(\text{Fe}_{0.8}\text{M}_{0.2})_2\text{O}_{7-\delta}$, where M was either Co, Ni, or Mn, was seen to increase the oxygen storage capacity (OSC) of the material. The $\mu\text{mol-O}_2 / \text{g}$ of the material was seen to increase as shown in Table 2.5 below [65].

Table 2.5 – OSC in $\mu\text{Mol O}_2/\text{g}$ for doped $\text{Sr}_3(\text{Fe}_{0.8}\text{M}_{0.2})_2\text{O}_{7-\delta}$ reported in reference [65]

$\text{Sr}_3(\text{Fe}_{0.8}\text{M}_{0.2})_2\text{O}_{7-\delta}$	OSC ($\mu\text{Mol O}_2 / \text{g}$)
M=Fe	520
M=Mn	610
M=Co	741
M=Ni	810

As shown doping in all cases increased the oxygen capacity of the material, which may improve the suitability of the material for redox cycling.

Other materials such as the lanthanide ferrites have been well studied in the literature for use in solid oxide fuel cells and semiconductor applications. The most commonly discussed of the family, $\text{LuFe}_2\text{O}_{4+\delta}$, has recently been of interest as an oxygen storage material, due to a large oxygen capacity equivalent to a $\delta = 0.5$, or a weight change of approximately 2.2% by weight [66]. The crystal structure of the compound alternates between layers of LuO_2 and Fe_2O_4 , with the Fe layers forming as trigonal bipyramids [67]. A detailed study of the material was performed in [66], and the authors showed a small amount of oxygen uptake at 200°C ($\approx 0.1\%$ wt. in approximately three hours), with more notable oxygen incorporated at 300°C and 500°C (1.1% and 2.2 % after three hours at each temperature) at low oxygen partial pressures (0.2×10^{-3} atm). Additionally, the authors claim that the mechanism for the oxygen incorporation and release should allow for long lifetimes of the material, and in the supplementary information of this work, five cycles between oxygen-containing environment and 5% H_2/Ar were performed, showing a modest increase in the amount of oxygen incorporated over each cycle, suggesting that the full oxygen capacity of the material was not being utilized.

The material was seen to incorporate large amounts of oxygen at low $p\text{O}_2$ s, but this stored oxygen also required hydrogen to remove. This would make it expensive and impractical to remove the oxygen for an oxygen production process, as well as giving added losses from side reactions between hydrogen and oxygen during the reduction step.

2.3 Oxygen carriers with hysteresis behaviour in the oxygen capacity

Some non-stoichiometric materials do not undergo gradual changes in oxygen non-stoichiometry with temperature or $p\text{O}_2$, an example of which is the perovskite $\text{SrCo}_{0.2}\text{Fe}_{0.8}\text{O}_{3-\delta}$ [68]. At high temperatures (approx. 700°C) the material stops gradually changing oxygen content with increased $p\text{O}_2$, instead of staying at a steady non-stoichiometry as the $p\text{O}_2$ increases, until a threshold $p\text{O}_2$ is reached, at which point the non-stoichiometry rapidly changes.

This feature is a hysteresis, a phenomenon in which a physical property lags behind the changes in the effect causing it. It was first, and is most commonly, referenced when

discussing magnetic systems [69], however, this phenomenon can also affect the oxygen non-stoichiometry, as well as phase transitions of non-stoichiometric materials.

Eyring et.al [70] explained the effect using the Van der Waals function. Figure 2.2 describes the transition between two states as a function of a physical property. The two stable paths of this reaction are shown as solid blue lines, AEB and DFC, while an unstable and unrealisable reaction path is shown by the dashed blue pathway, connecting points D to B. During a reversible phase transition from state A to state B, the reaction follows the equilibrium pathway AEFC. However, when a material exhibits hysteresis, an additional energy barrier is present, preventing the transition from occurring along this equilibrium pathway. As such, metastable regions must be used to facilitate state change. In this example, the material would be metastable from point A to point B. As these are irreversible phase changes, it would be impossible to move past point B while still in the original state, and as such there would be a rapid change from the original state if the energy barrier preventing the transition was overcome, following the ABC pathway. As such, a hysteresis loop is formed, cycling through points ABCDA to undergo any changes, ignoring the equilibrium pathway, AEFC.

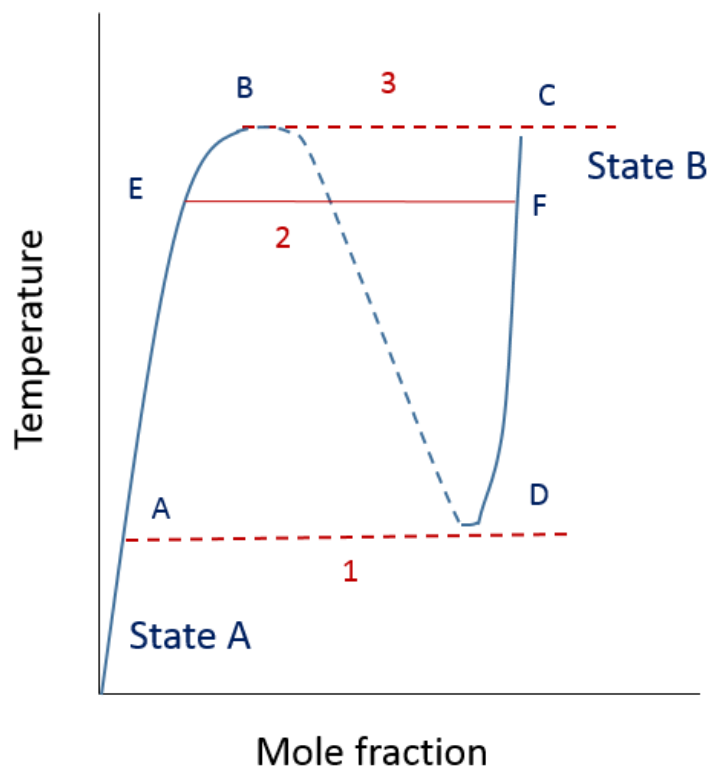


Figure 2.2 - Van der Waals plot representing phase transition between a state A and B as a function of temperature

It is hoped that non-stoichiometric materials with a hysteresis of the oxygen content could be useful for oxygen cycling processes due to several reasons, such as:

- Large changes in oxygen non-stoichiometry over narrow temperature or pO_2 ranges should allow for the easier design of systems, as the materials should either be in their oxygenated or reduced state.
- Potentially smaller temperature swings may be needed to incorporate and release large quantities of oxygen.
- Potentially more stability when compared to metal oxide systems which often show sintering quickly.

Three potential oxygen carrier materials with rapid loss of oxygen have been identified from literature reviews, namely, the rare earth manganates [71-72], the rare earth cobaltite's [73-74], and $Ca_2AlMnO_{5+\delta}$ [75].

2.3.1 Hexagonal rare-earth manganites

Hexagonal rare-earth manganites, $RMnO_{3+\delta}$ in which R is a rare earth metal (europium (Eu), yttrium (Y), holmium (Ho), and dysprosium (Dy)), are interesting non-stoichiometric materials that have high oxygen capacities at temperatures below 300°C [76].

When $RMnO_{3+\delta}$ is heated to 500°C in a pO_2 of 1 bar, at a rate of 0.1°C/min, the material incorporates oxygen at approximately 180°C. Oxygen continues to be incorporated into the upon further heating, with $HoMnO_{3+\delta}$ shown to have the largest oxygen capacity with a $\delta=0.25$ at 280°C [77]. Further heating causes the material to release excess oxygen, returning to a low oxygen content, $\delta\approx 0$, at temperatures between 300 and 350°C depending on the R metal used. Incorporated oxygen is shown to be weakly bound, and reducing the pO_2 by switching from oxygen to argon removes the oxygen from the samples. The low-temperature oxygen incorporation/release behaviour of $RMnO_{3+\delta}$ is due to the incorporated oxygen occupying interstitial sites, instead of vacancy sites [78]. This allows use at low temperatures since interstitial oxygen ion diffusion is often characterized by lower activation energies [79]. The size of the R ion has a significant impact on performance, with a larger radius giving larger oxygen capacities [80-81].

Improvements in the oxygen capacity have been shown by several methods. Klimkowicz et al. looked at improving the synthesis process and found material produced by the sol-gel route exhibits oxygen storage capacity almost twice that of a solid-state synthesized material [82] – although this is due to oxygen incorporation rates and surface area, not the thermodynamic maximum.

Doping has also been shown to improve oxygen capacity. A site doping has given improvements. Commonly seen in the literature is $\text{Dy}_{0.7}\text{Y}_{0.3}\text{MnO}_{3+\delta}$, which was found to have a significantly larger oxygen capacity than undoped $\text{DyMnO}_{3+\delta}$ [83]. Tb and Ce doping have been shown to give some of the best performing materials, lowering operation temperatures to below 200°C , as well as increasing the oxygen storage capacity [81]. Substitution of Tb into $\text{YMnO}_{3+\delta}$ increased the δ in the oxidized phase to 0.44 compared to 0.27 in a $p\text{O}_2$ of 1 bar [84].

To investigate the structural changes caused by this incorporation and release of oxygen, neutron diffraction work was carried out [77]. In this experiment, the material was seen to undergo a phase change corresponding to the temperature of oxygen release.

Three phases were found in hexagonal $\text{RMnO}_{3+\delta}$ compounds, with the phase dependant on the oxygen non-stoichiometry. P63cm , R3C and Pca2 were found for a $\delta \approx 0$, ≈ 0.24 – 0.29 and $\delta \approx 0.35$ – 0.41 respectively [86]. The low oxygen content structure ($\delta \approx 0$) consists of corner-sharing MnO_5 trigonal bipyramids. These are separated by eight-fold coordinated R^{3+} cations. Increasing the oxygen content maintains a similar structure, but there is an increased coordination number of cations due to the interstitial oxygen [83].

Dabrowski et al. performed redox cycling of $\text{Y}_{0.95}\text{Pr}_{0.05}\text{MnO}_{3+\delta}$ between 220 and 300°C and saw a steady drop in oxygen incorporated over 20 cycles of 2.6%, although they did not explain in the text this drop in performance [78]. In this study, the low oxidation rates of the material were apparent. Upon heating to 400°C , the amount of oxygen incorporated using a heating rate of $1^\circ\text{C}/\text{min}$, was $1/3$ of that when a heating rate of $0.1^\circ\text{C}/\text{min}$ was used.

While this material is thermodynamically interesting, both the low oxidation rates, as well as the drop in performance over cycling shown in ref. [78] currently limit the application. Also shown in ref.[78] was a dramatic decrease in oxygen incorporation at a $p\text{O}_2$ of 0.21 bar compared to 1 bar. For a truly efficient oxygen storage material, as much oxygen as possible should be taken from the oxidising stream, to ensure the most efficient use of them. Low-efficiency use of the stream will require extra heating and pumping, which at such low operating temperatures, the energy will be difficult to recover well.

2.3.2 $\text{Ca}_2\text{AlMnO}_{5+\delta}$

$\text{Ca}_2\text{AlMnO}_{5+\delta}$ is a brownmillerite with similar oxygen incorporation and release properties to RMnO_3 . Upon heating in a TGA at a rate of $1^\circ\text{C}/\text{min}$ in a $p\text{O}_2$ of 1 bar, oxygen incorporation begins at 300°C , incorporating an oxygen excess of 3wt%. Further heating reduces the oxygen content gradually until approximately 650°C where the oxygen excess is reduced to 2.5 wt%.

Heating the material past this temperature causes the remaining oxygen to be released over a narrow temperature range, with the material returning to its starting stoichiometry by 670°C. Thermodynamic experiments show that the oxygen capacity of the material lies mainly in the pO_2 range of $\log 0.1 - 1$ bar [87]. For this material, it has been shown that the synthesis method has a significant impact on the oxygen storage capacity, with different sintering times changing the oxygen capacity by up to 20% [88]. Redox cycling between a pO_2 of 1 or 0.21 bar, and nitrogen between 450 and 550°C has been performed [89], and it was found that while the greatest oxygen capacity was at 450°C, oxygen release was poor at this temperature. For an isothermal redox cycle between a pO_2 of 1 bar and nitrogen, 500°C was found to give the greatest change in oxygen content per cycle. It was also seen that during a dynamic heating ramp at a rate of 1°C /min, significantly less oxygen was incorporated upon heating in a pO_2 of 0.21 bar (max weight change of approximately 0.6 wt% at 400°C) compared to in a pO_2 of 1 bar (max weight change of approximately 2 wt% at 350°C). Interestingly, XRD studies of the material have shown that during oxidation, AlO_4 tetrahedra convert to AlO_6 octahedra and the Mn oxidation state increases from +3 to +4 [90].

$Ca_2AlMnO_{5+\delta}$ has been studied for a combined chemical looping combustion and air separation by Tobiesen et al. [91]. In this experiment, a bed of $Ca_2AlMnO_{5+\delta}$ was oxidised in an airstream, producing oxygen-lean gas. This oxygen lean gas was then sent to a bed of a metal oxide (Cu) to recover the heat and take advantage of the lower pO_2 requirements to oxidise copper. The process was thought to be promising in the study, with potential efficiency improvements of between 5 and 7% calculated. It was noted that the re-oxidation of $Ca_2AlMnO_{5+\delta}$ was slow, which is likely a major area for improvement.

Further work in optimizing this material has been performed, with Pt nanoparticles shown to increase oxygen incorporation and release rates by approximately 38 and 26% respectively, compared to an uncoated sample [92]. It should be noted that different average particle size was found for the untreated and Pt treated sample (11.43 versus 10.04 μm) which may have accounted for some of this improvement. The samples in this study were shown to give repeatable behaviour over 25 incorporation/release cycles, making this material promising for future study. Strontium doping has also been examined and found to improve the efficiency of the redox cycle, with $Ca_{1.2}Sr_{0.8}AlMnO_{5+\delta}$ the best performing composition synthesized [93]. Fifty cycles redox cycles between a pO_2 of 1 bar and argon were performed in this study, and a decrease in the amount of oxygen stored was noted. The authors attributed this to drift in the analysis, and not degradation of the material and XRD patterns showed no additional phases after cycling. Ga doping has also been examined, and while this decreased the oxygen storage

capacity, it did low the operational temperature, which may provide benefits in its own right [94].

2.3.3 Rare earth cobaltites

The $\text{RBaCo}_4\text{O}_{7+\delta}$ family has been well shown in the literature to have easily reversible oxygen capacity, where each molecule of $\text{YBaCo}_4\text{O}_{7+\delta}$ (the most commonly discussed of this group) can uptake 1.5 oxygen atoms at 300 °C [95-96]. A maximum δ of 1.56 was recorded by Karpinen et al, requiring a $p\text{O}_2$ of 2×10^4 atm, alongside additional KClO_3 to provide excess oxygen [97]. The low temperature and reversible oxygen content make the material interesting for many applications ranging from catalytic oxidations to ion transport membranes [98-107]. Recently, studies using the material for NO_x storage and oxidation were performed, and it has been found suitable for these processes [108].

There have been various R metals explored of which yttrium (Y) is the most common – however metals such as dysprosium (Dy), holmium (Ho), ytterbium (Yb), europium (Eu) and lutetium (Lu) have also been used [109]. Larger cations on the R site have been seen to destabilize the structure, improving oxygen storage properties [110]. Additionally, a smaller ionic radius of R ions lowers the temperature of oxygen release upon heating [111]. Hao et al found that the materials gained weight in proportion to their atomic radius – i.e. oxygen absorption followed the behaviour of $\text{Dy} > \text{Ho} > \text{Y} > \text{Er} > \text{Yb} > \text{Lu}$ [112], although these experiments were dynamic the samples may not have reached equilibrium. Podbereskaya likewise found a correlation between the atomic radii of the A-site ion, and the cell volume at room temperature [113] The $p\text{O}_2$ range that the material operates at is quite high, as the material can be returned to the original oxygen non-stoichiometry by lowering the partial pressures of oxygen using nitrogen [112].

Karpinen et al performed *In-situ* x-ray diffraction (XRD) studies of YBaCo_4O_7 showing complex crystallographic changes in a $p\text{O}_2$ of 1 bar, when heated from 300 to 500°C. Upon oxygen incorporation the material transitions from a hexagonal to an orthorhombic space group at 300°C. Heating to temperatures above 400°C returned the sample to the original hexagonal structure, consistent with the rapid loss of oxygen [114]. The oxygen storage capacity of this material is among the largest recorded non-stoichiometric materials in literature. The operating temperature of the material is only ~400 °C [115-116], significantly lower than its calcination temperature which begins at 1000°C [117-118], likely making $\text{YBaCo}_4\text{O}_{7+\delta}$ less prone to thermal sintering during operation.

The material is typically synthesized at high temperatures (1000 – 1300 °C), however, this can be lowered by ball milling, which has been seen to reduce the synthesis temperature to 900°C [119]. Wu et al synthesised YBaCo_4O_7 at temperatures between 1050 and 1250°C, and it was seen that there were no clear trends between performance and calcination temperature – however, the duration of the calcination did appear to have an impact if the duration was too long [120].

When $\text{RBaCo}_4\text{O}_{7+\delta}$ is heated in an oxygen-containing environment, the material incorporates oxygen at approximately 200°C and this continues until 400°C. Further heating causes the material to release the incorporated oxygen, returning the material to the original non-stoichiometry [121]. A second weight gain is seen upon heating above 650°C to approximately 900°C but this is due to an oxidative decomposition, due to metastability of the material. A third oxygen incorporation/release step was reported by Zhao et al between 900 and 1000°C, however, this was significantly smaller, and normally not discussed in other literature [122]. Frade et al. studied this high-temperature behaviour and found that upon heating, the material decomposed to BaCoO_2 , Y_2O_3 , and Co_3O_4 [123]. this stability has ruled out the use of this family in many different high-temperature areas although there is much interest in extending this temperature range of operation [124-125].

Multiple dopings have been tried to improve the high temperature stability of the material. Aluminium and gallium doping have been shown to improve high-temperature stability; however, this lowers the amount of oxygen incorporated into the sample [126-127]. Although at low temperatures (<100°C) for magnetic properties, co-doping of Al and Ca was seen to mitigate the effect of Al^{3+} on the cobalt oxidation state which is responsible for this drop in performance [128], and a co-doping strategy may improve the oxygen capacity. Calcium and iron doping have both been tried on this material, however, these did not increase the oxygen capacity [53-54]. Calcium doping was also seen to reduce the high-temperature stability [129]. Replacing the Co for 50% Fe gave an oxygen capacity of approximately 25% of the undoped material [130]. Zn doping has also been tried, but this was seen to decrease the oxygen content significantly, particularly at low temperatures [131]. This was explained by Hou et al [132], who explained that during oxygen incorporation of one oxygen ion, two Co^{2+} ions convert to Co^{3+} . Zn cations could not alter their oxidation states from 2+ to 3+, so the substitution decreased the oxygen incorporation. Ni doping was found to be possible up to 5% to form $\text{YBaCo}_{3.8}\text{Ni}_{0.2}\text{O}_{7+\delta}$, although this was only studied at low temperatures (<100°C) for magnetic properties [133]. Similarly, Cu doping is possible up to 17% of the Co [134]. Scandium doping has also been attempted and found to be possible to 30% - although the

impact of this on the oxygen content has not been shown [135]. Bi doping was found to be possible to 5%, however, this was seen to greatly diminish the oxygen incorporation ability [136]. Manthiram et al investigated attempting to prevent the higher temperature decomposition and found Zn improved high-temperature stability. They found better improvements however with completely replacing the a-site metal with In for improved stability at high temperatures further. They interestingly found a combination co-doping of the a and b-sites gave the best results, with $Y_{0.5}In_{0.5}BaCo_3Zn_1O_{7+\delta}$ the most stable of all their samples [137]. Further studies showed that less In was needed to give significantly improved stability, with substitution of less than 20% of the Y for In seen to improve the high-temperature stability [138]. It has however been noted that this partial substitution of Y for In decreases the amount of oxygen that can be cycled at low temperatures [139]. Co-doping of Fe was seen to slightly improve the reduction in low-temperature oxygen incorporation, but not enough to make it attractive for the process [140].

Few metal dopants have been seen to improve the low-temperature oxygen incorporation of the material. Terbium doping to 25% was seen to increase the oxygen capacity by approximately 30% [141]. This was supported by data from Song et al, who found that Tb doping of 50% increased the amount of oxygen incorporated, as well as lowering the temperature that oxygen incorporation began [142]. Zhang et al performed a more comprehensive study of doping and found that 5-10% Ti, 50-75% Dy or 50-75% Pr gave improved oxygen incorporation during 1°C/min heating ramps in a pO_2 of 0.21 bar [143]. They also found potential benefit in co-doping of Ti and Pr to 5 and 75% ratios. Gd doping was seen by Zhao et al to improve the oxygen incorporation of $YbBaCo_4O_{7+\delta}$, with doping of 60% approximately doubling the oxygen content reached during isothermal redox cycles between a pO_2 of 1 bar and nitrogen, at 340°C [144]. Potassium doping was seen to improve the reduction kinetics of the oxygen release [145]. Na doping of the b-site has been seen to increase the electrical conductivity, which has links to the oxygen content of the material – however, no relationship in the oxygen incorporation or release was studied [146].

Yang et al. found that $Y_{0.5}Dy_{0.5}BaCo_4O_{7+\delta}$ and $Y_{0.95}Ti_{0.05}BaCo_4O_{7+\delta}$ incorporated approximately 10% more weight than the undoped species, however this result was a dynamic heating ramp, and isothermal investigations did not show as significant a difference in oxygen incorporation or release [147]. Further study into the activation energy of the oxidation and reduction process saw that the addition of Dy, Ti and Zn increased the activation energy of the oxidation step by between 6 and 10 kJ/mol, and the reduction step by between 10 and 30 kJ/mol [148].

A simple method for improving the oxygen incorporation rate of $\text{YBaCo}_4\text{O}_{7+\delta}$ was found to be ball milling to increase the surface area. Yin et al [149] demonstrated that increased surface area gave good improvement. Increasing the surface area from 0.4 to 3.2 m^2/g by ball milling, increased the amount of oxygen incorporated during a dynamic heating ramp from 1.79 to 2.89 wt%.

Investigations into the oxygen incorporation and release have also been performed. Qin et al investigated the reduction kinetics and found that the rate of oxygen release increased with higher temperature, however, the difference between the time taken for oxygen release to finish for 390 as opposed to 450°C differed by approximately 2 minutes [150]. Yang et al conducted reactor studies using ceramic monoliths coated with $\text{Y}_{0.95}\text{Ti}_{0.05}\text{BaCo}_4\text{O}_{7+\delta}$. [151]. It was found during this study that for good cycling performance, the oxygen concentration during the incorporation step should be as high as feasible, and the temperature of the oxygen release step as high as possible.

Whilst the potential of $\text{YBaCo}_4\text{O}_{7+\delta}$ for oxygen separation has been demonstrated qualitatively, no detailed study of how the release of oxygen from the material changes in different $p\text{O}_2$ s has been conducted. Concerns have been raised that cycling between the orthorhombic and hexagonal phase may cause damage to particles [152], and this has been reported in the literature, with S.E.M images from Smolentsev et al. of the surface of $\text{YBaCo}_4\text{O}_{7+\delta}$ before and after oxygen saturation showing cracking [153]. To the author's knowledge, no long-term cycling of the material has been performed, so the impact this may have on performance stability has not been quantified. The largest number of cycles seen by the author is approximately 5, and during this cycling, there was a drop in performance between the first and fifth cycles. This drop in performance was small and inconsistent, however, and in the fourth cycle, almost as much oxygen was incorporated as the first, suggesting that this was not a drop in performance, but rather instability in the first few redox cycles [154].

The lattice expansion upon heating was seen to be anisotropic, favouring an increase in the C-axis of approximately 5-9% compared to the C-axis, and thermal expansions of approximately $10 \times 10^{-6} \text{ C}^{-1}$ have been reported, depending on the R ion of the material, with zinc doping seen to lower this [155]. The low thermal expansion has been compared favourably to similar materials such as $\text{La}_{0.9}\text{Sr}_{0.1}\text{Ga}_{0.8}\text{Mg}_{0.2}\text{O}_{3-\delta}$ [156] and $\text{La}_{0.6}\text{Sr}_{0.4}\text{CoO}_{3-\delta}$ [155-156]. Thermal expansion can be reduced by Fe or Co doping, due to suppression of change in the Co-O bond length in CoO_4 polyhedra in the structure [157].

Deng et al investigated $\text{YBaCo}_4\text{O}_{7+\delta}$ a thermochemical cycle and found the material was able to remove significant quantities of oxygen, reducing the $p\text{O}_2$ of a vacuum chamber from 21 kPa to 0.5 kPa. They also found that the particle size played a large impact on the rate of oxygen incorporation, with almost 35% more oxygen incorporated upon heating to 300°C when the surface area was increased from 0.48 to 2.42 m^2/g [158]. Investigations by Wohlrab et al. showed the material was suitable for removing trace amounts of oxygen (approx. 4000 ppm) from a methane/ CO_2 gas stream, showing the potential for efficient use of a heated oxygen stream [159].

An investigation of the material was performed for oxy-fuel combustion, and the material was seen to be able to incorporate oxygen from an air stream, and release oxygen into a CO_2 stream isothermally [160]. A scheme was proposed to oxidise the material upon heating in air to 345°C, before releasing the oxygen upon cooling into a CO_2 stream to 200°C. In a practical application, this would not be feasible. This is due to the required oxygen content of a CO_2 stream for oxy-fuel combustion, where a $p\text{O}_2$ of 0.3-0.42 bar is required. Dynamic TGA ramps from multiple sources show that YBaCo_4O_7 will not release its oxygen in a $p\text{O}_2$ of 0.21 bar until approximately 370 – 400 °C. Oxygen release was planned to occur upon cooling from 345°C in the scheme suggested in ref [160], lower than the reduction temperatures in a $p\text{O}_2$ of 0.21 bar, making the scheme unfeasible. Additionally, the oxygen incorporation rates were seen to be fastest at 310°C - contrary to the proposed oxidation temperature of 200°C in their scheme. CO_2 stability tests at 400°C were also performed which are useful and show no degradation of the material, however, this author would suggest stability studies including H_2 , CO , and H_2O as other potential contaminants would be useful, particularly at slightly higher temperatures as oxygen desorption has been shown to occur faster at higher temperatures.

2.3.4 Summary of material literature review

During this section, $\text{YBaCo}_4\text{O}_{7+\delta}$ was identified as a potentially useful oxygen carrier, due to several reasons, namely:

- Comparable oxygen capacity to metal oxide systems
- Temperature-induced redox behavior over a comparably narrow temperature range to the metal oxide systems
- Low-temperature oxygen incorporation (<500°C) which is useful for economic considerations for a process, and potentially improved stability
- A non-stoichiometric crystal structure should hopefully allow for repeatable oxygen cycles over long-time scales

The reason this material was selected versus the $\text{RMnO}_{3+\delta}$ family was favorable kinetics, as TG experiments have shown oxygen incorporation occurs over much longer durations. $\text{YBaCo}_4\text{O}_{7+\delta}$ was chosen versus $\text{Ca}_2\text{AlMnO}_{5+\delta}$ due to favourable thermodynamics, as the operating temperature is lower and the temperature swing required lower.

2.4 Characterisation techniques for non-stoichiometric materials

There are two important characteristics to quantify the effectiveness of a non-stoichiometric material – the oxygen content of the material as a function of temperature and $p\text{O}_2$, and the rate of oxygen diffusion through the material. In this section, the current methods of characterizing the oxygen non-stoichiometry and the diffusion rates of these materials will be discussed.

2.4.1 Techniques to determine oxygen non-stoichiometry

Finding the oxygen non-stoichiometry of an oxygen carrier is important, as it is necessary to know the amount of oxygen that can be exchanged per redox cycle for a reactor design. In literature there are several techniques to quantify the non-stoichiometry of an oxygen carrier and Table 2.6 reviews the most common of these techniques. Other methods such as optical transmission spectroscopy do exist, however, these are less common in literature and as such have been omitted.

Table 2.6 – Review of characterisation techniques to measure oxygen non-stoichiometry

Technique and description	Benefits	Limitations
<p>Thermogravimetric (TGA) analysis</p> <p>A sample of a non-stoichiometric material equilibrates at a known temperature and $p\text{O}_2$, with the weight change is measured. From this change in weight, the non-stoichiometry is calculated from a reference point [161]</p>	<p>Allows for information regarding rates of the oxygen incorporation or release</p> <p>Easy access</p>	<p>Requires an assumed starting stoichiometry to reference against</p> <p>Requires several different gas compositions to get a large range of $p\text{O}_2$'s.</p> <p>Susceptible to gas leaks</p>
<p>Neutron diffraction</p> <p>A similar technique to x-ray</p>		

<p>diffraction, a sample is placed in a focused beam of neutrons, and the angle of incidence changed. From the scattering, information regarding lattice positions in the material can be obtained [162]</p>	<p>Oxygen position in the lattice can be seen</p> <p>No reference points needed</p>	<p>Difficult to get access to</p>
<p>Iodometric titration</p> <p>Several variations of iodometric techniques exist, however these methods involve dissolving the non-stoichiometric material in acid in the presence of a reducing ion such as iodide. From the simple calculation, the oxidation state of the transition metal can be calculated [163]</p>	<p>Easy to gain access to and perform</p> <p>Requires a manual titration and destroys the sample</p>	<p>Can only be performed at room temperatures</p> <p>Requires prepared sample and cannot be performed in-line with an experiment</p>
<p>Columetric titration</p> <p>During this experiment, a sample is sealed in a reactor with an electrochemical sensor and pump. As oxygen is pumped into the chamber, the potential of the electrode changes. From the Nerst equation, the amount of oxygen in the chamber can be calculated [164]</p>	<p>Very accurate</p> <p>Allows very small changes in the pO_2 to be made giving multiple points easily</p>	<p>Susceptible to oxygen leaks</p>

TGA techniques are most commonly used, due to the ease of use and the difficulty of access to neutron diffraction services. TGA analysis to obtain useful thermodynamic data requires multiple gas compositions which can be expensive, particularly with the use of buffer gases and ppm concentrations. A more ideal system would use one gas cylinder, and by changing the pressure of the system, obtain the required pO_2 .

2.4.2 Techniques to determine oxygen diffusion co-efficients

The rate of diffusion of oxygen through and from the material is important for the design of any reactor using the material and the evaluation of its effectiveness. Table 2.7 shows a brief review of the more common diffusion characterisation techniques used in literature

Table 2.7 – Review of characterisation techniques to measure oxygen diffusion

Technique	Benefits	Limitations
<p>Electrochemical relaxation</p> <p>During electrochemical relaxation, electrodes are attached to a dense non-stoichiometric pellet, where a current is passed through. A step change in the pO_2 of the sample environment is performed, causing the sample to change non-stoichiometry. The change in the voltage passing through the sample can be measured and linked to the change in oxygen non-stoichiometry [165-166]</p>	<p>Commonly used technique in literature</p> <p>Accurate results easy to interpret</p>	<p>Requires wiring to be added to the sample</p> <p>Sample must be in the form of a dense pellet</p> <p>Questions about the validity of the results due to mass transfer limitations</p>
<p>TGA experiments</p> <p>During thermogravimetric experiments, the change in weight after a step change in pO_2 is fitted to a solution of Fick's law. This technique has been often used in literature for materials such as $La_{0.6}Sr_{0.4}Co_{0.8}Fe_{0.2}O_{3-\delta}$ [167]</p>	<p>Allows the use of powders</p> <p>Easily understandable data</p> <p>Easy access to TGA</p>	<p>If powders are used, a general assumption must be made on particle geometry</p> <p>Vulnerable to mass transfer limitations and gas leaks. Often researchers perform additional runs at different gas flow rates to determine if any impact [168]</p> <p>Stagnant layers can form</p>

		in TGA crucible, preventing accurate measurements [169]
<p>Optical transmission spectrometry</p> <p>Optical transmission spectrometry is a technique where light is shone through a sample and measured, with the change in the amount of light being absorbed is dependent on the degree of oxidation of the sample. Some experiments have been carried out using iron oxide and measuring the colour change as the material changes oxidation state. From the change in absorbance, rates can be calculated [170]</p>	Useful for testing a coated sample where a very thin covering is desired	<p>Requires difficult preparation and very thin samples</p> <p>Hard to ensure that gas flow is evenly spread through the sample</p>
<p>Pulsed isotopic exchange</p> <p>A powder sample is loaded into a packed bed, and an oxygen-containing gas flows through the bed. Intermittent pulses of different isotopes of oxygen are sent through the reactor, and from the delay and the rate of their incorporation and release through the material is measured by a mass spectrometer at the end of the reactor [171-172]</p>	A large amount of information about the surface and bulk kinetics, as well reaction pathways can be obtained	<p>Expensive isotopes needed</p> <p>Susceptible to leaks</p>
<p>Partial pressure relaxation</p> <p>During this technique, a non-stoichiometric sample can equilibrate in a packed bed reactor at a known pO_2. The pO_2 of the gas flow is then changed and the outlet gas composition measured. From the change in the gas concentration, diffusion</p>	<p>A cheap easy technique to perform</p> <p>Can give accurate data</p>	<p>Susceptible to mass transfer limitations and leaks</p> <p>Potential shifting of the bed</p>

co-efficients can be obtained [173]

As discussed in Table 2.7, many of these techniques for calculating diffusion coefficients suffer from mass transfer limitations, preventing accurate calculations of diffusion coefficients of the material.

A new method to reduce the impact of mass transfer upon diffusion readings is the microfluidized bed TGA (MFB-TGA) [174]. In a comparison of a traditional TGA and MFB-TGA, Yao et al. found mass transfer limitations prevented high-temperature reaction measurements in a traditional TGA but found no such issue with the MFB-TGA [175]. It was also found that the activation energy and low-temperature reaction rates were similar with the TGA and MFB-TGA, giving more credibility to the use of the technology. This technique has already been demonstrated to give good measurement of the reaction rates of perovskite [176]. Additionally, pressure measurements in the system have been shown to give useful information regarding agglomeration when redox cycling of manganese ores was conducted [177]. Further improvements of the method are being developed, such as a combination of mass spectroscopy, which is showing very promising results [176], and this method has been used in many recent studies [178-180].

Figure 2.3 below compares the oxygen diffusion between a traditional, and MFB TGA. As shown, in a traditional TGA, gas flow typically goes across the surface of a pan, making gas diffusion more difficult. For MFB-TGA, the gas flows through the bed, limiting mass transfer possibilities.

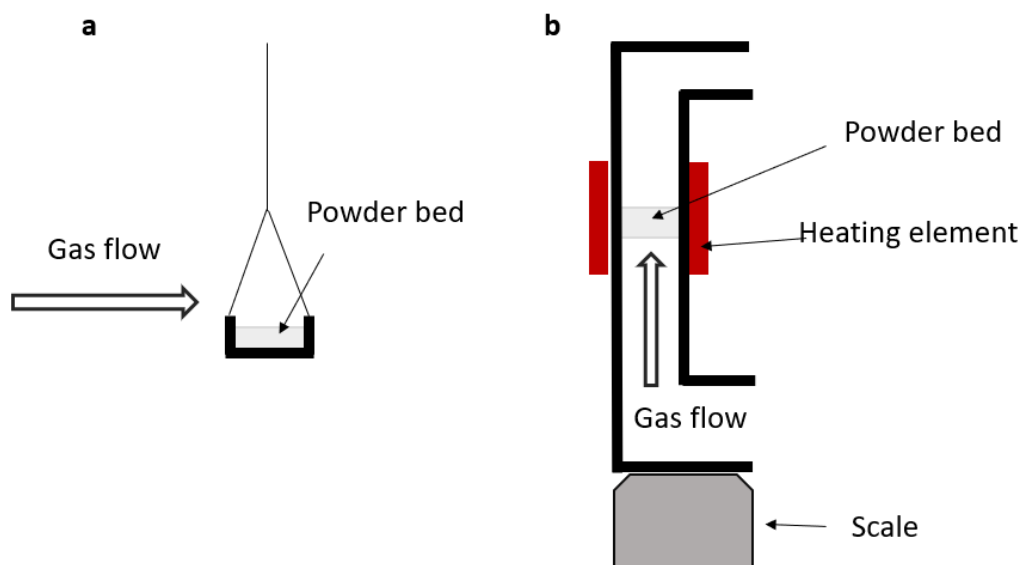


Figure 2.3 – Schematic of (a) – traditional TGA powder pan and gas flow, and (b) – MFB-TGA set up

One major potential issue with this technique is that a fluidized bed must be created, requiring large amounts of material. In Ref [171] and [181], a bed of 16g of silica sand, and 3 or 0.4g of active material were used respectively for the studies. This blend is to ensure a good ratio of oxygen to active material in the bed but gives rise to the possibility of mixing or measurement errors having impacts on any results. Additionally, gas flows and gas mixing must be well controlled, as this has a large potential to impact the measurement, or potentially remove the sample if too high [174,182].

Mass transfer of gases to reactants has been shown repeatedly to be a significant factor in determining oxidation and reduction kinetics. As part of this work, the use of pure gases, to avoid multi-gas diffusion limitations is explored.

2.5 References

- [1] M.H.Jeong D.H.Lee, J.W.Bae - Reduction and oxidation kinetics of different phases of iron oxides, *International Journal of Hydrogen Energy*, 40, 6, 2015, 2613-2620
- [2] E.R.Monazamb, R. W.Breaulta, R. Siriwardanea - Reduction of hematite (Fe₂O₃) to wüstite (FeO) by carbon monoxide (CO) for chemical looping combustion, *Chemical Engineering Journal*, 242, 2014, 204-210
- [3] L.Schramm, G.Behr, W.Löser, and K.Wetzig - Thermodynamic Reassessment of the Cu-O Phase Diagram, *Journal of Phase Equilibria and Diffusion*, 26, 2005, 605-612
- [4] N.Birkner, A.Navrotsky - Thermodynamics of Manganese Oxides: Effects of Particle Size and Hydration on Oxidation-Reduction Equilibria Among Hausmannite, Bixbyite, and Pyrolusite, *American Mineralogist*, 97, 2012, 1291-1298
- [5] M.Chen, B.Hallstedt, L.J.Gauckler - Thermodynamic Assessment of the Co-O System, *Journal of Phase Equilibria*, 24, 2003, 212- 227
- [6] T. Mattisson, A. Lyngfelt, H. Leion, - Chemical-looping with oxygen uncoupling for combustion of solid fuels, *International Journal of Greenhouse Gas Control*, 3, 2009, 11-19
- [7] K.Wang, Q.Yu, Q.Qin - The thermodynamic method for selecting oxygen carriers used for chemical looping air separation. *Journal of Thermal Analysis and Calorimetry*, 112, 2013, 747-753
- [8] K.Shah, B.Moghtaderi, J.Zanganeh, T.Wall - Integration options for novel chemical looping air separation (ICLAS) process for oxygen production in oxy-fuel coal fired power plants, *Fuel*, 107, 2013, 356-370
- [9] X.Tian, Y.Weii, H.Zhao - Using a hierarchically-structured CuO@TiO₂-Al₂O₃ oxygen carrier for chemical looping air separation in a paralleled fluidized bed reactor, *Chemical Engineering Journal*, 334, 2018, 611-618
- [10] C.C.Cormos - Assessment of copper-based chemical looping air separation system for energy efficiency improvements of oxy-combustion and gasification power plants, *Applied Thermal Engineering*, 130, 2018, 120-126
- [11] Y.Cao, B.He, W.Tong, H.Yao, Z.Duan - On the kinetics of Mn₂O₃/ZrO₂ oxygen carrier for chemical looping air separation, *Chemical Engineering and Processing - Process Intensification*, 136, 2019, 82-91
- [12] C.C.Cormos - Techno-Economic Evaluations of Copper-Based Chemical Looping Air Separation System for Oxy-Combustion and Gasification Power Plants with Carbon Capture, *Energies*, 11, 11, 2018, 3095
- [13] Y.Tang, F. You - Life cycle environmental and economic analysis of pulverized coal oxy-fuel combustion combining with calcium looping process or chemical looping air separation, *Journal of Cleaner Production*, 181, 2018, 271-292
- [14] K.Wang, Q.Yu, Q.Qin, Z.Zuo, T.Wu - Evaluation of Cu-based oxygen carrier for chemical looping air separation in a fixed-bed reactor, *Chemical Engineering Journal*, 287, 2016, 292-301
- [15] H.Song, K.Shah, E.Doroodchi, T.Wall, B.Moghtaderi - Analysis on Chemical Reaction Kinetics of CuO/SiO₂ Oxygen Carriers for Chemical Looping Air Separation, *Energy Fuels* 28, 1, 2014, 173-182
- [16] T.Block, M.Schmücker - Metal oxides for thermochemical energy storage: A comparison of several metal oxide systems, *Solar Energy*, 126, 2016, 195-207
- [17] Y.Ku, H.Wu, C.Chang, S.Shii - Chemical looping with air separation (CLAS) in a moving bed reactor with CuO/ZrO₂ oxygen carriers, *International Journal of Greenhouse Gas Control*, 70, 2018, 225-235
- [18] C. M. Kramer, R. M. German - Low-Temperature Sintering of Iron Oxides, *Journal of The American Ceramic Society*, 61, 2006, 340-342
- [19] C.D. Bohn, J.P. Cleeton, C.R. Müller, S.Y. Chuang, S.A. Scott, J.S. Dennis - Stabilizing iron oxide used in cycles of reduction and oxidation for hydrogen production, *Energy Fuel*, 24, 2010, 4025-4033
- [20] L.Liu, Z.Li, Ye Li, N.Cai - Evaluation of oxygen uncoupling characteristics of oxygen carrier using micro-fluidized bed thermogravimetric analysis, *Chinese Journal of Chemical Engineering*, 32, 2021, 408-415
- [21] K.Wang, Q.Yu, Q.Qin - Reduction Kinetics of Cu-Based Oxygen Carriers for Chemical Looping Air Separation, *Energy Fuels*, 27, 9, 2013, 5466-5474

- [22] H.Song, K.Shah, E.Doroodchi, T.Wall, B.Moghtaderi - Reactivity of Al₂O₃- or SiO₂-Supported Cu-, Mn-, and Co-Based Oxygen Carriers for Chemical Looping Air Separation, *Energy Fuels* 28, 2, 2014, 1284–1294
- [23] H.Song, K.Shah, E.Doroodchi, B.Moghtaderi - Development of a Cu–Mg-Based Oxygen Carrier with SiO₂ as a Support for Chemical Looping Air Separation, *Energy and Fuels*, 28, 1, 2014, 163–172
- [24] A.Murugan , A.Thursfield, I.S.Metcalfé - A chemical looping process for production using iron-containing perovskites, *Energy and Environmental Science*, 4, 2011, 4639-4649
- [25] M.Orfila, M.Linares, R.Molina, J.A. Botas, R.Sanz, J.Marugán - perovskite materials for hydrogen production by thermochemical water splitting, *International Journal of Hydrogen Energy*, 41, 2016, 19329-19338
- [26] P. Benzi, E. Bottizzo, N Rizz - Oxygen determination from cell dimensions in YBCO superconductors, *Journal of Crystal Growth*, 269, 2004, 625–629
- [27] A.Chroneos, B. Yildiz, A. Tarancón, D. Parfitt, J.A. Kilner - Oxygen diffusion in solid oxide fuel cell cathode and electrolyte materials: mechanistic insights from atomistic simulations. *Energy & Environmental Science*, 4, 2011, 2774–2789
- [28] I.E.Animitsa, E.Dogodaeva, N.A.Tarasova, A.Neiman - Oxygen-ion and proton transport in Ba₄Na₂W₂O₁₁, *Solid state ionics*, 185, 2011, 1-5
- [29] M. Sjøgaard, P. V. Hendriksen, M. Mogensen - Oxygen nonstoichiometry and transport properties of strontium substituted lanthanum ferrite - *Journal of solid state chemistry*, 180, 4, 2007, 1489-1503
- [30] C.Dueso, C.Thompson, I.S.Metcalfé - High-stability, high-capacity oxygen carriers: Iron oxide-perovskite composite materials for hydrogen production chemical looping, *Applied energy*, 157, 2015, 382-390
- [31] J. Vietena, B. Bulfina, F. Calla, M. Langea, M. Schmückerb, M. Schmückerb, A. Franckeb, M. Roeba, C.Sattler - Perovskite oxides for application in thermochemical air separation and oxygen storage, *Journal of material chemistry A*, 04, 2016, 13652-13659
- [32] H.Ikeda, S.Nikata, E.Hirakawa, A.Tsuchida, N.Miuraa - Oxygen sorption/desorption behaviour and crystal structural change for SrFeO_{3-δ}, *Chemical Engineering Science*, 147, 2016, 166-172
- [33] B. Bulfin, J. Vieten, S. Richter, J. M. Naik, G. R. Patzke, M. Roeb, C. Sattler, A. Steinfeld - Isothermal relaxation kinetics for the reduction and oxidation of SrFeO₃ based perovskites, *Physical Chemistry Chemical Physics*, 22, 2020, 2466-2474
- [34] H. Falco, J. A. Barbero, J. A. Alonso, M. J. Martí'nez-Lope, J. L. G. Fierro - SrFeO_{3-δ} Perovskite Oxides: Chemical Features and Performance for Methane Combustion, *Chem. Mater*, 14, 2002, 2325-2333
- [35] E.Mareka, W.Hu, M.Gaultois, C.P.Grey, S.A.Scott - The use of strontium ferrite in chemical looping systems, *Applied Energy*, 223, 2018, 369-382
- [36] J.Vieten , B.Bulfin, D.E.Starr, A.Hariki, F.M.F.de Groot, A.Azarpira, C.Zachäus, M.Hävecker, K.Skorupska, N.Knoblauch, M.Schmücker, M.Roeb, C.Sattler – Redox Behavior of Solid Solutions in the SrFe_{1-x}Cu_xO_{3-δ} System for Application in Thermochemical Oxygen Storage and Air Separation, *Energy technology*, 7, 2019, 131-139
- [37] G.Luong , F.Donat, C.R.Müller - Structural and thermodynamic study of Ca A- or Co B-site substituted SrFeO_{3-δ} perovskites for low temperature chemical looping applications, *Physical Chemistry Chemical Physics*, 22,2020, 9272-9282
- [38] T.Jia, E.J. Popczun, J.W.Leksea, Y.Duan – The optimal co-doping of SrFe_{1-x}CoxO_{3-δ} oxygen carriers in redox applications, *Physical Chemistry Chemical Physics*,22,2020,16721-16726
- [39] J. Dou, E. Krzystowczyk, X. Wang, T. Robbins, L. Ma, X. Liu, F. Li – A- and B-site Codoped SrFeO₃ Oxygen Sorbents for Enhanced Chemical Looping Air Separation, *ChemSusChem*, 13, 2020, 385-393
- [40] E. J. Popczun, T. Jia, S. Natesakhawat, C. M. Marin, T.-D. Nguyen-Phan, Y. Duan, J. W. Lekse - Investigation of Sr_{0.7}Ca_{0.3}FeO₃ Oxygen Carriers with Variable Cobalt B-Site Substitution, *ChemSusChem*, 14, 2021 1893-1901
- [41] T.P.Farr, N.P.Nguyen, E.Bush, A.Ambrosini, P.G.Loutzenhiser - An A- and B-Site Substitutional Study of SrFeO_{3-δ} Perovskites for Solar Thermochemical Air Separation, *Materials*, 13, 2020, 5123.

- [42] J.Vieten, B.Bulfin, D.E.Starr, A.Hariki, F.M.F.de Groot, A.Azarpira, C.Zachäus, M.Hävecker, K.Skorupska, N.Knoblach, M.Schmücker, M.Roeb, C.Sattler – Redox Behavior of Solid Solutions in the $\text{SrFe}_{1-x}\text{Cu}_x\text{O}_{3-\delta}$ System for Application in Thermochemical Oxygen Storage and Air Separation, *Energy technology*, 7, 2019, 131-139
- [43] B.Bulfin, J.Lapp, S.Richter, D.Gubà, J.Vieten, S.Brendelberger, M. Roeb, C.Sattler -Air separation and selective oxygen pumping via temperature and pressure swing oxygen adsorption using a redox cycle of SrFeO_3 perovskite, *Chemical Engineering Science*, 203, 2019, 68-75
- [44] B. Bulfin, L. Buttsworth, A. Lidor, A. Steinfeld, High-purity nitrogen production from air by pressure swing adsorption combined with SrFeO_3 redox chemical looping, *Chemical Engineering Journal*, 421, 2021, 127734
- [45] X.Chen, M.Kubota, S.Yamashita, H.Kita - Investigation of Sr-based perovskites for redox-type thermochemical energy storage media at medium-high temperature, *Journal of Energy Storage*, 38, 2021, 102501
- [46] E.Krzystowczyk, X.Wang, J.Dou, V.Haribala L.Fanxing - Substituted SrFeO_3 as robust oxygen sorbents for thermochemical air separation: correlating redox performance with compositional and structural properties, *Physical Chemistry Chemical Physics*, 22, 2020, 8924-8932
- [47] V.Sereda, A.Sednev, D.Tsvetkov, A.Zuev - Enthalpy increments and redox thermodynamics of $\text{SrFeO}_{3-\delta}$. *Journal of Materials Research*, 34, 2019, 34, 3288-3295
- [48] E.Heifets, E.A.Kotomin, A.A.Bagaturyants, J.Maier - Thermodynamic stability of non-stoichiometric $\text{SrFeO}_{3-\delta}$: a hybrid DFT study, *Physical Chemistry Chemical Physics*, 21, 2019, 3918-3931
- [49] E.Mareka, W.Hu, M.Gaultois, C.P.Grey, S.A.Scott - The use of strontium ferrite in chemical looping systems, *Applied Energy*, 223, 2018, 369-382
- [50] E.I. Goldyreva, I.A.Leonidov, M.V.Patrakeev. et al. Thermodynamics of oxygen in $\text{CaMnO}_3 - \delta$, *Journal of Solid State Electrochemistry*, 17, 2013, 3185–3190 2013
- [51] B.Bulfin, J.Vieten, D.E.Starr, C.Sattler - Redox chemistry of CaMnO_3 and $\text{Ca}_{0.8}\text{Sr}_{0.2}\text{MnO}_3$ oxygen storage perovskites, *Journal of Materials Chemistry A*, 5, 2017, 7912-7919
- [52] E.L.Leonidova,, I.A.Leonidov, M.V.Patrakeev - Oxygen non-stoichiometry, high-temperature properties, and phase diagram of $\text{CaMnO}_3-\delta$, *J Solid State Electrochem*, 15, 2011, 1071–1075
- [53] E.Bakken, T.Norby, S. Stølen - Nonstoichiometry and reductive decomposition of $\text{CaMnO}_3-\delta$, *Solid State Ionics*, 176, 2005, 217-223
- [54] N.Yu, M.M.Nair, N.Mahinpey, - Structure and phase evolution of CaMnO_3 perovskite during isothermal redox cycles, *Canadian journal of chemical engineering*, 97, 2019, 2131-2136
- [55] A.Zaabout, S.Cloete, J.R.Tolchard, S.Amini - A pressurized Gas Switching Combustion reactor: Autothermal operation with a $\text{CaMnO}_3-\delta$ -based oxygen carrier, *Chemical Engineering Research and Design*, 137, 2018, 20-32
- [56] L.Imponenti, K.Albrecht, J.Wands, M.Sanders, G.S.Jackson - Thermochemical energy storage in strontium-doped calcium manganites for concentrating solar power applications, *Solar Energy*, 151, 2017, 1-13
- [57] J.Kim, X.Chen, Y.Pan, P.Shih, H.Yang - W-Doped $\text{CaMnO}_{2.5}$ and CaMnO_3 Electrocatalysts for Enhanced Performance in Oxygen Evolution and Reduction Reactions, *Journal of the electrochemical society*, 164, 2017, F1074
- [58] E.Mastronardo, X.Qian, J.M.Coronado, S.M.Haile - The favourable thermodynamic properties of Fe-doped CaMnO_3 for thermochemical heat storage, *J. Mater. Chem. A*, 8, 2020, 8503-8517
- [59] M.M.Nair, N.Yu, N.Mahinpey - Dopant-Induced Tailoring of Isothermal Redox Properties of CaMnO_3 Perovskites, *Industrial and Engineering Chemical Research*, 59, 43, 2020, 19406-19414
- [60] E.Mastronardo, X.Qian, J.M. Coronado, S.M. Haile - Impact of La doping on the thermochemical heat storage properties of $\text{CaMnO}_3-\delta$, *Journal of Energy Storage*, 40, 2021, 102793
- [61] N.Kuganathan, A.Chroneos - Defect and dopant properties in CaMnO_3 , *AIP Advances* 11, 2021, 055106

- [62] N.Arunan - Fabrication and processing of next-generation oxygen carrier materials for chemical looping combustion. United States, 2017
- [63] K.Beppu, S.Hosokawa, K.Teramura, T.Tanaka – Oxygen storage capacity of $\text{Sr}_3\text{Fe}_2\text{O}_7-\delta$ having high structural stability, *Journal of material chemistry. A*, 3, 2015, 13540–13545.
- [64] K. Beppu, S.Hosokawa, T.Shibano, A.Demizu, K.Kato, K.Wada, H.Asakura, K.Teramura, T.Tanaka - Enhanced oxygen release/storage properties of Pd-loaded $\text{Sr}_3\text{Fe}_2\text{O}_7-\delta$, *Physical Chemistry Chemical Physic*, 19, 2017, 14107–14113.
- [65] K.Beppu, S.Hosokawa, A.Demizu, Y.Oshino, K.Tamai, K.Kato, K.Wada, H.Asakura, K.Teramura, T.Tanaka - Striking Oxygen-Release/Storage Properties of Fe-Site-Substituted $\text{Sr}_3\text{Fe}_2\text{O}_7-\delta$, *Physical Chemistry Chemical Physic*, 122, 2018, 11186–11193
- [66] M. Hervieu, A. Guesdon, J. Bourgeois, E. Elkaïm, M. Poienar, F. Damay, J. Rouquette, A. Maignan and C. Martin - Oxygen storage capacity and structural flexibility of $\text{LuFe}_2\text{O}_{4+x}$ ($0 \leq x \leq 0.5$), *Nature Materials*, 14, 2014, 74-80
- [67] M.Isobe, N.Kimizuka, J.Iida, S.Takekawa - Structures of LuFeCoO_4 and LuFe_2O_4 , *Acta Crystallographica*, 46, 1990, 1917–1918
- [68] A. Caneiro, L. Mogni, N. Grunbaum, F. Prado - Physicochemical properties of non-stoichiometric oxides: Mixed conductors: Part II, *Journal of Thermal Analysis and Calorimetry*, 104, 2011, 781–788
- [69] A.Ewing – Magnetic induction in iron and other metals, *Philosophical Transactions of the Royal Society, London*, 523
- [70] D.R.Knittel, S.P.Pack, S.H.Lin, L.Eyring – A thermodynamic model of hysteresis in phase transition and its applications to rare earth oxide systems, *Journal of chemical physics*, 67, 1977, 1
- [71] R.Mahesh, M.Itoh - The effect of oxygen stoichiometry on the structure, magnetism and electron transport properties of the rare earth manganates exhibiting charge ordering, *Solid State Ionics*, 108, 1–4, 1998, 201-208
- [72] S.Remsen, B.Dabrowski - Synthesis and Oxygen Storage Capacities of Hexagonal $\text{Dy}_{1-x}\text{Y}_x\text{MnO}_3$, *Chem Mater.* 23, 2011, 3818–3827
- [73] O.Parkkima, H.Yamauchi, M.Karppinen - Oxygen Storage Capacity and Phase Stability of Variously Substituted $\text{YBaCo}_4\text{O}_7+\delta$, *Chem. Mater.* 25, 2013, 599–604
- [74] M.Karppinen, H.Yamauchi, S.Otani, T.Fujita, T.Motohashi - Oxygen stoichiometry in $\text{YBaCo}_4\text{O}_7+\delta$ Large Low-Temperature Oxygen Absorption/Desorption Capability, *Chem Mater* 18, 2006, 490-494
- [75] T.Motohashi, Y.Hirano, Y.Masubuchi, K.Oshima, T.Setoyama, S.Kikkawa - Oxygen Storage Capability of Brownmillerite-type $\text{Ca}_2\text{AlMnO}_5+\delta$ and Its Application to Oxygen Enrichment, *Chem. Mater*, 25, 2013, 372–377
- [76] C. Abughayada, B. Dabrowski, S. Kolesnik, D. E. Brown, O. Chmaissem - Characterization of Oxygen Storage and Structural Properties of Oxygen-Loaded Hexagonal $\text{RMnO}_3+\delta$ (R = Ho, Er, and Y), *Chem. Mater*, 27, 2015, 6259–6267
- [77] K.Swierczek, A.Klimkowicz, K.Nishihara, S.Kobayashi, A.Takasaki, M.Alanizy, S. Kolesnik, B. Dabrowski, S.Seonge, J. Kang - Oxygen storage properties of hexagonal $\text{HoMnO}_3+\delta$, *Physical Chemistry Chemical Physics*, 19, 2017, 19243-19251
- [78] K.Cichy, K.Świerczek, K.Jarosz, A.Klimkowicz, M.Marzec, M.Gajewska, B.Dabrowski -Towards efficient oxygen separation from air: Influence of the mean rare-earth radius on thermodynamics and kinetics of reactivity with oxygen in hexagonal $\text{Y}_{1-x}\text{R}_x\text{MnO}_3+\delta$, *Acta Materialia*, 205, 2021, 116544
- [79] S.H. Skjærvø, E.T. Wefring, S.K. Nesdal, N.H. Gaukås, G.H. Olsen, J. Glaum, T. Tybell, S.M. Selbach - Interstitial oxygen as a source of p-type conductivity in hexagonal manganites, *Nature communications*, 7, 2016, 1-8
- [80] M.Otomo, T.Hasegawa, Y.Asakura, S.Yin - Remarkable Effects of Lanthanide Substitution for the Y-Site on the Oxygen Storage/Release Performance of $\text{YMnO}_3+\delta$, *Applied materials and interfaces*, 13, 2021, 31691–31698

- [81] A.Klimkowicz, T.Hashizume, K.Cichy - Oxygen separation from air by the combined temperature swing and pressure swing processes using oxygen storage materials $Y_{1-x}(Tb/Ce)_xMnO_{3+\delta}$, *Journal of Material Science*, 55, 2020, 15653–15666
- [82] A. Klimkowicz, K. Świerczek, S. Kobayashi, A. Takasaki, W. Allahyani, B. Dabrowski - Improvement of oxygen storage properties of hexagonal $YMnO_{3+\delta}$ by microstructural modifications, *Journal of Solid State Chemistry*, 258, 2018, 471-476
- [83] S.Reimsen, B.Dabrowski - Synthesis and Oxygen Storage Capacities of Hexagonal $Dy_{1-x}Y_xMnO_3$, *Chem. Mater.* 23, 2011, 3818–3827
- [84] A.Klimkowicz, K.Cichy, O.Chmaissem, B.Dabrowski, B.Poudel, K.Świerczek, K.M. Taddei, A.Takasakif - Reversible oxygen intercalation in hexagonal $Y_{0.7}Tb_{0.3}MnO_{3+\delta}$: toward oxygen production by temperature-swing absorption in air, *J. Mater. Chem. A*, 7, 2019, 2608-2618
- [85] C. Abughayada, B. Dabrowski, M. Avdeev, S. Kolesnik, S. Reimsen, O. Chmaissem -Structural, magnetic, and oxygen storage properties of hexagonal $Dy_{1-x}Y_xMnO_{3+\delta}$, *Journal of solid state chemistry*, 217, 2014, 127-135
- [86] A.S. Gibbs, K.S. Knight, P. Lightfoot - High-temperature phase transitions of hexagonal $YMnO_3$ *Physics review B.*, 83, 2011, 094111
- [87] T.Motohashi, Y.Hirano, Y.Masubuchi, K.Oshima, T.Setoyama, S.Kikkawa - Oxygen Storage Capability of Brownmillerite-type $Ca_2AlMnO_{5+\delta}$ and Its Application to Oxygen Enrichment, *Chem. Mater.*, 25, 2013, 372–377
- [88] T.Nomura, C.Zhu, N.Sheng, R.Muraia,T.Akiyama - Solution combustion synthesis of Brownmillerite-type Ca_2AlMnO_5 as an oxygen storage material, *Journal of Alloys and Compounds*, 646, 2015, 900-905
- [89] A.W. Kunlun; Z.Qin, X.Wang, J.Jia, X.Hu, H.Song - Investigation on the Oxygen Resistance Properties of $Ca_2AlMnO_{5+\delta}$ Ceramics, *Sensor Letters*,13, 2015, 236-239
- [90] G.Saito, Y.Kunisada, K.Hayami, T.Nomura, N.Sakaguchi - Atomic and Local Electronic Structures of $Ca_2AlMnO_{5+\delta}$ as an Oxygen Storage Material, *Chem. Mater* 29, 2017, 648–655
- [91] Y.Larring, S.Cloete, A.Giuffrida, M.C.Romano, P.Chiesa, J.Morud, M.Pishahang, A.Chikukwa, S.Amini, A.Tobiesen, COMPOSITE: A Concept for High Efficiency Power Production with Integrated CO2 Capture from Solid Fuels, *Energy Procedia*, 114, 2017, 539-550,
- [92] A.Sato, G.Saito, K.Abe, Y.Kunisada, N.Sakaguchi, T.Akiyama, T.Nomura -Rapid oxygen storage and release with Brownmillerite-structured Ca_2AlMnO_5 , *Journal of Alloys and Compounds*, 851, 2021, 156817
- [93] K.Tanahashi, Y.Omura, H.Naya, K.Miyazaki, G.Saito, Y.Kunisada, N.Sakaguchi, T.Nomura - Sr-Doped $Ca_2AlMnO_5 + \delta$ for Energy-Saving Oxygen Separation Process, *ACS Sustainable Chemistry and Engineering*, 9, 2021, 9317–9326
- [94] X.Huang, C.Ni, J.T.S.Irvine - Oxygen storage capacity and thermal stability of brownmillerite-type $Ca_2(Al_{1-x}Ga_x)MnO_{5+\delta}$ oxides, *Journal of Alloys and Compounds*, 810, 2019, 151865
- [95] O.Parkkima, H.Yamauchi, M.Karppinen - Oxygen Storage Capacity and Phase Stability of Variously Substituted $YBaCo_4O_{7+\delta}$, *Chem. Mater.* 25, 2013, 599–604
- [96] M.Karppinen, H.Yamauchi, S.Otani, T.Fujita, T.Motohashi -Oxygen stoichiometry in $YBaCo_4O_{7+\delta}$ Large Low-Temperature Oxygen Absorption/Desorption Capability, *Chem Mater* 18, 2006, 490-494
- [97] S.Rasanen, H.Yamauchi, M.Karppinen - Oxygen Absorption Capability of $YBaCo_4O_7$, *Chemistry Letters*, 37, 2008, 638-639
- [98] N.A.Danilov, A.P.Tarutin, J.G.Lyagaeva, E.Yu.Pikalova, A.A.Murashkin, D.A.Medvedev, M.V.Patrakeev, A.K.Demin- Affinity of $YBaCo_4O_{7+\delta}$ -based layered cobaltites with protonic conductors of cerate-zirconate family, *Ceramics International* 43, 17, 2017, 15418-15423
- [99] K.Lai, A.Manthiram - Effects of trivalent dopants on phase stability and catalytic activity of $YBaCo_4O_7$ -based cathodes in Solid oxide fuel cells, *J. Mater. Chem. A*, 6, 2018, 1641
- [100] G.Tian, H.Chen, C.Lu, Y.Xin, Q.Li, J.A. Anderson Z.Zhang - An oxygen pool from $YBaCo_4O_7$ -based oxides for soot combustion, *Catal. Sci. Technol.*, 6, 2016, 4511-4515

- [101] O.Parkimma, A.S.Albero, J.S.Albero, M.Karpinnen - Oxygen-Nonstoichiometric YBaCo₄O_{7+δ} as a Catalyst in H₂O₂ Oxidation of Cyclohexene, *Catalysis Letters* 145, 2014, 576-582
- [102] M.A.Kirsanova, V.D.Okatenko, D.A. Aksyonov, R.P.Forslund, J.T.Mefford, K.J.Stevenson, A.M.Abakumov, Bifunctional OER/ORR catalytic activity in the tetrahedral YBaCo₄O_{7.3} oxide, *Journal of Material Chemistry A*, 7, 2019, 330-337
- [103] S.Park, K.Park, J.Shin, G.Ko, W.Kim, J.Park, K.Kwon - Utilizing the Intrinsic Thermal Instability of Swedenborgite Structured YBaCo₄O_{7+δ} as an Opportunity for Material Engineering in Lithium-Ion Batteries by Er and Ga Co-Doping Processes, *Materials* 14, 2021, 4565
- [104] V.D.Craia-Joldes, M.L.Dan, D.A.Duca, N.Vaszilcsin- Calcium-Doped Y114 Layered Cobalt Perovskite, a Promising Anodic Material for Direct Methanol Fuel Cell, *Advanced Engineering Forum*, 27, 2018, 63–73
- [105] M.A.Bhati, R.A.Zargar, A.Modi, M.Arora, N.K.Gaur - Structural, electrical and magnetic features of Kagome YBaCo₄O₇ system, *Materials Science-Poland*, 34, 4, 2016, 786-793
- [106] N.Hollmann, Z.Hu, M.Valldor, A.Maignan, A.Tanaka, H.Hsieh, H.J.Lin, C.T.Chen, L.H.Tjeng- Electronic and magnetic properties of the kagome systems, *Physics Review B*, 80, 8, 2009, 085111-085116
- [107] B.Kouadio, F.Mei, T.Li, L.Pang - High performance Pd–Rh/YBaCo₄O₇/γ-Al₂O₃ three-way catalysts for gasoil engine, *Journal of Taibah University for Science*, 11, 6, 2017, 1306-1316
- [108] H.Okamoto, T.Kajino, H.Yoto, K.Tamai, Y.Yoshiyama, S.Hosokawa, T.Tanaka, T.Yamada, T.Motohashi - TI Low-Temperature NO_x Storage Capability of YBaCo₄O_{7+δ} Originating from Large Oxygen Nonstoichiometry, *Industrial and engineering Chemistry Research*, 60, 2021, 9817 - 9823
- [109] T.Motohashi, S.Kadota, H.Fjellvåg, M.Karppinen, H.Yamauchi - Uncommon oxygen intake/release capability of layered cobalt oxides, REBaCo₄O_{7+δ}: Novel oxygen-storage materials, *Materials Science and Engineering: B*, 148, 1–3, 2008, 196-198
- [110] M. Avdeev, V.V. Kharton, E.V. Tsipis -Geometric parameterization of the YBaCo₄O₇ structure type: Implications for stability of the hexagonal form and oxygen uptake, *Journal of Solid State Chemistry*, 183, 10, 2010, 2506-2509
- [111] S. Kadota, M. Karppinen, T. Motohashi, H. Yamauchi - R-Site Substitution Effect on the Oxygen-Storage Capability of RBaCo₄O_{7+δ}, *Chem. Mater.* 20, 20, 2008, 6378–638
- [112] H.S.Hao, J. Cui, C.Chen, L.Pan, JHu, X, Hu - Oxygen adsorption properties of YBaCo₄O₇-type compounds, *Solid State Ionics*, 177, 7–8, 2006, 631-637
- [113] L. P. Kozeeva, M. Yu. Kameneva, A. N. Lavrov, and N. V. Podberezskaya - Synthesis and Oxygenation Behavior of RBaCo₄O_{7 + δ} (R = Y, Dy–Lu), *Journal of Inorganic Materials*, 49, 2013, 668-673
- [114] M. Valkeapa, M. Karppinen, T. Motohashi, R. Liu, J. Chen, H. Yamauchi - In Situ and Ex Situ Monitoring of Oxygen Absorption in YBaCo₄O₇, *Chemistry Letters*, 36, 2007, 1368-1369
- [115] L.Hou, Q.Yu, K.Wang, Q.Qin, M.Wei, Fan Yang - Oxidation kinetics of YBaCo₄O_{7+δ} and substituted oxygen carriers, *R.Soc.Open.Sci*, 5, 2018, 180150
- [116] L.Hou, Q.Yu, K.Wang, T.Wang, F.Yang, S.Zhang - Oxygen storage capacity of substituted YBaCo₄O_{7+δ} oxygen carriers, *Journal of Thermal Analysis and Calorimetry*, 137, 2018, 317-325
- [117] M.Valldor - Syntheses and structures of compounds with YBaCo₄O₇-type structure, *Solid State Sciences*, 6, 2004, 251-266
- [118] M. Valldor, M. Andersson - The structure of the new compound YBaCo₄O₇ with a magnetic feature, *Solid State Sci.* 4, 2002, 923-931
- [119] E.A. Juarez-Arellano, M. Kakazey, M. Vlasova, G. Urquiza-Beltran, M. Aguilar-Franco, X. Bokimi, E. Martinez, E. Orozco - Microstructural evolution in BaO–Y₂O₃–Co₃O₄ mixtures during high-energy milling and its role in the formation of Y_xBa_{1–x}Co_{3–δ} and YBaCo₄O₇, *Journal of Alloys and Compounds*, 492, 1, 2010, 368-372
- [120] L.Hou, Q.Yu, K.Wang, Q.Zhenfei, Q.Qin & W.Tianwei - Optimal synthesis of YBaCo₄O₇ oxygen carrier for chemical looping air separation, *Energy Sources, Part A: Recovery, Utilization, and Environmental Effects*, 40, 19, 2019, 2354-2366

- [121] H.Hao, L.Zhao, J.Hu, X.Hu, H.Hou - Oxygen adsorption/desorption behavior of $\text{YBaCo}_4\text{O}_{7+\delta}$ and its application to oxygen removal from nitrogen, *Journal of Rare Earths*, 27, 5, 2009, 815-818
- [122] H.Hao, Q.He, Y.Cheng, L. Zhao - Oxygen adsorption and electronic transport properties of Fe-substituted YBaCo_4O_7 compounds, *Materials Research Bulletin*, 53, 2014, 84-88
- [123] E.V.Tsipis, V. V. Kharton, J.R.Frade - Transport properties and electrochemical activity of $\text{YBa}(\text{Co,Fe})_4\text{O}_7$ cathodes, *Solid State Ionics*, 177, 2006, 1823-1826
- [124] D.S.Tsvetkov, V.Pralong, N.S.Tsvetkova, A.Y.Zuev - Oxygen content and thermodynamic stability of $\text{YBaCo}_4\text{O}_{7 \pm \delta}$, *Solid State Ionics*, 278, 2015, 1-4
- [125] D.S.Tsvetkov, N.S.Tsvetkova, I.L.Ivanon, A.Y.Zuev - Thermodynamic stability, oxygen content, defect structure and related properties of $\text{YBaCo}_4 - x\text{Zn}_x\text{O}_7 + \delta$ ($x = 0-3$) oxides, *Solid State Ionics*, 309, 2017, 92-99
- [126] Q.L.He, X.X Shang, H.Song, H.S.Hao - Effect of Al doping on the oxygen adsorption and electronic transport properties of YBaCo_4O_7 , *Journal of Functional Materials*, 45, 2014, 16148-16152
- [127] S.Räsänen, O.Parkkima, E.Rautama, H.Yamauchi, M.Karppinen - Ga-for-Co substitution in $\text{YBaCo}_4\text{O}_{7+\delta}$: Effect on high-temperature stability and oxygen-storage capacity, *Solid State Ionics* 208, 2012, 31-35
- [128] A. Maignan, V. Caignaert, V. Pralong, D. Pelloquin, S. Hébert - Impact of metal substitutions for cobalt in YBaCo_4O_7 , *Journal of Solid State Chemistry*, 181, 5, 2008, 1220-1226
- [129] Y.N.Kim, J.Kim, A.Manthiram - Characterization of $(\text{Y}_{1-x}\text{Ca}_x)\text{BaCo}_4\text{-yZn}_y\text{O}_7$ as cathodes for intermediate temperature solid oxide fuel cells, *International Journal of Hydrogen Energy*, 36, 23, 2011, 15295-15303
- [130] S.M.Zhang, H.Z.Song, X.Su., J.F.Jia, D.L.Yang, H.W.Sun, X.Hu, X. - Preparation and Oxygen Intake/Release Characteristics of $\text{YBaCo}_2\text{Fe}_2\text{O}_7$. *Advanced Materials Research*, 306, 2011, 1520-1523
- [131] D. S. Tsvetkov, P. S. Maram, N. S. Tsvetkova, A. Yu. Zuev, and A. Navrotsky- High-Resolution Thermochemical Study of Phase Stability and Rapid Oxygen Incorporation in $\text{YBaCo}_4 - x\text{Zn}_x\text{O}_{7+\delta}$ 114-Cobaltites, *Journal of Physical Chemistry*, 122, 2018, 50, 9597-960
- [132] H.Hao, L.Zhao, X.Hu, - Effect of metal substitution for cobalt on the oxygen adsorption properties of YBaCo_4O_7 . *Journal of thermal analysis and calorimetry*, 95, 2009, 585-588
- [133] A. Maignan, S. Hébert, V. Caignaert, V. Pralong, D. Pelloquin - Nickel substitution in YBaCo_4O_7 : Effect on the physical properties, *Solid State Communications*, 147, 2008, 470-473
- [134] L. P. Kozeeva, M. Yu. Kameneva, V. Yu. Komarov, A. N. Lavrov, E. A. Maksimovskii, N. V. Podberezskaya - Preparation and Characterization of $\text{YBaCo}_4 - y\text{Cu}_y\text{O}_7 + x$ Compounds, *Inorganic Materials*, 52, 2016, 1116-1121
- [135] M.Y.Kameneva, L.P.Kozeeva, AN.Lavrov - Preparation and Investigation of Compounds with the 114-Type Structure in the Y-Sc-Ba-Co-O System, *Journal of structural chemistry*, 61, 2020, 29-43
- [136] Y.M.Zhang, R.Q.Han, X.S.Wu, Z.Wang - An X-Ray Diffraction and Thermogravimetric Study of Layered Perovskite $\text{Y}_{1-x}\text{Bi}_x\text{BaCo}_4\text{O}_7$, *Chinese Physics letters*, 28, 2011, 128202
- [137] Y.N. Kim, J.H. Kim, A. Huq, M.P. Paranthaman, A. Manthiram - $(\text{Y}_{0.5}\text{In}_{0.5})\text{Ba}(\text{Co,Zn})_4\text{O}_7$ cathodes with superior high-temperature phase stability for solid oxide fuel cells, *Journal of Power Sources*, 214, 2012, 7-14
- [138] M.West, A.Manthiram - Improved phase stability and electrochemical performance of $(\text{Y,In,Ca})\text{BaCo}_3\text{ZnO}_{7+\delta}$ cathodes for intermediate temperature solid oxide fuel cells, *International Journal of Hydrogen Energy*, 39, 34, 2014, 19722-19730
- [139] M.West, S.Sher, A.Manthiram - Effects of In substitution in $\text{Y}_{1-x}\text{In}_x\text{BaCo}_3\text{ZnO}_{7+\delta}$ ($0 \leq x \leq 0.5$) cathodes for intermediate temperature solid oxide fuel cells, *Journal of Power Sources*, 271, 2014, 252-261
- [140] M.West, C.Ortiz, A.Manthiram - High-performance $\text{Y}_{0.9}\text{In}_{0.1}\text{BaCo}_3(\text{Zn,Fe})\text{O}_7 + \delta$ swedenborgite-type oxide cathodes for reduced temperature solid oxide fuel cells, *International Journal of Hydrogen Energy*, 40, 2, 2015, 1186-1194,

- [141] H.Song, J.Jia, S.Zhang, D.Yang, H.Sun - X.Hu Remarkable oxygen adsorption/desorption capability of $\text{Y}_{0.5}\text{Tb}_{0.5}\text{BaCo}_4\text{O}_{7+\delta}$ under temperature cycles, *Materials Research Bulletin* 47, 3, 2012, 518-520
- [142] K.Wang, Y.Chen, X.Hu, H.Song, Q.He - Oxygen Resistance Sensor Properties of $\text{YBaCo}_4\text{O}_{7+\delta}$ and $\text{Y}_{0.5}\text{Tb}_{0.5}\text{BaCo}_4\text{O}_{7+\delta}$, *Int. Journal of applied ceramic technologies*, 12, 2015, 1184-1188
- [143] L.Hou, Q.Yu, K.Wang, T.Wang, F.Yang, S.Zhang - Oxygen storage capacity of substituted $\text{YBaCo}_4\text{O}_{7+d}$ oxygen carriers, *Journal of Thermal Analysis and Calorimetry*, 137, 2019, 317–325
- [144] H.Hao, Y.Cheng, J.Zhang, L.Zhao - Improvement of oxygen adsorption capacity of $\text{YbBaCo}_4\text{O}_{7+\delta}$ by Gd-for-Yb substitution, *Materials Research Bulletin*, 63, 2015,226-230
- [145] L.Hou,C.Qiao, Q.Yu, W.Wu - Effects of introducing foreign ion K on the reduction kinetics of oxygen carriers in chemical looping air separation process, *Environmental Progress and Sustainable Energy*, 2021, e13720.
- [146] S.L.Leng, X.X.Wang, H.Z. Song - Enhanced thermopower of $\text{YBaCo}_4\text{O}_{7+\delta}$ by Na-for-Ba substitution, *IOP Conference Series.: Earth and Environmental Sciences*, 61, 2017, 01201
- [147] L.Hou, Q.Yu, K.Wang, T.Wu, M.Wei, F.Yang, - Practicability study of $\text{YBaCo}_4\text{O}_{7+\delta}$ and substituted samples for chemical looping air separation process, *Environmental Progress and Sustainable Energy*, 38, 2019, 563-569.
- [148] L.Hou, Q.Yu, T.Wang - Kinetics of perovskite-like oxygen carriers for chemical looping air separation, *Korean Journal of Chemical Engineering*, 35, 2018, 626–636
- [149] T.Chen, Y.Asakura, T.Hasegawa, T.Motohashi, S.Yin - A simple and novel effective strategy using mechanical treatment to improve the oxygen uptake/release rate of $\text{YBaCo}_4\text{O}_{7+\delta}$ for thermochemical cycles, *Journal of Materials Science & Technology*, 68, 2021, 8-15
- [150] L.Hou, Q.Yu, K.Wang, S.Zhang, Q.Qin - Reduction Kinetics of $\text{YBaCo}_4\text{O}_{7+\delta}$ Oxygen Carrier for Chemical Looping Air Separation, *IOP Conference Series: Earth and Environmental Science*, 237, 3, 2019
- [151] L.Hou, Q.Yu, K.Wang - Sensitivity analysis of key factors in controlling absorption and desorption of oxygen to oxygen carriers, *Korean Journal of Chemical Engineering*, 36, 2019, 84–91
- [152] A. V. Alekseev, M. Yu. Kameneva, L. P. Kozeeva, A. N. Lavrov, N. V. Podberezskaya, A. I. Smolentsev, A. N. Shmakov - Structural Phase Transitions in $\text{YBaCo}_4\text{O}_7 + x$ Cobaltate upon Variations in Oxygen Content, According to XRay Diffraction Data Obtained Using Synchrotron Radiation, *Bulletin of the Russian Academy of Sciences. Physics*,77, 2013, 151–15
- [153] N. V. Podberezskaya, N. B. Bolotina, V. Yu. Komarova, M. Yu. Kamenevaa, L. P. Kozeevaa, A. N. Lavrova, A. I. Smolentseva - Orthorhombic $\text{YBaCo}_4\text{O}_{8.4}$ Crystals As a Result of Saturation of Hexagonal YBaCo_4O_7 Crystals with Oxygen, *Crystallography Reports*, 60, 2015, 484–492
- [154] L.Hou, Q.Yu, K.Wang • F.Yang, T.Wu - Oxidation and reduction kinetic of $\text{YBaCo}_4\text{O}_{7+d}$ and substituted oxygen carriers, *Journal of Thermal Analysis and Calorimetry*,134:, 2018, 2213–2221
- [155] J.Kim, A.Manthiram - Low Thermal Expansion $\text{RBa}(\text{Co},\text{M})_4\text{O}_7$ Cathode Materials Based on Tetrahedral-Site Cobalt Ions for Solid Oxide Fuel Cells, *Chem. Mater*,22, 3,2010, 822–831
- [156] Q.Zhou, Y.Shi, J.Hu, T.Wei, Z.Li, Y.Li, X.Qi, W.Zhao, W.Zhang - Preparation, characterization, and electrochemical properties of $\text{YBaCo}_{3.4}\text{Al}_{0.3}\text{Ga}_{0.3}\text{O}_{7+\delta}$ and $\text{YBaCo}_{3.2}\text{Al}_{0.4}\text{Ga}_{0.4}\text{O}_{7+\delta}$ cathodes for IT-SOFCs, *Ceramics International*, 40, 8, 2014, 13481-13485
- [157] W.Kan, K.Lai, A Huq, M.Arumugam - Unravelling the low thermal expansion coefficient of cation-substituted $\text{YBaCo}_4\text{O}_{7+\delta}$, *Journal of Power Sources*, 307, 2016, 454-461
- [158] M.Xu, I.Ermanoski, E.B.Stechel, S.Deng -Oxygen pumping characteristics of $\text{YBaCo}_4\text{O}_{7+\delta}$ for solar thermochemical cycles, *Chemical Engineering Journal*, 389, 2020,124026,
- [159] T.Peppel, D.Seeburg, G.Fulda, M.Kraus, U.Trommler, U.Roland, S.Wohlrab - Methods for the Trace Oxygen Removal from Methane-Rich Gas Streams, *Chemical Engineering and Technology*, 40, 2017, 153-161
- [160] Z.Rui, J.Ding, L.Fang, Y.S. Lin, Y.Li - $\text{YBaCo}_4\text{O}_{7+\delta}$ sorbent for oxygen-enriched carbon dioxide stream production at a low-temperature, *Fuel*, 94, 2012, 191-196

- [161] E.I. Leonidova, I.A. Leonidov, M.V. Patrakeev, V.L.Kozhevnikov - Oxygen non-stoichiometry, high-temperature properties, and phase diagram of $\text{CaMnO}_{3-\delta}$, *Journal of Solid State Electrochemistry*, 15, 5, 2011, 1071–1075
- [162] S.McIntosh, J.F.Vente, W.G.Haije, D.H.A.Blank, H.J.M.Bouwmeester - Phase stability and oxygen non-stoichiometry of $\text{SrCo}_{0.8}\text{Fe}_{0.2}\text{O}_{3-\delta}$ measured by in situ neutron diffraction, *Solid State Ionics*, 177, 2006 9–10, 833-842
- [163] S.Georgieva, T.Nedeltcheva, A.Stoyanova-Ivanova - Development of the Titrimetric and Spectrophotometric Methods for Determination of the Oxygen Content in Superconducting Cuprates. *American Chemical Science Journal*. 13,2016, 1-15
- [164] M.V.Patrakeev, I.A.Leonidov, V.L.Kozhevnikov - Applications of coulometric titration for studies of oxygen non-stoichiometry in oxides, *J Solid State Electrochem*, 2011, 15, 931–954
- [165] B. Ma, J. H. Park and U. Balachandran - Analysis of Oxygen Transport and Stoichiometry in Mixed-Conducting $\text{SrFeCo}_{0.5}\text{O}_x$ by Conductivity and Thermogravimetric Analysis, *J Electrochem Soc*, 144, 1997, 2816-2823.
- [166] A. Berenov, A. Atkinson, J. Kilner, M. Ananyev, V. Eremin, N. Porotnikova, A. Farlenkov, E. Kurumchin, H. J. M. Bouwmeester, E. Bucher and W. Sitte - Oxygen tracer diffusion and surface exchange kinetics in $\text{Ba}_{0.5}\text{Sr}_{0.5}\text{Co}_{0.8}\text{Fe}_{0.2}\text{O}_{3-\delta}$, *Solid State Ionics*, 268, Part A, 2014 102-109.
- [167] M.Katsuki, S.Wang, M.Dokiya, T.Hashimoto - High temperature properties of $\text{La}_{0.6}\text{Sr}_{0.4}\text{Co}_{0.8}\text{Fe}_{0.2}\text{O}_{3\delta}$ oxygen nonstoichiometry and chemical diffusion constant, *Solid State Ionics*, 156, 2003, 453–461
- [168] W.Huo, Z.Zhou, X.Chen, Z.Dai, G. Yu - Study on CO_2 gasification reactivity and physical characteristics of biomass, petroleum coke and coal chars, *Bioresource Technology*, 159, 2014, 143-149
- [169] P.Geng, Y.Zhang, Y.Zheng - Experimental estimate of CO_2 concentration distribution in the stagnant gas layer inside the thermogravimetric analysis (TGA) crucible, *Fuel*, 224, 2018,250-254
- [170] N.H.Perry, J.J.Kim, H.L.Tuller - Oxygen surface exchange kinetics measurement by simultaneous optical transmission relaxation and impedance spectroscopy: $\text{Sr}(\text{Ti,Fe})\text{O}_{3-x}$ thin film case study, *Science and Technology of Advanced Materials*, 19,1,2018 130-141
- [171] H.J.M.Bouwmeester, C.Song, J.Zhu, J.Yi, M.van Sint Annalanda, B.A.Boukampa - A novel pulse isotopic exchange technique for rapid determination of the oxygen surface exchange rate of oxide ion conductors, *Physical Chemistry Chemical Physics*, 11, 2009, 9640-9643
- [172] E.Tropin, M.Ananyev, N.Porotnikova, A.Khodimchuk, S.Saher, A.Farlenkov, E.Kurumchin, D. Shepel, E.Antipov, S.Istominef, H.Bouwmeester - Oxygen surface exchange and diffusion in $\text{Pr}_{1.75}\text{Sr}_{0.25}\text{Ni}_{0.75}\text{Co}_{0.25}\text{O}_{4\pm\delta}$ *Phys. Chem. Chem. Phys.*, 21, 2019, 4779-4790
- [173] S.F. Bychkov, I.I. Gainutdinov, S.A. Chizhik, A.P. Nemudry - Novel oxygen partial pressure relaxation technique for study of oxygen exchange in nonstoichiometric oxides. The model of relaxation kinetics, *Solid State Ionics*, 320, 2018, 297-304
- [174] Y. Li, H. Wang, W. Li, Z. Li, N. Cai - CO_2 gasification of a lignite char in microfluidized bed thermogravimetric analysis for chemical looping combustion and chemical looping with oxygen uncoupling, *Energy Fuels*, 33, 1, 2018, 449-459
- [175] Y.Fang, R.Zou, G.Luo, J.Chen, Z.Li, Z.Mao, X.Zhu, F.Peng, S.Guo, X.Li, H.Yaoi - Kinetic Study on Coal Char Combustion in a Microfluidized Bed, *Energy Fuels* 2017, 31, 3, 3243–3252
- [176] L.Liu, Z.Li, Z.Li, Y.Larring, Y.Li, N.Cai - Fast redox kinetics of a perovskite oxygen carrier measured using micro-fluidized bed thermogravimetric analysis, *Proceedings of the Combustion Institute*, 38, 4, 2021, 5259-5269
- [177] L.Liu, Z.Li, Y.Li, N.Cai - Evaluation of oxygen uncoupling characteristics of oxygen carrier using micro-fluidized bed thermogravimetric analysis, *Chinese Journal of Chemical Engineering*, 32, 2021, 408-415
- [178] T.Shen, J.Yan, X.Zhu, L.Wang, L.Shen -Catalytic combustion behaviors of petroleum coke with hematite catalyst in a micro fluidized bed thermogravimetric analysis, *Chemical Engineering Journal*, 422, 2021, 130087

- [179] Y.Li, Z.Li, H.Wang, N.Cai -CaO carbonation kinetics determined using micro-fluidized bed thermogravimetric analysis, *Fuel*, 264, 2020, 116823
- [180] L.Liu, Z.Li, Z.Li, Y.Larring, Y.Li, N.Cai - Fast redox kinetics of a perovskite oxygen carrier measured using micro-fluidized bed thermogravimetric analysis, *Proceedings of the Combustion Institute*, 38, 4, 2021, 5259-5269
- [181] Y.Li, Z.Li, L.Liu, N.Cai -Measuring the fast oxidation kinetics of a manganese oxygen carrier using microfluidized bed thermogravimetric analysis, *Chemical Engineering Journal*, 385, 2020, 123970,
- [182] P.S. Fennell, J.S. Dennis, A.N. Hayhurst -The order with respect to oxygen and the activation energy for the burning of an anthracitic char in O₂ in a fluidised bed, as measured using a rapid analyser for CO and CO₂, *Proceedings of the Combustion Institute*, 32, 2, 2009, 2051-2058

Chapter 3 Aims and objectives

3.1 Aims and novelty

In chapter 1, it was shown oxygen demand has increased significantly over the past decades, with uses in multiple applications [1]. One process of note is oxy-fuel combustion, which offers a significant global impact [2]. The major issue preventing more widespread use of oxy-fuel combustion is the high cost of oxygen, as this is most often produced by cryogenic distillation which is energy-intensive [3]. Therefore, finding a cheaper way to add pure oxygen to a CO₂ stream is of great import for the feasibility of oxy-fuel combustion.

One potential process identified to reduce the cost of oxygen production is the CLAS process. [4]. Much work has been performed to find a suitable oxygen non-stoichiometric material for the process, however, issues with material stability (for metal oxide materials) [5], or low oxygen storage capacity (perovskites) are common [6].

In this work, a potentially useful material (YBaCo₄O_{7+δ}) has been selected for further detailed studies for a chemical looping air separation for oxy-fuel combustion. The literature of this material shows high oxygen capacity (approx. 3.5% by mass) and low operating temperatures (300 – 500°C) [7]. An interesting oxygen release behaviour during heating is also seen, where the incorporated oxygen is released over narrow temperature ranges upon heating. It is hoped that the low operating temperatures and high oxygen content will provide a stable, high-capacity material, which requires small temperature swings to incorporate and release the stored oxygen. This work is primarily a feasibility study of this material, examining the kinetics, stability and thermodynamics and comparing to other oxygen carriers, to determine if the material has potential for oxygen enrichment processes. It is the hypothesis of this work, that redox cycling using YBaCo₄O_{7+δ} may offer significant advantages in terms of both efficiency of oxygen incorporation and release, and stability over redox cycling, compared to transition metal oxides and other non-stoichiometric materials.

The major novelty in this work surrounds the study of the oxygen incorporation and determination of the best method of performing redox cycles with this material. To the best of the authors knowledge, no significant number of redox cycles of this material are available in literature.

The first step will require determining the amount of oxygen that can be incorporated and released over redox cycling. Unfortunately, most papers that study the oxygen content of the sample, do so using dynamic heating ramps, meaning the oxygen contents may be kinetically

limited. Also in literature, the pO_2 of oxygen incorporation and release are not examined in the pO_2 range for oxy-fuel combustion (0.31-0.4 bar), with results typically shown at 0.21 or 1 bar.

While this previous work is important, to determine the true feasibility of $YBaCo_4O_{7+\delta}$, the oxygen incorporation and release should be studied in the pO_2 range of 0.025 to 0.45. This is important for two reasons. The first is the pO_2 of the gas phase is likely to vary significantly depending upon what region of a reactor the material is in during the oxidation and reduction steps, creating different oxygen gradients between the gas and solid phases through a bed. Therefore, examining how $YBaCo_4O_{7+\delta}$ will oxidise and reduce at different pO_2 's and temperatures will determine how efficient the material may be. Secondly, the desired oxygen concentration of the oxygen-enriched flue gas for oxy-fuel combustion is between 0.31 and 0.42 bar. Therefore, any study relating to this material for this process must include data in this region, which is currently missing from literature. To this end, a detailed study of $YBaCo_4O_{7+\delta}$ in the pO_2 range of interest for oxy-fuel combustion is performed, which was missing from literature. Multiple redox cycling schemes are tested, and the cycle design is shown to be critical for maintaining performance and stability. Finally, a model is produced to examine how packed beds of $YBaCo_4O_{7+\delta}$ may be used for this process.

To aid in this work, a novel method of determining oxygen content, and gas diffusion coefficients is developed. This method relies upon allowing a non-stoichiometric material to equilibrate in a pure oxygen gas phase, before a sudden change in the pressure is applied, forcing the material to re-equilibrate. From measuring the change in total pressure, the change in oxygen non-stoichiometry can be determined.

This work is above all a feasibility study. Chapter 4, the development of a novel pressure relaxation technique, was intended to improve some issues with oxygen diffusion measurements, as well as make a novel technique that could help characterise the material. Chapter 5 is intended to give thermodynamic data of $YBaCo_4O_{7+\delta}$, to help design redox cycling schemes of the process. These schemes are then used in chapter 6, where the thermodynamic data from chapter 5 is used to perform a feasibility study of the material.

3.2 Objectives

This work aims to attempt to find more suitable oxygen carriers for redox cycling. During this work currently, non-stoichiometric materials with more sudden changes in oxygen non-stoichiometry have been identified as promising materials for oxygen separation technologies,

namely $\text{YBaCo}_4\text{O}_{7+\delta}$. To quantify their potential four objectives will be fulfilled during this thesis.

- **Creation of a useful technique to characterise oxygen non-stoichiometry and diffusion coefficients** – As discussed in chapter 2, there are issues with the current methods of calculating diffusion coefficients. As part of this work, a new characterisation technique known as pressure relaxation will be developed to help give accurate kinetic information about the material.
- **Detailed investigation into the thermodynamics of the selected oxygen carrier** – Detailed study into both the oxygen content and phase changes of $\text{YBaCo}_4\text{O}_{7+\delta}$ as a function of $p\text{O}_2$ and temperature will be performed to help design the best redox cycles using the material.
- **Investigation into the stability of the non-stoichiometric material** – If $\text{YBaCo}_4\text{O}_{7+\delta}$ has suitable kinetics and thermodynamics, it would also be required to be stable over redox cycling, resistant to both sintering and phase degradation. Additionally, the chemical stability of $\text{YBaCo}_4\text{O}_{7+\delta}$ in different reducing gases should be studied, to ascertain which processes the material would be suitable for.
- **Investigation into the kinetics of the selected oxygen carrier** – Kinetics of $\text{YBaCo}_4\text{O}_{7+\delta}$ will be gathered, so a working bed of the material can be modelled, to help see the effectiveness of the material as a potential oxygen carrier.

Once these objectives have been fulfilled, the information will be collated and discussed to determine if $\text{YBaCo}_4\text{O}_{7+\delta}$ has promise as an oxygen carrier, and if so, where improvements must be made to make it viable.

3.3 References

- [1] Production volume of oxygen in Japan from 2012 to 2017 (in billion cubic meters) – Statista, retrieved from <https://www.statista.com/statistics/737094/japan-oxygen-production-volume/>. Accessed 14/11/2018.
- [2] R.Stanger, T.Wall, R.Spörl, M.Paneru, S.Grathwohl, M.Weidmann, G.Scheffknecht, D.McDonald, K.Myöhänen, J.Ritvanen, S.Rahiala, T.Hyppänen, J.Mletzko, A.Kather, S.Santos - Oxyfuel combustion for CO₂ capture in power plants, *International Journal of Greenhouse Gas Control*, 40, 2015, 55-125
- [3] J.Ahn, T.Kim - Effect of oxygen supply method on the performance of a micro gas turbine-based triple combined cycle with oxy-combustion carbon capture, *Energy*, 211, 2020, 119010,
- [4] B.Moghtaderi - Application of Chemical Looping Concept for Air Separation at High Temperatures, *Energy Fuels*, 24, 2010, 190–198
- [5] C. M. Kramer, R. M. German - Low-Temperature Sintering of Iron Oxides, *Journal of The American Ceramic Society*, 61 7-8, 2006, 340-342
- [6] B.Bulfin, J.Vieten, D.E.Starr, C.Sattler - Redox chemistry of CaMnO₃ and Ca_{0.8}Sr_{0.2}MnO₃ oxygen storage perovskites, *Journal of Materials Chemistry A*, 5, 2017, 7912-7919
- [7] T.Motohashi, S.Kadota, H.Fjellvåg, M.Karppinen, H.Yamauchi - Uncommon oxygen intake/release capability of layered cobalt oxides, REBaCo₄O_{7+δ}: Novel oxygen-storage materials, *Materials Science and Engineering: B*, 148, 1–3, 2008, 196-198

Chapter 4 – Methods of creating and characterising non-stoichiometric materials

This chapter will describe the analytical methods used to characterise samples, as well as the specific experiments performed in the experimental chapters.

4.1 X-ray diffraction

X-ray diffraction is a useful tool for identifying a crystal's structure. The technique works by directing a beam of incident x-rays into the crystalline structure. The electrons will eventually get enough energy to dislodge inner shell electrons giving characteristic x-ray spectra. These spectra consist of $K\alpha$ and $K\beta$ which can be broken down into further subgroups of wavelengths, $K\alpha_1$ and $K\alpha_2$. $K\alpha_1$ has a shorter wavelength, however, $K\alpha_2$ has half the intensity. Foils or crystal monochromators filter the waves and produce monochromatic X-rays by leaving only $K\alpha$. A weighted average of $K\alpha_1$ and $K\alpha_2$ is used for this method. Copper is the most common source of x-rays for single-crystal diffraction, with Cu $K\alpha$ radiation = 1.5418\AA .

During the test, a crystal is mounted on a goniometer which is used to orientate the crystal at the required angles. A fine monochromatic beam of X-rays is directed into the crystals, producing a diffraction pattern. When the x-ray angle satisfies the Bragg equation, the crystals diffract x-rays in different directions. The different angles and intensities of the diffracted beams can be used to quantify the density of electrons in a crystal and hence the chemical bonds within the crystal. Figure 3.1 below demonstrates the operation of an XRD unit.

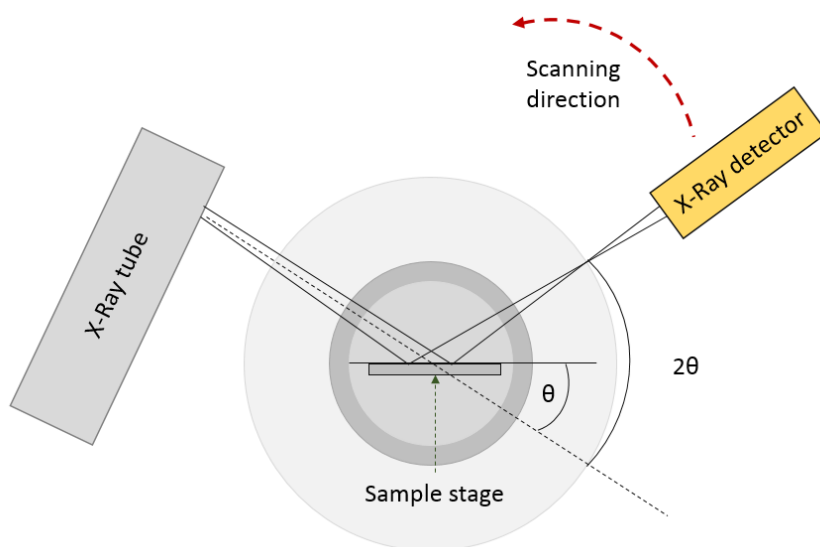


Figure 4.1 – Diagram showing simplified workings of an XRD unit

An X-ray diffraction profile will often be compared against standards or other results in the literature. Variations between reported spectra can be a clear indication of chemical impurities (or a secondary phase) within a sample and there are two variables, peak location, and peak intensity. The peak intensity is the amount of radiation diffracted to the detector, the greater the number of counts will mean there is a greater amount of that corresponding crystal face within the sample which diffracts at that angle. The peak location is given by the angle of incidence that gives the peak. By a combination of the peak heights and the peak location, a phase can be identified.

The major advantage of this technique is that it is a quick and non-destructive method of analyzing the sample; the issues with it however come from the analysis, and a reference file is needed for the comparison.

Two types of XRD were used for this work, *ex-situ* (where the sample was tested at room temperatures in an uncontrolled gas environment) and *in-situ* (where the temperature and gas environment of the sample was controlled to determine how the material behaved as a function of these properties). *Ex-situ* XRD was used to test a samples phase purity for this thesis and these experiments were conducted using an X-pert pro-PANalytical machine.

In-situ XRD was used for more detailed experiments probing effects to a sample such as phase changes or chemical expansion as an effect of temperature and pO_2 . An X-pert pro-PANalytical machine was used with a heated stage to obtain the temperatures required for analysis. Gas flows of 150 ml/min were used, with gases of a pO_2 of between 0 (inert) and 1 bar.

4.2 Thermogravimetric analysis (TGA)

Thermogravimetric analysis is a technique which measures a sample's mass changes in a controlled atmosphere. Both the temperature and gas environment can be controlled during this process meaning that the technique can perform thermodynamic analysis for many different types of processes, such as absorption in oxygen which currently is the main characterisation technique used for this report. The method will be used to obtain changes in delta for the materials in different gas environments. It is expected to see that in environments of increased oxygen partial pressures, an increased equilibrium oxygen delta of the samples will be achieved, or that oxygen uptake and saturation of a sample will occur faster.

TGA measurements often take place within a furnace where the sample's temperature is controlled. For these tests a Rubotherm unit was used, and a schematic of this system can be seen in Figure 4.2.

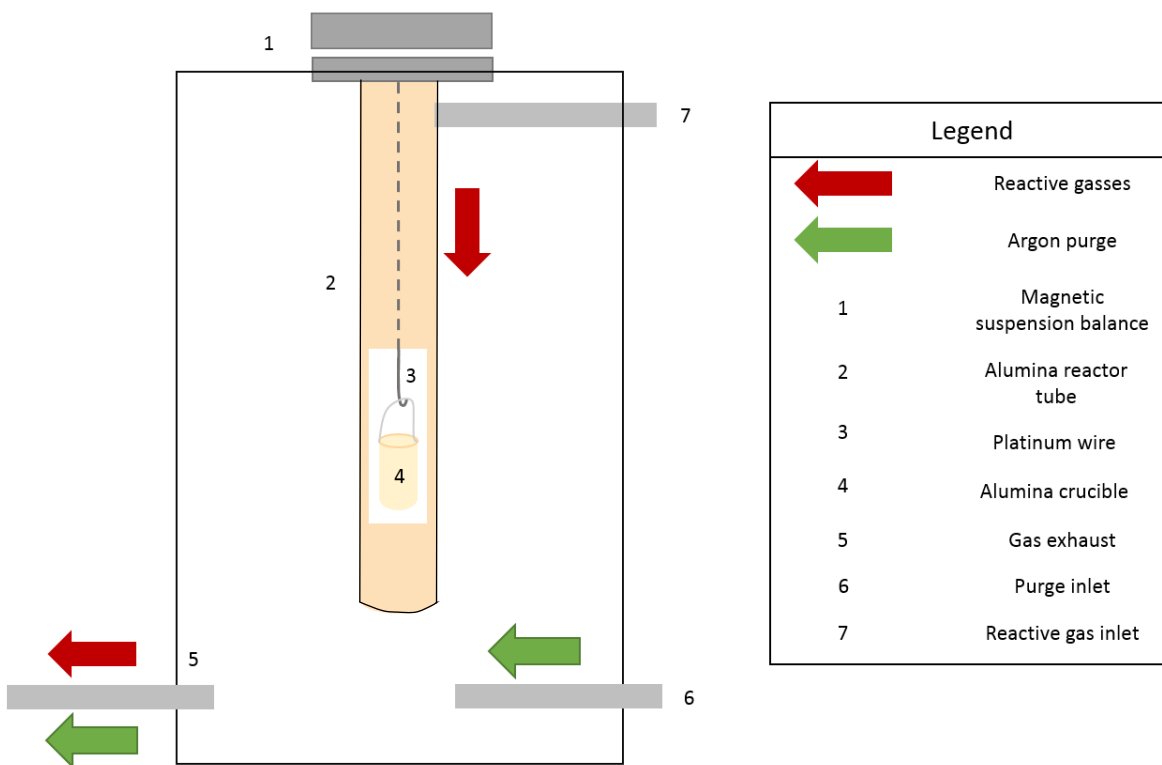


Figure 4.2 – Schematic of TGA used for experiments

This unit uses a magnetic coupling to connect the sample to a precision balance within the furnace which will allow the mass to be monitored throughout testing while a purge gas controls the environment. The balance hangs freely on a platinum wire, making it susceptible to vibrations within the lab, giving a high level of noise.

The advantage of this unit is that the gas environment, that the sample is tested in, can be better controlled and there are much lower pO_2 leaks in the system. This means accurate thermodynamic measurements can be taken at very low pO_2 s. The magnetic suspension allows for testing in high-pressure environments and drift is corrected using an auto-zero function.

The TGA contains a 6 L chamber which will be filled with the reactant gas.

The noise from the magnetically suspended balance is noticeable and the most likely source of error in this technique. All data presented in the TGA section of the results has been filtered to try and remove the noise in the system, but there is still a large amount of uncertainty that will become evident in this section of the report. The balance has an accuracy of 1 μ g, so samples in the range of 100s of mgs are used to ensure the weight change is measured accurately.

Detail about each specific TGA experiment will be given during the experimental section for each individual chapter.

As previously discussed, the TGA used for these experiments was sensitive to vibrations in the laboratory and so a simple filter was used to try limit this error. This filter used a simple excel “if” statement to compare a given value to the previous and next value and determine if the original value was significantly far from these values to be an outlier and this is shown below in Eq.3.1.

$$IF(AND(((V1 - V0)^2)^{0.5} > tf, ((V2 - V1)^2)^{0.5} > tf), "no", V1) \quad \text{Eq. 4.1}$$

Where V0 is the previous data point, V1 is the current data point being checked, V2 is the next data point and tf is the tolerance factor allowable before a data point is considered an outlier.

If the original value was too far from the neighboring values the original value was returned as a “no” value which could be separated by the use of the in-built excel sort function, otherwise the if statement returned the original value to be plotted. Figure 4.3 below shows a set of data from this thesis before and after filtering to show the effect on the data quality.

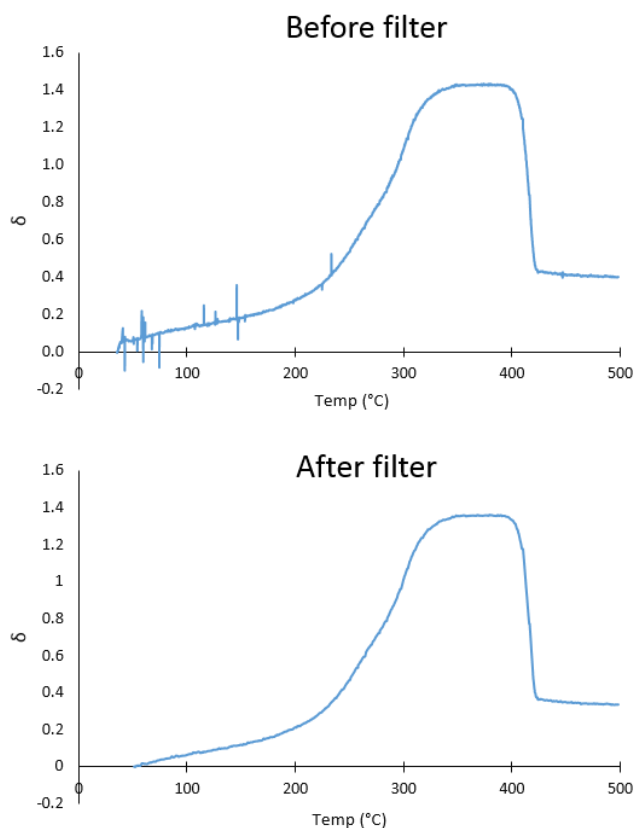


Figure 4.3– Examples of data (a) unfiltered, (b) filtered

In the original unfiltered data multiple noise points between 50 and 300°C can be seen, however after filtering it is clear to see that the data quality has been significantly improved

with these outliers removed. As such the data in this thesis underwent this filtering when appropriate.

4.2.1 TGA heat pre-treatment

TGA investigations of the samples were conducted using a Rubotherm dynTHERM unit. Brooks mass flow controllers (calibrated at 0°C and 1 bar) were used to control the gas flow rates, and for each experiment sample masses between 200 and 400 mg of 80 – 160 micron particles were used. Before each experiment, a helium pre-treatment was performed (BOC, 99.995% purity) by heating the sample to 500°C and then holding the sample at 500°C for at least 3 hours until a stable final mass was achieved (δ change < 0.001 over 1 hour). It is this point in every TGA experiment, that $\delta=0$ is attributed to throughout this work, so all δ 's used in this work are consistent. The low oxygen content sample was then cooled in helium to the required starting temperature for each TGA experiment, unless otherwise stated.

Figure 4.4 below shows this weight loss during the heat treatment, which matches references from literatures. As seen, the weight of the sample is steady for several hours, which is taken as reference $\delta = 0$.

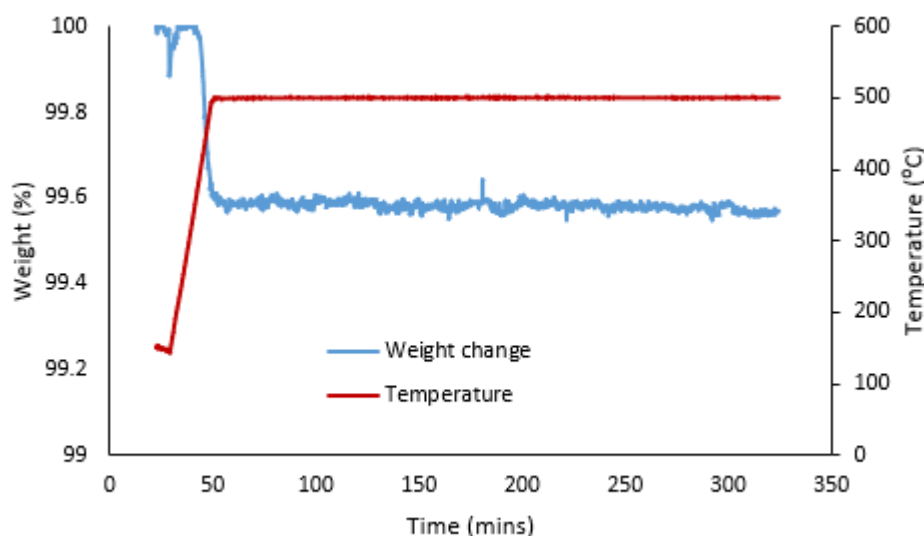


Figure 4.4 – Plot of weight versus time showing the weight change of YBaCo₄O₇ during inert pre-treatment, alongside the temperature of the sample

This reference point is taken as a $\delta = 0$ throughout this work, in agreement with reference, although slight variation is possible [1]. It is also seen in work performed, that the difference in oxygen content at 500°C in a pO₂ of 0.05 bar, and helium is equal to a change in δ of

<0.01, making it unlikely that any trace oxygen in the inert gas stream will have a significant impact on the oxygen content.

4.3 Synthesis of $\text{YBaCo}_4\text{O}_{7+\delta}$

The most common method for producing $\text{YBaCo}_4\text{O}_{7+\delta}$ is a solid-state reaction involving a two-stage sintering with grindings in between calcinations. For the first calcination, stoichiometric amounts of Y_2O_3 , BaCO_3 and Co_3O_4 were mixed, before being heated to 1000°C using a ramp rate of $10^\circ\text{C}/\text{minute}$. The sample was allowed to dwell at 1000°C for 12 hours. The sample was then cooled to room temperature at a rate of $10^\circ\text{C}/\text{min}$. The sample was then removed and ground, before undergoing a second calcination. The ground material was heated at a rate of $10^\circ\text{C}/\text{min}$ to 1200°C , where the sample was allowed to dwell for 12 hours. After this the sample was cooled to room temperature at a rate of $10^\circ\text{C}/\text{min}$. Both stages were performed in a Nubotherm furnace with a 30 cm isothermal zone under air. The batch sizes produced were between 10 and 20g of final product. Figure 4.5 below shows the scheme used for the sample preparation.

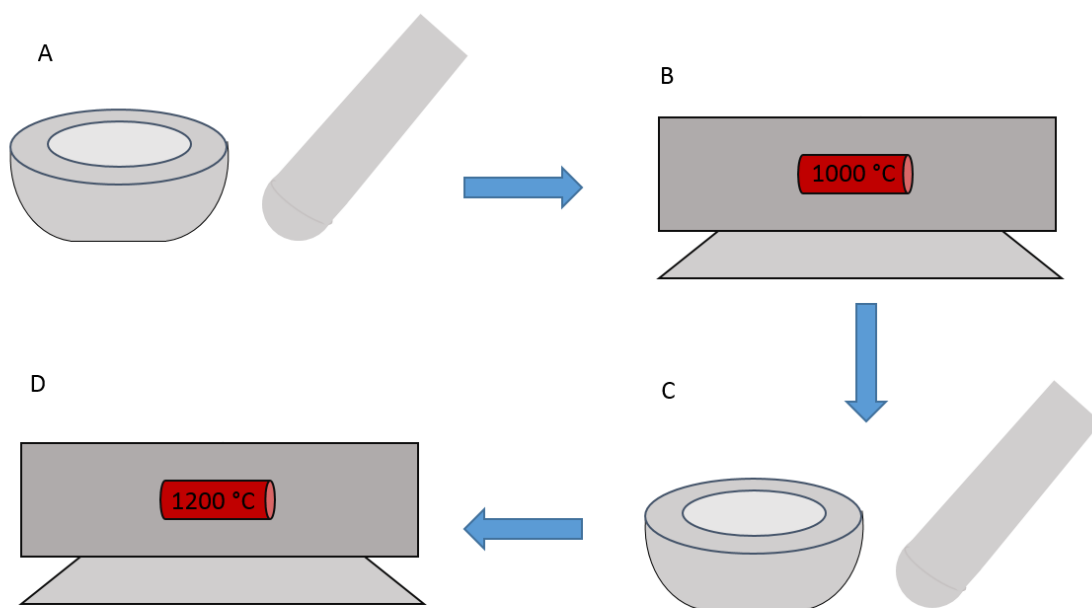


Figure 4.5 – Schematic of preparation of YBaCo_4O_7 powders undergoing, (A) grinding of precursors, (B) 1000°C sintering for 12 hours, (C) intermittent grinding of intermediate phases, (D) final 1200°C sintering for 12 hours

The reagents used for the production were 99.9% purity Y_2O_3 , BaCO_3 and Co_3O_4 purchased from Sigma Aldrich.

4.4 Chapter 5 experiments

As discussed in Section 2.5, obtaining correct diffusion co-efficient of non-stoichiometric materials with fast kinetics is difficult due to mass transfer limitations. In literature many methods have been attempted to measure fast oxygen transfer co-efficient, with ECR being the most common [2]. However, even with gas flows of up to a liter a minute, it has been shown there is still some error for ECR and partial pressure relaxation techniques, due to mass transfer limitations [3-5].

One of the major issues is that these techniques use multi-component gases. When a gas phase is comprised of mixed species, it cannot be assumed that the diffusion coefficient is independent of the gas phase composition, as the intermolecular forces become significant [6]. To describe the change in diffusion coefficient in multi-gas systems, the Maxwell-Stefan equation is used [7-8], shown below in Eq.4.2, where ∇ is the vector differential operator, X is the mole fraction, μ is the chemical potential, a is the activity, n the number of components, D_{ij} the Maxwell-Stefan diffusion coefficient, \vec{v}_j diffusion velocity, C the molar concentration, and \vec{J}_j the flux

$$\frac{\nabla\mu_i}{RT} = \nabla \ln a_i = \sum_{j=1}^n \frac{X_i X_j}{D_{ij}} (\vec{v}_j - \vec{v}_i) = \sum_{j=1}^n \frac{c_i c_j}{c^2 D_{ij}} \left(\frac{\vec{J}_j}{c_j} - \frac{\vec{J}_i}{c_i} \right) \quad \text{Eq.4.2}$$

A much simpler system would involve the use of pure gas. Figure 4.6 demonstrates how diffusion differs in a system with multiple gas species versus a pure gas system.

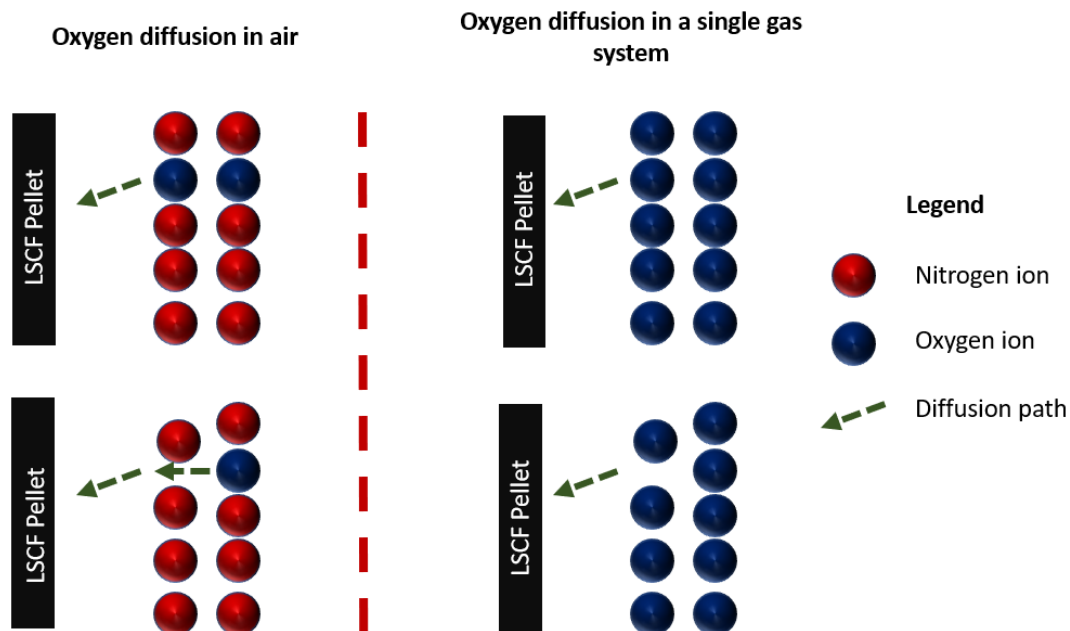


Figure 4.6 – Oxygen diffusion from the gas phase into a solid sample from (a) air, (b) oxygen

As shown in Figure 4.6 (a), when oxygen diffusion occurs in air, oxygen travels from the gas mixture into the sample, leaving a lower oxygen concentration at the surface/gas interface for

oxygen incorporation to occur. Oxygen from the bulk of the gas phase must travel to the material's surface, adding another diffusion barrier. This can reduce the rate of oxygen incorporation, particularly when attempting to characterise non-stoichiometric materials with fast kinetics.

To reduce mass transfer limitations, it is always advantageous to use pure gases for diffusion measurements, changing the pressure of the system in a pure gas, rather than the gas composition in a mixed gas. This is demonstrated in Figure 4.69b), which shows oxygen diffusion from a pure oxygen environment into a sample. As seen, when oxygen is incorporated from the surface/gas interface, more oxygen is already present at the surface to be readily incorporated by the sample. This incorporated oxygen is then replaced by oxygen from the bulk of the gas phase, which travels as a small pressure wave making it many times faster than multi-gas diffusion.

In most diffusion measurement processes, a sample equilibrates in a mixed gas of a known pO_2 , before the pO_2 of the gas is changed suddenly at constant pressure, making gas transfer dependent upon the Maxwell Stefan equation. In this work a simple system will be created, relying upon a sudden change in the gas pressure rather than gas composition, hopefully increasing the measured diffusion coefficients.

4.4.1 Preparation of LSCF pellet

LSCF powder purchased from Praxair was ground and sieved to achieve a particle size range of 80-160 microns, before being pressed into a pellet with a load of three tonnes for three minutes. Pellets were then sintered at 1000°C for 10 hours in air, with a heating and cooling rate of 2°C/min. The pellet dimensions were 16.2 mm wide, and 1.16 mm thick

4.4.2 Pressure relaxation rig

The schematic of the pressure relaxation system is shown in Figure 4.7. The system comprises of the alumina reactor vessel and attached pipework (112 ml) in which the pellet of non-stoichiometric material to be tested is placed, and an attached reservoir vessel with pipework (161 ml) maintained at room temperature. These measured volumes were confirmed by performing room temperature blanks, to ensure that the ratio between the reactor and reservoir was correct. These two vessels are separated by valve V1. The valves, V2 and V3, allow the pressure of both the reactor and reservoir sides of V1 to be altered. The bottom of the reactor is placed within a tubular furnace, which controls the temperature of the reactor, and the non-stoichiometric material inside. The reactor temperature is measured by a thermocouple attached to the bottom of the outside of the reactor tube, and it is assumed that the temperature at the bottom of the reactor is the same as the nonstoichiometric sample inside. The reactor

temperature is not isothermal, so an average reactor vessel temperature will need to be calculated. The temperature of the top of the reactor is controlled by the use of a cooling jacket, circulating water from a water/ice mixture through copper piping attached to the reactor. The pressure within the system is measured using pressure transducers on both the reactor and reservoir side of V1.

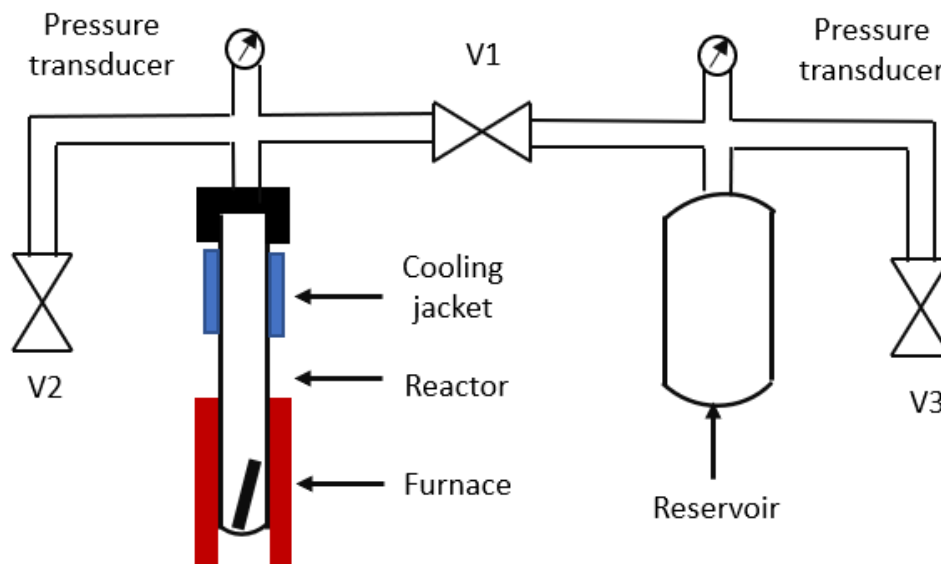


Figure 4.7 – Schematic of the pressure relaxation system

Recording of voltage from the pressure transducers was performed using either a Pico ADC-20 high resolution (20-bit) data logger or a digital multimeter provided by Multilab. The pressure transducers used in this work were supplied by SensorOne, namely the 33-x series with an error of 0.1%.

4.4.3 Pressure relaxation experiments

During this work, two types of experiments were performed to highlight the potential of this technique, calculations of oxygen non-stoichiometry and oxygen diffusion experiments.

In the experiment to calculate the oxygen non-stoichiometry of the sample, a pelletised disc of LSCF was heated to the required starting temperature, and the pressure in the reactor decreased to less than 100 Pa. The reactor was subsequently flushed with oxygen three times to remove any absorbed species before the pressure was reduced to < 100 Pa. The pressure in the reservoir vessel was set higher than the reactor vessel, and V1 opened to allow oxygen to flow into the reactor. A mole balance of the reactor and reservoir vessels before V1 opened and after V1 opened and the non-stoichiometric pellet equilibrated, with the new pO_2 of the reactor vessel was performed using the ideal gas law. The difference in the moles of gas

before and after the opening of V1 was attributed to a change in non-stoichiometry of the LSCF pellet.

To calculate the D and k values of a material, a sintered pellet of LSCF was placed in the reactor vessel and allowed to equilibrate at a known pressure. The reservoir vessel pressure was then set at $\frac{1}{4}$ of the reactor pressure vessel. V1 was then opened and closed to cause a reduction in the reactor vessel pressure, allowing for oxygen to be released from the non-stoichiometric material. The rate of the oxygen release was measured by the pressure change in the system, allowing diffusion coefficients of the material to be found.

4.5 Chapter 6 experiments

4.5.1 Chapter 6 oxygen measurement experiments

In Chapter 5 of this work, three types of TGA experiments were conducted,

- temperature programmed oxidations (TPOs) in a constant atmosphere,
- isothermal oxygen incorporation/release experiments
- stepwise heating and cooling of the material.

For all experiments, unless stated, a helium pre-treatment described in section 4.2 was performed.

To determine the effect on pO_2 on the oxygen release of $YBaCo_4O_{7+\delta}$, a set of dynamic heating ramps were conducted, heating samples of $YBaCo_4O_{7+\delta}$ after helium pre-treatment from 50 to 500°C with a ramp rate of 1-10 °C/min, in a gas flow rate of 200 ml/min, and a pO_2 of between 0 (inert) and 0.42 bar. This can be seen in Figure 6.1

In Figure 6.2, a similar experiment to Figure 6.1 was conducted. After a helium pre-treatment, a sample was annealed in air ($pO_2 = 0.25$ bar) at 320°C for various times, ranging between 30 and 120 minutes, to give the material a different starting δ . The material was then heated at a rate of 10°C per minute to 500°C in a pO_2 of 0.25 bar, and the results can be seen in Figure 6.2. A gas flow rate of 200 ml/min was used for this experiment.

In Figure 6.3, an isothermal oxygen incorporation experiment was performed. In this experiment, after the helium pre-treatment at 500°C, a sample was cooled to a temperature of between 300 and 400°C in helium. The gas environment was then changed to a pO_2 of either 0.05, 0.25 or 0.42 bar, where the sample dwelled for 3 hours. After the 3-hour dwell at a temperature, the material underwent the helium pre-treatment, to reduce the oxygen content. Once the oxygen content was reduced, the sample was once again cooled to the next

temperature in helium, before the same experiment was conducted. Gas flows for this experiment were 200 ml/min. Fresh samples were to investigate each pO_2 .

In Figure 6.4, a sample underwent the helium pre-treatment previously described, before the sample was cooled to 430°C in helium. The gas was then switched to obtain a pO_2 of 0.25 bar, where the sample was allowed to dwell for 4-hours. At the end of the four hours, the sample was allowed to cool to a temperature 10°C lower, for another 4-hour dwell. These cooling steps were performed from 430 to 300°C. The four-hour dwell includes the cooling time of the experiment, and the temperature profile is marked on the figure. The gas flow for this experiment was 200 ml/min.

In Figure 6.5, an isothermal oxygen incorporation experiment was performed. In this experiment, after the helium pre-treatment at 500°C, a sample was cooled to a temperature of 340°C in helium. The gas environment was then switched, to obtain a pO_2 of between 0.05 and 0.42 bar, as marked on the figure, and the sample left for 2 hours to incorporate oxygen. After the dwell, the sample underwent the helium pre-treatment again, before being once again cooled to 340°C, prepared for the next pO_2 . The gas flow for this experiment was 200 ml/min.

In Figure 6.6, a stepwise isothermal oxygen incorporation experiment was performed. In this experiment, after the helium pre-treatment at 500°C, a sample was cooled to a temperature of 430°C in helium. The gas environment was then switched from helium to a pO_2 of between 0.05 and 0.42 bar. The sample was allowed to rest for 1 hour at this temperature. The sample was then cooled in 5°C steps, in the same gas atmosphere. The sample was allowed to rest for 1 hour, minus the time taken to cool, at this temperature. Cooling was conducted in these 5°C steps from 430 to 300°C. The gas flow for this experiment was 200 ml/min.

In Figure 6.7 (a), a stepwise isothermal oxygen incorporation experiment was performed. In this experiment, after the helium pre-treatment at 500°C, a sample was cooled to a temperature of 300°C in helium. The gas environment was then switched from helium to a pO_2 of 0.25 bar, and the sample allowed to rest for 10 hours to incorporate oxygen. The sample was heated in 5°C steps, in the same gas atmosphere. The sample was allowed to rest for 1 hour, minus the time taken to heat, at this temperature. Heating was conducted in these 5°C steps from 300 to 430°C. The gas flow for this experiment was 200 ml/min.

In Figure 6.7 (b), a stepwise isothermal oxygen incorporation experiment was performed. In this experiment, after the helium pre-treatment at 500°C, a sample was cooled to a temperature of 430°C in helium. The gas environment was then switched from helium to a pO_2 of 0.25 bar, and the sample allowed to rest for 2 hours to incorporate oxygen. The sample

was cooled in 5°C steps, in the same gas atmosphere. The sample was allowed to rest for 1 hour, minus the time taken to cool, at this temperature. Cooling was conducted in these 5°C steps from 300 to 430°C. The gas flow for this experiment was 200 ml/min.

In Figure 6.8, a stepwise isothermal oxygen incorporation experiment was performed. In this experiment, after the helium pre-treatment at 500°C, a sample was cooled to a temperature of 200 or 430°C in helium. The gas environment was then switched to a pO₂ of either 0.25 or 0.42 bar. The samples were then either heated to 430°C or cooled to 200°C. At each marked point, the sample was held for long enough to ensure that a stable mass was obtained (change in $\delta < 0.001$ over 1 hour).

In Figure 6.9, a stepwise isothermal oxygen incorporation experiment was performed using pressure relaxation equipment. A sample was heated to 500 °C under vacuum for 2 hours, before being cooled to the starting temperature under vacuum. At this point it was assumed to have a starting $\delta = 0$ from the data seen in Figure 6.1 – however, there is a chance of slight error. Pure oxygen was added to the reaction chamber, and a mole balance across the chambers was performed to calculate the non-stoichiometry, following the method described in section 4.4. The value was taken after half an hour of no pressure change.

In Figures 6.17 and 6.18, oxygen annealed samples were produced by heating individual crucibles filled with a thin bed of YBaCo₄O₇ in air at 310°C in a furnace for times between 30 - 720 minutes. The samples were then taken from the furnace and allowed to cool. Some of the samples were sent to XRD, where the percentage of the orthorhombic phase was calculated. The rest of the material was heated to 500°C in helium, to calculate the oxygen content. Figure 6.16 shows a portion of this heating, where each sample was loaded into the TGA, and heated at a rate of 10°C/min to 500°C. Gas flows for this experiment were 200ml/min. Before this oxygen annealing, the samples were pre-reduced by the helium pre-treatment step using the TGA apparatus.

4.5.2 *In-situ* XRD studies

For all *in-situ* XRD studies, the samples underwent a similar pre-treatment to that described previously, however nitrogen and not helium was used for this.

Unit cell parameters and phase fraction were determined by Rietveld refinement of the hexagonal phase (P6_3mc, spacegroup 186) and orthorhombic phase (Cmc2_1, spacegroup 36) against the collected diffraction patterns. Unit cell parameters and phase fraction were allowed to freely vary, while the atomic positions and isotropic displacement parameters of all

crystallographic sites was fixed to the values in the reported structures. A separate function was used to model the specimen displacement along the z-axis, and a 6-term Chebyshev polynomial was used to fit the background. Peak broadening was modelled as a convolution of instrumental and sample broadening and broadening from the sample was fit best by models arising solely from crystallographic strain. Rietveld refinement was performed using TOPAS Academic V5. Refinements were performed by M.Gaultious – experimental design, sample preparation and data interpretation were performed by the author.

In Figure 6.10, a thermal expansion coefficient was calculated. The sample underwent a nitrogen pre-treatment to remove the oxygen, before being cooled to 200°C in 50°C steps. At each intermediate temperature, the sample was allowed to dwell for 1 hour to obtain a stable reading.

In Figure 6.11, a stepwise isothermal oxygen incorporation experiment was performed. In this experiment, after the nitrogen pre-treatment at 500°C, a sample was cooled to a temperature of 200 or 430°C in helium. The gas environment was then switched to a p_{O_2} of between 0.05-1 bar. The samples were then either heated to 430°C, or cooled to 200°C, with 10°C steps between 300 and 430, and 50°C steps between 200 and 300°C. Each step lasted for 1 hour. Figure 6.12 -6.13 the refined data from Figures 6.11. 6.15 shows the temperature that the orthorhombic phase was shown to grow upon cooling or heating at different p_{O_2} 's. The data for these experiments was refined from performing the same experiments as described for Figure 6.11, however at different p_{O_2} 's.

In Figure 6.14, an in-situ XRD experiment was performed, where a sample of $YBaCo_4O_7$ was heated to 310°C and allowed to dwell for 6 hours at this temperature in a p_{O_2} of 0.21 bar, with a gas flow rate of 150ml/min. In this experiment, it is worth noting the sample did not undergo any pre-treatment, and the sample began with some oxygen in the structure.

4.5.3 Thermodynamic calculations

Thermodynamic calculations were performed, and the results are shown in Figures 6.20 to 6.25 using the data obtained through the rest of the work. A detailed description of the calculation is available with each Figure.

4.6 Chapter 7 experiments

In Chapter 7 of this work, three types of TGA experiments were conducted,

- Temperature programmed reductions (TPR's) in a constant atmosphere (namely CO, H₂ or CO₂),
- isothermal oxygen incorporation/release experiments
- Redox cycling experiments between an oxidising condition and reducing condition. This oxidation and reduction were brought about by both changes in pO₂ and temperature

For all experiments, unless stated, a helium pre-treatment described in section 4.2 was performed.

In Figure 7.1, the stability of YBaCo₄O_{7+δ} in CO, H₂ and CO₂, was investigated using a TPR method. In this experiment, after the helium pre-treatment at 500°C, a sample was cooled to a temperature of 50°C in helium. The gas environment was switched from helium to one of 5 mol% CO, 5 mol% H₂ and 50 mol% CO₂ with helium balance, provided by BOC. During these experiments, a sample was heated from 100 to 500°C (800°C in the case of CO₂) with a heating rate of 1°C/min. A fresh sample was used for each experiment. The material from the TGA was then cooled in helium to remove any dangerous gases, and the sample was taken for XRD analysis. XRD of the as synthesised and used material was performed at ambient conditions to determine any new phases that had grown in the sample. Energy dispersive x-ray spectroscopy (EDX) analysis of samples were conducted using a Rontec Quantax unit.

The stability of YBaCo₄O₇ in water vapour was examined by flowing water vapour (pH₂O of 0.05 bar, balanced in Ar (99.995% purity)) over 1 g of YBaCo₄O₇ in a packed bed (internal diameter 5 mm) at 450°C for 3 hours, with a gas flow rate of 200ml/min.

In Figure 7.2, an isothermal oxygen incorporation/release experiment was performed. In this experiment, after the helium pre-treatment at 500°C, a sample was cooled to a temperature of between 270 and 330°C in helium. The gas environment was then changed to a pO₂ of 0.21 bar, where the sample dwelled for 1 hour. After the hour dwell at temperature, the gas was switched to inert, to show the oxygen release characteristics. After this hour dwell, the material underwent the helium pre-treatment, to reduce the oxygen content back to its starting position. Once the oxygen content was reduced, the sample was once again cooled to the next temperature in helium, before the same experiment was conducted. Gas flows for this experiment were 200ml/min.

In Figure 7.3, a stepwise isothermal oxygen incorporation experiment was performed. In this experiment, after the helium pre-treatment at 500°C, a sample was cooled to a temperature of 300°C in helium. The gas environment was then switched from helium to a pO₂ of between 0.05 to 0.42 bar, and the sample allowed to rest for 10 hours to incorporate oxygen. The sample was then heated in 5°C steps, in the same gas atmosphere. The sample was allowed to rest for 1 hour, minus the time taken to cool, at this temperature. Cooling was conducted in these 5°C steps from 300 to 430°C. The gas flow for this experiment was 200ml/min

In Figure 7.5, an isothermal oxygen incorporation experiment was performed. In this experiment, after the helium pre-treatment at 500°C, a sample was cooled to a temperature of between 340 and 370°C in helium. The gas environment was then changed to a pO₂ of 0.21 or 0.42 bar, where the sample dwelled for 1 hour. After this hour dwell, the material was heated to 500°C in helium, to reduce the oxygen content back to its starting content. Once the oxygen content was reduced, the sample was once again cooled to the next temperature in helium, before the same experiment was conducted. Gas flows for this experiment were 200ml/min.

In Figure 7.14 an oxygen release experiment was performed. In this experiment, after the helium pre-treatment at 500°C, a sample was cooled to a temperature of 310°C in helium. The gas environment was then changed to a pO₂ of 0.21 bar, where the sample dwelled for 1 hour. After the hour dwell at temperature, the temperature was ramped at a rate of 20°C/min to between 370 and 430°C in a pO₂ of between 0 (inert) and 0.42 bar. When the temperature was at the desired setpoint, a rate of oxygen release was measured from the TGA data. After each measurement, the material underwent the pre-treatment, before the process started again.

To demonstrate the potential of YBaCo₄O_{7+δ} for oxygen enrichment, a series of redox cycles were performed. In all these experiments, the sample was pre-reduced by the helium pre-treatment before the cycling. The gas flow rates for all gases used in all schemes 200ml/min.

In Figure 7.4, after the helium pre-treatment, a sample was cooled in Helium to 310°C. After cooling, the gas was switched to a pO₂ of 0.21 bar, and the temperature held for 2 to incorporate oxygen. After the initial dwell, the temperature was ramped to 430°C at a rate of 20°C/min in a pO₂ of 0.31 bar, to demonstrate the oxy-fuel combustion process. The total time of the heating and dwell was 1 hour. After this hour was completed, the sample was cooled in a pO₂ of 0.21 bar to 310°C, at which temperature it was left to dwell. The cooling was uncontrolled but took approximately 6 minutes. The total time of the cooling and dwell was 2 hours. The cycle was then repeated for the required number of cycles. In this figure, 15 cycles were demonstrated.

In Figure 7.7, after a pre-treatment, a sample was cooled in argon to 310 or 340°C. After cooling, the gas was switched to a pO₂ of 0.21 or 0.42 bar respectively, and the temperature was held for 30 minutes to incorporate oxygen. After the dwell, the temperature was ramped to 370°C at a rate of 20°C/min in inert. The total time of the heating and dwell was 30 minutes. After this higher temperature dwell, the gas environment was returned to its previous state (either a pO₂ of 0.21 or 0.42 bar), and the sample was cooled to the original temperature. The cycle was then repeated for the required number of cycles. In this figure, 5 cycles of both schemes were demonstrated.

In Figure 7.8, after the pre-treatment, a sample was cooled in argon to 310°C. After cooling, the gas was switched to a pO₂ of 0.21 bar, and the temperature was held for 120 minutes to incorporate oxygen. After the dwell, the temperature was ramped to 430°C at a rate of 20°C/min in inert. The total time of the heating and dwell was 60 minutes. After this higher temperature dwell, the gas environment was returned to a pO₂ of 0.21 bar, and the sample was cooled to the original temperature, taking approximately 15 minutes. The oxidative half of this cycle lasted 120 minutes, including both the isothermal dwell and the cooling time. The cycle was then repeated for the required number of cycles. In this figure, 30 cycles were demonstrated.

In Figure 7.9, after the pre-treatment, a sample was cooled in argon to 310°C. After cooling, the gas was switched to a pO₂ of 0.21 bar, and the temperature was held for 120 minutes to incorporate oxygen. After the dwell, the temperature was ramped to 430°C at a rate of 20°C/min in inert. The total time of the heating and dwell was 60 minutes. After this higher temperature dwell, the sample was cooled to 310°C in inert. After the cooling step was completed, the gas environment was switched to a pO₂ of 0.21 bar for 120 minutes. The cycle was then repeated for the required number of cycles. In this figure, 30 cycles were demonstrated.

In Figure 7.10, after the pre-treatment, a sample was cooled in argon to 310°C. After cooling, the gas was switched to a pO₂ of 0.21 bar, and the temperature held for 120 minutes to incorporate oxygen. After the dwell, the temperature was ramped to 430°C at a rate of 20°C/min in inert. The total time of the heating and dwell was 60 minutes. After this higher temperature dwell, the sample was cooled to 310°C. For the first 10 cycles, this cooling was performed in argon, and for the last ten cycles, this cooling was performed in a pO₂ of 0.21 bar. After the cooling step was completed, the gas environment was switched or kept in a pO₂ of 0.21 bar for 120 minutes, including both the isothermal dwell and the cooling time. .The

cycle was then repeated for the required number of cycles. In this figure, ten cycles were demonstrated cooling in argon, and ten cycles cooling in a pO_2 of 0.21 bar.

In Figure 7.11, after the pre-treatment, a sample was cooled in argon to 310°C. After cooling, the gas was switched to a pO_2 of 0.21 bar, and the temperature was held for 60 minutes to incorporate oxygen. After the dwell, the temperature was ramped to 430°C at a rate of 20°C/min in inert. The total time of the heating and dwell was 60 minutes. After this higher temperature dwell, the sample was cooled to 310°C in inert. After the cooling step was completed, the gas environment was switched to a pO_2 of 0.21 bar for 120 minutes. The cycle was then repeated for the required number of cycles. In this figure, 30 cycles were demonstrated.

In Figure 7.12, after the pre-treatment, a sample was cooled in argon to 310°C. After cooling, the gas was switched to a pO_2 of 0.21 bar, and the temperature held for 120 minutes to incorporate oxygen. After the dwell, the temperature was ramped to 430°C at a rate of 20°C/min in inert. The total time of the heating and dwell was 60 minutes. After this higher temperature dwell, the sample was cooled to 310°C. For the first 10 cycles, this cycling was uninterrupted, however, after cycle 10, the sample underwent a pre-treatment to reduce the sample back to the original oxidation state. The cycle was then repeated for the required number of cycles. The cycling then began again as described.

In Figure 7.13, after the pre-treatment, a sample was cooled in argon to 310°C. After cooling, the gas was switched to a pO_2 of 0.21 bar, and the temperature held for 120 minutes to incorporate oxygen. The cycle was then repeated for the required number of cycles. For the first 15 cycles shown in Figure 7.13, the temperature was ramped to 500°C at a rate of 20°C/min in inert. For the last 14 cycles, the sample was heated to 430°C in inert. The total time of the heating and dwell was 60 minutes. After this higher temperature dwell, the gas was switched to a pO_2 of 0.21 bar, and the sample was cooled to 310°C. The time of both the isothermal dwell and the cooling time was 120 minutes, with cooling taking approximately 15 minutes.

4.7 References

- [1] T.Motohashi, S.Kadota, H.Fjellvåg, M.Karppinen, H.Yamauchi - Uncommon oxygen intake/release capability of layered cobalt oxides, REBaCo₄O_{7+δ}: Novel oxygen-storage materials, *Materials Science and Engineering: B*, 148, 1–3, 2008, 196-198
- [2] Z.Zhang, D.Chen, F.Dong, Z.Shao - Efficient and CO₂-tolerant oxygen transport membranes prepared from high-valence B-site substituted cobalt-free SrFeO_{3-δ}, 495, 2015, 187-197
- [3] A.Murgan, A.Thursfield, I.S.Metcalf - A chemical looping process for hydrogen production using iron-containing perovskites, *Engineering and environmental science*, 4, 2011, 4639-4649
- [4] M.liu, D.Ding, K.Blinn, X.Li, L.Nie, M.Liu - Enhanced performance of LSCF cathode through surface modification, *International journal of Hydrogen energy*, 37, 2015 8613-8620
- [5] S.P.S.Badwal, M.J.Bannister, M.J.Murray - Non-stoichiometric oxide electrodes for solid state electrochemical devices, *Journal of Electroanalytical Chemistry and Interfacial Electrochemistry*, 168, 1984, 363-382
- [6] J. Maier - Interaction of oxygen with oxides:How to interpret measured effective rate constants, *Solid State Ionics*, 135, 2000, 575 –588
- [7] A.Galdikas, N.Bion, D. Duprez, V.Virbikaas, D.Mazelis - Modeling of Diffusion Process in the Isotopic Oxygen Exchange - Experiments of C_xZr(1-x)O₂ Catalysts, *Journal of material science*, 19, 2013, 1320–1392
- [8] G. K. Vdovin, E. K. Kurumchin, E. V. Isaeva, D. I. Bronin - Isotopic Exchange and Oxygen Diffusion in the La_{0.88}Sr_{0.12}Ga_{0.82}Mg_{0.18}O_{3-α}-Molecular Oxygen System, *Russian Journal of Electrochemistry*, 37, 2001, 304-307

Chapter 5 – Development of novel pressure relaxation technique for characterisation of non-stoichiometric materials

During this chapter, the development of a novel technique for collecting oxygen diffusion data unimpeded by limitations imposed by multi-gas systems, along with the degree of non-stoichiometry, of oxygen non-stoichiometric materials will be discussed. Techniques in literature for measuring oxygen diffusion through non-stoichiometric materials are often mass transfer limited due to gas mixing and too low gas flow rates. To avoid these limitations, pressure relaxation allows for a non-stoichiometric sample to equilibrate at a known partial pressure of oxygen created by varying the pressure of pure oxygen in a reactor. This pressure inside the reactor is then changed by a step-wise lowering of the pressure, causing oxygen to be released from the non-stoichiometric material. From measuring the pressure change, the total amount of oxygen released and the rate at which this is released are calculated. From this information, the degree of oxygen non-stoichiometry and the diffusion coefficients can be calculated.

5.1 Introduction

Non-stoichiometric oxide materials are of interest in a wide variety of applications, ranging from ion transport membranes, oxygen carriers for chemical looping systems, solid oxide fuel cells, and electrochemical sensors [1-4]. It is important accurate values of the chemical diffusion coefficient (D) and the surface exchange coefficient (k) is known to allow the easier design of processes.

Maier [5] described three different techniques of diffusion characterization, the use of a tracer isotope, a chemical experiment where the non-stoichiometry of a sample is changed, and a stationary conductivity experiment [6-10].

The most common techniques are relaxation experiments. After a system has observed a sudden change of physical or chemical state, a system attempts to re-establish equilibrium. For oxygen non-stoichiometric materials, oxygen is incorporated or released. The re-equilibration is referred to as a relaxation, and any physical property which correlates with this change can be used to measure this (i.e. weight, conductivity, etc) [11]. Examples of these include thermogravimetric (TG) techniques [12-13] and optical transmission spectrometry [14].

Currently, electrochemical conductivity relaxation (ECR) is most often in literature to determine D and k values of materials [15-17]. The technique relies on a step-change in the pO_2 of a sample's gas environment by alternating a sample between two gas flows of different pO_2 s. The degree of oxygen non-stoichiometry (δ) of the sample is calculated from the change in the electrical conductivity of the samples before and after the gas change. The change in δ can then be used to calculate the D and k values of the sample, using Fick's Law. There are several issues with the use of ECR, namely:

- The sample must be in the form of a well-sintered pellet, as porous spaces in a pellet make the calculation difficult
- Electrodes must be attached to the sample, preventing further testing of the sample.
- There are issues with the known partial pressure of oxygen in the sweep gas at the solid sample/gas interface which can cause significant differences in the oxygen release or incorporation (studies have shown higher oxygen concentrations at the samples due to oxygen being released which can cause a variation in the k and D values obtained by an order of magnitude).

Literature shows determining D and K at the same time may be misleading, and that two separate experiments should be performed. To calculate K , a pellet thickness less than the characteristic diffusion length (L_c) should be used, and for bulk diffusion, a larger thickness

should be used [18]. This characteristic length provides an estimate of whether bulk or surface exchange dominates the reaction, and can vary significantly among perovskite materials [19].

Several publications question the accuracy of k and D values obtained from ECR experiments, particularly when the δ change in the sample is large, or the pO_2 of the gas phase is low [20-21]. This is due to a higher pO_2 at the gas/solid interface than the bulk gas phase if the large volumes of oxygen are released by the sample, or simply not removed quickly enough. This has been shown in experiments that measured the pO_2 close to a sample with an oxygen sensor, and low gas flow rates were shown to have a significant effect on the k and D values obtained. In these experiments, the calculated k and D values for the same sample tested with 25 and 1000 ml/min flow rates varied by two orders of magnitude [22]. Numerical modeling of the oxygen release showed significant gas phase diffusion limitations at low oxygen partial pressures, giving k values that deviated by an order of magnitude from expected values [23]. Large gas flow rates are required if the amount of oxygen released by the sample is not negligible, and unless the flush time of the reactor is significantly faster than the rate of oxygen release, mass transfer limitations can occur.

In several recent publications, efforts have been made to circumvent these issues using partial pressure relaxation techniques [24-25]. These experiments typically use powder samples that are equilibrated at a known pO_2 , after which a step-change in the pO_2 of the gas is performed – similarly to ECR. This step-change allows the sample to re-equilibrate, releasing oxygen into the gas phase. The amount of oxygen released by the sample is measured by an oxygen sensor, which is used to calculate the rate of oxygen release. However, as this method still requires the use of a gas flow, the same issues with mixed gas flows and too low flow rates can occur.

In this work, a novel technique, pressure relaxation is developed, and the potential benefits are explored. In this technique, a non-stoichiometric sample equilibrates at a known temperature and pO_2 in a sealed vessel. The gases used in this experiment are pure, so pO_2 is equal to the pressure. The pressure is then quickly lowered by opening a valve to another chamber, decreasing the pressure inside the chamber. As the pellet re-equilibrates to the new pressure, the change in reactor pressure can be recorded and modelled using Fick's law, and the ideal gas law.

The pressure relaxation system offers several advantages over other techniques to obtain diffusion coefficients, namely:

- The samples are tested in pure oxygen, removing mixed gas mass transfer limitations.
- No electrical wiring of the sample is needed.

- Powdered samples may be used, although the particle size distribution must be narrow and well determined.
- The technique can be used to calculate oxygen non-stoichiometry by measuring absolute pressure changes.

The fact that the experiments can be performed using powders is significant. Firstly, there are often experimental and mechanical issues with forming and using pellets. Breaking of pellets during sintering is a common problem, and for samples that have required difficult synthesis, this may cause significant issues. To prevent this, a binder is often added to make the powder more cohesive, which is removed during the sintering step. These binders add potential impurities and unknown porosity into the sample, which can make measurement difficult. Additionally, as a new high-temperature step is required to sinter the sample, this can lead to chemical changes such as strontium segregation, impacting the behaviour of the material [26]. The use of powders allows more freedom to test the impact of particle synthesis methods, without compressing and sintering them, changing the morphology. The downside however is that calculation of D and K values becomes more difficult due to changing surface area and size range of particles.

During this chapter, a new rig for this method is characterised before it is used to measure the oxygen non-stoichiometry and relaxations of $\text{La}_{0.6}\text{Sr}_{0.4}\text{Co}_{0.2}\text{Fe}_{0.8}\text{O}_{3-\delta}$ (LSCF), to demonstrate the potential of the technique. LSCF was chosen for the preliminary testing as there is significant literature regarding the diffusion and non-stoichiometry of the system [27-28].

In this chapter, a pellet was used for all LSCF experiments, bar the equilibria plot in Figure 5.10. Powder was used in this experiment to prevent any unknown chemical changes in the sample due to high-temperature sintering, which might impact the non-stoichiometry [26].

5.1.1 Method of calculating oxygen diffusion rates using pressure relaxation

Typically for modeling ECR, a combination of Wagners theory, and Ficks law is used to relate the change in conductivity, to the change in oxygen content in the sample. Conversely, modeling the pressure relaxation system is a combination of the perfect gas and Fick's laws.

The perfect gas law is shown in equation 5.1, with P equal to pressure, n equal to the moles of gas, V equal to volume, T equal to temperature, and R equal to the gas constant.

$$PV = nRT \quad \text{Eq.5.1}$$

This can be used to relate the pressure change in the reactor to the number of moles of oxygen absorbed or desorbed from the pellet as shown in Eq.5.2, where V_{rea} is the reactor volume,

which is constant, P_2 is the final pressure of the system, P_1 is the starting pressure and Δn_{gas} is the number of moles which leave or enter the gas phase during the time of the pressure change.

$$P_2 V_{rea} = P_1 V_{rea} - \Delta n_{gas} RT \quad \text{Eq.5.2}$$

Rearranging this equation gives eq 5.3.

$$\Delta n_{gas} = \frac{P_1 V_{rea} - P_2 V_{rea}}{RT} \quad \text{Eq. 5.3}$$

This change in the number of moles of gas absorbed or desorbed from the pellet can be related to the oxygen non-stoichiometry (δ) change of a sample by equation 5.4 as the δ is defined as the moles of additional oxygen per mole of sample and n_{solid} the moles of non-stoichiometric materials.

$$\frac{2\Delta n_{gas}}{n_{solid}} = \Delta\delta \quad \text{Eq. 5.4}$$

The average concentration at a given time is the integral of the local concentrations within the sample and can be shown as equation 5.5, where a is the half-thickness of the sample.

$$\bar{c}(t) = \frac{1}{2a} \int_{-a}^a c(x, t) dx \quad \text{Eq.5.5}$$

Once the pressure of the system changes suddenly the non-stoichiometric sample will release oxygen. The change in pressure can be related to the change in the oxygen concentration of the pellet, where V_{sol} is the volume of the pellet, and this is described by equations 5.6 – 5.8. In the equations below ΔP is equal to $P(t)$ minus $P(o)$. Δc is the difference between oxygen concentrations at $P(o)$ and $P(i)$ in the pellet.

$$\Delta n_{gas} = -2\Delta c V_{sol} \quad \text{Eq.5.6}$$

$$\Delta P = \frac{\Delta n_{gas} RT}{V_{rea}} \quad \text{Eq.5.7}$$

$$\Delta P = -\frac{2\Delta c V_{sol} RT}{V_{rea}} \quad \text{Eq.5.8}$$

Relating this change of pressure to time can be done by differentiating equations 5.7 and 5.8, giving equation 5.9.

$$\frac{dP}{dt} = -\frac{2V_{sol} RT}{V_{rea}} \frac{d\bar{c}}{dt} \quad \text{Eq.5.9}$$

Equation 5.7 can be differentiated with regards to time to give a term for $\frac{d\bar{c}}{dt}$ yielding equation 5.12 which can then be substituted into equation 5.11 to give 5.13.

$$\frac{d\bar{c}(t)}{dt} = \frac{1}{a} \int_{-a}^a \frac{dc(x,t)}{dt} dx \quad \text{Eq.5.10}$$

$$\frac{dP}{dt} = \frac{-V_{sol}RT}{V_{rea}} \frac{1}{2a} \int_{-a}^a \frac{dc(x,t)}{dt} dx \quad \text{Eq.5.11}$$

These equations show how the stoichiometry of the pellet changes with pressure, and this must be related to Fick's law for one-dimensional mass transfer shown in equation 5.12 to get the diffusion coefficient for the sample where D is the diffusion co-efficient.

$$\frac{\partial c}{\partial t} = D \frac{\partial^2 c}{\partial x^2} \quad \text{Eq.5.12}$$

The boundary conditions of equation twelve are equal to equations 5.15, which shows a one d flux of molecules from the material dependant on both the surface diffusion and bulk diffusion coefficients. A half-thickness is used as there are two sides to the pellet where oxygen can leave from. In this equation, j is equal to the flux, D is the bulk diffusion coefficient, k is the surface exchange rate, and c_g is the oxygen concentration in the gas phase.

$$\begin{aligned} j(a,t) &= -D \frac{dc(a,t)}{dx} = k(c(a,t) - c_g(t)) \\ j(-a,t) &= -D \frac{dc(-a,t)}{dx} = -k(c(-a,t) - c_g(t)) \end{aligned} \quad \text{Eq.5.13}$$

The flux can then be modeled by solving a combination of equations 5.11 and 5.12, with the boundary conditions defined in equation 5.16, giving equation 5.14.

$$\frac{dp}{dt} = -\frac{V_{sol}RT}{V_{rea}} \frac{1}{a} \int_{-a}^a \frac{D \partial^2 c(x,t)}{\partial x^2} dx \quad \text{Eq.5.14}$$

The values obtained can give an estimation of the pressure change over time which can be compared with the experimental data.

Although this method was not used to calculate the diffusion coefficient in this work due to experimental error, the calculation should still be correct and useful to others attempting to reproduce the work.

5.2 Results

In describing these results, there will often be reference to Figure 4.7 in Chapter 4. When V1, V2 or V3 are mentioned in this text, this is in reference to the valves shown in Figure 4.7. For a reminder, V1 is the valve between the reactor and reservoir chamber, V2 is the reactor feed valve, and V3 is the reservoir feed valve.

5.2.1 Leak rates of the pressure relaxation system

The pressure relaxation method measures the absolute pressure of a sealed vessel, so leak rates of the system must be negligible during experiments. To determine the leak rate of the system, the reactor vessel was sealed by closing V1 at a starting pressure of approximately 1 mbar. The pressure of the reactor vessel was recorded with a sampling rate of one point per second. Figure 5.1 shows the total pressure of the reactor vessel over 20 minutes with the system at room temperature; and the reservoir vessel and surroundings at atmospheric pressure.

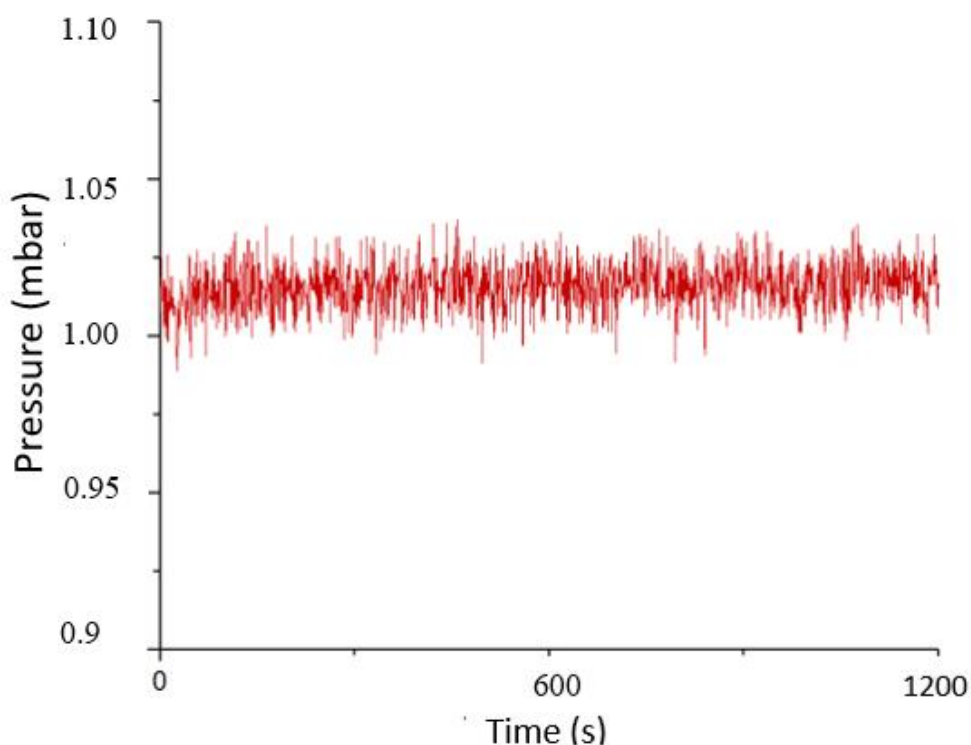


Figure 5.1 – Plot of pressure in the sealed pressure relaxation reactor vessel versus time at a starting pressure of 1 mbar and a room temperature of 22°C

Figure 5.1 shows no notable increase in pressure during the 20-minute experiment. Operation of the unit would be performed at higher temperatures, so further leak rate tests were performed between 300 and 800°C, to determine the impact of temperature on leak rates. During these tests, the reactor vessel pressure was between 20 and 30 mbar. The pressure was

measured over 20 minutes at each temperature, with a sampling rate of 1 data point per second. The reservoir was left open to the atmosphere (V3 open) during this experiment to ensure no possible leak through V1 at higher temperatures. Figure 5.2 shows the average leak rate of the reactor vessel during these tests.

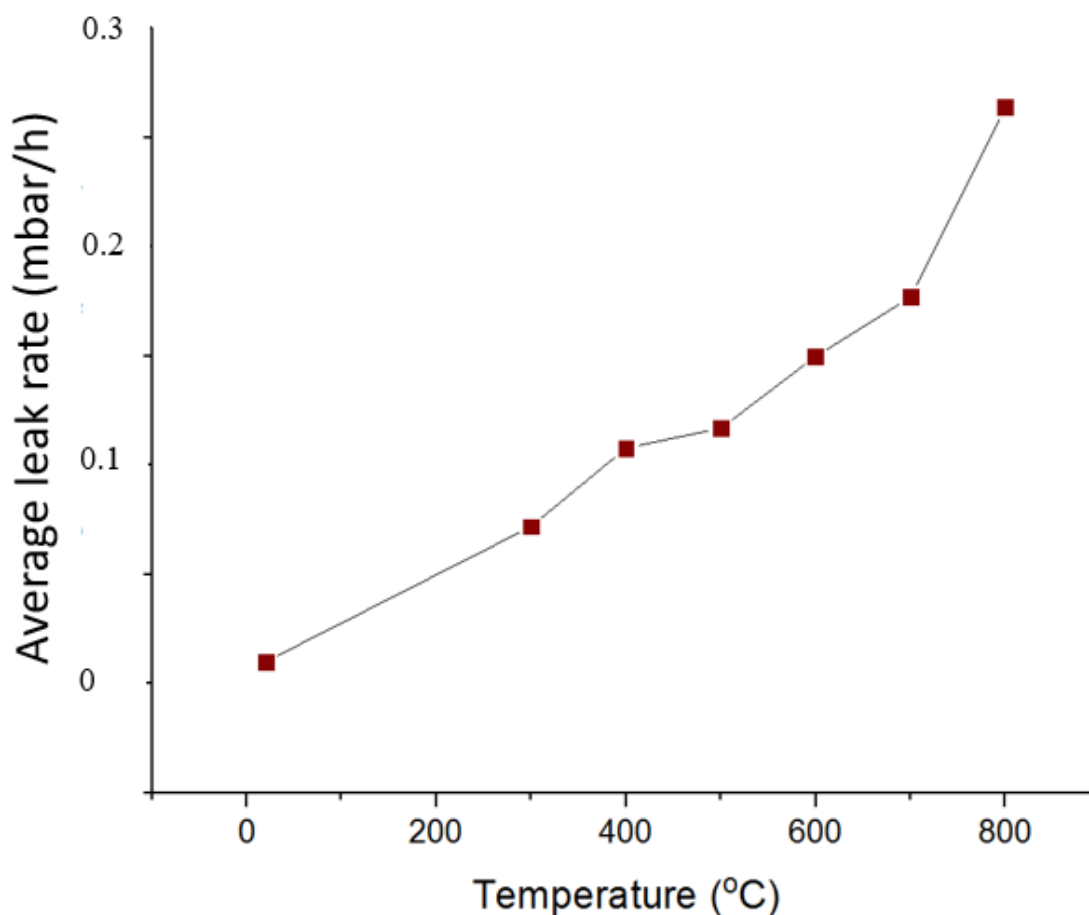


Figure 5.2 – Scatter plot showing average leak rate in mbar/h as a function of temperature, with the starting pressure of the reactor vessel between 20 and 30 mbar

Figure 5.2 shows the leak rate of the system increases with increasing temperature, with a maximum leak rate of 0.26 mbar/h seen at 800°C.

To reduce the leak rate, a water jacket was installed, flowing approximately 100 ml/min of water from an ice/water mixture (assumed to be constantly 0°C due to the use of ice), around the top half of the reactor in contact with the seal between the alumina reactor tube and the Swagelok piping. A leak test was performed on the system with this cooling jacket. The reactor pressure was reduced to 5.8 mbar and sealed by closing V1 and V2, at 800°C. The pressure inside the reactor was then recorded at a sample rate of 1 scan per second for 10 minutes, approximately twice the duration of an LSCF pressure relaxation experiment at this

temperature. As before, the reservoir vessel was left open to the atmosphere. The results of this leak test are shown in Figure 5.3.

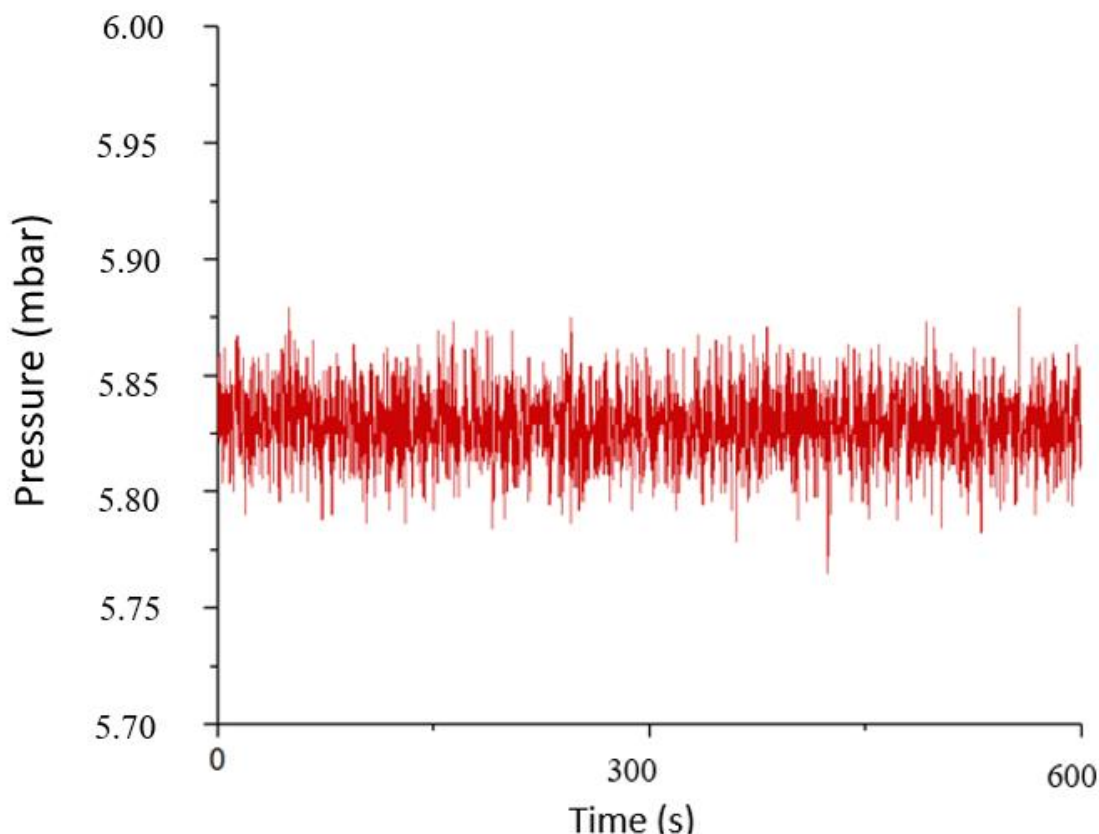


Figure 5.3 – A plot of recorded pressure versus time of a sealed reactor heated to 800°C, with the reservoir left open to the atmosphere

Figure 5.3 shows no discernible increase in pressure during the experiment. It is assumed from the data in Figure 5.2, that if no leak was detected at 800°C, there should be no detectable leak at lower temperatures.

5.3.2 Thermal profiling of the reactor

To calculate the change in non-stoichiometry from a pressure change, it is necessary to perform a mole balance using the ideal gas law. This requires the temperature of the system to be known, to relate the pressure changes to moles of oxygen incorporated/released. As a temperature gradient will be present in the reactor, an average temperature must be found for the calculations. It was desired to calculate two potentially useful average temperatures. These were the average temperature of only the reactor (V1 closed), and the average temperature of the combined reactor/reservoir system (V1 open).

To calculate these average temperatures, the pressure of the reservoir and reactor vessels were reduced to approximately 20 mbar, with V1 either open or closed. The bottom of the reactor

was then heated to multiple temperatures between room temperature and 800°C. At each recorded point in Figure 5.4, the temperature was held until a stable pressure was reached (no change in pressure over 10 minutes), at which point the new vessel pressure was recorded. The results of this experiment can be seen in Figure 5.4.

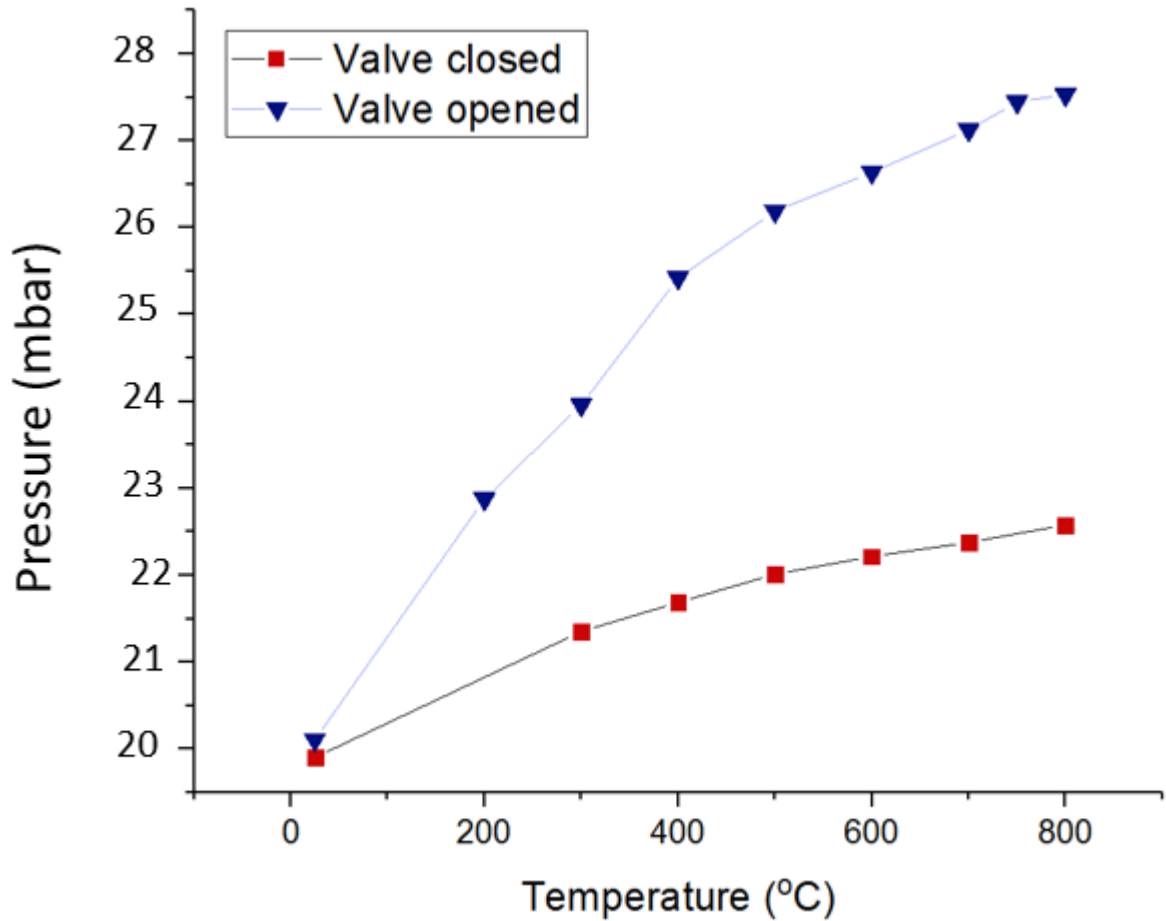


Figure 5.4– Scatter plot of recorded pressure in the reactor versus temperature for the pressure relaxation system heated from room temperature to 800°C with V1 either open (red) or closed (blue)

As expected, the pressure in the system increased upon heating in both cases, with greater pressure changes with V1 closed and the reactor sealed. This would be expected, as a smaller percentage of the volume of the system is held in the furnace when V1 is open. Using the perfect gas law (shown in Eq.5.15), where P is equal to the pressure, V is equal to the volume, n is equal to the number of moles of gas, R is equal to the universal gas constant and \tilde{T} is equal to the average temperature of the system, it is possible to calculate the number of moles of gas sealed in the system, by re-arranging the formula shown in Eq.5.15 to that shown in Eq.5.16.

$$PV = nR\tilde{T} \quad \text{Eq.5.15.}$$

$$n = \frac{PV}{R\tilde{T}} \quad \text{Eq.5.16.}$$

If the pressure relaxation system is considered well sealed, V and n can be considered constant. As only part of the reactor vessel is heated, the average temperature of the system will be used to determine the system's pressure. Since the terms n , V and R are considered constant, and the pressure in the system is recorded, the average temperature (\tilde{T}) can then be calculated by re-arranging Eq.5.16 to Eq.5.17 below.

$$\tilde{T} = \frac{PV}{Rn} \quad \text{Eq.5.17.}$$

Using this methodology, a plot of the reactor temperature (i.e., the temperature at the bottom of the reactor, measured by a thermocouple) versus the average system temperature was produced and can be seen in Figure 5.5.

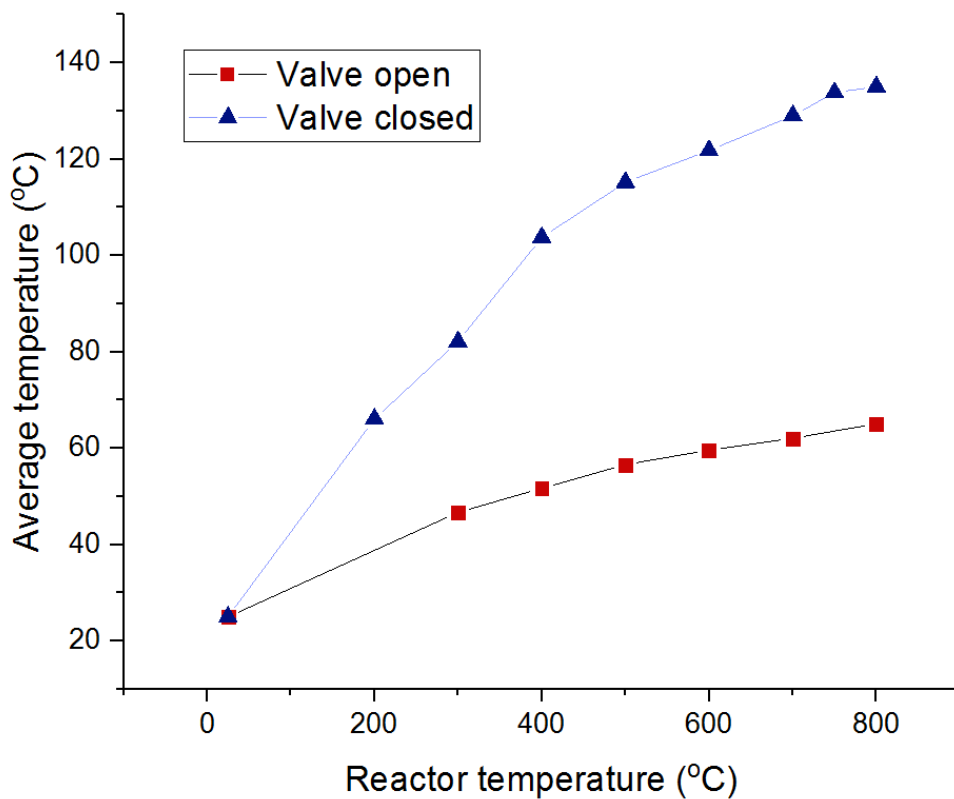


Figure 5.5 – Scatterplot showing average system temperature for the pressure relaxation system as a function of reactor temperature

Figure 5.5 shows the relationship between the average temperature in the system and the reactor temperature. As shown, the average temperature is significantly lower than the reactor temperature for both cases, with the system remaining on average cooler, when V1 remained open.

5.2.3 Blank runs of the pressure relaxation system

Blank runs of the system were performed to see how quickly pressure equilibrated across the two chambers during the opening of V1. To do this, the reactor vessel was heated to 800°C and the pressure of the reactor vessel was reduced to 15, 30, or 60 mbar (± 0.20 mbar). The pressure of the reservoir vessel was set to be half the pressure of the reactor vessel for the experiment (7.5, 15, 30 mbar for reactor vessel pressures of 15, 30, and 60 mbar respectively, with the pressures obtained being ± 0.20 mbar of the desired setpoint). V1 was then opened and closed, and the pressure change was recorded at a sampling rate of 10 samples a second.

Figure 5.6 shows the normalised pressure change in the system, where 0 is the pressure of the system before the switch and -1 is the pressure of the system after the switch, versus time.

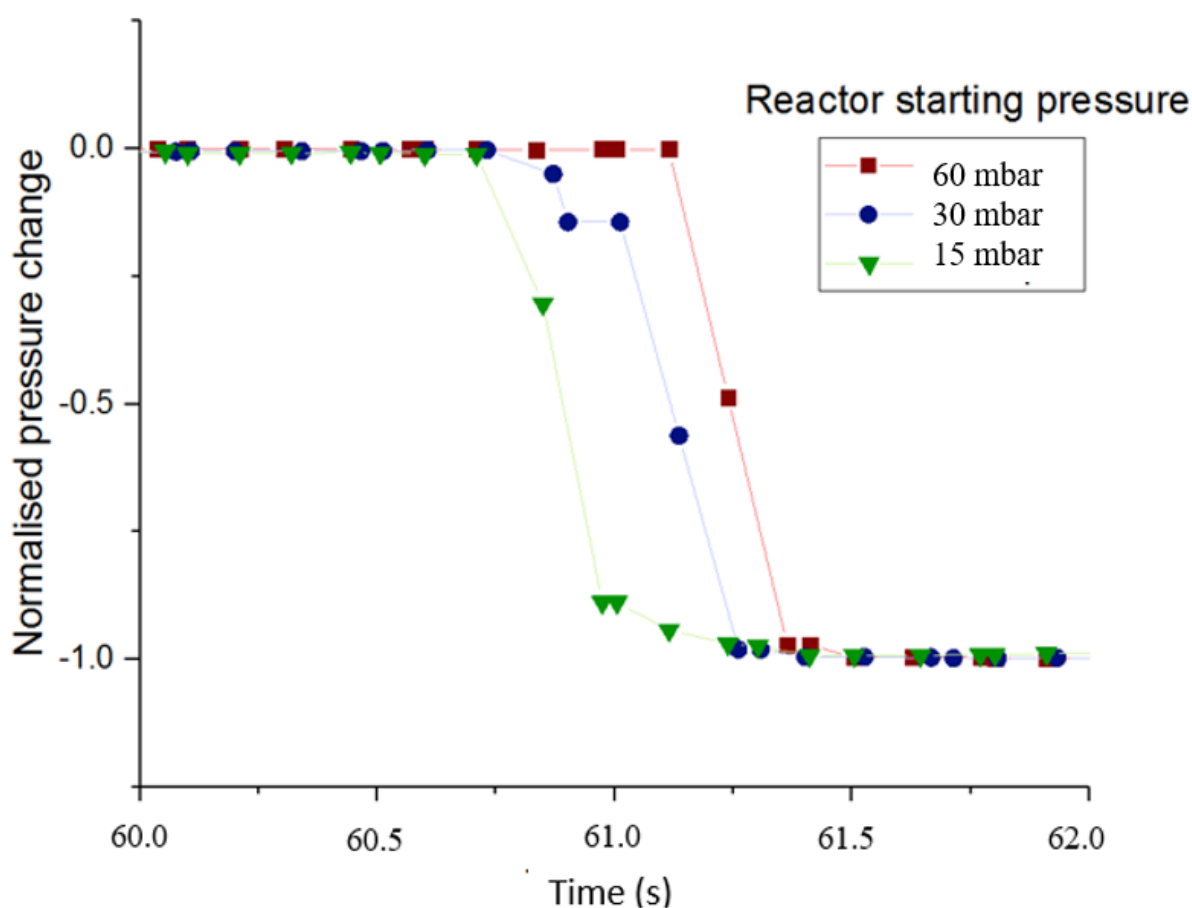


Figure 5.6 – Plot of normalised pressure change of the reactor vessel, when V1 is opened, with the reactor pressure between 15 and 60 mbar, and the reservoir pressure equal to half the reactor vessel pressure, versus time at 800°C

Figure 5.6 shows that during each run of the experiment, the pressure equilibrated within 0.5 seconds, however, the length of time taken varied per run. The shortest equilibration time was

0.3 seconds with a reactor vessel pressure of 60 mbar. The equilibration time increased slightly at lower pressures.

The experiment was repeated, with the reactor vessel temperature set at 500°C, using the same set pressures of the reactor vessel (15, 30, and 60 mbar) and the reservoir vessel pressure (7.5, 15, and 30 mbar) as used in Figure 5.7. V1 was then opened, and the pressure change of the reactor vessel was recorded at a sampling rate of 10 samples per second.

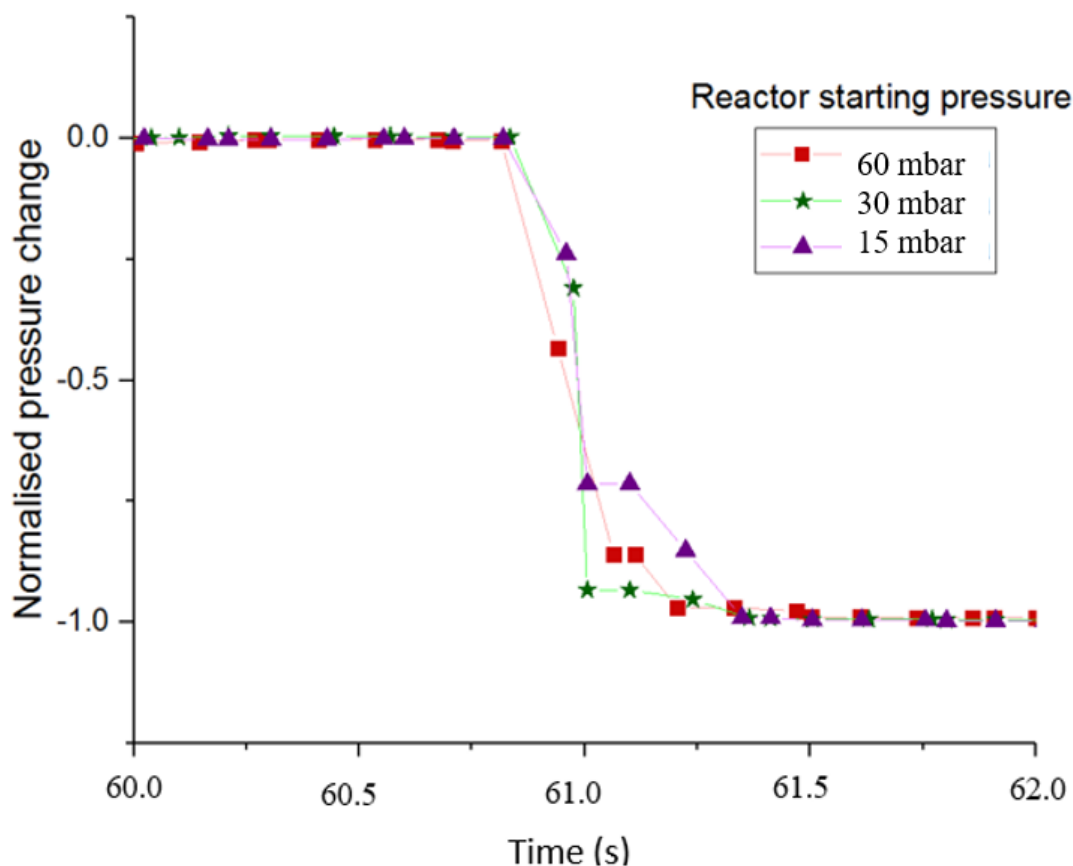


Figure 5.7 – Plot of normalised pressure change of the reactor vessel, when V1 is opened, with the reactor vessel pressure between 15 and 60 mbar, and the reservoir pressure equal to half the reactor vessel pressure, versus time at 500°C

As with Figure 5.6, the time taken for the pressure in the system to equilibrate in Figure 5.7 varied from 0.6 to 0.8 seconds. The time taken was approximately 0.3 seconds longer than the data in Figure 5.6, potentially suggesting slower oxygen diffusion at lower temperatures.

From the results shown in Figures 5.6 and 5.7, it appears that the pressure switch is likely to mask the pressure released from any sample for approximately one second after V1 is opened. This may cause issues for the calculation of the surface exchange coefficient (k) which relies more heavily upon earlier data from the gas switch.

To ensure the pressure in the system after the pressure switch did not fluctuate due to changing temperature of the gas in the reactor, a blank run at 800°C was repeated, with the pressure recorded for 5 minutes after V1 was opened and closed. The pressure in the reactor and reservoir vessel before V1 was opened and closed was 20 and 5 mbar respectively. The data is shown in Figure 5.8.

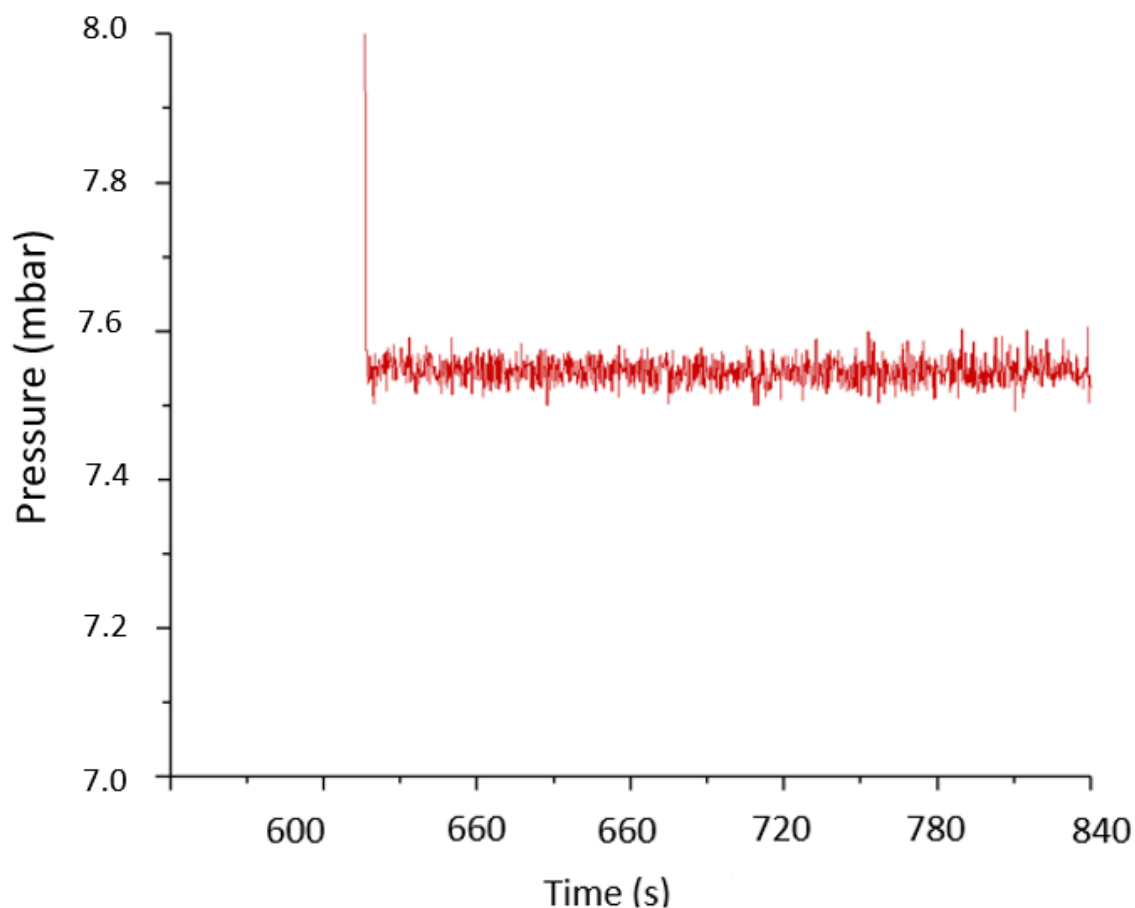


Figure 5.8– Plot of pressure in the reactor vessel versus time for a blank run after V1 was opened, with the reactor vessel temperature at 800°C

Figure 5.8 shows stable pressure throughout the experiment. This suggests re-equilibration of the temperature in the system occurs rapidly, and likely will not impact the measurement.

To determine the impact of leaving V1 open or closed during the re-equilibration of the pressure, a series of blanks were performed at four different conditions, with one run at each condition leaving V1 open, and the other closing V1, after V1's initial actuation. The first set of blanks were performed at room temperature and the second set at a reactor temperature of 800°C. Both sets of blanks had a starting reactor pressure of approximately 30 or 60 mbar. The reservoir pressure was set to approximately half the starting pressure of the reactor during

the run. The results of these experiments can be seen in Figures 5.9 (A-D). The sampling rate for all experiments was set at 10 samples per second.

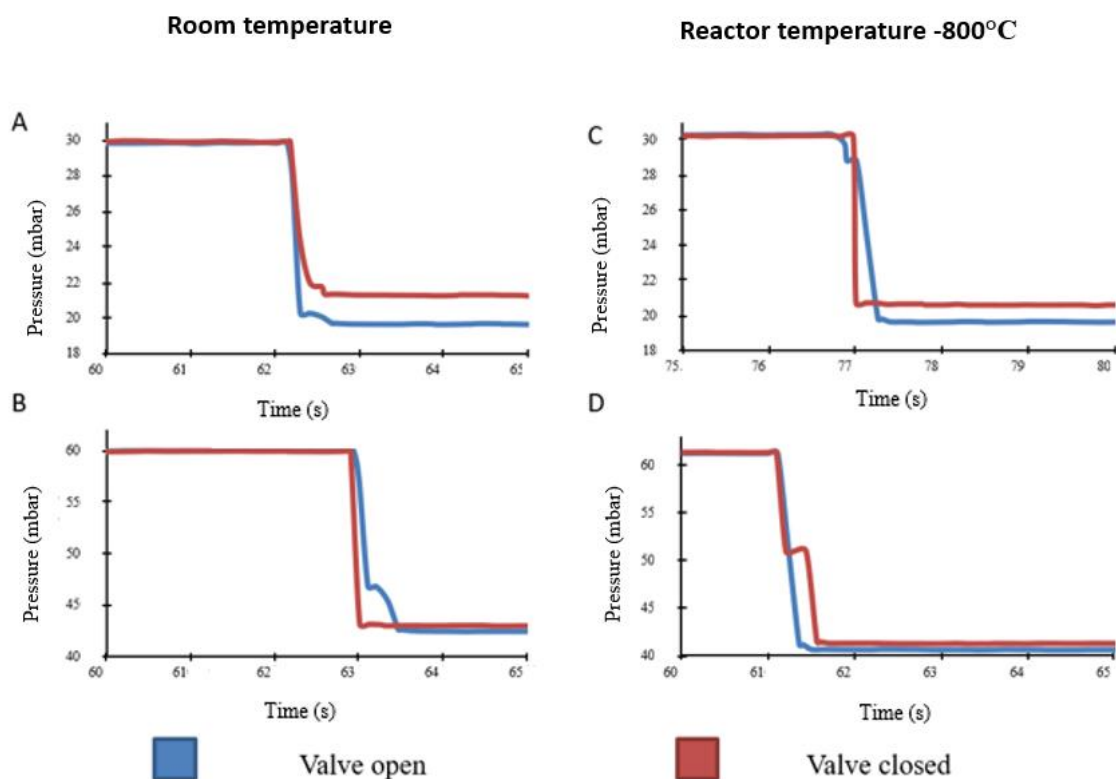


Figure 5.9 – Plot of the reactor pressure versus time showing the pressure re-equilibration of the system after V1 vessel was opened (blue lines) or opened and quickly closed (red lines) with, (A) reactor at room temperature, starting pressure of 30 mbar, (B) reactor at room temperature, starting pressure of 60 mbar, (C) reactor at 800 °C, starting pressure of 30 mbar, (D) reactor at 800°C, starting pressure of 60 mbar. The reservoir pressure for each run was half the starting pressure of the reactor and data sampling occurred at a rate of 10 samples a second. In Figures 5.9 (A-D), the pressure in the system re-equilibrated within 0.8 seconds of V1 being opened. For all runs, bar Figure 5.9 (D), the blank run during which V1 was closed after opening, re-equilibrated quicker than the blank with V1 left open. It appears that during the blank run shown in Figure 5.9 (D), the valve may not have turned smoothly, causing a pressure spike making the system take longer to re-equilibrate. From Figures 5.9 (A-D), it appears that closing the valve does not add additional time to the pressure re-equilibration of the system.

From the data shown in Figures 5.9 (A-D), the first second of data after V1 is opened should be discounted, whether V1 is closed or opened, as there is no consistent behaviour in the pressure re-equilibration. However, having the reactor sealed during the pellet re-equilibration offers the advantage of a smaller volume in which the oxygen is released from the non-

stoichiometric pellet. This will give a larger pressure change to record, reducing potential error for modelling.

Due to the non-repeatability and noise at the time of the gas switch shown in Figures 5.7 and 5.9, it is likely that for this process to be used, an estimated pressure of the system after the opening of V1 should be used. This value should be calculated from a mole balance of the two chambers, and the relaxation fitted through this estimated point. This will however require a much more accurate recording of when the valve is opened for the data to be fitted accurately.

5.2.4 Determination of oxygen non-stoichiometry using pressure relaxation

To demonstrate the potential of the system for measuring the change of oxygen non-stoichiometry, a powdered sample of LSCF was placed in the reactor and subsequently heated to either 700, 800, or 900°C with V3 open, and the reactor vessel under vacuum. The sample was allowed to equilibrate at 1 mbar at the set temperature. The reservoir vessel was subsequently filled with oxygen to a higher pressure than the reactor vessel. V1 was then opened and closed, injecting oxygen into the reactor. A mole balance of the oxygen in the gas phase of the reactor and reservoir vessels before and after the re-equilibration was performed, to calculate how the new non-stoichiometry of the sample. A reference point from literature was then used as a starting δ , with the change in non-stoichiometry linked to the known point. The results of this experiment are shown in Figure 5.10, compared to ref [29].

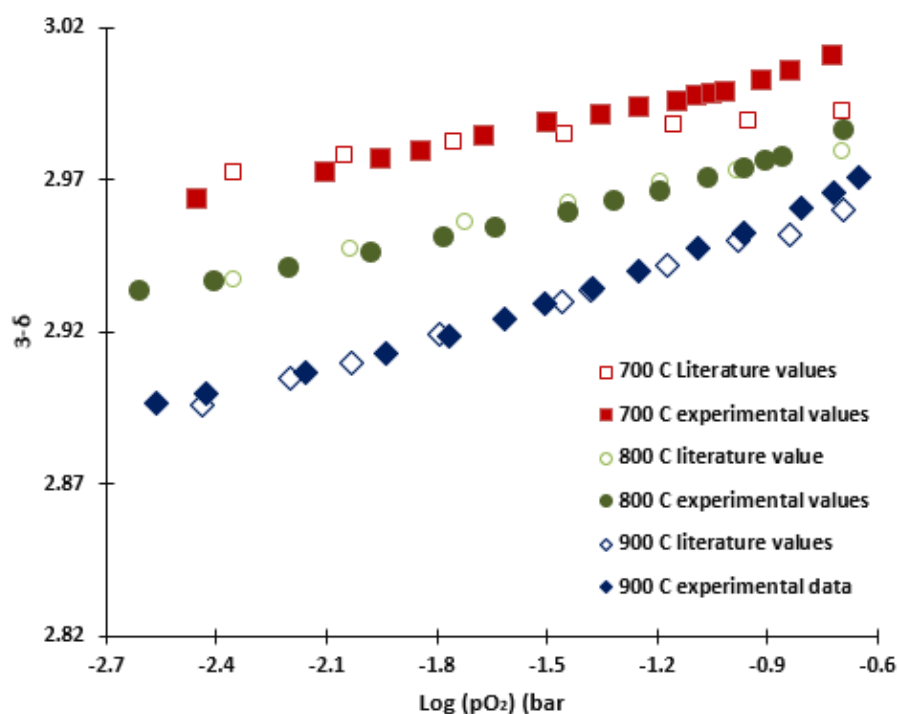


Figure 5.10 – Plot showing oxygen non-stoichiometry versus pO_2 at temperatures between 700 and 900°C obtained from the literature (open symbols) or experimentally using the pressure relaxation rig (closed symbols)

Figure 5.10 shows good agreement between literature values and experimental results for 800 and 900°C, with some deviation at $\log p_{O_2}$'s greater than -0.9 bar. A more significant deviation from the literature values was found at 700°C, and a steeper gradient for the change in δ as a function of p_{O_2} was recorded. The most likely cause of this variation is an issue with the temperature measurement of the system.

To investigate the potential error in the system, the data presented in Figure 5.11 was re-interpreted changing the average reactor temperature, the temperature of the reservoir, and the volume of the reactor or reservoir vessels used in the calculation. Figures 5.11 show the effects of changing the temperature by $\pm 10^\circ\text{C}$ or the volumes of the chambers by $\pm 5\text{ml}$.

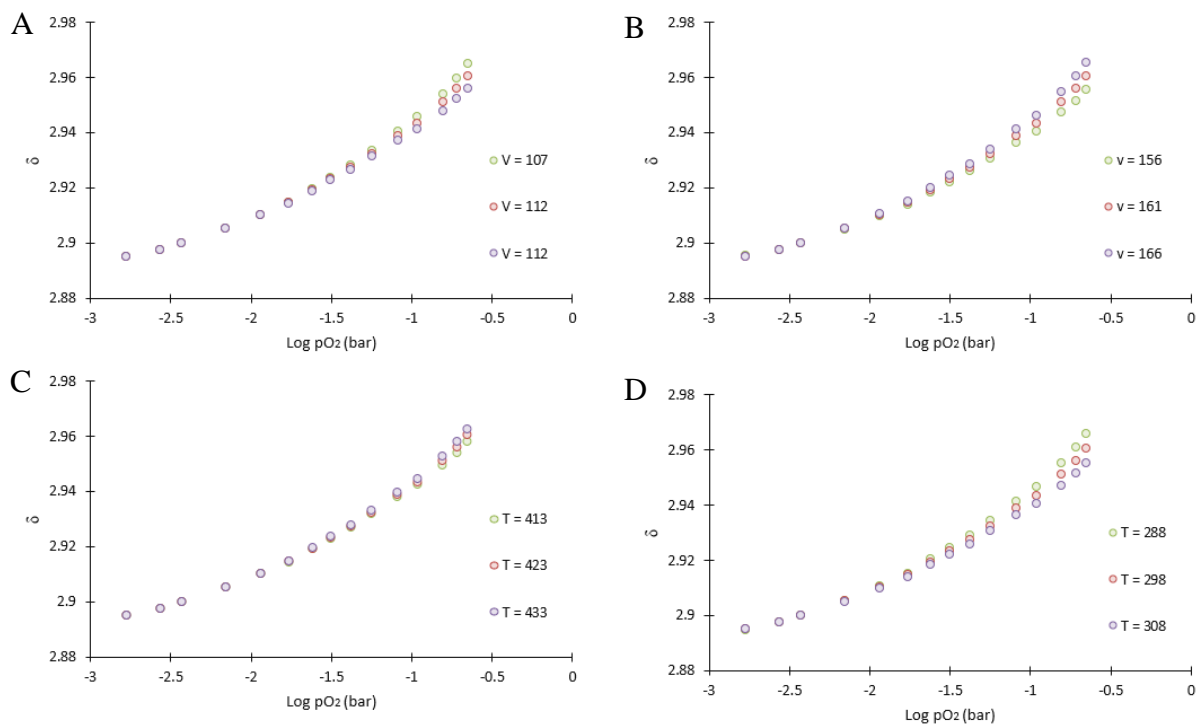


Figure 5.11 – Plot showing oxygen non-stoichiometry versus p_{O_2} at 900°C obtained experimentally using the pressure relaxation rig (closed symbols) with different conditions to show the sensitivity of calculations. The parameter changed in each graph was, (A) - reactor volume, (B) – reservoir volume, (C) – reactor temperature, and (D) – reservoir temperature

As shown, there is good agreement between the calculated values for each condition below a $\log p_{O_2}$ of -1. From this data, any reference δ should be taken at a $\log p_{O_2}$ lower than -1 to ensure errors from changing temperatures and miscalculated volumes do not have a systemic impact on the system. More notable changes were calculated above this value.

It was seen in the calculations that errors in expected reservoir volume and temperature had a bigger impact than the reactor vessel, so these should be well controlled. One likely explanation for the differences with literature for Figure 5.10 at 700°C was an error in the

recorded temperature. Figure 5.11 D shows that if the average temperature of the reactor used in the calculation was lower than expected, the change in non-stoichiometry would be greater. This is due to the same pressure change relating to a greater number of moles of gas at lower temperatures, as can be seen in Eq.5.15. Therefore, in Figure 5.10, if calculations were performed at 700°C, but the true average temperature was higher, then such a shift as seen in Figure 5.10 would be expected. One possibility was that the connection of the thermocouple was poor, meaning the wrong temperature was used for the calculation. Also, variations in the room temperatures, such as a radiator turning on, may have impacted the calculation.

The advantage of calculation of non-stoichiometry using this method is the ease at which various p_{O_2} s can be accessed, allowing numerous pressures to be investigated. To perform similar experiments using TG techniques, multiple gas cylinders, or the blending of gases using mass flow controllers would be required, which would allow quite a large uncertainty of the p_{O_2} of the gases. The use of pure oxygen and different pressures eliminates this issue, allowing multiple p_{O_2} s to be tested, using only one gas cylinder. An issue with this technique, however, is that it requires a reference δ to calculate the changes in non-stoichiometry. This requires a different technique to be used in combination with pressure relaxation. From these experiments, it appears that the technique is very useful as a guide for material screening – however, some doubts over the accuracy of the technique for finding absolute values of δ are raised. A particular concern shown is the potential impact of small temperature variations.

5.2.5 Oxygen relaxation studies using pressure relaxation

The pressure relaxation technique allows the recording of the relaxation profiles during p_{O_2} changes, which can be useful for calculating D and K values. This is demonstrated in Figure 5.12 (A-D), which shows the pressure in the reactor, when the equilibrium of the reactor and a pellet of LSCF is disturbed by opening V1, with the reservoir at a different pressure. Since the sample is no longer in equilibrium, oxygen is released. During these experiments shown in Figure 5.12 (A-D), the reactor and reservoir vessel pressures were in the ratio of 4:1, and sampling was performed at a rate of 10 data points per second.

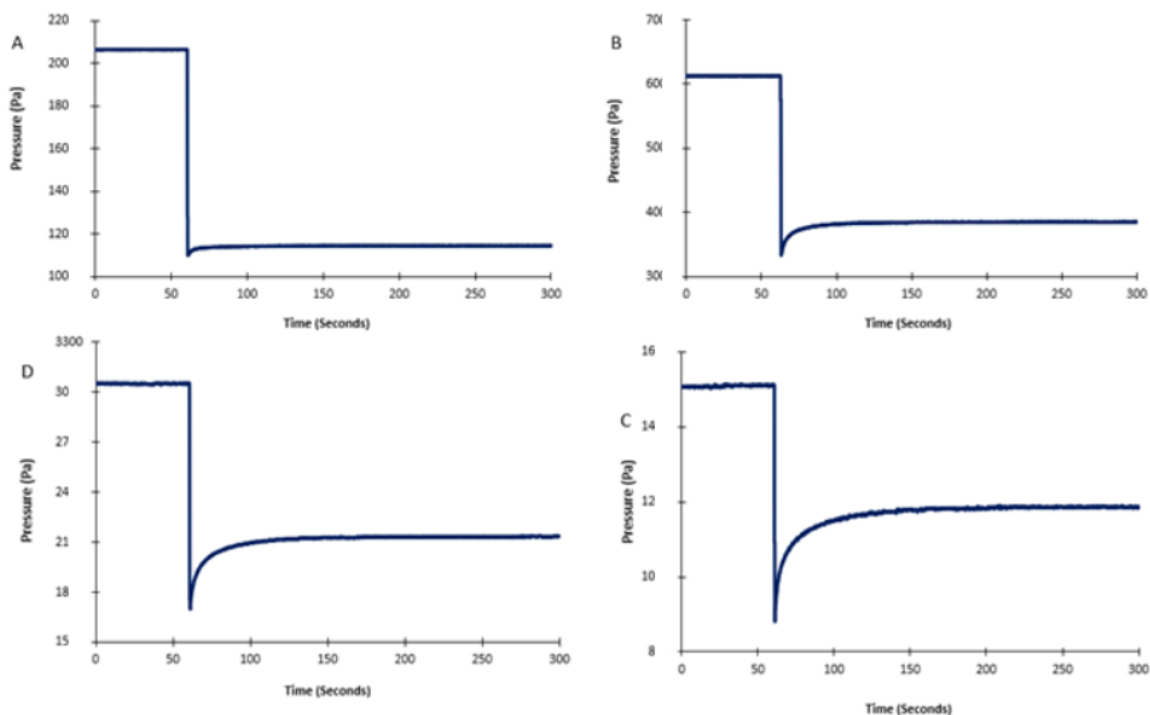


Figure 5.12 (A-D)– Plots showing pressure in the reactor vessel versus time, highlighting the pressure change as the non-stoichiometric LSCF re-equilibrates to the new pO_2 after the opening of V1. The starting pressures of the reactor vessel during the experiment were approximately, (A) – 210 mbar, (B) – 60 mbar, (C) – 30 mbar and (D) – 15 mbar. The reservoir pressure was set at $\frac{1}{4}$ of the starting reactor vessel pressure, and sampling was performed at a rate of 10 points per second.

During this experiment, significant pressure change from the pellet was noted, with all experiments giving a pressure change of at least 3 mbar. This large release of oxygen at these conditions ensures a high signal-to-noise ratio in the system, which would improve the accuracy of any calculation.

5.2.6 Upgrading the measurement system

In Figures 5.7 and 5.8, small steps in the pressure are noted during the opening of V1 when the reservoir and reactor are at different pressures. These steps are unlikely to be real and are likely due to the measurement technique. In the previous results, a Pico Logger was used to measure the response from the pressure transducers. However, to improve this, a national instrument DMM was tested to obtain faster sampling rates. This device was capable of recording 1000 points per second, compared to that of the Pico logger, which could only manage 10. Figures 5.13 below compares the opening and closing of V1 with a reactor and reservoir pressure of 80 and 20 mbar respectively before the valve actuation.

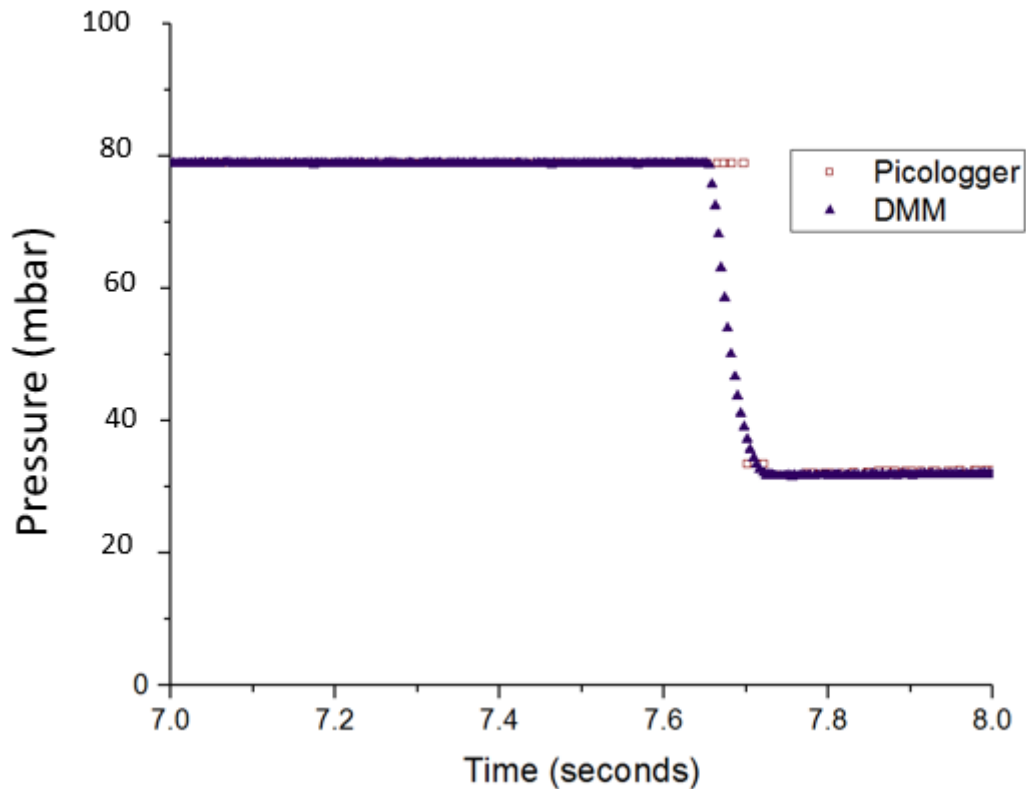


Figure 5.13 – Plot showing pressure in the reactor vessel versus time, showing the pressure change as the non-stoichiometric LSCF re-equilibrates to the new pO_2 after the opening of V3. The starting pressures of the reactor vessel during the experiment were approximately 80 mbar and the temperature 700°C. The reservoir pressure was set at $\frac{1}{4}$ of the starting reactor vessel pressure, and sampling was performed at a rate of 10 points per second using the Picologger, and 100 points per second using the DMM.

As seen, measuring the data using the DMM gives more data points during the opening of V1 and a smoother relaxation. What is most important from this result, is that the actuation of V1 can be accurately seen in the data, allowing for accurate fittings to the data.

5.2.7 - Further investigations of the pressure change

Further investigation into the pressure change was conducted, and an LSCF pellet underwent a relaxation at temperatures between 700 and 850°C. During these experiments, the ratio of the pressure between the reactor and reservoir was 4:1, with the starting pressure of the reactor approximately 60 mbar. The full relaxation profiles can be seen in Figure 5.14.

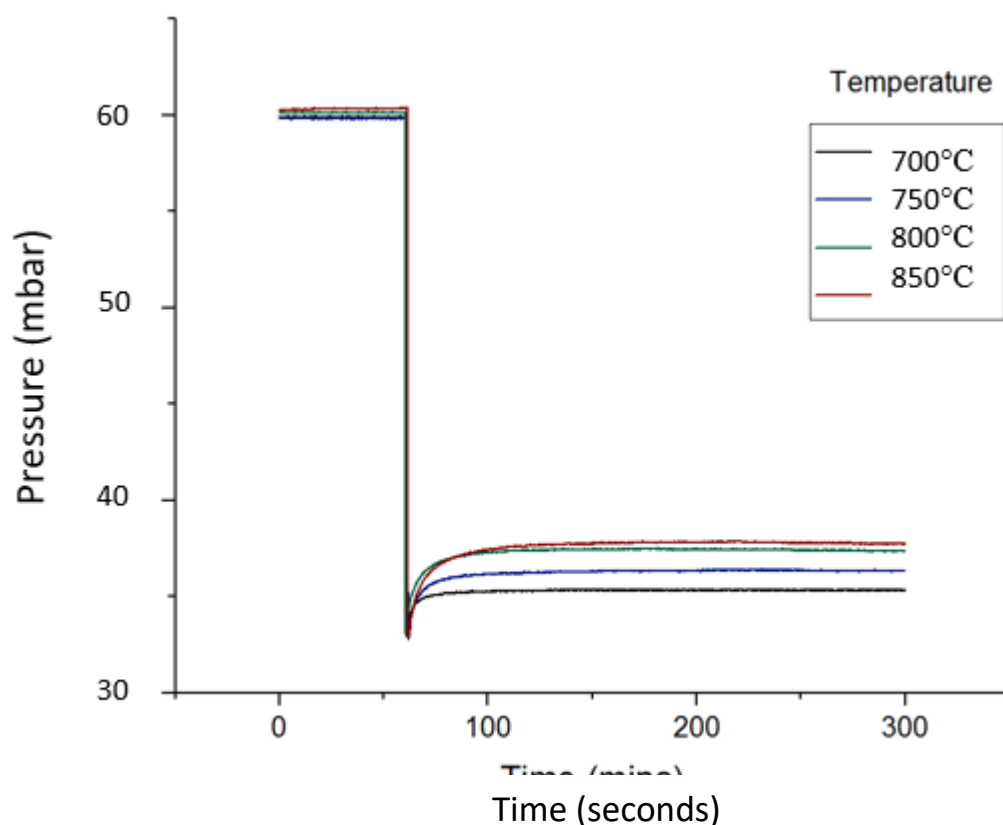


Figure 5.14– Plot showing pressure in the reactor vessel versus time, highlighting the pressure change as the non-stoichiometric LSCF re-equilibrates to the new pO_2 after the opening of V3. The starting pressures of the reactor vessel during the experiment were approximately 60 mbar and the temperatures between 700 and 850°C. The reservoir pressure was set at $\frac{1}{4}$ of the starting reactor vessel pressure, and sampling was performed at a rate of 10 points per second.

While each experimental run had a good signal-to-noise ratio, the pressure change in the reactor during these relaxations was smaller than expected. As previously performing mole balances across the reactor and reservoir chambers gave good agreement to literature values, as seen in Figure 5.11, further investigation was conducted. The change in the oxygen non-stoichiometry was plotted against time for the experiments, with $t=0$ at the lowest recorded pressure in the system after the valve was opened. From this point, the change in non-stoichiometry was calculated. The data for these relaxations can be seen in Figure 5.15 (a)

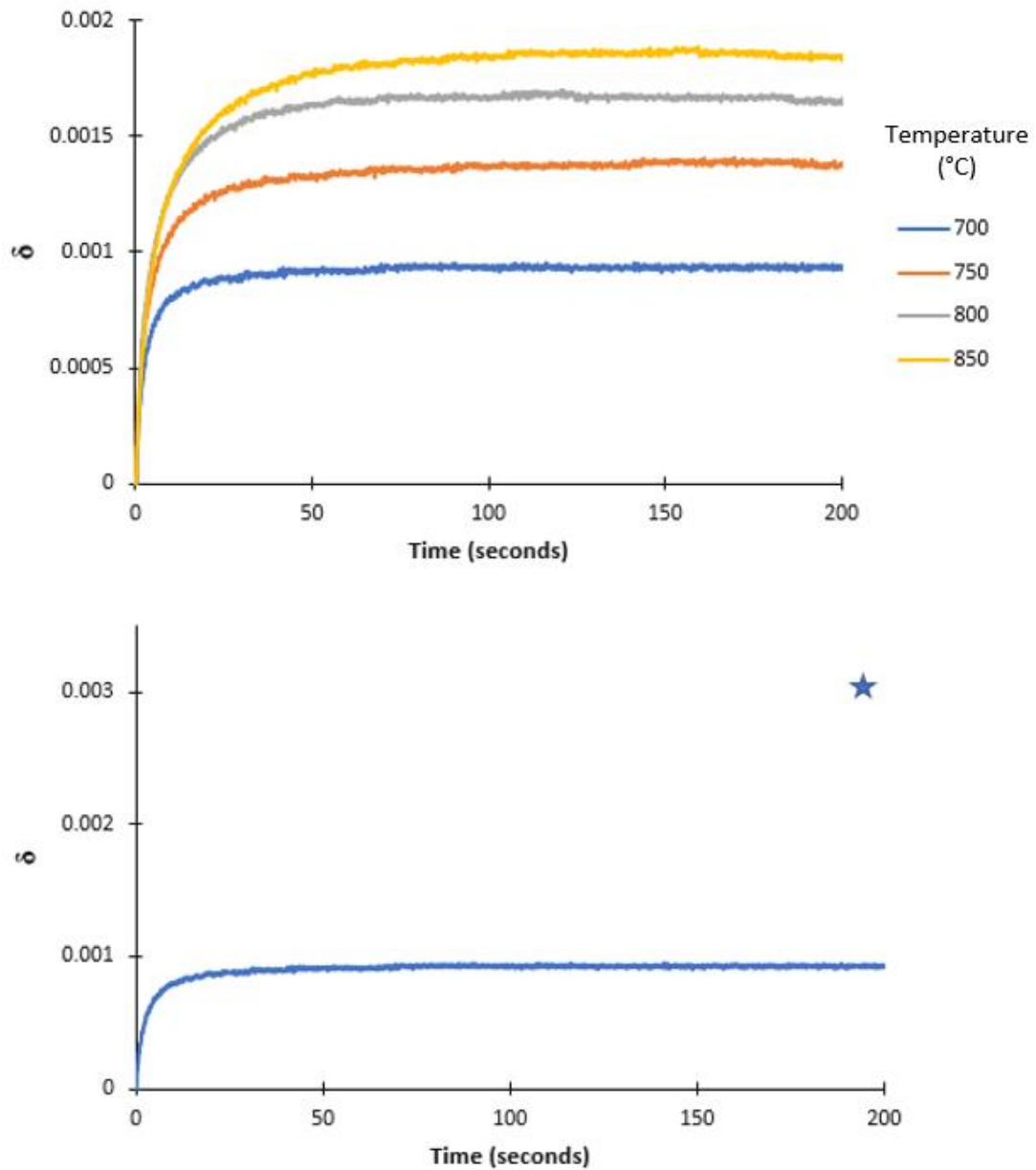


Figure 5.15 (a)– Plot showing the change in the non-stoichiometry of the dense LSCF pellet versus time, calculated from the change in pressure of the reactor vessel. The starting pressures of the reactor vessel during the experiment were approximately 60 mbar and the temperatures between 700 and 850°C. The reservoir pressure was set at $\frac{1}{4}$ of the starting reactor vessel pressure, and sampling was performed at a rate of 10 points per second. **(b)** – Plot showing the data shown in Figure 5.16 (a) for 700°C (blue line) compared to the estimated change in oxygen non-stoichiometry from thermodynamic data. The blue star refers to the expected change in non-stoichiometry from calculations

Figure 5.16 (a), shows the relaxation of all experimental runs, however, the actual change in oxygen capacity was significantly lower than expected. This is highlighted in Figure 5.16 (b), where the data for the relaxation at 700°C is plotted, with the blue star representing the expected change in non-stoichiometry from thermodynamic data from ref [29]. As seen, the change in non-stoichiometry measured solely using the reactor pressure transducer is

approximately 1/3 of the expected change in non-stoichiometry, and this was the case with all four runs. To ensure the material was performing as expected a mole balance across the reactor and reservoir chambers was performed, and this can be seen in Table 5.1.

Table 5.1 – Mole balance across the reactor and reservoir before and after V1 opening

	Before valve opens		After valve opening	
	Reactor	Reservoir	Reactor	Reservoir
Pressure (mbar)	59.93	15.23	35.34	32.50
Temp (°C)	120	25	120	25
Volume (ml)	112	161	112	161
Moles O ₂	0.000205	0.0000990	0.000121	0.000211
Total moles	0.000304		0.000332	

From the calculation, the number of moles of oxygen present in the gas phase across the reactor and reservoir after the valve was opened, was 0.000028 greater than before the opening of the valve. The difference in moles before and after the opening of the valve must be due to the release of oxygen from the pellet into the gas phase. The change in δ of the LSCF pellet required to give this difference in moles seen in Table 5.1 was calculated, and this is shown in Table 5.2, and compared to the expected literature result.

Table 5.2 – Calculated values from change in δ of LSCF pellet

Calculated value	Moles
Difference in moles in the gas phase	0.000028
Moles of LSCF	0.0086
Change in δ	0.0032
Estimated change in δ (calculated from ref [29])	0.0030

From this result, it is apparent that approximately the expected amount of oxygen is being released by the sample during the experiment, with a difference of 10% in the calculated and recorded non-stoichiometry. In Figure 5.16 (b), it is shown that most of the relaxation profile is missed, suggesting an issue with the technique.

5.3 Discussion

It has been shown that pressure relaxation has the potential for calculating oxygen non-stoichiometry in Figures 5.10, and this technique offers some advantages over the issues shown with different methods of calculating oxygen non-stoichiometry discussed in Table 2.6 [30-31]. In this work, the method of characterising the apparatus has been shown, along with the governing equations which would be of use to any who wish to create similar apparatus.

Literature data and the experimental data gathered using this technique agreed only partially, with some errors found, particularly during the 700°C run. As a powder sample was used which underwent no further treatment, it is clear that any error must be technique or equipment. The most likely cause of this error is an issue with the temperature measurement. As shown in Figure 5.11, if the average temperature used in the experiment was incorrect, the calculated change in non-stoichiometry would be significant.

Despite this issue, the experiments do show the potential of the technique. One particular benefit of the technique is the set-up is simple, requiring only two pressure transducers, a small benchtop furnace, and a measurement device with the associated computer. It was also seen to allow good control of pressure steps, allowing multiple pO_2 's to be tested easily using one gas cylinder. The major issue of the technique is the potential instability of the room temperature, as well as the potential for errors in the average temperature.

It was found that calculating the oxygen diffusion rates from this technique was not possible from the experimental data. This was due to the majority of the relaxation not being measured, as discussed in Figure 5.16. It was shown that the oxygen was released, and accounted for in the mole balance between each chamber. This means the missed oxygen which is approximately 66% of the total oxygen released, must have been released within approximately 1 second of the valve actuation, as this is the period of uncertainty when no data was measured.

When comparing this data to relaxations in literature, it can be seen that the relaxation from these techniques takes in the order of 100's of seconds to complete at 800°C. In ref [32], ECR was employed on a pellet of LSCF, and the relaxation between a pO_2 of 18 and 21 mbar was seen to take 4000 to 5000 seconds to complete. In ref [33], at 750°C, a similar result to ref [32] was seen, and even with the addition of $BaCoO_3$ to the surface as a catalyst, the relaxation still took 500 seconds. Other examples of similar time constants are seen in ref [34-36]. In these examples, the work is compared to other literature, with a good correlation between results, and with similar durations. The closest example of similar relaxation profiles

in literature required surface coating with Pt nanoparticles, however, this behaviour was still significantly slower than seen in this work [35]. One possibility to explain the extremely rapid kinetics is that strontium segregation may have an impact. In ref [36], SrCoO₃ on the surface was seen to reduce the time taken for the relaxation from approximately 2000 to 500 seconds. Strontium segregation is a known issue with LSCF, and a strontium oxide monolayer has been shown to form by low energy ion scattering by Kilner et al. [26] and Druce et al [37], act as a catalyst. It was also seen in ref [38] that the performance of a LSCF membrane stored in air was significantly lower than expected, showing the potential for unwanted reactions. The author does not believe this is likely a feasible explanation however to explain the magnitude of the difference.

The use of pure gases are likely to improve oxygen diffusion rates, however the times taken in these experiments are unfeasible. Additionally, unpublished work performed by Wei Chen using this same technique, showed more reasonable times (approximately 500 seconds at 800°C). In this work, the relaxation was completed in 50 seconds using the same conditions.

The easiest explanation for the difference would be an incorrect temperature measurement of the system. Oxygen release would be faster at a higher temperature as oxygen diffusion rates will increase [39-40]. Additionally, a higher temperature would mean fewer moles than currently calculated would be released. Incorrect measurement of the system is feasible, as the temperature was measured by thermocouple connected to the bottom of the outside of the reactor. It is possible that this slipped, meaning the temperature measured was wrong. Regardless, the diffusion profiles of the relaxation are visible, showing the technique has merit. The data produced in this chapter however likely does not show the full potential of the technique due to an unknown issue with the system.

5.4 Conclusions and future work

During this chapter, a new technique for measuring oxygen diffusion and non-stoichiometry has been developed. The process has been shown to have the potential for measurements in the change of oxygen non-stoichiometry, allowing multiple pO_2 s to be tested with no need for multiple gas cylinders. Disagreement with literature values occurs at higher pO_2 's, suggesting more work is required in fine-tuning the set-up.

When the technique was employed to measure the relaxation of oxygen release from LSCF, it was seen that the majority of the relaxation was missed, and the relaxation was unfeasibly fast. Several methods are discussed below for potential to improve the system, namely:

- **Removal of a temperature gradient** – a fully sealed system at one temperature may improve the confidence in the temperature which is thought likely to be the issue with this work
- **Improvement of temperature measurement** – a system with an internal thermocouple could improve accuracy, and reduce the chance of errors.
- **Oxygen injection** – Currently the change in the equilibrium of the reactor vessel is performed by the opening of a valve between the reactor and reservoir vessel, lowering the pressure. It may be that using a micro-pump and injecting small volumes of pure oxygen into the reactor may give a more stable change in the system pressure. This would have the additional benefit of reducing the system to one reactor and one valve, reducing potential for leaks.

5.5 References

- [1] Z.Zhang, D.Chen, F.Dong, Z.Shao - Efficient and CO₂-tolerant oxygen transport membranes prepared from high-valence B-site substituted cobalt-free SrFeO_{3-δ}, *Journal of membrane science*, 495, 2015, 187-197
- [2] A.Murgan, A.Thursfield, I.S.Metcalf - A chemical looping process for hydrogen production using iron-containing perovskites, *Engineering and environmental science*, 4, 2011, 4639-4649
- [3] M.liu, D.Ding, K.Blinn, X.Li, L.Nie, MLiu - Enhanced performance of LSCF cathode through surface modification, *International journal of Hydrogen energy*, 37, 2015 8613-8620
- [4] S.P.S.Badwal, M.J.Bannister, M.J.Murray - Non-stoichiometric oxide electrodes for solid state electrochemical devices, *Journal of Electroanalytical Chemistry and Interfacial Electrochemistry*, 168, 1984, 363-382
- [5] J. Maier - Interaction of oxygen with oxides:How to interpret measured effective rate constants?, *Solid State Ionics*, 135, 2000, 575 –588
- [6] A.Galdikas, N.Bion, D. Duprez, V.Virbikaas, D.Mazelis - Modeling of Diffusion Process in the Isotopic Oxygen Exchange - Experiments of CexZr(1-x)O₂ Catalysts, *Journal of material science*, 19, 2013, 1320–1392
- [7] G. K. Vdovin, E. K. Kurumchin, E. V. Isaeva, D. I. Bronin - Isotopic Exchange and Oxygen Diffusion in the La_{0.88}Sr_{0.12}Ga_{0.82}Mg_{0.18}O₃ – α-Molecular Oxygen System, *Russian Journal of Electrochemistry*, 37,2001, 304-307
- [8] E.M.Sadovskay, A.S.Bobin, V.V.Skask - Isotopic transient analysis of oxygen exchange over oxides, *Chemical Engineering Journal*, 348, 2018, 1025-1036
- [9] E.Boehm, J.M.Bassat, P.Dordor, F.Mauvy, J.-C.Grenier, Ph.Stevens - Oxygen diffusion and transport properties in non-stoichiometric Ln₂ – xNiO₄ + δ oxides, *Solid State Ionics*, 176, 2005, 2717-2725
- [10] G.Kim, S.Wang, A.J.Jacobson, C.L.Chen - Measurement of oxygen transport kinetics in epitaxial La₂NiO_{4+δ} thin films by electrical conductivity relaxation, *Solid State Ionics*, 177, 2006, 1461-1467
- [11] D.Rupasov, T.Makarenko, A.J.Jacobson - Oxygen diffusion in Sr₃YCo₄O_{10.5}: An electrical conductivity relaxation and thermogravimetric analysis approach, *Solid State Ionics*, 265, 2014, 68-72
- [12] A.P.Mozhaev, S.V.Chernyaev - Oxygen diffusion in YBa₂Cu₃O_{6+x} ceramics, *Journal of Material Chemistry*, 4, 1994, 1107-1110
- [13] M.Katsuki, S.Wang, M.Dokiya, T.Hashimoto - High temperature properties of La_{0.6}Sr_{0.4}Co_{0.8}Fe_{0.2}O_{3d} oxygen nonstoichiometry and chemical diffusion constant, *Solid State Ionics*, 156, 2003, 453–461
- [14] I.Denk, F.Noll, J.Maier - In situ profiles of oxygen diffusion in SrTiO₃: Bulk behaviour and boundary effects, *Journal of American ceramic society*, 80, 1997, 279-285

- [15] B. Ma, J. H. Park, U. Balachandran - Analysis of Oxygen Transport and Stoichiometry in Mixed-Conducting SrFeCo_{0.5}O_x by Conductivity and Thermogravimetric Analysis, *Journal of the Electrochemical Society*, 144, 1997, 2816-2823.
- [16] A. Berenov, A. Atkinson, J. Kilner, M. Ananyev, V. Eremin, N. Porotnikova, A. Farlenkov, E. Kurumchin, H. J. M. Bouwmeester, E. Bucher, W. Sitte - Oxygen tracer diffusion and surface exchange kinetics in Ba_{0.5}Sr_{0.5}Co_{0.8}Fe_{0.2}O_{3-δ}, *Solid State Ionics*, 268, 2014, 102-109.
- [17] M.-B. Choi, S.-Y. Jeon, H.-S. Yang, J.-Y. Park, S.J. Song - Oxygen nonstoichiometric and chemical expansion of mixed conducting La_{0.1}Sr_{0.9}Co_{0.8}Fe_{0.2}O_{3-δ}, *Journal of the Electrochemical Society*, 158, 2011, B189-B193
- [18] R.A.Cox-Galhotra, S.McIntosh - Unreliability of simultaneously determining k_{chem} and D_{chem} via conductivity relaxation for surface-modified La_{0.6}Sr_{0.4}Co_{0.2}Fe_{0.8}O_{3-δ}, *Solid State Ionics*, 181, 2010, 31-32,
- [19] H.J.M. Bouwmeester, H. Kruidhof, A.J. Burggraaf - Importance of the surface exchange kinetics as rate limiting step in oxygen permeation through mixed-conducting oxides, *Solid State Ionics*, 72, 2, 1994, 185-194
- [20] J. E. Elshof, M. H. R. Lankhorst, H. J. M. Bouwmeester - Oxygen Exchange and Diffusion Coefficients of Strontium-Doped Lanthanum Ferrites by Electrical Conductivity Relaxation, *Journal of the Electrochemical Society*, 144, 1997, 1060-1067.
- [21] F. Ciucci - Electrical conductivity relaxation measurements: Statistical investigations using sensitivity analysis, optimal experimental design and ECRTOOLS, *Solid State Ionics*, 239, 2013, 28-40.
- [22] A. Falkenstein, D. N. Mueller, R. A. De Souza, M. Martin - Chemical relaxation experiments on mixed conducting oxides with large stoichiometry deviations, *Solid State Ionics*, 280, 2015 66-73.
- [23] Ø. F. Lohne, M. Sjøgaard, K. Wiik, - The significance of gas-phase mass transport in assessment of k_{chem} and D_{chem} , *Journal of the electrochemical society*, 160, 2013 F1282-F1292.
- [24] S.F. Bychkov, I.I. Gainutdinov, S.A. Chizhik, A.P. Nemudry - Novel oxygen partial pressure relaxation technique for study of oxygen exchange in nonstoichiometric oxides. The model of relaxation kinetics, *Solid State Ionics*, 320, 2018, 297-304
- [25] A. Esquirol, N. P. Brandon, J. A. Kilner, M. Mogensen - Electrochemical Characterization of La_{0.6}Sr_{0.4}Co_{0.2}Fe_{0.8}O₃ Cathodes for Intermediate-Temperature SOFCs, *Journal of the electrochemical society*, 151, 2004, A1847-A1855.
- [26] M.Niania, R.Podor, T.B.Britton, C.Li, S.J.Cooper, N.Svetkov, S.Skinner, J.Kilner - In situ study of strontium segregation in La_{0.6}Sr_{0.4}Co_{0.2}Fe_{0.8}O_{3-δ} in ambient atmospheres using high-temperature environmental scanning electron microscopy, *Journal of materials chemistry A*, 6, 2018, 14120-14135
- [27] X. Y. Tan, Z. G. Wang, B. Meng, X. X. Meng, K. Li - Pilot-scale production of oxygen from air using perovskite hollow fibre membranes - *Journal of Membrane Science*, 352, 2010 189-196.
- [28] J. M. Serra, J. Garcia-Fayos, S. Baumann, F. Schulze-Küppers, W. A. Meulenbergh - Oxygen permeation through tape-cast asymmetric all-La_{0.6}Sr_{0.4}Co_{0.2}Fe_{0.8}O_{3-δ} membranes, *Journal of Membrane Science*, 447, 2013, 297-305.

- [29] S.R.Bishop, K.L.Duncan, E.D.Wachsman - Surface and Bulk Defect Equilibria in Strontium-Doped Lanthanum Cobalt Iron Oxide, *Journal of the Electrochemical Society*, 156, 2009, 1242-1248
- [30] S.Georgieva & T.Nedeltcheva, A.Stoyanova-Ivanova - Development of the Titrimetric and Spectrophotometric Methods for Determination of the Oxygen Content in Superconducting Cuprates. *American Chemical Science Journal*, 13, 2016, 1-15
- [31] M.V.Patrakeev, I.A.Leonidov, V.L.Kozhevnikov - Applications of coulometric titration for studies of oxygen non-stoichiometry in oxides, *J Solid State Electrochem*, 15, 2011, 931-954
- [32] Y.Li, K.Gerdes, T.Horita, X.Liu - Surface Exchange and Bulk Diffusivity of LSCF as SOFC Cathode: Electrical Conductivity Relaxation and Isotope Exchange Characterizations, *Journal of The Electrochemical Society*, 160, 2013, F343-350
- [33] K.Pei, Y.Zhou, K.Xu, Z.He, Y.Chen, W.Zhang, S.Yoo, B.Zhao, W.Yuan, M.Liu, Y.Chen - Enhanced Cr-tolerance of an SOFC cathode by an efficient electro-catalyst coating, *Nano Energy*, 72, 2020, 104704
- [34] Y.Zhang, J.Ma, M.Li, Y.Chen, M.Yan, C.Xia, - Plasma Glow Discharge as a Tool for Surface Modification of Catalytic Solid Oxides: A Case Study of $\text{La}_{0.6}\text{Sr}_{0.4}\text{Co}_{0.2}\text{Fe}_{0.8}\text{O}_{3-\delta}$ Perovskite, *Energies*, 9, 2016, 786.
- [35] W.Yang, Z.Wang, Z.Wang, Z.Yang, C.Xia, R.Peng, X.Wu, Y.Lu - Enhanced Catalytic Activity toward O_2 Reduction on Pt-Modified $\text{La}_{1-x}\text{Sr}_x\text{Co}_{1-y}\text{Fe}_y\text{O}_{3-\delta}$ Cathode: A Combination Study of First-Principles Calculation and Experiment, *Applied material interfaces*, 6, 23, 2014, 21051-21059
- [36] M.Li, Z.Sun, W.Yang, T.Hong, Z.Zhu, Y.Zhang, X.Wu, C. Xia - Mechanism for the enhanced oxygen reduction reaction of $\text{La}_{0.6}\text{Sr}_{0.4}\text{Co}_{0.2}\text{Fe}_{0.8}\text{O}_{3-\delta}$ by strontium carbonate, *Physical Chemistry, Chemical Physics*, 19, 2017, 503-509
- [37] J. Druce, T.Ishihara, J. Kilner, Surface composition of perovskite-type materials studied by Low Energy Ion Scattering (LEIS) - *Solid State Ionics*, 262, 2014, 893 - 896
- [38] N.Han, C.Zhang, X.Tan, Z.Wang, S.Kawi, S.Liu - Re-evaluation of $\text{La}_{0.6}\text{Sr}_{0.4}\text{Co}_{0.2}\text{Fe}_{0.8}\text{O}_{3-\delta}$ hollow fiber membranes for oxygen separation after long-term storage of five and ten years, *Journal of Membrane Science*, 587, 2019, 117180
- [39] J.Y.Chen, J.Rebello, V.Vashook, D.M.Trots, S.R.Wang, T.L.Wen, J.Zosel, U. Guth - Thermal stability, oxygen non-stoichiometry and transport properties of $\text{LaNi}_{0.6}\text{Fe}_{0.4}\text{O}_3$, *Solid State Ionics*, 192, 1, 2011, 424-430
- [40] A.A.Asadi, A.Behrouzifar, M.Iravaninia, T.Mohammadi, A.Pak - Preparation and Oxygen Permeation of $\text{La}_{0.6}\text{Sr}_{0.4}\text{Co}_{0.2}\text{Fe}_{0.8}\text{O}_{3-\delta}$ (LSCF) Perovskite-Type Membranes: Experimental Study and Mathematical Modeling, *Industrial and Engineering Chemical Research*, 51, 7, 2012, 3069-3080

Chapter 6 -An investigation into the thermodynamic and structural changes of $\text{YBaCo}_4\text{O}_{7+\delta}$

Here we report the investigation of the non-stoichiometric material $\text{YBaCo}_4\text{O}_{7+\delta}$ with promising thermodynamics for oxygen enrichment. In-depth studies of the crystal structure and the oxygen content of the material were performed using a combination of techniques, including TGA, *ex* and *in-situ* XRD, and the novel pressure relaxation technique discussed in Chapter 4. From this information, the interesting oxygen incorporation and release behaviour of the material are probed more deeply, before the thermodynamics of the material are directly compared to other oxygen carrier materials for reference.

I acknowledge that Michael Gaultious performed the XRD work shown in Figures 6.10 – 6.14, as part of collaboration with myself.

6.1 Introduction

The low temperature and reversible oxygen content of $\text{YBaCo}_4\text{O}_{7+\delta}$ make the material interesting for many applications ranging from catalytic oxidations to ion transport membranes [1-4]. This material was selected as an oxygen carrier of interest for oxygen enrichment processes due to its large and easily reversible oxygen capacity, accessible at low temperatures (approx. 400°C). A common figure in the literature of the material is a dynamic heating curve, where a sample is heated at a constant heating rate from room temperature to 500°C, typically at rates from 1-5°C/min. Most of the literature involving this material has such a figure [5-17], and from this data researchers often estimate the oxygen capacity. This is particularly evident when researchers use these dynamic heating ramps to quantify changes to the oxygen capacity of the material when doping or substitution of the cations is performed [18-21]. There are three major issues with using these literature experiments for examining material for oxygen enrichment processes. The first is that these processes are dynamic and hence vulnerable to kinetic limitations. Secondly, the data is often discussed as if it is thermodynamic, which is problematic. And finally, these experiments are normally performed at only two oxygen partial pressures: $p\text{O}_{2s}$ of 0.21 bar and 1 bar, and no data for 0.31 – 0.42 bar is collected because of practical limitations. However, as this is the $p\text{O}_2$ range of interest oxygen enrichment processes, thermodynamic data in this region is essential. In this work, a detailed study of the thermodynamics of the material for oxygen enrichment was performed to investigate this critical region. To begin, the current literature experiments, namely dynamic heating curves and isothermal oxygen incorporation experiments were performed in a $p\text{O}_2$

range of 0.05 – 0.42 bar to compare to the current literature, and to examine the effect that pO_2 has upon the oxygen incorporation/release behaviour of the material. With these preliminary studies performed, more detailed equilibria experiments were performed to examine the oxygen content as a function of temperature and pO_2 in the region from $pO_2 = 0.05$ bar to $pO_2 = 0.42$ bar. Changes to the crystal structure as a function of oxygen content and the effect this has upon the oxygen release behaviour of the material were examined. Finally, the thermodynamic properties of the material were examined to explain the complex oxygen release behaviour. Using this information, the amount of oxygen the material can produce per °C of a temperature swing, and how efficient the material is at removing oxygen from an oxidising stream, will be compared directly to other oxygen carriers.

6.2 Results

From the literature review, three important pieces of information are required for a detailed comparison of the material to others for oxygen enrichment processes are missing, namely:

- Useful thermodynamic data, namely the temperature of oxygen release and incorporation as a function of pO_2 , and the maximum oxygen content, in the pO_2 range of 0 – 0.42 bar, which is useful for many oxygen enrichment processes,
- The effect of δ on the crystal structure of the material, namely the δ at which the recorded phase transition from hexagonal to orthorhombic occurs [15], alongside information of how this transition affects the oxygen release of the material
- The effect of δ on the oxygen release of the material

This chapter presents the work done here to address these shortcomings and demonstrate the performance of $YBaCo_4O_{7+\delta}$ for oxygen cycling processes, compared to other oxygen carriers.

6.2.1 Oxygen release of $YBaCo_4O_{7+\delta}$

As a starting point to understand the oxygen incorporation and release of the material, dynamic heating ramps of $YBaCo_4O_{7+\delta}$ were performed from room temperature to 500°C in pO_2 s ranging from 0.05 to 0.42 bar, with a heating rate of 1°C/min, following the helium pre-treatment. The results of these dynamic heating ramps are shown in Figure 6.1.

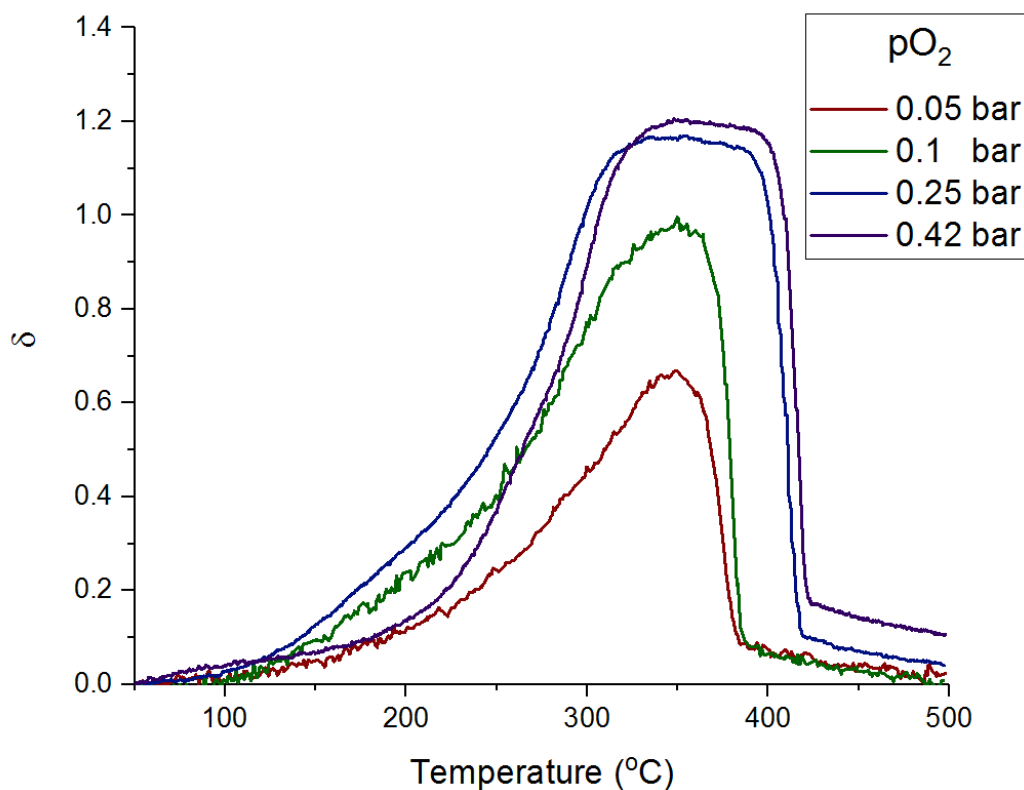


Figure 6.1 – Plot showing δ versus temperature of $\text{YBaCo}_4\text{O}_{7+\delta}$ heated between 50°C to 500°C , with a heating rate of $1^\circ\text{C}/\text{min}$, in $p\text{O}_2$ s between 0.05 and 0.42 bar with gas flow rates of 200. ml/min (S.T.P).

Small amounts of oxygen were slowly incorporated into the sample at temperatures below 100°C , in agreement with literature for pre-treated samples [21]. Further heating of the sample to between 100 and 300°C , increased the rate of oxygen incorporation. At 300°C for a $p\text{O}_2$ of 0.21 and 0.42 bar, the rate of oxygen incorporation decreased, until a maximum δ of 1.15 and 1.21 was reached at 310°C and 330°C respectively. Typically, literature values peak at approximately this temperature, and recorded δ 's in air are between 1.1 to 1.2 for a $p\text{O}_2$ of 0.21 bar. The curves for the change in δ during experiments at lower $p\text{O}_2$ s showed the sample continued to incorporate oxygen until 350°C , at which temperature the maximum δ recorded was 0.65 and 0.98 for a $p\text{O}_2$ of 0.05 and 0.1 bar, respectively. This is likely as the rate of oxygen incorporation is lower at these $p\text{O}_2$'s and the maximum oxygen content has not been achieved.

Importantly, the temperature of oxygen release increases with $p\text{O}_2$, clearly shown in Figure 6.1. The onset temperature of rapid oxygen loss (δ change $>0.02/^\circ\text{C}$) in a $p\text{O}_2$ of 0.42 bar was approximately 400°C . Reduction of the $p\text{O}_2$ was shown to decrease the temperature at which the oxygen was released, with the lowest $p\text{O}_2$, 0.05 bar, showing rapid oxygen loss occurring at 350°C . This onset of oxygen loss agrees with the literature for a $p\text{O}_2$ of 0.21 bar [22].

The oxygen loss of $\text{YBaCo}_4\text{O}_{7+\delta}$ occurs over significantly shorter temperature ranges than most non-stoichiometric materials, behaving more like the oxygen loss from transition metal oxides – although with a much smaller oxygen capacity. These characteristics have the potential to allow oxygen separation using smaller temperature swings than most non-stoichiometric materials, whilst operating at much lower temperatures than transition metal oxides.

The experiment shown in Figure 6.1, demonstrated that the $p\text{O}_2$ of the gas phase during the dynamic heating ramps had a significant impact on the temperature of oxygen loss from the sample. As the oxygen content increased with increased $p\text{O}_2$'s, it is necessary to determine whether the increasing temperature of oxygen loss was due to larger oxygen content in the material, a higher $p\text{O}_2$ in the gas phase, or a combination of the two.

To quantify the effect of δ on the temperature of the oxygen release, a controlled dynamic heating ramp was performed. A sample was annealed in air ($p\text{O}_2 = 0.25$ bar) at 320°C for between 30 and 120 minutes, to give the material a different starting δ . The material was then heated at a rate of 10°C per minute to 500°C in a $p\text{O}_2$ of 0.25 bar, and the results can be seen in Figure 6.2.

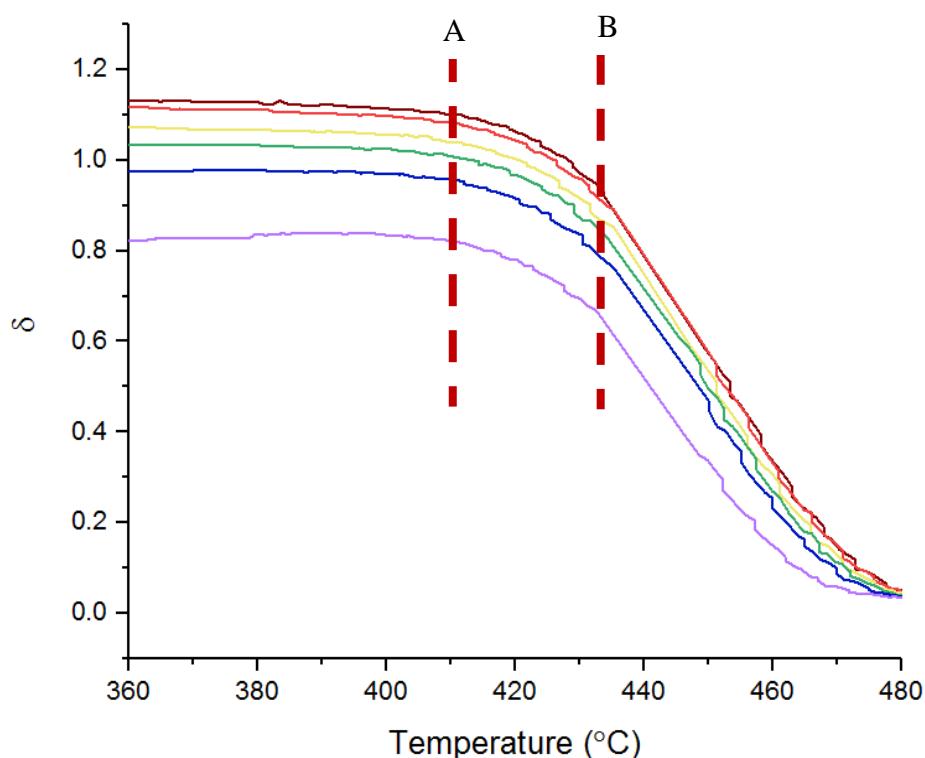


Figure 6.2 – Dynamic TG curves showing δ versus temperature for $\text{YBaCo}_4\text{O}_{7+\delta}$ when heated from 380°C to 500°C with a heating rate of $10^\circ\text{C}/\text{min}$ with various starting δ 's in a $p\text{O}_2$ of 0.25 bar with gas flow rates of 200. ml/min (S.T.P).

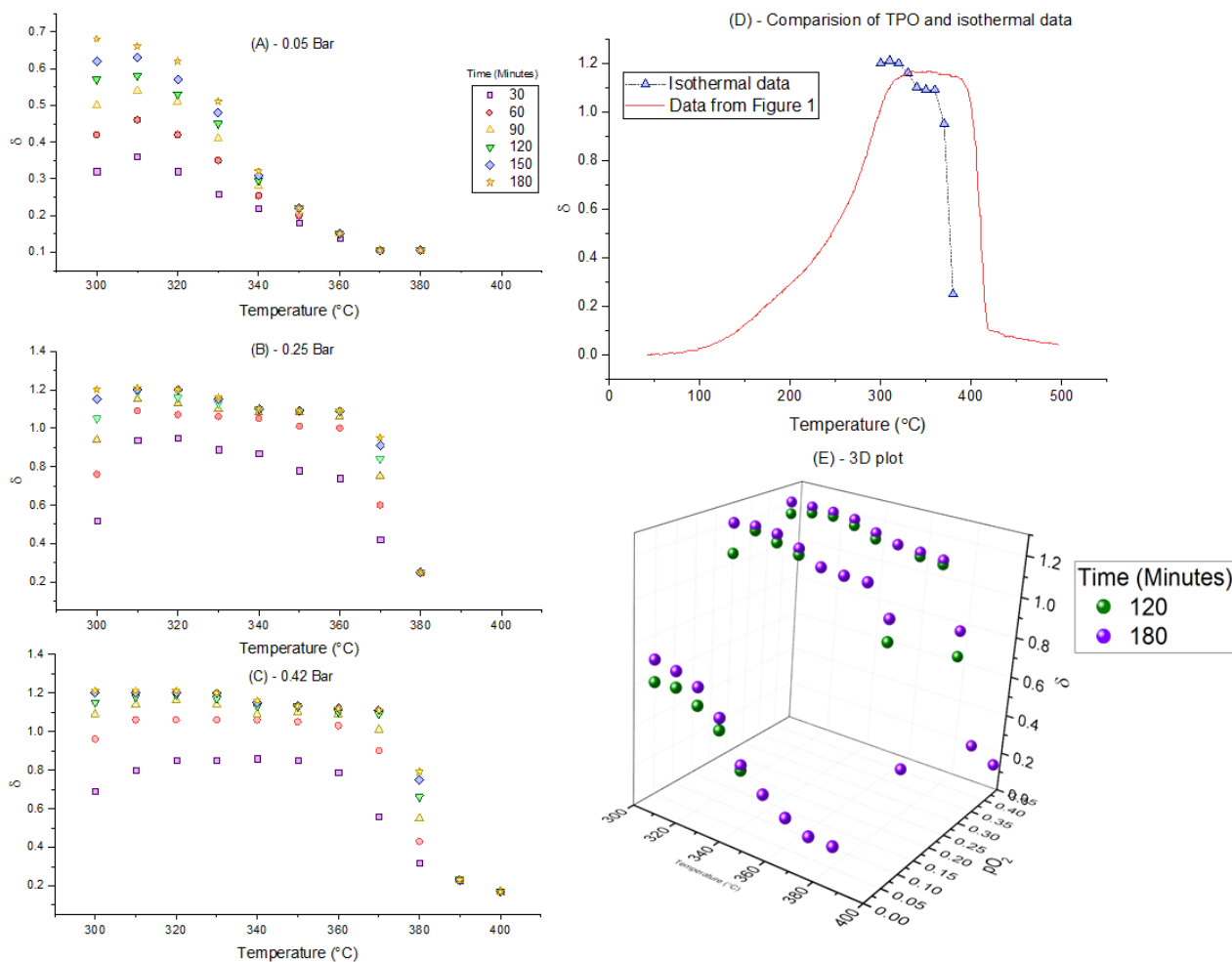
From Figure 6.2 it is clear the temperature of oxygen release from $\text{YBaCo}_4\text{O}_{7+\delta}$ remained independent of the starting δ s within the range of 1 – 1.2. Both the temperatures at which the

oxygen loss began (A), and the rate of oxygen loss was linear (B) had the same onset temperature, independent of starting non-stoichiometry. In Figure 6.1, the temperature of oxygen release for the TPOs performed at 0.25 and 0.42 bar differed by approximately 20°C, with a difference in non-stoichiometry of $\delta=0.1$. As the material incorporated oxygen of between 0.8 and 1.1 during the dynamic heating ramps shown in Figure 6.3, it is clear the main cause of the shifting temperature of oxygen release is the pO_2 of the gas environment, if $\delta>0.8$. This agrees with literature, where Lin et al [23] produced dynamic heating ramps of $YBaCo_4O_{7+\delta}$, where samples with different surface areas were heated between 50 and 500°C in a pO_2 of 0.21 bar. During the oxygen incorporation step of the experiments, the oxygen content differed by approximately 30% between the samples, but the temperature of oxygen loss remained the same.

In literature, the material was noted to undergo a phase change between hexagonal and orthorhombic structures at 350°C in a pO_2 of 1 bar. Further heating of the sample to 500°C caused the material to revert to the original hexagonal form [15], which is likely responsible for this oxygen release, with the stored oxygen secure in the orthorhombic phase, until the increased temperature causes the crystal structure to revert to the hexagonal phase.

6.2.2 Isothermal oxygen incorporation of $YBaCo_4O_{7+\delta}$

To investigate the impact of pO_2 and temperature on the oxygen capacity and rate of oxygen incorporation of $YBaCo_4O_{7+\delta}$, isothermal oxygen incorporation experiments were conducted. A helium pre-treated sample was left for 3 hours in a pO_2 of 0.05, 0.25 or 0.42 bar, at temperatures ranging from 300 to 430°C. Figure 6.3 shows the amount of oxygen incorporated versus temperature after different lengths of time for each pO_2 investigated.



Figures 6.3 – Plotted data points showing the amount of oxygen incorporated (δ) into a sample of YBaCo₄O_{7+ δ} after different lengths of time for samples held isothermally in a pO₂ of (A) 0.05 bar, (B) 0.25 bar, (C) 0.42 bar versus temperature, after the helium pre-treatment. Figure 6.3 (D) compares the δ achieved upon heating during the dynamic heating ramp in Figure 6.1 and isothermally in Figure 6.3, for a pO₂ of 0.21 bar (B) in a pO₂ of 0.25 bar after 180 minutes. The data points for the oxygen content of the material gained isothermally after 120 and 180 minutes are rendered onto a 3-d graph in Figure 6.3 (E)

At a pO₂ of 0.05 bar, the highest oxygen incorporation rates occurred at 300°C, with increasing temperatures reducing the rate of oxygen incorporated. Negligible oxygen for redox cycling processes ($\delta < 0.2$) was incorporated at temperatures above 350°C at this pO₂. An increase in the pO₂ to 0.25 bar increased the temperature at which there was negligible oxygen incorporation to 370°C. Further increase of the pO₂ to 0.42 bar increased the temperature of negligible oxygen incorporation to 390°C.

For all pO₂s investigated, oxygen incorporation rates were seen to decrease with increased temperatures. The magnitude of this decrease was reduced at higher pO₂s. Heating a sample in a pO₂ of 0.05 bar by as little as 20°C above the optimum temperature range for oxygen incorporation (300 to 320°C) halved the amount of oxygen gained over the experiment, while in a pO₂ of 0.25 bar, the amount of oxygen incorporated decreased by less than 10% over the

same 20°C range. The recorded decrease in the affinity of the material to incorporate oxygen with temperature increases at a pO_2 of 0.21 bar, agrees with the literature [24], however, no data at a pO_2 of 0.42 or 0.05 bar could be found for comparison.

Oxygen incorporation with this material has been shown in the literature to have the potential for both oxygen removal and oxygen enrichment processes [25-26]. Typically, oxygen incorporation for enrichment processes would occur in a higher pO_2 range (e.g. 0.21bar for air) as opposed to oxygen removal processes, such as the cleaning of oxygen from methane from coal mines (e.g. gob gases), which will occur at a $pO_2 < 0.05$ bar. It is therefore important to note that for lower pO_2 applications, a temperature of approximately 300°C is desirable. For higher pO_2 s the temperature of incorporation can be increased, potentially decreasing the required temperature swing to regenerate the material, at the expense of lowering the efficiency of the use of the oxidising gas.

When the data presented in Figures 6.1 and 6.3 (B) are compared as shown in Figure 6.3(D), the temperature at which oxygen is released from the material in Figure 6.1, is significantly higher than the temperature at which little oxygen ($\delta < 0.2$) is incorporated in Figure 6.3(B). This is particularly evident when comparing the δ 's at 400°C in a pO_2 of 0.42 bar in both figures. This behaviour suggests a hysteresis of the oxygen content, where if the oxygen is incorporated in the material at lower temperatures, it can remain stored in the material upon heating to a higher temperature, where it would not have been incorporated.

To demonstrate the repeatability of this oxygen incorporation behaviour, a sample was cooled in a pO_2 of 0.21 bar from 430 to 280°C in 10°C increments (dwelling for four hours at each increment) and the weight change recorded, and the results can be seen in Figure 6.4.

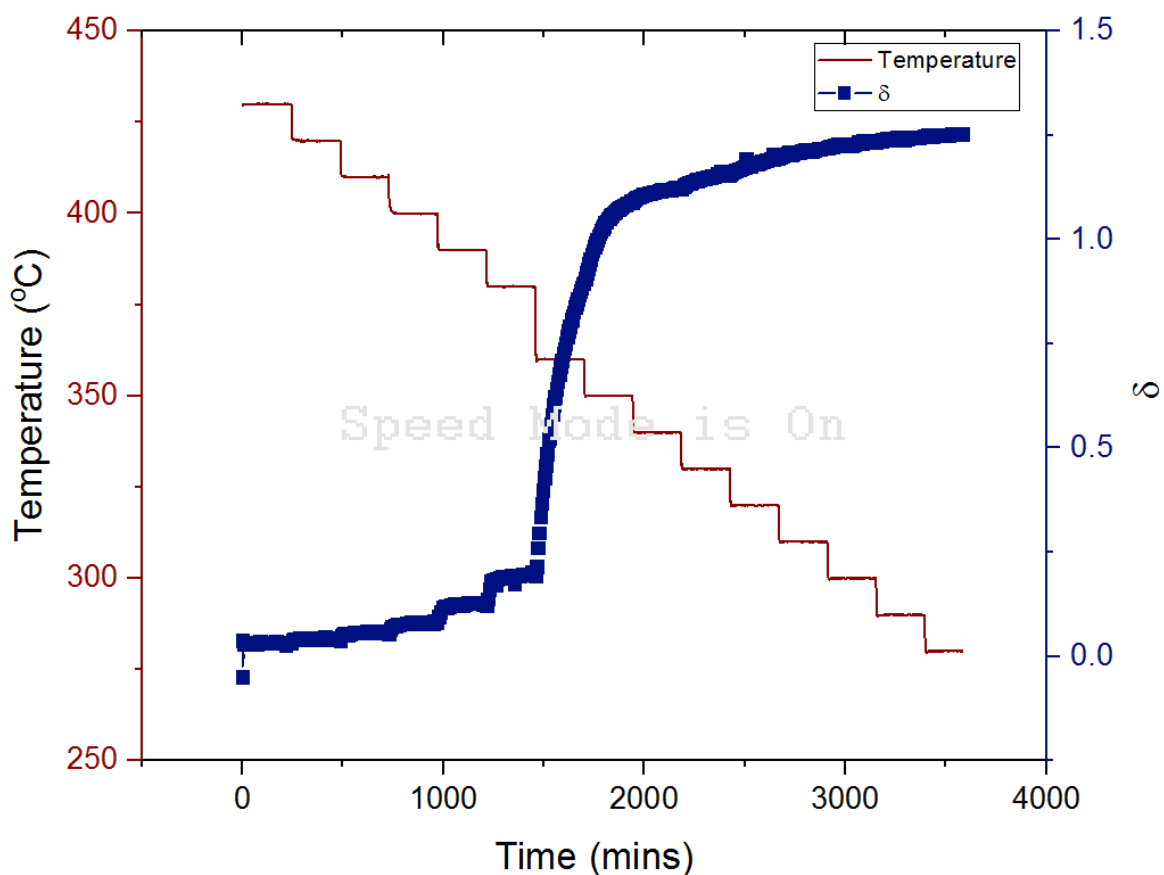
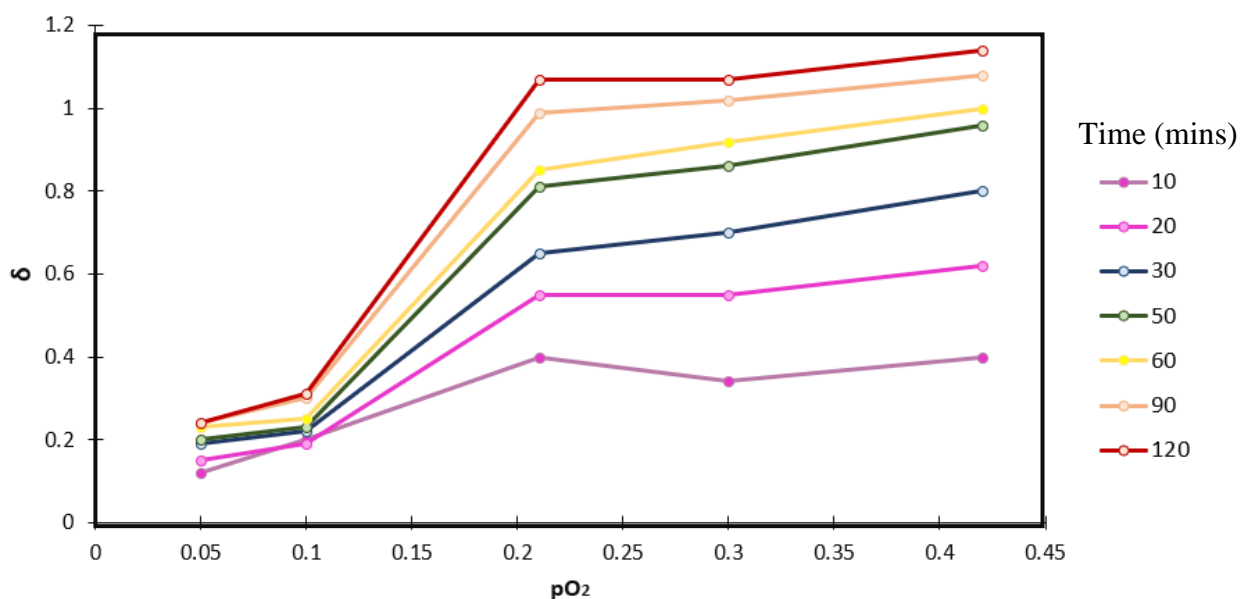


Figure 6.4 – A plot of δ versus time for a sample of YBaCo_4O_7 cooled stepwise between 430 and 280°C in four hour long, 10 °C increments in a $p\text{O}_2$ of 0.25 bar.

Figure 6.4 shows the oxygen content of the material quickly equilibrated at higher temperatures, with the weight of the material remaining stable within 10 minutes at temperatures of 380°C or higher. At 360°C the material did not stabilize, and a slow, but constant weight gain was recorded during the four-hour hold. During this step, a much greater amount of oxygen was incorporated into the sample, in agreement with the data shown in Figure 6.3(B).

As the experiments shown in Figures 6.3 were conducted with different fresh samples, to appropriately compare the effect of $p\text{O}_2$ on the rate of oxygen incorporation at a given temperature, another set of isothermal oxygen incorporation experiments at different $p\text{O}_2$'s were conducted to remove any effects of particle morphology on the oxygen incorporation, so that rates between $p\text{O}_2$'s could fairly be compared. The sample was held at 340°C for 2 hours at $p\text{O}_2$'s ranging from 0.05 to 0.42 bar after a helium pre-treatment, with the data presented in Figure 6.6. Once an isotherm at a given $p\text{O}_2$ was completed, the material underwent the helium pre-treatment, and was cooled in helium to 340°C, after which the gas was switched to

the next pO_2 . The marked points on Figure 6.5, show the δ obtained at that pO_2 after the duration noted in the legend in each isotherm, at each pO_2 , and should be read vertically.



Figures 6.5 – Plotted data points showing the amount of oxygen incorporated (δ) into a sample of $YBaCo_4O_7$ after different lengths of time for samples held isothermally in a gas flow rate of 200 ml/min at a temperature of 340°C, with the pO_2 changing between 0.05 and 0.42 bar.

Figure 6.5 shows similar rates of oxygen incorporation at pO_2 s between 0.21 and 0.42 bar, with an increase in the rate of oxygen incorporation of approximately 10% at a pO_2 of 0.42 bar compared to 0.21 bar. As expected, pO_2 s lower than 0.21 bar incorporated relatively small amounts of oxygen when compared to 0.21 bar, with the two-hour isotherm at a pO_2 of 0.1 bar only incorporating 30% of the oxygen capacity of 0.21 bar. It is clear therefore that for favourable oxygen incorporation, the pO_2 should be kept above 0.21 bar.

To examine how the pO_2 affects the temperature at which significant oxygen incorporation occurs, a sample was heated to 500°C in helium for four hours, before being cooled to 430°C. The gas environment was then switched from helium to an oxygen-containing environment of a pO_2 between 0.05 and 0.42 bar. The temperature of the sample was then reduced in 5°C steps from 430 to 300 °C, with each 5°C-increment lasting 1 hour. The results of this experiment can be seen in Figure 6.6

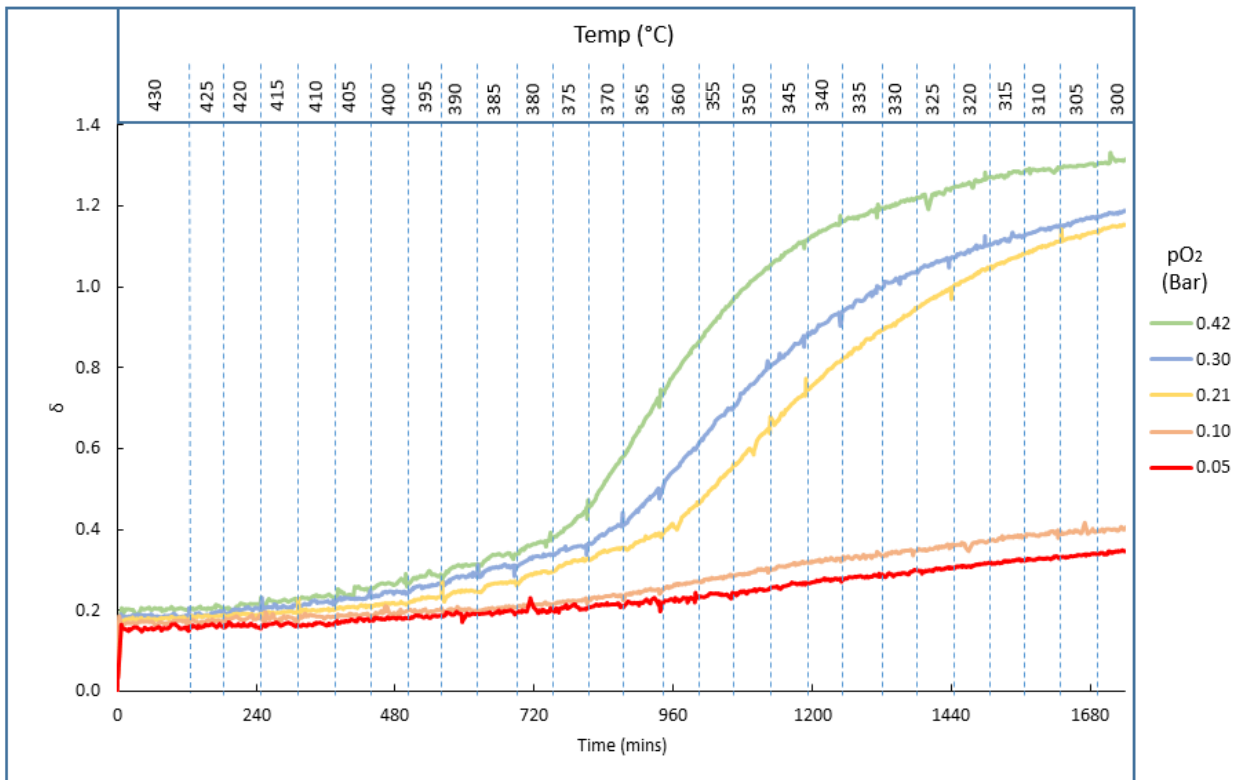


Figure 6.6 – Stepwise cooling curve showing δ of $\text{YBaCo}_4\text{O}_{7+\delta}$ after being held at 430°C under He for four hours, followed by stepwise cooling in hour-long 5°C steps to 300°C in pO_2 of between 0.05 and 0.42 bar.

Figure 6.6 shows that at 430°C , when the gas environment is switched from inert to an oxygen-containing environment, the material rapidly incorporates oxygen, with a δ of between 0.16 and 0.21 achieved for a pO_2 of 0.05 and 0.42 bar respectively. Upon cooling, there was a gradual increase in the oxygen capacity of the material for all pO_2 s, with the oxygen content of the samples at higher pO_2 s increasing at a faster rate. At a threshold temperature, the amount of oxygen incorporated increased significantly. This threshold temperature was seen to increase with increasing pO_2 s, and it appears that shifting the pO_2 by 0.1bar, in the pO_2 range of 0.21 to 0.42 bar, causes a change in the temperature of oxygen incorporation by 10°C .

6.2.3 Stepwise heating and cooling of $\text{YBaCo}_4\text{O}_{7+\delta}$

To examine the differences in the oxygen capacities measured in Figure 6.1 (dynamic heating) and Figure 6.3 (isothermal incorporation), a sample of $\text{YBaCo}_4\text{O}_{7+\delta}$ was cooled and heated in a stepwise manner in a $p\text{O}_2$ of 0.25 bar between 300°C and 430°C in 5°C steps. For the heating curve (Figure 6.7 (a), the material was held for 10 hours at 300°C before being heated in 5 °C steps where the material dwelled isothermally for one hour at each step. For the cooling curves (Figure 6.7 (b)) the material was held for four hours at 430°C before being cooled in 5°C steps where the material was held isothermally for one hour.

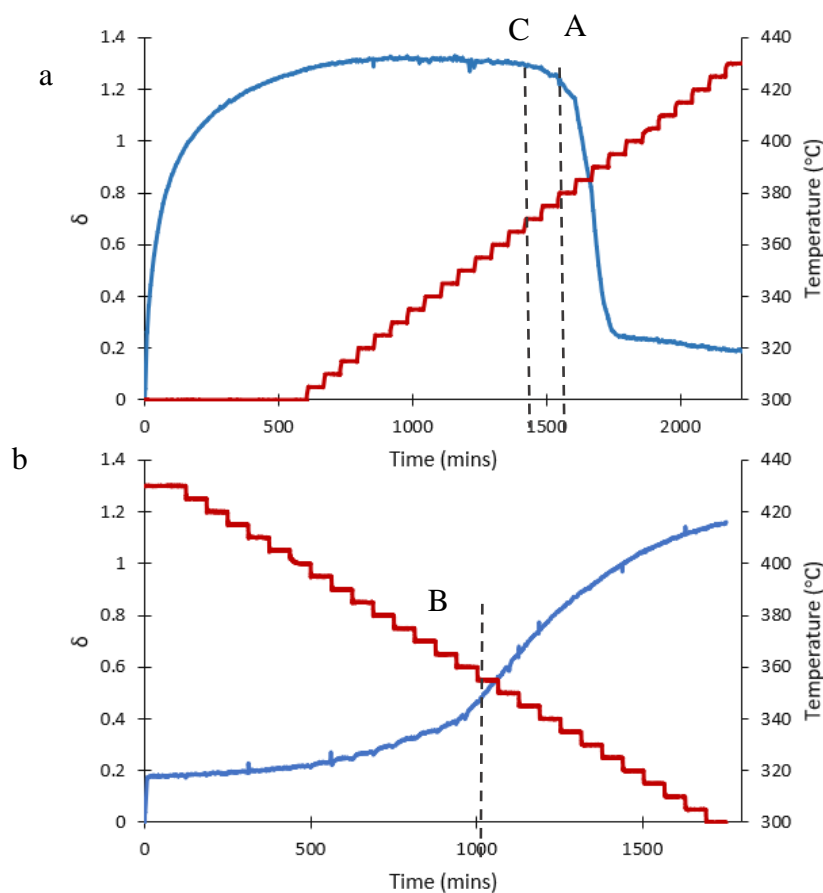


Figure 6.7 (a) - Stepwise heating curve showing δ of YBaCo_4O_7 after being held at 300°C for ten hours in a $p\text{O}_2$ of 0.21 bar, before being heated in hour long 5°C steps to 430°C at the same $p\text{O}_2$. **(b)** Stepwise cooling curve showing δ of $\text{YBaCo}_4\text{O}_{7+\delta}$ after being held at 430°C in a $p\text{O}_2$ of 0.25 bar for two hours before being cooled in hour long 5°C steps to 300°C at the same $p\text{O}_2$. The red line shows the change in temperature, while the blue line shows the change in δ . The marked lines A, B and C display areas of interest discussed in the text.

Figure 6.7 (a) shows that oxygen is stored in the material upon heating until 380°C, (marked line A) at which point the oxygen begins to be released from the material. The temperature at which oxygen begins to be readily incorporated upon cooling, shown by marked line B in Figure 6.7 (b), is approximately 370°C, in agreement with the data shown in Figure 6.4 for a

pO_2 of 0.25 bar. Oxygen incorporation does occur at higher temperatures; however, this is small stepwise increases and not the significant gain seen at 365°C. It appears that the temperature of oxygen incorporation and release differ by approximately 15°C, and this is seen when examining the data at 365°C upon heating, (shown by line C), where the weight change is stable.

To clarify the oxygen incorporation and release behaviour seen previously, an equilibria plot of the material upon heating and cooling was needed. A sample was pre-reduced in helium at 500°C before being cooled in helium to either 200 or 430°C. The gas environment was switched from helium to either a pO_2 of 0.25 or 0.42 bar. The sample cooled to 200°C was held at this temperature until the mass was stable before undergoing stepwise heating to 430°C, allowing the sample to dwell until stable at each of the marked points. Likewise, the sample cooled to 430°C was cooled stepwise until 200°C, holding until stable at each of the marked points. The results of this equilibria plot can be seen in Figure 6.8. It should be noted that these points may not be at true equilibrium, and if left long enough, the samples oxygen content may change. For this plot, equilibrium is defined as no notable mass change ($\delta=0.01$) over 2 hours.

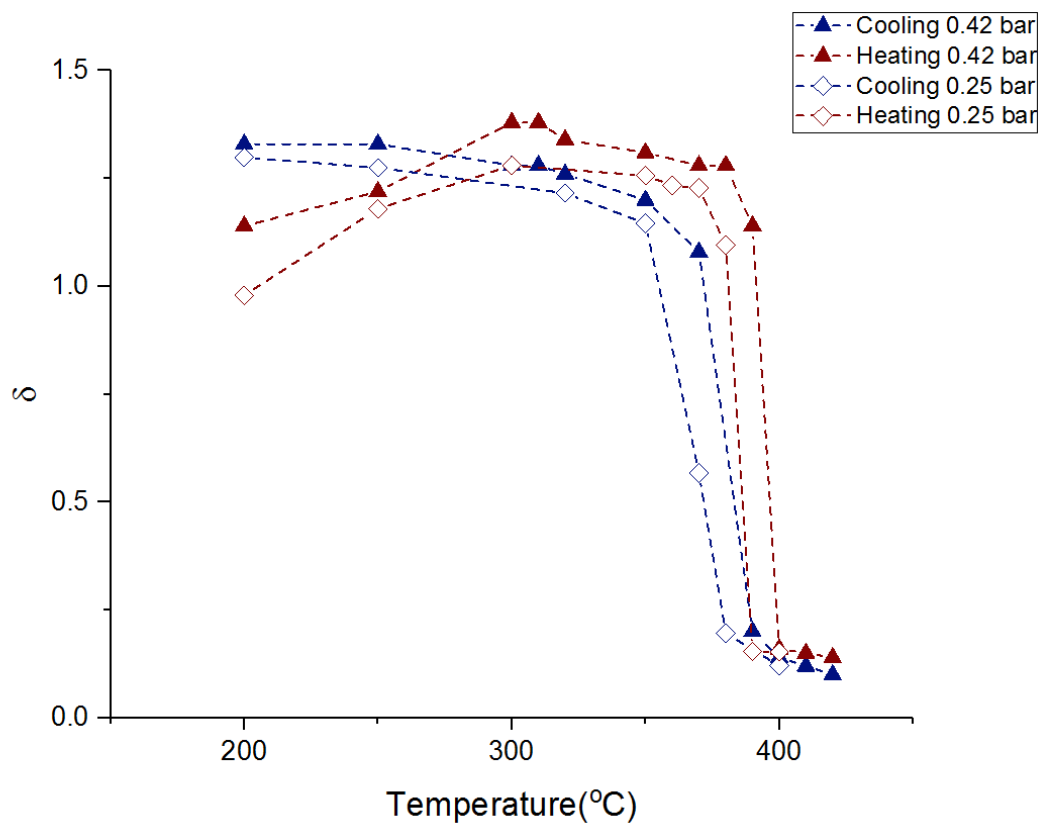


Figure 6.8 - Hysteresis equilibria plot of $YBaCo_4O_{7+\delta}$ in a pO_2 of 0.42 and 0.25 bar upon different directions of heating and cooling.

Figure 6.8 shows a significant difference in the oxygen content of the sample, depending upon whether the sample was heated or cooled. This is evident when comparing the oxygen content of the material at a pO_2 of 0.42 bar at 390°C, where the heated sample was shown to incorporate a significant amount of oxygen ($\delta=1.14$), while during cooling at this temperature the material incorporated little oxygen ($\delta=0.18$). This behaviour extends to a pO_2 of 0.25 bar, seen clearly at 380°C, where a δ equal to 1.10 and 0.20 was achieved upon heating and cooling respectively, again agreeing with the results shown in Figures 6.2 and 6.4.

Figure 6.8 shows a difference of approximately 20°C between the temperature oxygen is released upon heating or incorporated upon cooling for both pO_2 s, slightly larger than that seen in Figures 6.7, however, this is likely due to a step size of 10°C here, as opposed to 5°C in Figure 6.7. Additionally, it can be shown that changing the pO_2 from 0.25 to 0.42 bar, increased the oxygen incorporation release and incorporation temperature by 10°C.

This behaviour of the material suggests that for an oxygen looping process, such as oxy-fuel combustion, a 30°C cycle is possible, with oxygen incorporation occurring at 370°C in a pO_2 of 0.25 bar, and release occurring at 400°C to enrich a pO_2 of at least 0.3 bar, required for oxy-fuel combustion. These 30°C cycles would give a change in δ of over 0.8, approximately 2% by weight.

6.2.4 Equilibria plot of $YBaCo_4O_{7+\delta}$

One of the most important factors for a non-stoichiometric material for oxygen enrichment processes is the efficiency of oxygen removal from an oxidising stream. Low efficiency of oxygen use will require more oxygen to be added during the oxidation step in a process. This extra gas will require to be heated and pumped through the system, increasing costs, so an ideal material will remove almost all the oxygen, to reduce the amount of hot gas needed for the process.

To quantify the amount of oxygen that can be removed from a gas stream, a δ versus pO_2 plot was created using the pressure relaxation rig described in Chapter 5. A sample of $YBaCo_4O_{7+\delta}$ was heated to 500°C and reduced under vacuum in pure oxygen to a pO_2 of 0.001 bar for one hour. For each experiment, this point was assumed to be a $\delta = 0$, as this step mimicked the inert pre-treatment used for each TGA treatment. In Figure 6.1, $\delta = < 0.01$ at 500°C at a pO_2 of 0.05 bar, so assuming a negligible δ in the sample after a longer reduction at 500°C and a lower pO_2 is reasonable. The sample was then cooled to the starting temperature of either 320°C, 350°C or 380°C. The pO_2 of the gas phase was then increased in stages, and the sample was allowed to equilibrate to the new reactor pO_2 . A mole balance was then carried out over the reactor and reservoir, converting the pressure change to a change in the moles of

oxygen, and the difference in the number of moles of oxygen before and after the pressure change was assumed to be due to oxygen incorporation of the sample. The results of this experiment can be seen in Figure 6.9. It should be noted that these points may not be at true equilibrium, and if left long enough, the sample's oxygen content may change. For this plot, equilibrium is defined as no notable mass change ($\delta=0.01$) over 30 minutes. The author recognizes there may be errors in the values reported here from the issues with the technique described in chapter 5 – however, the data matched well with the previous TGA results and in this work will be treated as true.

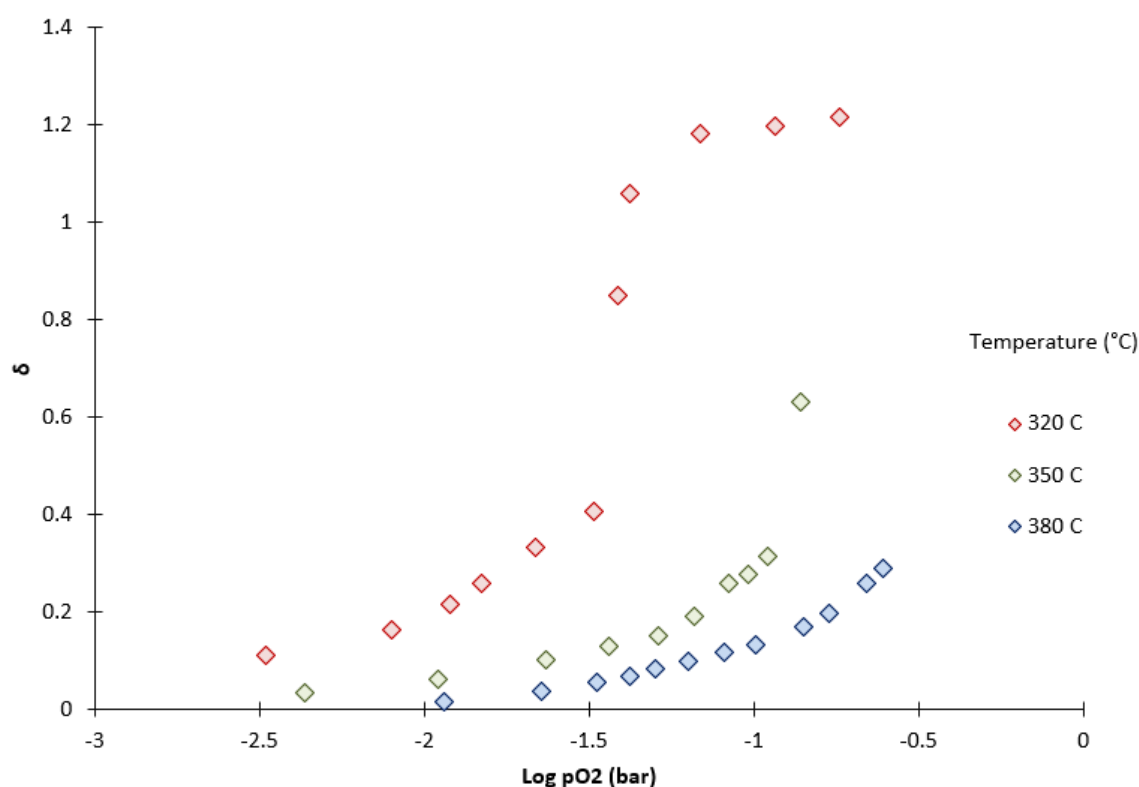


Figure 6.9—Equilibria plot showing δ versus $\log pO_2$ for $YBaCo_4O_{7+\delta}$ equilibrated at 320, 350, and 380°C.

At 320°C, the δ of the material increases slowly with increasing pO_2 , with a δ of less than 0.1 achieved below a pO_2 of approximately 0.02 bar ($\log pO_2 = -1.69$). Above 0.02 bar, the amount of oxygen incorporated significantly increases, with a linear increase of δ until a value of 0.4 is achieved at a pO_2 of 0.035 bar ($\log pO_2 = -1.46$). Further increases of the pO_2 caused a step in the oxygen content, with an increase in δ to approximately 1.02 at 0.042 bar ($\log pO_2 = -1.38$). The amount of oxygen incorporated further increases with pO_2 until a $\delta = 1.12$ was achieved at a pO_2 of 0.19 bar ($\log pO_2 = -0.7$).

This behaviour was seen at all temperatures investigated, however, the pO_2 at which the step-in oxygen content of the sample was noted increases with increased temperature. This is evident comparing a $\delta = 0.4$, which occurs at $\log pO_2$ of -1.4 at 320°C, and -0.9 at 350°C, a

difference in pO_2 of approximately 0.07 bar. This required increase in pO_2 agrees with the relationship between temperature and pO_2 shown in Figure 6.8, and Ref [28] showed similar results, however, the experiments were only conducted between $\delta=0$ and 0.3. From the data it appears that small temperature swings can be used to cycle oxygen from low to higher pO_2 s, however, this may not make efficient use of the oxidising stream.

This stepwise behaviour in the oxygen content would be familiar with a phase change occurring. A good example of this behaviour in literature can be found in $YBaMn_2O_{5+\delta}$, where both the $YBaMn_2O_{6.5}$ and $YBaMn_2O_6$ phases had oxygen non-stoichiometry. The materials underwent a gradual increase in oxygen content with pO_2 before a more sudden step in δ was seen [29-31]. The authors attributed this stepwise behaviour to the existence of two thermodynamically stable phases at the transition pO_2 range. They believed that a structural transformation of the material was occurring, and an activation barrier was preventing the phase transition. Similar behaviour is likely occurring in the $YBaCo_4O_{7+\delta}$ system, between the hexagonal and orthorhombic phases, and structural investigations will be performed to confirm this transition is at $\delta=0.4$.

6.2.5 *In-situ* XRD study of $YBaCo_4O_{7+\delta}$

To quantify the effect of the change of pO_2 on the crystal structure a base line thermal expansion co-efficient was required so that the chemical and temperature changes could be separated. This co-efficient was obtained by heating the material to 500°C in nitrogen to bring the material to a reference δ of 0, before the material was cooled in 50°C steps in nitrogen. The cell volume and the changes to the A and C lengths were then calculated using a Rietveld refinement, and the results can be seen in Figure 6.10. The material was seen to maintain a hexagonal structure, so the length of the A axis is equal to the length of the B axis. The equation for the linear fit of the thermal expansion can be seen in Figure 6.10.

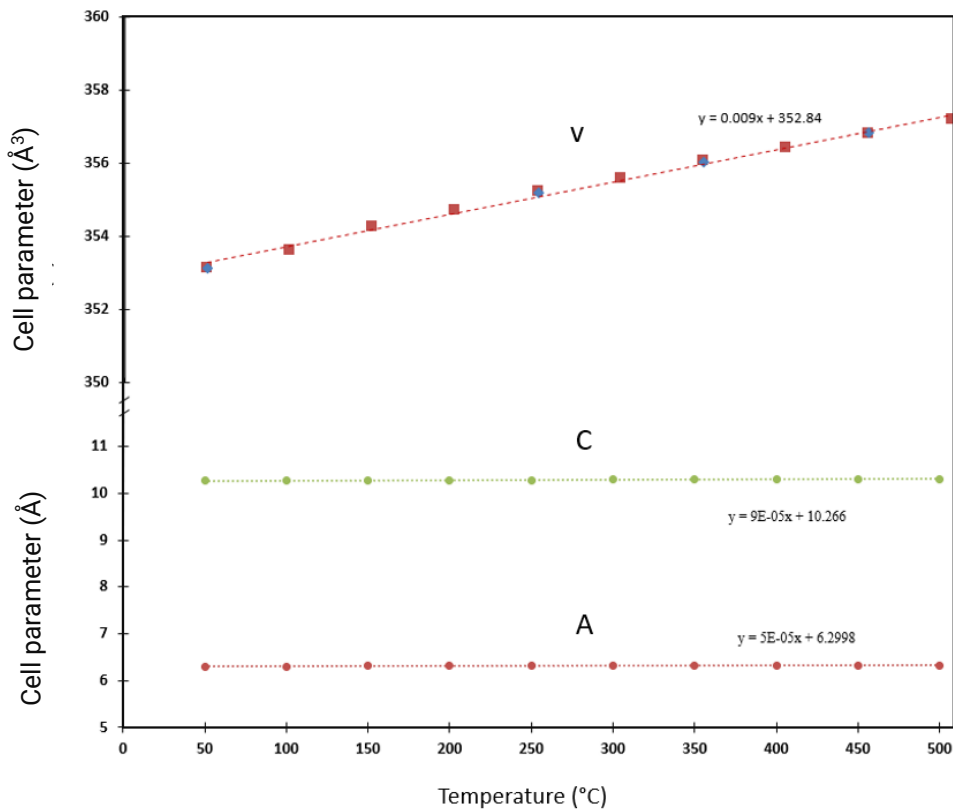
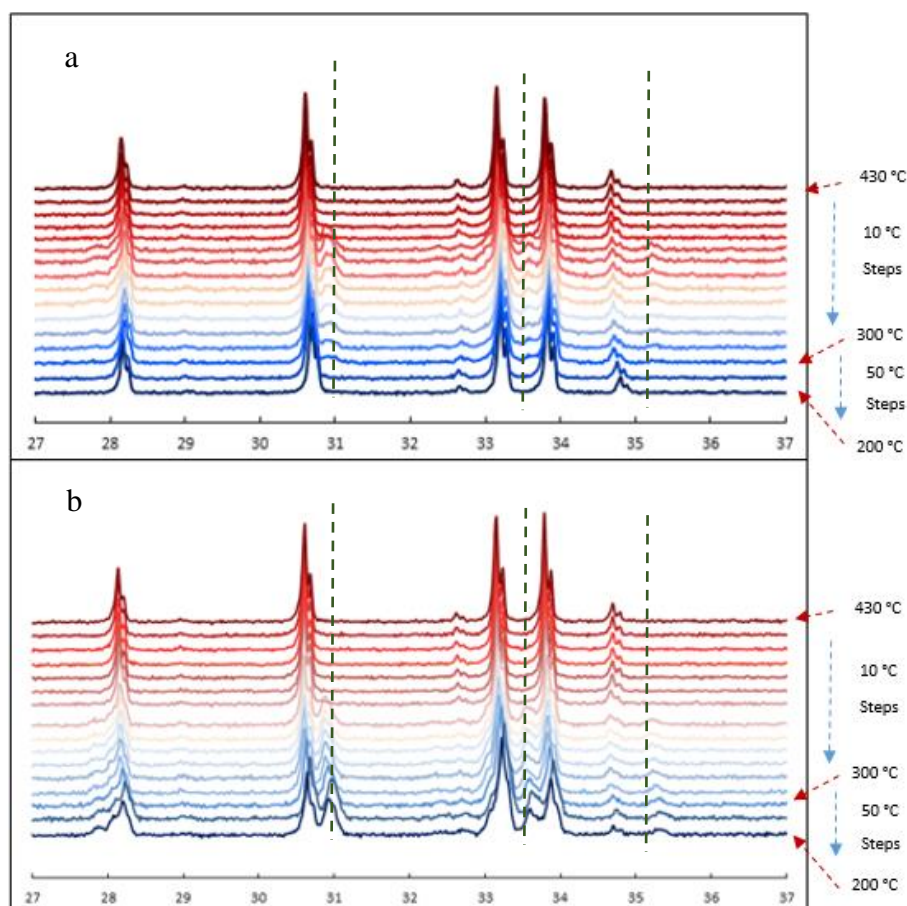


Figure 6.10 – Scatter plot showing the change in cell parameters of $\text{YBaCo}_4\text{O}_{7+\delta}$ versus temperature, used to calculate the thermal expansion co-efficient

It can be seen that a linear increase of the cell dimensions of the hexagonal phase can be seen. To investigate the differences in heating and cooling as shown in Figure 6.8, *in-situ* XRD scans were performed on the material in $p\text{O}_2$ s ranging from 0.05 to 1 bar. The material was heated to 500°C in N_2 before being cooled to either 430°C or 200°C in N_2 . The material was then scanned over an hour at each temperature. Previous 20-minute scans had shown no noticeable changes in structure when performed over 4 hours, leading to the longer scan times used. The sample was then cooled or heated in hour-long steps at the recorded temperatures in each $p\text{O}_2$.

Figure 6.11 shows the first of these results with heating and cooling XRD plots, shown between 27 and 37° in a $p\text{O}_2$ of 1 bar.



20

Figure 6.11 – XRD waterfall plot of YBaCo₄O₇ upon (a) heating and (b) cooling between 430 and 200°C with a rest of two hour at each recorded temperature at a pO₂ of 1 bar with flow rated of 150 ml/min (S.T.P.) The green line marks the peaks of the orthorhombic phase growing in

During both heating and cooling of the sample in a pO₂ of 1 bar a new orthorhombic phase is detected. Over time, the hexagonal phase of YBaCo₄O_{7+δ} shown at the beginning of each experiment is converted to a mixed orthorhombic and hexagonal phase upon heating and cooling. During heating from 200°C, shown in Figure 6.11 (a), the growth of the orthorhombic phase is noted at 300°C, with new peaks forming at approximately 31°, 33.7° and 36.3°, and the relative intensity of the original hexagonal peaks decreasing. This new phase continues to grow with heating until 390°C, after which the orthorhombic phase rapidly decomposes, returning the sample to the original hexagonal phase.

A similar experiment performed by Karpinen [15], took *in-situ* XRD scans during heating of YBaCo₄O_{7+δ} in a pO₂ of 1 bar, performing 3-minute scans every 50°C and a phase transition from hexagonal to orthorhombic was detected. The temperature of the growth of the orthorhombic phase, however, was noted at 350°C in Karpinen's study, while the data in this study shows the transition at 300°C. The difference is likely due to the time durations being too small in the previous literature. The experiment conducted here allowed the sample

to dwell for four hours at this temperature in the pO_2 and the slow growth of the new phase was therefore detected at a lower temperature. Unfortunately, while many XRD studies have been performed on the material, most focus on lower than room temperature [31-33] due to the interest of the material for superconducting applications.

The changes seen in Figure 6.11 are quantified in Figure 6.12, showing the percentage of $YBaCo_4O_{7+\delta}$ in the orthorhombic ($Pbc2_1$) and hexagonal ($P63mc$) structure as a function of temperature, and whether the sample was heated or cooled.

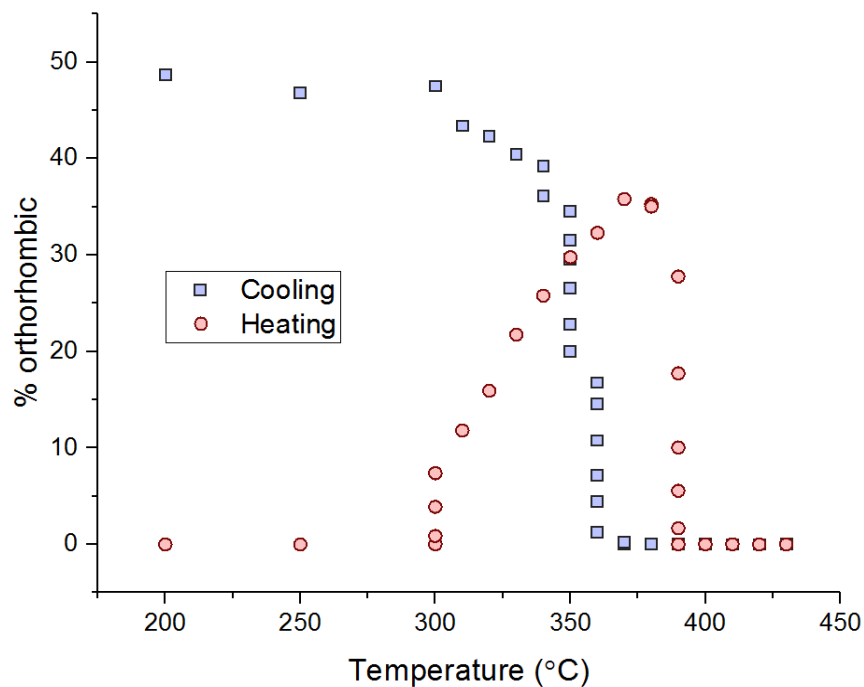


Figure 6.12 – Scatterplot showing the weight percentage of $YBaCo_4O_7$ in the hexagonal or orthorhombic phase in a pO_2 of 1 bar upon heating and cooling.

At temperatures greater than $400^\circ C$, no detectable traces of the orthorhombic phase exist. When the sample was heated from $200^\circ C$ the material began to transition to a mixed orthorhombic/hexagonal phase at $300^\circ C$ from the purely hexagonal phase seen at lower temperatures. Further heating of the sample increased the conversion of the material to the orthorhombic phase where a maximum value of 35% of the material in the orthorhombic phase was reached at $370^\circ C$. The material maintained this percentage in the orthorhombic phase for a further $10^\circ C$, after which the material began reverting to the fully hexagonal phase at $390^\circ C$. While the data from Figure 6.12 does not appear to be in equilibria, it clearly shows the hysteresis behaviour with different temperatures of growth and dissolution of the orthorhombic phase. The sudden dissolution and growth of the orthorhombic phase support the theory that the sudden changes in oxygen capacity of the material with pO_2 are due to a phase change. The changes in cell dimension from the experiment performed in Figure 6.12

were calculated and are the data from the cooling run presented in Figure 6.13. It is worth noting that the graph is best read from right to left, when comparing with changes in Figure 6.12.

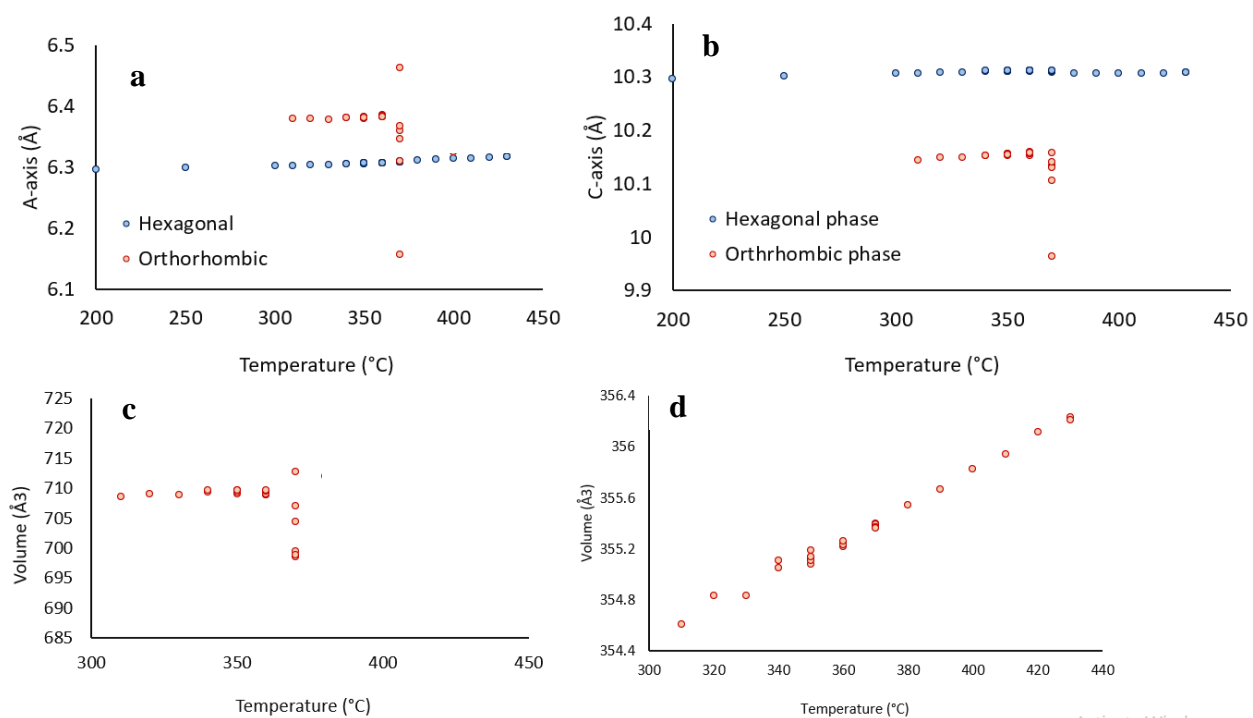


Figure 6.13 – Crystal expansion upon oxygen incorporation in a pO_2 of 1 bar with flow rate of 150 ml/min. Figures 6.13(a -b) show the c and a axis changes for both the hexagonal and orthorhombic phases. Figures 6.14 (c) show the volume change of the orthorhombic. and (d) the hexagonal cell upon cooling

It is clear from these Figures, that little change is occurring in the hexagonal phase throughout the oxygen incorporation, and the significant changes are happening in the orthorhombic phase. When the orthorhombic phase begins to grow at 360°C, there are significant changes in the cell volume and the C and A axis in the cell, which agrees with the literature [34]. However, once this initial growth occurs, the volume and axis length appear relatively steady in comparison. This does however warrant more investigation. It is also important to note the significant change in cell volume between the orthorhombic and hexagonal phases.

A further experiment was conducted to do this. Here, a sample of $YBaCo_4O_7$ was heated to cooled to 310°C, where it was allowed to rest for approximately 6 hours in a pO_2 of 0.21 bar. The advantage of this experiment was that oxygen incorporation was isothermal, so thermal expansion was not a concern. The changes in the crystal structure are presented in Figure 6.14

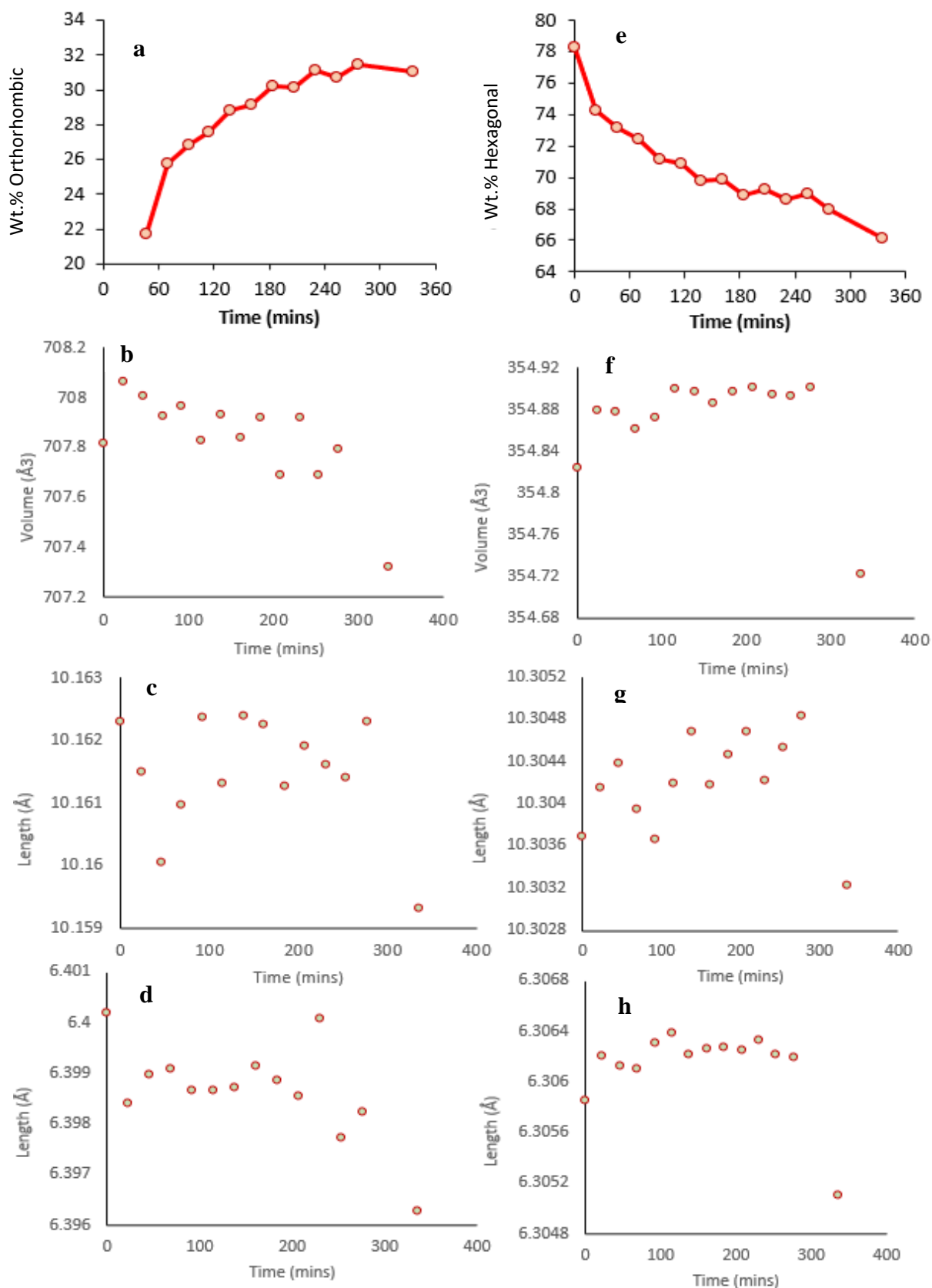


Figure 6.14 – Crystal expansion upon oxygen incorporation in a pO_2 of 0.21 bar with flow rated of 150 ml/min. Figures (a-d) show the orthorhombic changes, and (e-f) the hexagonal. The a and e, b and f, c and g and d and h show the phase wt.%, cell volume, c-axis length, and the a-axis length respectively

It is seen clearly, that during the oxygen incorporation, there is little change in the hexagonal structures, most likely due to the oxygen incorporating into orthorhombic sites. It is seen that

upon oxygen incorporation, the cell volume decreases in the orthorhombic phase, which is to be expected, as larger oxygen contents, generally reduce cell volume due to the internal attractions. Significant distortion to the cell during this transition can be seen, as the hexagonal cell is approximately half the volume of the orthorhombic, which will likely cause significant strain on the crystals.

To show the relationship between the growth and dissolution of the orthorhombic phase and the pO_2 , the temperature at which the phase change began to grow upon cooling or disappear at upon heating was plotted and this information is displayed in Figure 6.15.

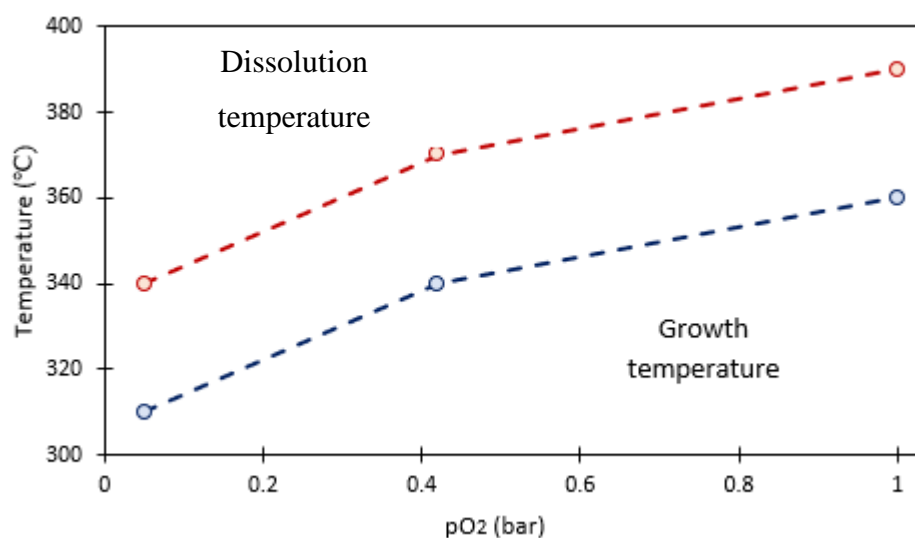


Figure 6.15 – Scatterplot showing temperature at which a sample of $YBaCo_4O_7$ lost its orthorhombic phase upon heating (red) or grew it upon cooling (blue). A strong correlation between the growth and dissolution of the orthorhombic phase as a function of pO_2 was found, with a notable shift in the temperature of growth and dissolution of $30^\circ C$, between 0.05 and 1 bar

There is a strong correlation between the temperatures of growth and dissolution of the orthorhombic phase as a function of pO_2 in the *in-situ* XRD data, with a consistent shift of approximately $30^\circ C$ in the temperature of growth and dissolution between 0.05 to 1 bar. This result also shows that a difference in pO_2 of 0.95 bar shifts the temperature of the growth and dissolution of the orthorhombic phase by approximately $40^\circ C$. This is slightly larger than that seen in Figure 6.8, however, this is likely as this is not an equilibrium experiment, but rather kinetically limited.

6.2.6 *Ex-situ* XRD study of $YBaCo_4O_{7+\delta}$

To determine the relationship between the growth of the orthorhombic phase and the value of δ in $YBaCo_4O_{7+\delta}$, 200 mg samples of $YBaCo_4O_7$ were reduced at $500^\circ C$ in helium and cooled in a helium environment, before being annealed for durations ranging from 30 to 720 minutes

in air. The ratio of orthorhombic to hexagonal phases was then determined by XRD analysis for each sample, and the degree of non-stoichiometry of each sample was found by heating the sample to 500°C in helium to create a reference state of $\delta=0$ using the TGA. Figure 6.16 shows the percentage of the material in the orthorhombic phase, versus the non-stoichiometry calculated.

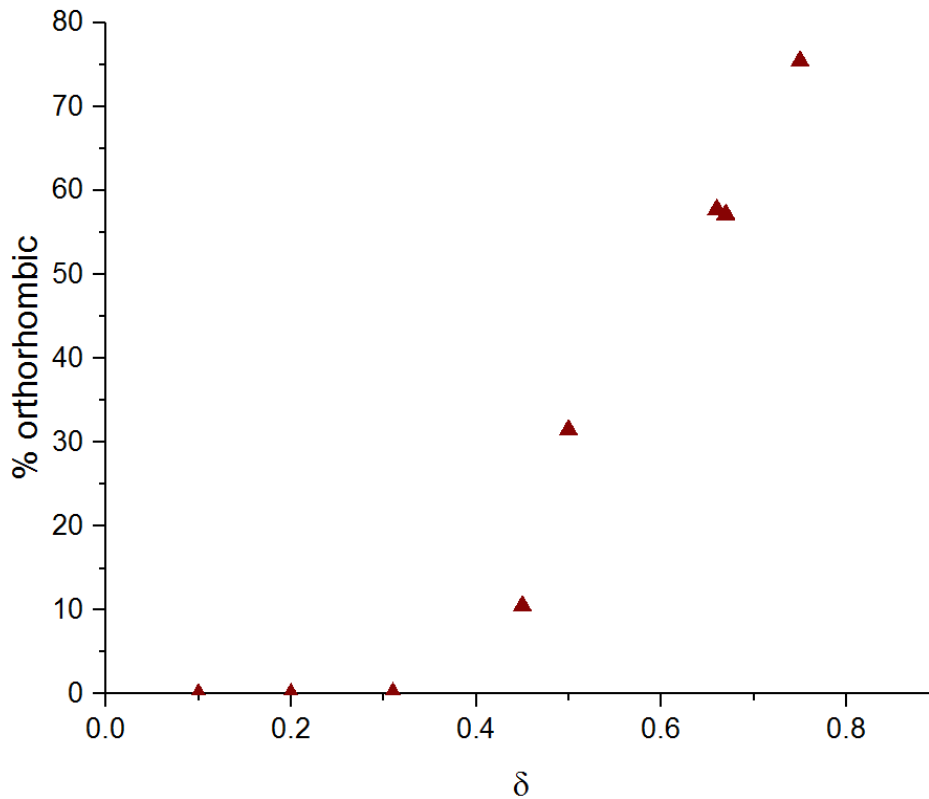


Figure 6.16– Scatterplot showing wt.% orthorhombic versus δ for $\text{YBaCo}_4\text{O}_{7+\delta}$ annealed at 310°C. It can be seen, that the orthorhombic phase was seen to grow in at a δ of 0.3-0.4

Figure 6.15 shows that for values of $\delta < 0.3$, no amount of the orthorhombic phase was detected in the sample. Between $\delta=0.3$ and $\delta=0.45$, the orthorhombic phase begins to form, and the orthorhombic phase fraction increases with δ . This value is consistent with the approximate δ in Figure 6.9 (the δ versus. $p\text{O}_2$ plot of $\text{YBaCo}_4\text{O}_{7+\delta}$), at which a step in the amount of oxygen is incorporated occurred, which would be consistent with a phase change as predicted.

To examine the effect of this orthorhombic phase on the temperature of the oxygen release, samples of different oxygen contents were heated in a TGA from room temperature to 500°C at a rate of 1°C/min in an argon atmosphere to examine at what temperature the stored oxygen would be released. The TPOs of this are shown in Figure 6.17

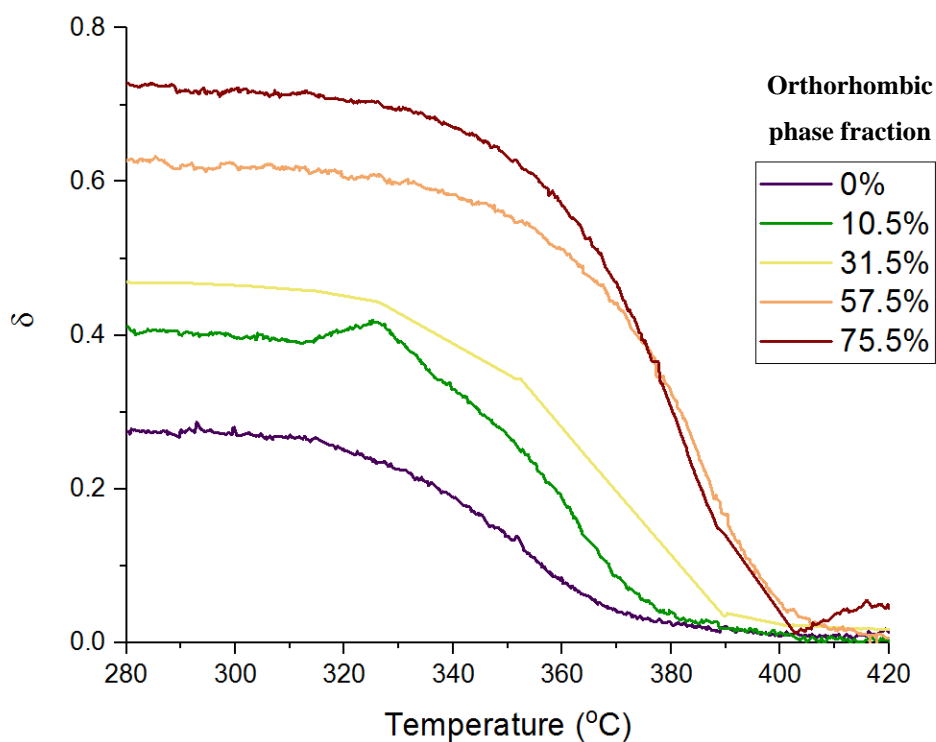


Figure 6.17 - Plot showing δ versus temperature from TPOs of samples of $\text{YBaCo}_4\text{O}_{7+\delta}$, annealed at 310°C in a $p\text{O}_2$ of 0.21 bar, heated between 50 to 500°C in argon at a heating rate of $1^\circ\text{C}/\text{min}$. Different temperatures of oxygen release is apparent for the different oxygen contents

Figure 6.17 shows that the onset temperature of oxygen loss increased with higher oxygen contents. The weight loss curves shift to higher temperatures with higher values of δ . Also apparent is the change in slope of the weight change, with the oxygen being removed from lower oxygen content samples over longer durations, unlike the previously noted constant rates of oxygen loss. It is likely therefore, that the orthorhombic phase is responsible for the hysteresis seen in the material, as when the amount of the material in the orthorhombic phase increases, the hysteresis behaviour become more apparent.

This is summarised more clearly in Figure 6.18 which shows the temperature at which rapid oxygen loss occurs, versus the orthorhombic phase fraction for each material.

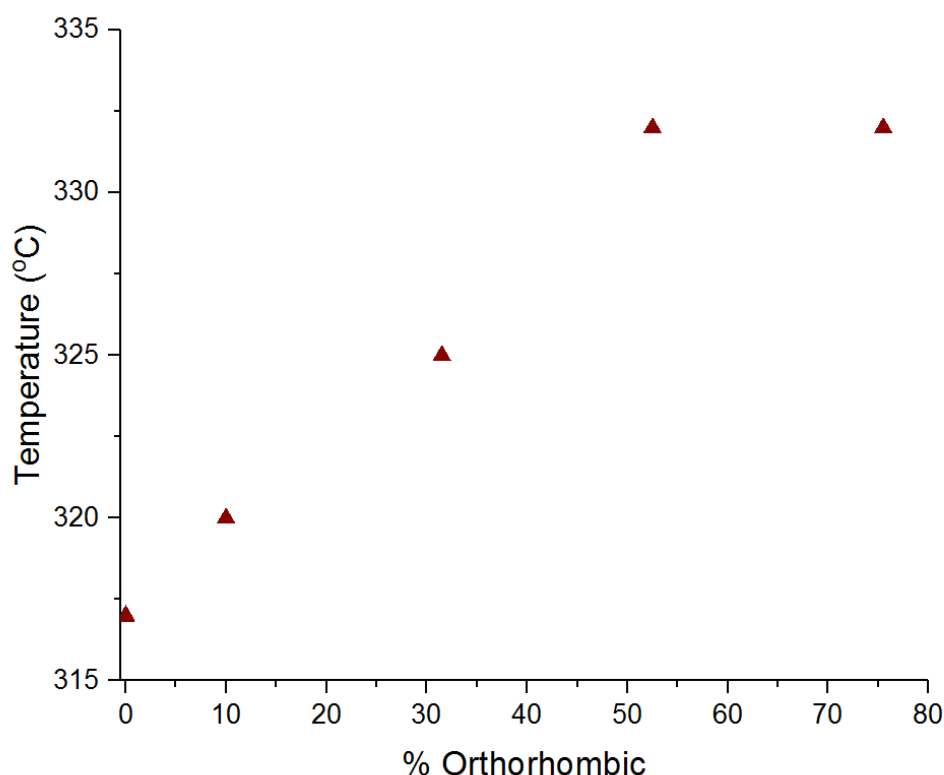


Figure 6.18 - Plot showing temperature of oxygen loss versus wt.% of the material in the orthorhombic phase, for the data shown in Figure 6.17

The temperature of oxygen release increases with the orthorhombic phase fraction up until ~50% orthorhombic phase fraction, above which no change in temperature is seen. This supports the previous findings in Figure 6.3, which found that the material maintained a constant temperature of oxygen loss when $\delta > 0.8$ in $\text{YBaCo}_4\text{O}_{7+\delta}$. This temperature effect is likely due to the orthorhombic phase, as it has already been theorized that this caused the stepwise oxygen incorporation behaviour with increasing $p\text{O}_2$'s, as seen previously in Figure 6.9. Therefore, if the oxygen content is kept lower than $\delta=0.6$, the reduction temperature during redox cycling can be decreased, however, this would reduce the efficiency of the cycles.

6.2.7 Thermodynamic study of $\text{YBaCo}_4\text{O}_{7+\delta}$

In this section of the work, the thermodynamic properties of the material will be calculated from the data gathered, namely the activation energy of oxygen incorporation, the chemical potential, and the change in entropy and enthalpy. A good reference that will be referred to throughout is ref [28]. This work shows in detail a useful method for performing this analysis. Unfortunately, the experiments were stopped at a $\delta = 0.3$, limiting the comparison to higher oxygen contents.

Activation energy is an important parameter for reactor design and is often thought of the amount of energy required to start a reaction. In literature the activation energy of $\text{YBaCo}_4\text{O}_{7+\delta}$ has been estimated [13], however, the authors mistakenly identified no phase change over the oxygen incorporation.

To confirm the reliability of the data in this work, the Arrhenius equation (Eq 6.1.) was used to estimate the activation energy of the overall reaction, to compare to ref [13]. In Eq.6.1, K is the rate constant, A is the pre-exponential factor, Ea is the activation energy, R is the gas constant and T is the temperature

$$K = A e^{-Ea/RT} \quad \text{Eq 6.1}$$

The K value for the equation was calculated from TG data collected, assuming a first-order reaction, shown in Eq.6.2. This was assumed as the change in the rate of oxygen incorporation was seen to change approximately linearly between 0.05 and 0.42 bar in the isothermal oxygen incorporation data, seen in Figure 6.3. To test this, a plot of Ln K versus temperature was created which gave a linear fit, supporting this conclusion.

$$\text{Rate} = K [O_2] \quad \text{Eq 6.2}$$

Using these equations, an Arrhenius plot was created and shown in Figure 6.19

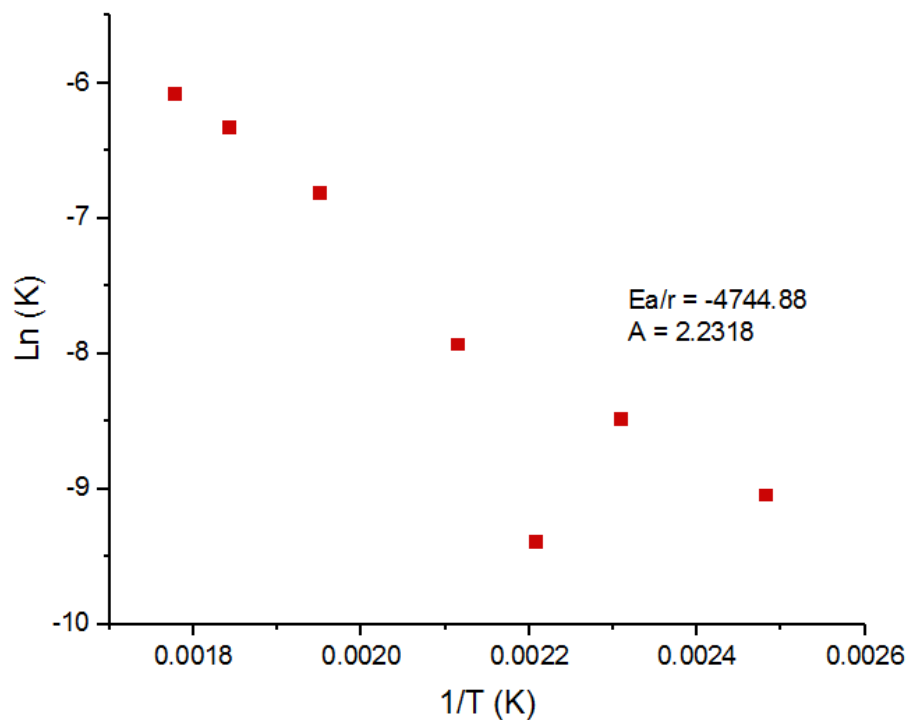


Figure 6.19 – Arrhenius plot for TG data collected at a p_{O_2} of 0.21 bar

From the gradient of Figure 6.19, an Ea value of 39.4 kJ/mol was calculated, which is within ± 5 kJ of the 43 kJ/mol value obtained in ref [15], supporting the data quality to be used in this

calculation. However, examining the data points used for the fit, it is seen that there are large changes in the gradient, particularly at a value of $1/T$ of 0.0022. This point corresponds to a δ of approximately 0.1, a region in the equilibria plot in Figure 6.9 at which the gradient of δ v.s. pO_2 changed.

To examine the change in the activation energy of oxygen incorporation as the oxygen content changes in the material, the K value over consistent steps of $\delta = 0.2$ (i.e. between 0 and 0.2, etc.) was calculated. This data was then placed into an Arrhenius plot displayed in Figure 6.20(a), with the activation calculated and displayed in Figure 6.20(b).

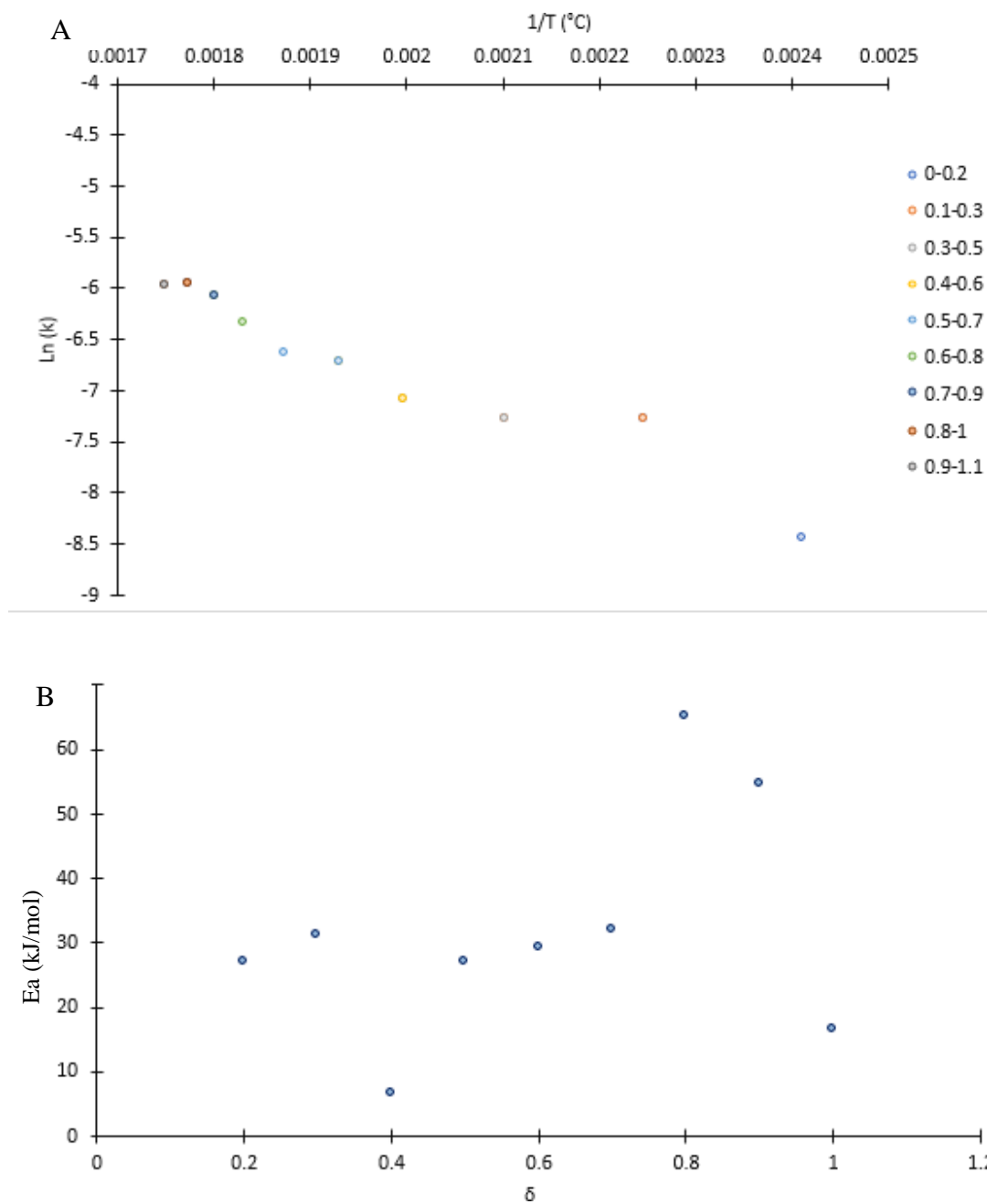
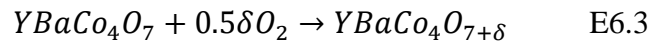


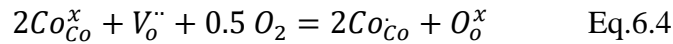
Figure 6.20 (A) - Arrhenius plot of the data shown in Figure 6.1, taking steps of $\delta=0.2$, **(B)** plot of activation energy versus δ

Figure 6.20 clearly shows that there is a difference in the activation energy depending upon the δ . Generally, the enthalpy increases slightly with oxygen non-stoichiometry, however, at a $\delta >$ than 0.3 and 0.6 significant step changes were seen. The change at $\delta = 0.3$, matches the results seen in Ref [28] at this δ range, however, no comparative data was found for $\delta=0.6$. The stoichiometries that these sudden changes in activation energy occurred correspond to two important structural transitions, seen in Figure 6.14. At a $\delta = 0.2 - 0.4$, a phase change began from hexagonal to orthorhombic, and at $\delta = 0.6-0.8$, the linear relationship between the percentage of the material in the orthorhombic phase and the delta changed, suggesting that these changes are caused by the orthorhombic phase transition.

As the calculation of the activation energy relies upon kinetic data, it is not the most accurate property to make assumptions on the materials from, so ideally more reliable thermodynamic properties require investigation. For $YBaCo_4O_7$, the oxidation equation is shown in Eq 6.3.



The exchange of oxygen between the solid and gas phase in this case is best described using equation 6.4 below with Kröger-Vink notation. Co_{Co} and Co_{Co}^x relates to Co^{3+} and Co^{2+} , $V_o^{''}$ is the empty oxygen vacancy, and O_o^x is the filled oxygen vacancy.



An equilibrium between the amount of cobalt in the different valence states at a certain pO_2 will be reached, following equation 6.5, where K_{ox} is the equilibrium constant and $a_{O_o^x}$, $2a_{Co_{Co}}$, $2a_{Co_{Co}^x}$ and $a_{V_o^{''}}$ are the activity of O_o^x , Co_{Co} , Co_{Co}^x and $V_o^{''}$ respectively, and pO_2 is the partial pressure of oxygen.

$$K_{ox} = \frac{a_{O_o^x} 2a_{Co_{Co}}}{a_{V_o^{''}} 2a_{Co_{Co}^x}} pO_2^{0.5} \quad Eq.6.5$$

It is clear the oxygen content of the sample can be linked to the partial pressure of oxygen in the system. If the partial pressure of oxygen increases, the equilibrium content of oxygen will increase if there is still cobalt in the 2+ state.

The calculation of the Gibbs energy of oxidation is shown in Eq.6.6, where ΔG_{oxi} is the Gibbs energy of oxidation of $YBaCo_4O_7$, ΔG_f is the Gibbs energy of formation, and μ_o is the chemical potential of the oxygen.

$$\Delta G_{oxi} = \Delta G_f YBaCo_4O_{7+\delta} - \Delta G_f YBaCo_4O_7 - \mu_o(O_2) \quad Eq 6.6$$

If it is assumed to be the unity behaviour of the solid phases, and the oxygen behaves as an ideal gas, the energy changed can be linked solely to the oxygen chemical potential [35]

The chemical potential of the gas phase can be calculated from the equilibrium data shown in Figure 6.9, using Eq.6.10, where μ_0 is the chemical potential of the experimental point, $\Delta\mu_0$ is the change of the chemical potential of oxygen, T is the temperature, R is the gas constant, and μ_{ref} is the chemical potential at a reference pO_2 , in this example 0.5 bar.

$$\Delta\mu_0 = \mu_0 - 0.5\mu_{ref} = \frac{RT}{2} \ln pO_2. \quad \text{Eq.6.10}$$

The chemical potential was then calculated for the equilibria data presented in Figure 6.9 and is displayed in Figure 6.21.

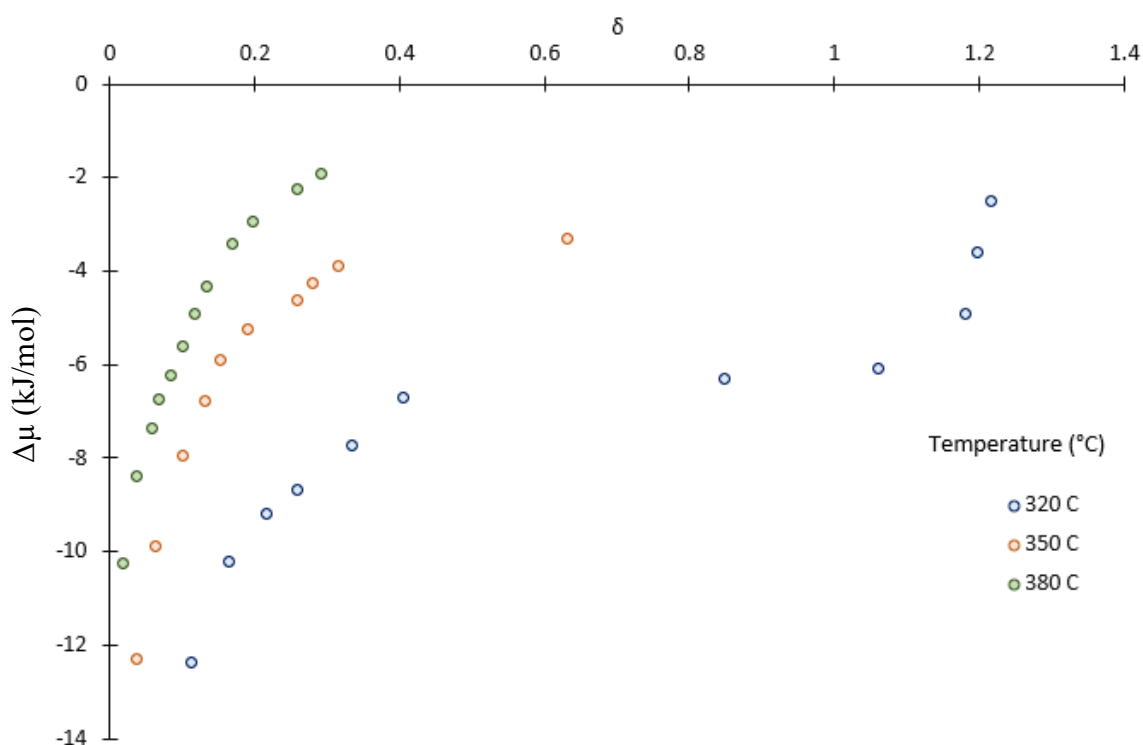


Figure 6.21 – Plot of Chemical potential of oxygen relative to a pO_2 0.21 mol oxygen in $YBaCo_4O_{7+\delta}$ versus δ at temperatures between 320 and 380°C

The chemical potential of oxygen was seen to decrease with increased temperatures, explaining the significantly lower amount of oxygen incorporated at higher temperatures. The rate of this decrease slows as the temperature increases, with a reduction from -17 to -12 kJ/mol between 320 and 350°C, decreasing to a reduction of approximately -12 to -10 from 350 to 380°C, at a δ of approximately 0.04. At 320°C, it was seen the chemical potential decreased steadily until a $\delta=0.4$, where the chemical potential stayed the same. In ref. [28], at 350°C and a $\delta = 0.1$, a chemical potential of approximately -7 kJ/mol was seen, approximately matching values seen in Figure 6.21. To calculate the change in standard

partial molar entropy ($\Delta S\hat{\delta}$) and enthalpy ($\Delta H\hat{\delta}$), Eq. 6.6 can be used, where the $pO_{2 \text{ ref}}$ is equal to a reference partial pressure of oxygen, in this case 0.5 bar.

$$\Delta\mu_0 = \Delta H\hat{\delta} - T\Delta S\hat{\delta} \quad \text{Eq.6.11}$$

Combining Eq.6.10 with Eq. 6.11, gives Eq. 6.12

$$\Delta\mu_0 = \frac{RT}{2} \ln pO_2 = \Delta H\hat{\delta} - T\Delta S\hat{\delta} \quad \text{Eq.6.12}$$

From this Eq.6.13 may be found

$$-\ln\left(\frac{p_{O_2}}{p_{O_2 \text{ ref}}}\right) = \frac{2\Delta H_O^\circ}{RT} - \frac{2\Delta S_O^\circ}{R} \quad \text{Eq.6.13}$$

Therefore plotting $-\ln\left(\frac{p_{O_2}}{p_{O_2 \text{ ref}}}\right)$ versus $1/T$ can be used to find the change in standard partial molar entropy ($\Delta S\hat{\delta}$) and enthalpy ($\Delta H\hat{\delta}$) for a constant δ [28, 35-37]

Figure 6.22(a) below shows the plot of $-\ln\left(\frac{p_{O_2}}{p_{O_2 \text{ ref}}}\right)$ versus $1/T$, for δ 's between 0.1 and 0.6, with the data taken from Figure 6.9, and Figure 6.22(b) shows the calculated standard partial molar entropy ($\Delta S\hat{\delta}$) and enthalpy ($\Delta H\hat{\delta}$) from Figure 6.22.

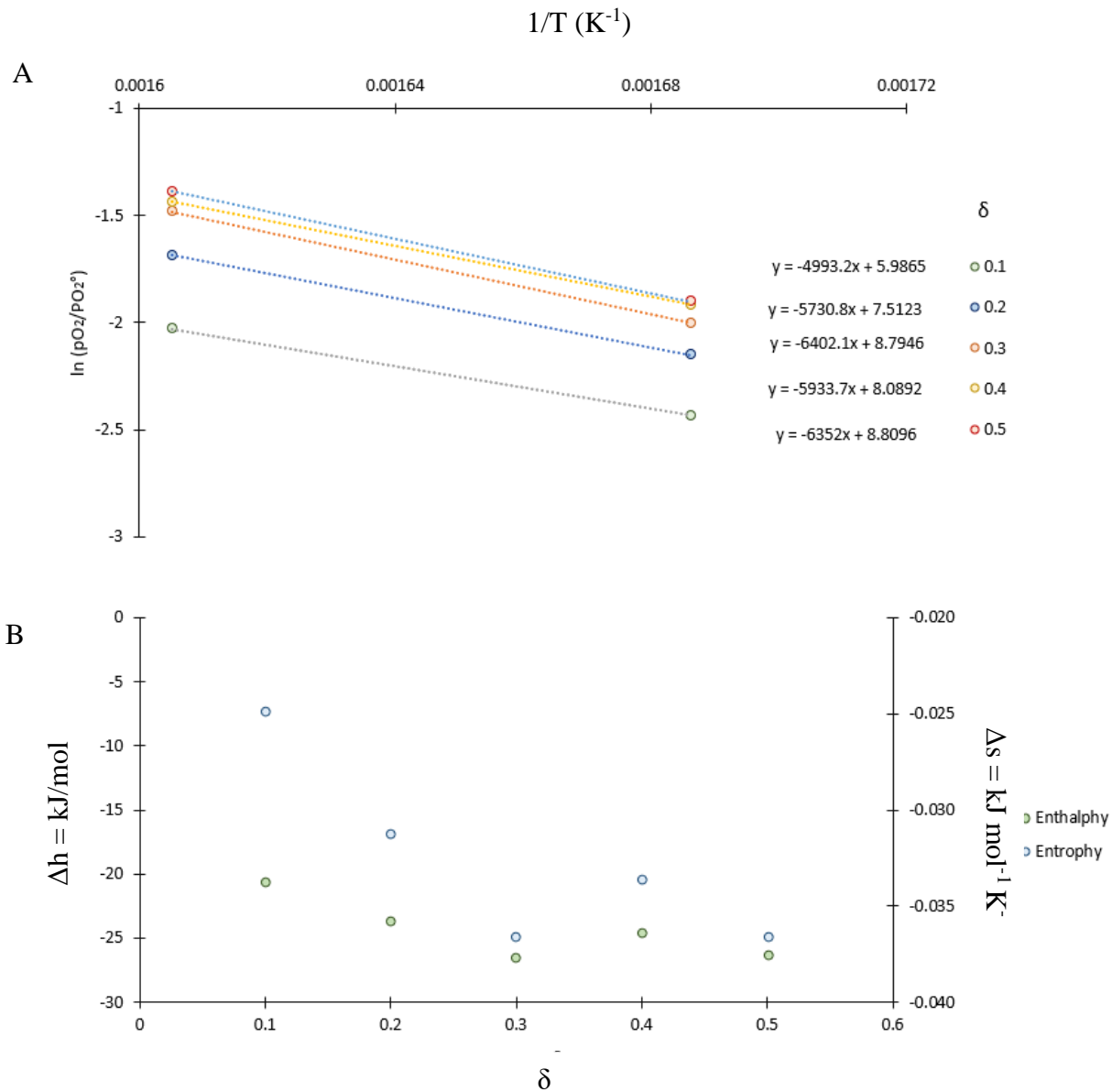


Figure 6.22 (a) - plot of $-\ln\left(\frac{p_{O_2}}{p_{O_2}^0}\right)$ versus $1/T$ for δ 's of between 0.1 and 0.6, **(b)** - Plot of the standard partial molar entropy (ΔS^0) and enthalpy (ΔH^0) versus δ

In Figure 6.21 (b), the ΔS^0 and ΔH^0 of the material increases from a δ of 0.1 to 0.3, increasing by four and 0.25 times their initial value at $\delta = 0.1$ respectively. Upon further incorporation of oxygen, the ΔS^0 and ΔH^0 stay, consistent with the δ of the previously noted phase transition between the hexagonal and orthorhombic phases. This suggests that oxygen incorporation begins easily into the hexagonal phase, however, as oxygen sites become more filled, more resistance to incorporation is found. When the threshold δ for the orthorhombic transition is reached ($\delta = 0.4$), the ΔS^0 and ΔH^0 for oxygen incorporation increases to account for the extra energy required for the phase transition.

To understand the differences in heating and cooling of the sample, and the effect of the hysteresis on the oxygen content of the materials, a plot of $-\ln\left(\frac{p_{O_2}}{p_{O_2}^0}\right)$ versus $1/T$ was

produced for the data shown in the Figure 6.8, the hysteresis plot of δ versus temperature upon heating and cooling in a pO_2 of 0.25 and 0.42 bar. A δ of 1.1 was chosen for the calculation, and values of the temperature of oxygen release or incorporation were estimated from reading off the experimental curves. The data for the cooling and heating curves were then plotted independently, and this can be seen in Figure 6.23.

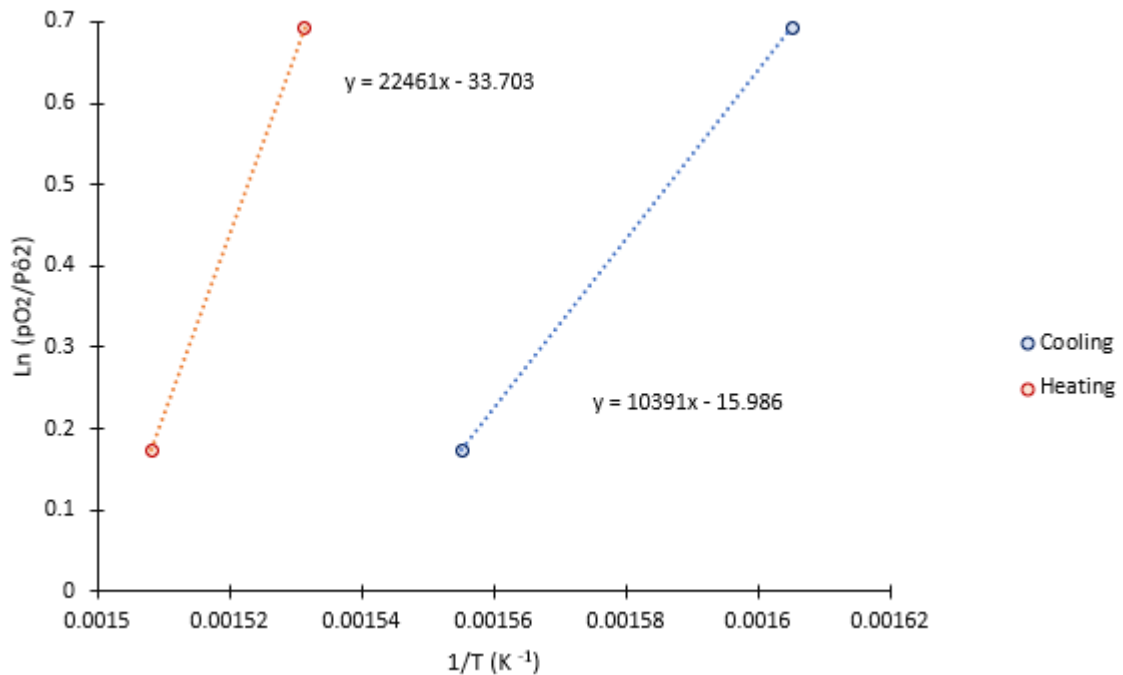


Figure 6.23 – plot of $-\ln\left(\frac{pO_2}{P\delta^2}\right)$ versus $1/T$ for a $\delta = 1.1$, comparing the data obtained in Figure 6.6? upon heating and cooling in a pO_2 of 0.25 and 0.42 bar

It is evident from Figure 6.22, that the $\Delta S\hat{o}$ and $\Delta H\hat{o}$ of the material upon cooling or heating is very different. From the gradient and intercept of the graph, the $\Delta S\hat{o}$ and $\Delta H\hat{o}$ upon heating and cooling were found and these can be found in Table 6.1. To explain the lack of the oxygen uptake at 380°C upon cooling in a pO_2 of 0.42 bar, and the storage of the oxygen upon heating at 380°C, $\Delta\mu$ was calculated at 380°C, using equation 6.5, using the $\Delta S\hat{o}$ and $\Delta H\hat{o}$ calculated from Figure 6.22 for heating and cooling. These calculated values can be found in Table 6.1.

Table 6.1 - Values of $\Delta S\hat{\delta}$ and $\Delta H\hat{\delta}$ calculated from Figure 5, and $\Delta\mu_0$ calculated at 380°C for both heating and cooling

Direction	Temperature (°C)	$\Delta H\hat{\delta}$ (kJ mol ⁻¹)	$\Delta S\hat{\delta}$ (kJ K ⁻¹ mol ⁻¹)	$\Delta\mu_0$ (kJ mol ⁻¹)
Heating	380	-93.37	-0.14	-1.89
Cooling	380	-43.20	-0.07	0.20

This calculation showed that the chemical potential of the material was negative at 380°C upon heating, and positive at 380°C upon cooling. The negative value of $\Delta\mu_0$ upon heating and the positive value upon cooling explains why the material had a large and small δ value respectively, as oxygen uptake was not thermodynamically feasible. The major difference in the materials state at each of these points was the crystal structure, as upon cooling, the material was completely hexagonal, and upon heating the material was found to have a significant proportion in the orthorhombic phase. Therefore, it is apparent that for oxygen storage, the material must be able to transform into the orthorhombic phase, which is not thermodynamically feasible if the temperature is too high.

To estimate the exact temperatures of the boundary of the hysteresis, the calculation was repeated, varying the temperature for both the heating and cooling directions. This can be seen in Figure 6.24, where the chemical potential versus the temperature is plotted. When the chemical potential is equal to zero, this should be the transition temperature between the oxygenated and de-oxygenated phase in a pO_2 of 0.42 bar.

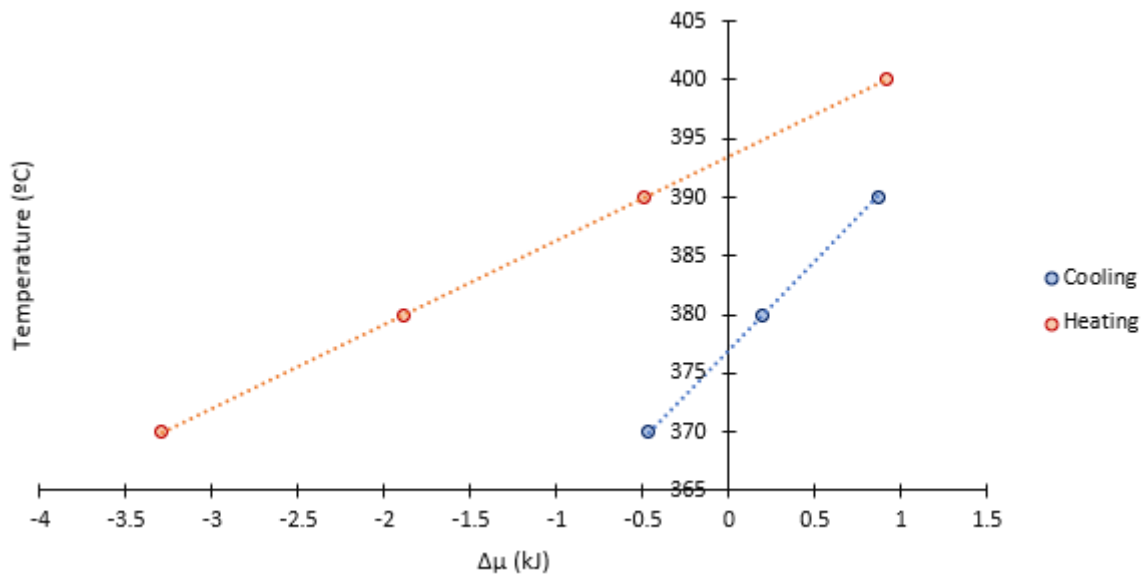


Figure 6.24 – Plot of $\Delta\mu$ versus temperature for $\text{YBaCo}_4\text{O}_{7+\delta}$ calculated using Eq.6.13, using the values of $\Delta S\delta$ and $\Delta H\delta$ shown in Table 6.1

As seen in Figure 6.24, upon cooling the transition appears at 376°C, and upon heating 393°C. These values agree with the previous results from Figure 6.8, where a $\delta > 1$ was recorded at 370°C, but not at 380°C upon cooling, and a $\delta > 1$ was recorded at 390 but not 400 °C upon heating. This narrow transition between thermodynamically favourable and unfavourable over such a small temperature range appears to be what is responsible for the rapid oxygen loss and gain of the material, with the change in transition temperature upon heating or cooling most likely caused by the transition of the orthorhombic phase.

6.4 Oxygen release and incorporation of YBaCo_4O_7 compared to other oxygen carriers

For oxygen enrichment processes, there are two major thermodynamic features for a useful oxygen carrier. The first major thermodynamic feature is the amount of oxygen produced per degree of a temperature swing. Oxygen release over smaller temperature swings is beneficial for multiple reasons, namely lower energy costs and potentially less mechanical degradation due to thermal expansion. The second major thermodynamic feature is the oxygen content of the material as a function of $p\text{O}_2$, which can be used to calculate the amount of oxygen removed from an inlet stream. Low-efficiency removal of oxygen from an air stream requires more air to be heated, increasing heating and pumping costs of a process. In this section, using the data provided earlier in this chapter, the thermodynamic potential of the use for oxygen enrichment will be compared to various other potential oxygen carriers.

6.4.1 Amount of oxygen released per $^\circ\text{C}$ of a temperature swing compared to other oxygen carriers

To examine the efficiency of the temperature swing, a detailed literature review was conducted examining the amount of oxygen transferable from an oxygen carrier per $^\circ\text{C}$ of a temperature swing. This was then compared to the data collected in this work (Figure 6.5) to give reasonable assumptions of the oxygen transfer. For this analysis, the oxygen non-stoichiometry or content at a $p\text{O}_2$ of 0.25 bar was compared to an oxygen non-stoichiometry at 0.42 bar at different temperatures to mimic a temperature swing process. The temperatures selected for each material were chosen to give the greatest change in oxygen non-stoichiometry per $^\circ\text{C}$. This data is shown below in Table 6.2, where oxygen carriers are ordered from greatest to least change in oxygen capacity per $^\circ\text{C}$, with data from references 38-51.

Table 6.2 – Calculated amount of oxygen released over cycling for multiple oxygen carriers

Material	Temperature of oxygen incorporation (°C) at a pO₂ of 0.25 bar	Temperature of oxygen release (°C) at a pO₂ of 0.42 bar	Δ°C	Change in weight %	Change in weight % per °C
Cu-Cu ₂ O [38]	1300	1350	50	10	0.2
MnO ₂ – Mn ₂ O ₃ [39]	650	700	50	9	0.18
Co ₃ O ₄ – CoO [40]	1150	1200	50	5	0.1
YBaCo ₄ O ₇	360	400	40	2.8	0.07
YBa ₂ Cu ₃ O _{7-δ} [41]	773	973	200	0.8	0.004
YBaMn ₂ O _{5+δ} [42]	650	750	100	0.37	0.0037
SrCo _{0.9} Nb _{0.1} O _{3-δ} [43]	500	650	150	0.42	0.0028
SrFeO _{3-δ} [44]	800	950	150	0.3	0.002
CaMnO _{3-δ} [45]	800	900	100	0.19	0.0019
Pr _{0.9} Y _{0.1} BaCo ₂ O _{6-δ} [46]	650	950	300	0.5	0.0017
LaMnO _{3-δ} [47]	600	800	200	0.32	0.0016
La _{0.9} Sr _{0.1} Fe _{0.1} Co _{0.9} O _{3-δ} [48]	800	900	100	0.14	0.0014
Ca _{0.25} Sr _{0.75} Fe _{0.75} Mo _{0.25} O _{3-δ} [49]	750	950	200	0.028	0.00014
La ₄ Ni _{2.7} Fe _{0.3} O _{10-δ} [50]	750	950	200	0.021	0.00011
BaTiO _{3+δ} [51]	800	1000	200	0.0007	3.5E-06

From the values shown in Table 6.2, YBaCo₄O_{7+δ} has the potential to exchange large amounts of oxygen over narrow temperature ranges, with the % weight change per °C at least an order of magnitude greater than any of non-transition metal oxides, and approximately one-third of the copper oxide systems which operate at temperatures ~900°C higher. As an air inlet stream would require to be heated to these temperatures for the oxidation step, this comparable capacity at such low temperatures may be advantageous in industry.

6.6.2 The use of oxygen from an air stream

For oxygen cycling processes, the highest efficiency process removes as much oxygen from the oxidising stream as possible. If a material only uses a small fraction of the oxygen available, then more air needs to be heated and pumped through the system, increasing the compression and heating costs of a process. The data shown in Table 6.2, shows that oxygen cycling for oxy-fuel combustion can occur with a temperature swing of as little as 40°C; however, the oxidation cycle may be inefficient if the active pO_2 range of the material is close to 0.21 bar, meaning the material will use little of the inlet gas stream.

Using the data from Figure 6.10 the amount of oxygen that could theoretically be removed from a gas stream was examined. From the data shown in this figure, it can be seen that at a $\log pO_2$ of -3 (0.001 bar), small amounts of oxygen ($\delta \approx 0.05$) can be incorporated at 310°C, suggesting that in theory 99.5% of oxygen could be removed from an air stream of 0.21 bar at this temperature in a long enough reactor bed. However, removing oxygen to this degree would likely be extremely impractical, and such a low oxygen content is unreasonable for oxygen enrichment. A more reasonable scheme is that the material should be allowed to incorporate a $\delta=1$ for oxygen cycling. This ensures the material has a large enough oxygen content to give a hysteresis of the oxygen capacity, as this effect occurs at δ 's greater than 0.6. From Figure 6.9, and the temperature of oxygen release for a pO_2 of 0.42 bar (400°C), Table 6.3 was produced, showing for different temperatures of oxygen incorporation, the pO_2 at which a $\delta=1$ was achieved, along with the required temperature swing. From this pO_2 , the theoretical efficiency of oxygen use from the gas stream was calculated.

Table 6.3 – Table of calculated efficiencies of oxygen use of inlet gas stream using $YBaCo_4O_7$

Temperature of oxygen incorporation (°C)	pO_2 at which $\delta = 1$	Temperature swing assuming oxygen released at 400°C	Theoretical amount of oxygen removable from air inlet stream to achieve $\delta = 1$ (%)
310	-1.5	90	84.5
330	-1.2	70	70.0
350	-0.9	50	40.1
370	-0.6	30	19.6

As seen in Table 6.3, the smaller the temperature swing of the process, the less efficient the potential use of oxygen during the oxygen incorporation step. At 350°C this oxygen content occurs at $\log p_{\text{O}_2} -0.9$, which would only use 40% of the inlet oxygen. Decreasing the temperature of oxygen incorporation to 310°C would allow $\delta=1$ to be reached at $\log p_{\text{O}_2} -1.5$, which would use over 80% of the oxygen in the inlet gas stream, but with an increased temperature swing of 40°C. For each process, depending upon the efficiency of the heat exchangers for heat recovery and the pumps, an individual decision about the size of the temperature swing can be made.

6.5 Discussion

Initially in this work, the oxygen incorporation and release of $\text{YBaCo}_4\text{O}_{7+\delta}$ was studied by dynamic heating ramps (Figure 6.1), to mimic results seen in literature. Good agreement can be seen between the literature data and results presented for both temperatures of oxygen incorporation, temperatures of the oxygen release, and oxygen capacities measured [5-11], although variation in the total oxygen content is found in literature due to the dynamic nature of most experiments is seen [52-53]. The novelty of these results relies upon the multiple p_{O_2} 's, and the p_{O_2} range tested. To the authors' knowledge, in literature heating ramps, such as seen in Figure 6.1, are only performed at 1 or 0.21 bar, and studies in range for oxy-fuel combustion have not been performed.

From these experiments. it was seen that increasing the p_{O_2} increased the temperature of oxygen release. The reason for this is likely due to the higher equilibrium oxygen content typically expected at higher p_{O_2} 's. This behaviour was seen by Karpinnien [6] when comparing a 1 bar and 0.21 bar experiment.

Oxygen incorporation at temperatures between 300 and 400°C, at a p_{O_2} of 0.05, 0.25, and 0.42 were studied. It was noted that at higher temperatures, oxygen incorporation slowed, and at high temperatures, wherein in Figure 6.1 a sample had a $\delta>1$, minimal oxygen was incorporated isothermally. Secondly, the range of temperatures for useful oxygen incorporation decreased at lower p_{O_2} 's. The results agree with literature, where at approximately 310°C the fastest rates of oxygen incorporation were found [54].

From the results it is apparent, oxygen storage is preferable at lower temperatures and higher p_{O_2} . This behaviour is characteristic of many non-stoichiometric systems [27, 55-57]. This is to be expected, particularly when one considers that metal achieves higher oxidation states at lower temperatures [58]. Equations 6.11 and 6.12, show that increasing the temperature at the

same pO_2 will lower the chemical potential of a system, which would decrease the oxygen content.

Upon investigating the differences between oxygen content measured in Figures 6.1 and 6.3, hysteresis in the oxygen content was found, with a dramatic step-change in oxygen content upon heating and cooling. In Figure 6.5, the step change was mapped upon cooling in the pO_2 range of 0.05 to 0.42 bar. Here it was demonstrated that this step was shifted to higher temperatures at higher pO_2 's. The oxygen content of the hysteresis was mapped clearly in Figure 6.8 for a pO_2 of 0.21 and 0.42 bar. The difference in oxygen release and incorporation upon heating and cooling was seen to be approximately $20^\circ C$ at both pO_2 's. The temperature of the hysteresis increased by $10^\circ C$ when increasing the pO_2 from 0.21 to 0.42 bar. From this information, the following can be determined. Firstly for oxy-fuel combustion, the oxygen release step must be performed at $390^\circ C$ or higher, otherwise, enough oxygen will not be released. For oxygen incorporation, the temperature must be cooled to a maximum temperature of $360^\circ C$ to allow oxygen incorporation in a pO_2 of 0.21 bar.

A δ versus pO_2 plot was also produced as part of this work. The data here matches with literature, however, literature data was limited to a $\delta=0.3$ [28]. The oxygen contents achieved agree with other TGA results in this work. In agreement with other data from this work, it was seen that oxygen incorporation was higher at lower temperatures and greater pO_2 's. A step-change in oxygen non-stoichiometry was seen in these plots, indicative of a phase transition. At $320^\circ C$ this step was seen at a $\delta = 0.4$, and a log pO_2 of -1.5 bar. A $30^\circ C$ increase in temperature shifted this step change to log pO_2 of -1 bar. The oxygen efficiency of the material is surprisingly high, in agreement with its use for oxygen removal processes [26]

From these plots, the efficiency of redox cycling was examined. The results are compared to literature in Tables 6.2 and 6.3. The amount of oxygen released per $^\circ C$ of a temperature swing of $YBaCo_4O_{7+\delta}$ was found to be at least one order of magnitude greater than the closest non-stoichiometry material. The amount of oxygen released per $^\circ C$ of a temperature swing was between $\frac{1}{2}$ and $\frac{1}{4}$ of Cu, Mn, and Co systems, which are of significant interest for oxygen cycling [59], showing strong thermodynamic potential. While redox cycling is possible over a narrow temperature range, more efficient use of oxygen occurs with increased temperature swings. This is as a lower percentage of the oxygen stream will be incorporated at higher temperatures. Lower efficiencies of oxygen use will require more gas to be heated and fed to a reactor. Additionally, in a reactor scheme, oxygen will be removed from the gas stream along the bed, so only material at the start of the reactor will see the highest entry pO_2 of the oxidising stream.

These results are contrary to the work performed in reference [60], who suggested oxidation upon heating, and reduction upon cooling – which with this data seems unfeasible.

The changes to crystal structure upon oxygen incorporation were then investigated. It is known that the oxygen content is related to the orthorhombic phase [61-62], however to the author knowledge, a plot showing the relationship as a function of oxygen non-stoichiometry is not available in literature. A relationship between the orthorhombic phase and the oxygen content is presented in this work. It was seen that the orthorhombic phase grew at approximately $\delta=0.4$. This matches the δ at which a change in gradient was seen in the δ v.s. pO_2 plot, explaining the behaviour.

The chemical expansion was examined during oxygen incorporation and release, and a significant distortion in the C-axis was seen at the approximate temperature of oxygen incorporation and release [34]. The growth of the orthorhombic phase during isothermal oxygen incorporation was studied, and it was seen upon oxygen incorporation the cell volume decreases, typical with most non-stoichiometric materials.

Interestingly, the temperature of oxygen release was linked to the percentage of the material that was orthorhombic. It was seen that until a wt.% of approximately 50% orthorhombic, the temperature of oxygen release varied. After 50% of the phase was orthorhombic, no difference in the oxygen release temperature upon heating was seen.

The thermodynamics of the system were explored to explain the behaviours seen.

The first significant finding was shown in Figure 6.19 (b). It was seen that there was a non-linear relationship between the oxygen content and the activation energy of oxygen incorporation. Oxygen content having an impact on activation energies is often seen in literature [63-64], with a decrease in vacancies seen to increase the activation energy. In this work, two interesting features were seen when mapping the activation energy. Firstly, a drop in activation energy at $\delta = 0.4$, and a significant jump at $\delta = 0.7$.

The first of these decreases corresponded to the δ at which the orthorhombic phase was found to grow. It can be assumed that the phase change allows for easier oxygen incorporation.

The second increase occurs at the δ equivalent to a wt% of 50% of the orthorhombic phase. This links the wt.% of the orthorhombic phase, after which oxygen release temperature became fixed in a given pO_2 . The extra energy required here likely explains why the release

temperature becomes fixed, as this energy barrier must be overcome to allow oxygen release from the sample.

The reason for this is unclear. Jia et al [65] determined three slightly different modulations to the structure for oxygenated $\text{YBaCo}_4\text{O}_{7+\delta}$ by T.E.M. investigations. It was seen, that with the heat produced by the T.E.M., oxygen could be removed from the first two modulations, A and B. For modulation C, it was seen the oxygen incorporated was stable. I would suggest, therefore, that the link to this energy barrier involves this slightly modulated form of YBaCo_4O_7 – however, this is purely speculative and the behaviour remains unexplained.

In Table 5.1, the partial molar enthalpy and entropy of $\text{YBaCo}_4\text{O}_{7+\delta}$ upon heating and cooling at 380°C were calculated. It was shown that at 380°C , the enthalpy of oxidation upon heating and cooling was -93 and -43 kJ mol^{-1} respectively, and the entropy of oxidation upon heating and cooling is -0.14 and -0.07 $\text{kJmol}^{-1}\text{K}^{-1}$. Using these values to calculate the chemical potential, it was seen that the chemical potential turned positive to negative. This explains why at the same temperature upon heating and cooling, different oxygen contents are achieved. The reason for this is likely due to the orthorhombic/hexagonal phase change that would occur upon oxygen incorporation. Similar results are seen in literature when examining oxygen incorporation of $\text{CaMnO}_{3-\delta}$, where a phase change from cubic to orthorhombic occurs upon oxygen incorporation. In ref [66] a difference in the oxidation enthalpy and entropy of the cubic and orthorhombic phases differed by approximately 100 kJ mol^{-1} and 90 $\text{kJmol}^{-1}\text{K}^{-1}$ respectively. Values reported here for the enthalpy of oxidation are between 100 and 300 kJ mol^{-1} lower than CaMnO_3 [66], Ceria [67], and manganese oxide [27]. The entropy of oxidation for YBaCo_4O_7 is between 0.09 and 0.75 $\text{kJ K}^{-1} \text{mol}^{-1}$ lower than the same references. These values suggest easier oxygen incorporation and release from $\text{YBaCo}_4\text{O}_{7+\delta}$.

6.6 Conclusions and future work

During this work, the oxygen incorporation and release of YBaCo_4O_7 were investigated by TGA and XRD. The degree of oxygen non-stoichiometry as a function of $p\text{O}_2$ was shown at a temperature between 330 and 370°C. Additionally, the oxygen release of the material was investigated, and the temperature of the rapid oxygen release was seen to shift to higher temperatures in higher $p\text{O}_2$ s. The oxygen content and degree of the material in the orthorhombic phase were also seen to impact the temperature of the oxygen release until an oxygen content of 0.6 or a % orthorhombic of 50%.

TG and XRD investigations showed a hysteresis in the oxygen capacity, with different oxygen contents at the same temperature and $p\text{O}_2$ achieved by cooling and heating. The difference in temperature of the oxygen uptake and release was seen to be approximately 20°C, with temperatures shifting 10°C higher between 0.21 and 0.42 bar. This makes the material very promising for oxygen enrichment processes, as large amounts of oxygen can be exchanged over small temperature swings.

From the data gathered, thermodynamic properties such as the chemical potential and activation energy of the material were calculated. The chemical potential of the material was calculated to change from negative to positive at the temperatures of oxygen release or low oxygen incorporation, consistent with experimental data – going some way to explaining the rapid oxygen loss behaviour.

With the results obtained, it is clear that thermodynamically, YBaCo_4O_7 is an attractive oxygen carrier for oxygen enrichment processes and compares well against other alternative redox materials. It can be seen however that the oxygen incorporation rates are quite low in this work, and while similar materials such as $\text{Ca}_2\text{AlMnO}_{5+\delta}$ and YMnO_3 have shown similar thermodynamic benefits (although at not as low a temperature or with such capacity respectively), the issues with these materials are the slow oxygen incorporation kinetics [68-69] which may prove a stumbling block, although work such as doping [70] or ball milling [71-72] may be useful for improving this further. The kinetics and redox cycling of this material are investigated further in Chapter 7.

6.7 References

- [1] N.A.Danilov, A.P.Tarutin, J.G.Lyagaeva, E.Yu.Pikalova, A.A.Murashkin, D.A.Medvedev, M.V.Patrakeev, A.K.Demin- Affinity of YBaCo₄O_{7+δ}-based layered cobaltites with protonic conductors of cerate-zirconate family, *Ceramics International* 43, 17, 2017, 15418-15423
- [2] K.Lai, A.Manthiram - Effects of trivalent dopants on phase stability and catalytic activity of YBaCo₄O₇-based cathodes in Solid oxide fuel cells, *Journal of Material Chemistry, A*, 6, 2018, 1641
- [3] G.Tian, H.Chen, C.Lu, Y.Xin, Q.Li, J.A. Anderson Z.Zhang - An oxygen pool from YBaCo₄O₇-based oxides for soot combustion, *Catal. Sci. Technol.*, 6, 2016, 4511-4515
- [4] O.Parkimma, A.S.Albero, J.S.Albero, M.Karppinen - Oxygen-Nonstoichiometric YBaCo₄O_{7+δ} as a Catalyst in H₂O₂ Oxidation of Cyclohexene, *Catalysis Letters* 145, 2014, 576-582
- [5] O.Parkkima, H.Yamauchi, M.Karppinen - Oxygen Storage Capacity and Phase Stability of Variously Substituted YBaCo₄O_{7+δ}, *Chemistry of Materials*. 25, 2013, 599-604
- [6] M.Karppinen, H.Yamauchi, S.Otani, T.Fujita, T.Motohashi -Oxygen stoichiometry in YBaCo₄O_{7+δ} Large Low-Temperature Oxygen Adsorption/Desorption Capability, *Chem Mater* 18, 2006, 490-494
- [7] T.Motohashi, S.Kadota, H.Fjellvåg, M.Karppinen, H.Yamauchi - Uncommon oxygen intake/release capability of layered cobalt oxides, REBaCo₄O_{7+δ}: Novel oxygen-storage materials, *Materials Science and Engineering: B*, 148, 1-3, 2008, 196-198
- [8] H.Hao, L.Zhao, J.Hu, X.Hu, H.Hou - Oxygen adsorption/desorption behavior of YBaCo₄O_{7+δ} and its application to oxygen removal from nitrogen, *Journal of Rare Earths*, 27, 5, 2009, 815-818
- [9] Q.L.He, X.X Shang, H.Song, H.S.Hao - Effect of Al doping on the oxygen adsorption and electronic transport properties of YBaCo₄O₇, *Journal of Functional Materials*, 45, 2014, 16148-16152
- [10] H.Song, J.Jia, S.Zhang, D.Yang, H.Sun, X.Hu Remarkable oxygen adsorption/desorption capability of Y_{0.5}Tb_{0.5}BaCo₄O_{7+δ} under temperature cycles, *Materials Research Bulletin* 47, 3, 2012, 518-520
- [11] H.S.Hao, J. Cui, C.Chen, L.Pan, JHu, X, Hu - Oxygen adsorption properties of YBaCo₄O₇-type compounds, *Solid State Ionics*, 177, 7-8, 2006, 631-637
- [12] D.S.Tsvetkov, V.Pralong, N.S.Tsvetkova, A.Y.Zuev - Oxygen content and thermodynamic stability of YBaCo₄O_{7 ± δ}, *Solid State Ionics*, 278, 2015, 1-4
- [13] L.Hou, Q.Yu, K.Wang, Q.Qin, M.Wei, Fan Yang - Oxidation kinetics of YBaCo₄O_{7+δ} and substituted oxygen carriers, *R.Soc.Open.Sci*, 5, 2018, 180150
- [14] D.S.Tsvetkov, N.S.Tsvetkova, I.L.Ivanon, A.Y.Zuev - Thermodynamic stability, oxygen content, defect structure and related properties of YBaCo₄ - xZn_xO_{7 + δ} (x = 0-3) oxides, *Solid State Ionics*, 309, 2017, 92-99
- [115] M. Valkeapa, M. Karppinen, T. Motohashi., R. Liu, J. Chen, H. Yamauchi - In Situ and Ex Situ Monitoring of Oxygen Absorption in YBaCo₄O₇, *Chemistry Letters*, 36, 2007, 1368-1369
- [16] L. P. Kozeeva, M. Yu. Kameneva, A. N. Lavrov, and N. V. Podberezskaya - Synthesis and Oxygenation Behavior of RBaCo₄O_{7 + δ} (R = Y, Dy-Lu), *Journal of inorganic materials*, 49 ,2013, 668-673
- [17] L.Hou, Q.Yu, K.Wang, T.Wang, F.Yang, S.Zhang - Oxygen storage capacity of substituted YBaCo₄O_{7+δ} oxygen carriers, *Journal of thermal and analytical calorimetry*, 137, 2018, 317-325
- [18] S.Räsänen, O.Parkkima, E.Rautama, H.Yamauchi, M.Karppinen - Ga-for-Co substitution in YBaCo₄O_{7+δ}: Effect on high-temperature stability and oxygen-storage capacity, *Solid State Ionics* 208, 2012, 31-35
- [19] K.Zhang, Z.Zhu, R.Ran, Z.Shao, W.Jin, S.Liu - Layered perovskite Y_{1-x}CaxBaCo₄O_{7+δ} as ceramic membranes for oxygen separation, *Journal of Alloys and Compounds* 492, 2010, 552-558

- [20] S. Wang, E.Haoshan, H.Baofeng, Z.Jianfeng, J.X.Hu - Modifying the oxygen adsorption properties of YBaCo₄O₇ by Ca,Al, and Fe doping, *J Mater Sci*, 43, 2008, 5385–5389
- [21] O.Parkkima, M.Karppinen -The YBaCo₄O_{7+δ}-Based Functional Oxide Material Family: A Review, *European Journal of Inorganic Chemistry*. 2014, 4056–4067
- [22] S.Rasanen, T.Motohashi, H.Yamahuchi, M.Karppinen – Stability and oxygen storage characteristics of Al substituted YBaCo₄O_{7+δ}, *Journal of Solid State Chemistry*,183, 2010, 692–695
- [23] Z.Rui, J.Ding, L.Fang, Y.S.Lin, Y.Li - YBaCo₄O_{7+δ} sorbent for oxygen-enriched carbon dioxide stream production at a low-temperature, *Fuel*, 94, 2012, 191-196
- [24] L.Hou , Q.Yu, K.Wang , Tianwei Wu, M.Weil , F.Yang - Practicability Study of YBaCo₄O_{7+δ} and Substituted Samples for Chemical Looping Air Separation Process, *Environmental Progress & Sustainable Energy*, 38, 2018, 563-568
- [25] M.Xu, I.Ermanoski, E.B.Stechel, S.Deng -Oxygen pumping characteristics of YBaCo₄O_{7+δ} for solar thermochemical cycles, *Chemical Engineering Journal*, 389, 2020,124026,
- [26] T.Peppel, D.Seeburg, G.Fulda, M.Kraus, U.Trommler, U.Roland, S.Wohlrab - Methods for the Trace Oxygen Removal from Methane-Rich Gas Streams, *Chemical Engineering and Technology*, 40, 2017, 153-161
- [27] B.Bulfin, J.Vieten, C.Agrafiotis, M.Roeb, C.Slatte - Applications and Limitations of Two Step Metal Oxide Thermochemical Redox Cycles; A Review, *Journal of Materials Chemistry A*, 5, 2017, 18951-18966
- [28] D. S. Tsvetkov, P. S. Maram, N. S. Tsvetkova, A. Yu. Zuev, and A. Navrotsky- High-Resolution Thermochemical Study of Phase Stability and Rapid Oxygen Incorporation in YBaCo_{4-x}Zn_xO_{7+δ} 114-Cobaltites, *Journal of Physical Chemistry*,122, 2018, 50, 9597–960
- [29] K.Beppu, S.Hosokawa, A.Demizu, Y.Oshino, K.Tamai, K.Kato, K.Wada, H.Asakura, K.Teramura, T.Tanaka - Striking Oxygen-Release/Storage Properties of Fe-Site-Substituted Sr₃Fe₂O_{7-δ}, *Journal of Physical Chemistry*, 122, 2018, 11186–11193
- [30] M. Hervieu, A. Guesdon, J. Bourgeois, E. Elkaïm, M. Poienar, F. Damay, J. Rouquette, A. Maignan and C. Martin - Oxygen storage capacity and structural flexibility of LuFe₂O_{4+x} (0 ≤ x ≤ 0.5), *nature materials*, 14, 2014, 74-80
- [31] M.Valldor, M.Andersson - The structure of the new compound YBaCo₄O₇ with a magnetic feature, *Solid State Sciences*, 4, 2002 7, 923-931
- [32] O.Chmaissem, H.Zheng, A.Huq, P.W.Stephens, J.F.Mitchell - Formation of Co³⁺ octahedra and tetrahedra in YBaCo₄O_{8.1}, *Journal of Solid State Chemistry*, 181, 2008, 664-672
- [33] A.K.Bera, S.M.Yusuf, S.Banerjee -Short-range magnetic ordering in the geometrically frustrated layered compound YBaCo₄O₇ with an extended Kagomé structure, *Solid State Sciences*, 16, 2013, 57-64
- [34] J.Kim, A.Manthiram - Low Thermal Expansion RBa(Co,M)₄O₇ Cathode Materials Based on Tetrahedral-Site Cobalt Ions for Solid Oxide Fuel Cells, *Chem. Mater*,22, 3,2010, 822–831
- [35] M.Takacs, M.Hoes, M.Caduff, T.Cooper, J.R.Scheffe, A.Steinfeld - Oxygen nonstoichiometry, defect equilibria, and thermodynamic characterization of LaMnO₃ perovskites with Ca/Sr A-site and Al B-site doping, *Acta Materialia*, 103, 2016, 700-710
- [36] I.A.Leonidov, E.IKonstantinova, M.V.Patrakeev, V.LKozhevnikov - Oxygen thermodynamics and defect chemistry of nonstoichiometric manganites Ca_{0.6-y}Sr_{0.4}La_yMnO_{3-δ} Author links open overlay panel, *Journal of Alloys and Compounds*, 690, 2017, 80-85
- [37] M.Oishi, K.Yashiro, K.Sato, J.Mizusaki, T.Kawada - Oxygen nonstoichiometric and defect structure analysis of B-site mixed perovskite-type oxide (La, Sr)(Cr, M)O_{3-δ} (M=Ti, Mn and Fe), *Journal of Solid State Chemistry*, 2008, 181, 3177 – 3184

- [38] L.Schramm, G.Behr, W.Löser, and K.Wetzig - Thermodynamic Reassessment of the Cu-O Phase Diagram, *Journal of Phase Equilibria and Diffusion*, 26, 2005, 605-612
- [39] N.Birkner, A.Navrotsky - Thermodynamics of Manganese Oxides: Effects of Particle Size and Hydration on Oxidation-Reduction Equilibria Among Hausmannite, Bixbyite, and Pyrolusite, *American Mineralogist*, 97, 2012, 1291–1298
- [40] M.Chen, B.Hallstedt, L.J.Gauckler - Thermodynamic Assessment of the Co-O System, *Journal of Phase Equilibria*, 24, 2003, 212- 227
- [41] T.Matthers, K.T. Jacob - Variation of the Partial Thermodynamic Properties of Oxygen with Composition in YBa₂Cu₃O₇, *metallurgical transactions A*, 23, 1992, 3325-3335
- [42] K.Jeanjumnunja, W.Gong, T.Makerenko, A.J.Jacobson – A determination of the oxygen non-stoichiometry of oxygen storage material YBaMn₂O₅, *Journal of solid state chemistry*, 230, 2015, 397-403
- [43] X.Jin, T.Yang, K.Huang - Defect structure, thermodynamic and transport properties of SrCo_{0.9}Nb_{0.1}O_{2.5+δ}: A combined experimental and defect chemistry approach, *Solid State Ionics*, 320, 2018 159–171
- [44] O.V.Merkulov, E.N.Naumovich, M.V.Patrakeev, A.A.Markov, H. J.M.Bouwmeester, I.A.Leonidov, V.L.Kozhevnikova - Oxygen non-stoichiometry and defect chemistry of perovskite-structured SrFe_{1-x}MoxO_{3-δ} solid solutions, *Solid State Ionics*, 292, 2016 116-121
- [45] J. Vietena, B. Bulfina, F. Calla, M. Langea, M. Schmückerb, M. Schmückerb, A. Franckeb, M. Roeba, C.Sattler - Perovskite oxides for application in thermochemical air separation and oxygen storage, *Journal of material chemistry A*, 04, 2016, 13652-13659
- [46] A.Y.Suntsov, B.V.Politov , L.A.Leonidov, M.V.Patrakeev, V.J.Kozhevnikov - Improved stability and defect structure of yttrium doped cobalite PrBaCo₂O_{6-δ}, *Solid state ionics*, 295, 2016, 90-95
- [47] J.Mizusaki, N.Mori, H.Takai, Y.Yonemura, H.Minamiue, H.Tagawa, M.Dokiya, H.Inaba, K.Naraya, T.Sasamoto, T.Hashimoto - Oxygen nonstoichiometry and defect equilibrium in the perovskite-type oxides La Sr MnO, *Solid State Ionics*, 129, 2000, 163–177
- [48] M.B.Choi, D.-K.Lim, E.D.Wachsman, S.J.Song - Oxygen nonstoichiometry and chemical expansion of mixed conducting La_{0.1}Sr_{0.9}Co_{0.8}Fe_{0.2}O_{3-δ}, *Solid State Ionics*, 221, 2012 22-27
- [49] O.V.Murkulov, E.N.Naumovich, A.A.Markov, L.A.Leonidov, M.V.Patrakeev – Oxygen non-stoichiometry and defect structure of perovskite type Ca_{0.25}Sr_{0.75}Fe_{0.75}Mo_{0.25}O_{3-δ}, *Materials letters*, 236, 2019, 719-722
- [50] E.V.Tsipis, M.V.Patrakeev, J.C.Waerenborgh, Y.V.Pivak, A.A.Markov, P.Gaczyński, E.N.Naumovich, V.V.Kharton - Oxygen non-stoichiometry of Ln₄Ni_{2.7}Fe_{0.3}O_{10-δ} (Ln=La, Pr), *Journal of Solid State Chemistry* , 180, 2007 1902-1910
- [51] M.B.Choi, S.Y.Jeon, H..N.Im, S.J.Song - Thermodynamic quantities and oxygen non-stoichiometry of undoped BaTiO_{3-δ} by thermogravimetric analysis, *Journal of Alloys and Compounds*, 513, 2012, 487-494
- [52] S.Rasanen, H.Yamauchi, M.Karppinen - Oxygen Absorption Capability of YBaCo₄O₇, *Chemistry Letters*, 37, 2008, 638-639
- [53] K.Wang, Y.Chen, X.Hu, H.Song, Q.He - Oxygen Resistance Sensor Properties of YBaCo₄O_{7+δ} and Y_{0.5}Tb_{0.5}BaCo₄O_{7+δ}, *Int. Journal of applied ceramic technologies*, 12, 2015, 1184-1188
- [54] T.Chen, Y.Asakura, T.Hasegawa, T.Motohashi, S.Yin - A simple and novel effective strategy using mechanical treatment to improve the oxygen uptake/release rate of YBaCo₄O_{7+δ} for thermochemical cycles, *Journal of Materials Science & Technology*, 68, 2021, 8-15
- [55] B.Bulfin, J.Vieten, D.E.Starr, C.Sattler - Redox chemistry of CaMnO₃ and Ca_{0.8}Sr_{0.2}MnO₃ oxygen storage perovskites, *Journal of Materials Chemistry A* , 5, 2017, 7912-7919

- [56] K.Swierczek, A.Klimkowicz, K.Nishihara, S.Kobayashi, A.Takasaki, M.Alanizy, S. Kolesnik, B. Dabrowski, S.Seonge, J. Kang - Oxygen storage properties of hexagonal $\text{HoMnO}_3+\delta$, *Phys.Chem.Chem.Phys.*, 19, 2017, 19243-19251
- [57] T.Motohashi, Y.Hirano, Y.Masubuchi, K.Oshima, T.Setoyama, S.Kikkawa - Oxygen Storage Capability of Brownmillerite-type $\text{Ca}_2\text{AlMnO}_5+\delta$ and Its Application to Oxygen Enrichment, *Chem. Mater.*, 25, 2013, 372–377
- [58] T. Mattisson, A. Lyngfelt, H. Leion, - Chemical-looping with oxygen uncoupling for combustion of solid fuels, *International Journal of Greenhouse Gas Control*, 3, 2009, 11–19
- Mobility in $\text{YBaCo}_4\text{O}_7+\delta$, *Journal of the American Chemical Society*, 131, 13, 2009, 4880–4883
- [59] H.Song, K.Shah, E.Doroodchi, T.Wall, B.Moghtaderi - Reactivity of Al_2O_3 - or SiO_2 -Supported Cu-, Mn-, and Co-Based Oxygen Carriers for Chemical Looping Air Separation, *Energy Fuels* 28, 2, 2014, 1284–1294
- [60] Z.Rui, J.Ding, L.Fang, Y.S. Lin, Y.Li - $\text{YBaCo}_4\text{O}_7+\delta$ sorbent for oxygen-enriched carbon dioxide stream production at a low-temperature, *Fuel*, 94, 2012, 191-196
- [61] A. V. Alekseev, M. Yu. Kameneva, L. P. Kozeeva, A. N. Lavrov, N. V. Podberezskaya, A. I. Smolentsev, A. N. Shmakov - Structural Phase Transitions in $\text{YBaCo}_4\text{O}_7 + x$ Cobaltate upon Variations in Oxygen Content, According to XRay Diffraction Data Obtained Using Synchrotron Radiation, *Bulletin of the Russian Academy of Sciences. Physics*, 77, 2013, 151–15
- [62] N. V. Podberezskaya, N. B. Bolotina, V. Yu. Komarova, M. Yu. Kamenevaa, L. P. Kozeevaa, A. N. Lavrova, A. I. Smolentseva - Orthorhombic $\text{YBaCo}_4\text{O}_{8.4}$ Crystals As a Result of Saturation of Hexagonal YBaCo_4O_7 Crystals with Oxygen, *Crystallography Reports*, 60, 2015, 484–492
- [63] C.Looney, J.E. Kline, F.Mascarenhas, J. Schilling, A.Hermann - Influence of oxygen content on the activation energy for oxygen ordering in $\text{Tl}_2\text{Ba}_2\text{CuO}_6$, *Physica C-superconductivity and Its Applications*, 351, 2001,215-226
- [64] T.Wang, J.Cao, X.Gou -Activation energy of oxygen diffusion: A possible indicator of supercurrents through $\text{YBa}_2\text{Cu}_3\text{O}_7$ grain boundaries, *Applied Surface Science*, 480, 2019, 765-769
- [65] Y.Jia, H.Jiang, M.Valkeapää, H.Yamauchi, M.Karppinen, E.I. Kauppinen - Oxygen ordering and mobility in $\text{YBaCo}_4\text{O}_7+\delta$, *Journal of the American Chemical Society*, 131,13,2009,4880-4883
- [66] E.I.Goldyreva, I.A.Leonidov, M.V.Patrakeev, V.L.Kozhevnikov - Oxygen non-stoichiometry and defect equilibria in $\text{CaMnO}_3-\delta$, *Journal of solid state Electrochemistry*, 16, 2012, 1187–1191
- [67] M. Takacs, M. Hoes, M. Caduff, T. Cooper, J.R. Scheffe, A. Steinfeld - Oxygen nonstoichiometry, defect equilibria, and thermodynamic characterization of LaMnO_3 perovskites with Ca/Sr A-site and Al B-site doping, *Acta Materialia*, 103, 2016, 700-710
- [68] A.Klimkowicz, T.Hashizume, K.Cichy - Oxygen separation from air by the combined temperature swing and pressure swing processes using oxygen storage materials $\text{Y}_{1-x}(\text{Tb/Ce})_x\text{MnO}_3+\delta$, *Journal of Material Science*, 55, 2020, 15653–15666
- [69] A.Sato, G.Saito, K.Abe, Y.Kunisada, N.Sakaguchi, T.Akiyama, T.Nomura -Rapid oxygen storage and release with Brownmillerite-structured $\text{Ca}_2\text{AlMnO}_5$, *Journal of Alloys and Compounds*, 851, 2021, 156817
- [70] H.Song, J.Jia, S.Zhang, D.Yang, H.Sun - X.Hu Remarkable oxygen adsorption/desorption capability of $\text{Y}_0.5\text{Tb}_0.5\text{BaCo}_4\text{O}_7+\delta$ under temperature cycles, *Materials Research Bulletin* 47, 3, 2012, 518-520
- [71] A. Klimkowicz, K. Świerczek, S. Kobayashi, A. Takasaki, W. Allahyani, B. Dabrowski -Improvement of oxygen storage properties of hexagonal $\text{YMnO}_3+\delta$ by microstructural modifications, *Journal of Solid State Chemistry*, 258, 2018, 471-476
- [72] L.Hou, Q.Yu, K.Wang, Q.Zhenfei, Q.Qin & W.Tianwei - Optimal synthesis of YBaCo_4O_7 oxygen carrier for chemical looping air separation, *Energy Sources, Part A: Recovery, Utilization, and Environmental Effects*, 40,19, 2019, 2354-2366

Chapter 7 – An investigation into the stability and use of non-stoichiometric $\text{YBaCo}_4\text{O}_{7+\delta}$ for oxygen enrichment processes

During this chapter, the use of $\text{YBaCo}_4\text{O}_{7+\delta}$ for engineering processes is studied. This work builds upon the thermodynamic and structural investigations shown in Chapter 6, which showed useful oxygen capacity accessible on practical timescales by both temperature and pressure swings below 400°C. One promising application for this reversible oxygen capacity is for oxygen enrichment of process gas streams. This chapter aims to investigate the use of the rapid oxygen release features of YBaCo_4O_7 previously studied to use this as a process stream oxygen enricher.

During this work, the stability, kinetics, and cycling regimes were investigated. Initially, the stability of the material in both CO_2 and other reducing gases (CO and H_2) was investigated by the use of temperature-programmed reductions (TPRs). To obtain the most effective way to cycle the material, oxygen uptake and release were studied by changing oxygen partial pressures ($p\text{O}_2$) and temperatures. To demonstrate the potential for employing this reversible oxygen capacity, the material was successfully used to supply oxygen into a gas stream with a $p\text{O}_2$ of 0.31 bar after oxidation in an airstream ($p\text{O}_2 = 0.21$ bar). Finally, the material stability over multiple cycles in a variety of cycling schemes was performed to determine the most effective way to cycle the material for long lifetimes.

A paper from the work in this chapter has been published by the author and supervisors in Solid State Ionics. The title of the paper is “An investigation into the stability and use of non-stoichiometric $\text{YBaCo}_4\text{O}_{7+\delta}$ for oxygen enrichment processes”, by - S.R.W.Johnston, B.Ray, W.Hu, I.S.Metcalf, published in SSI, in 2018.

7.1 Introduction

Many chemical processes benefit from oxygen enrichment. Examples of these are,

- the oxygen-enhanced water gas shift reaction (OWGS) [1-2]
- auto-thermal reforming of methane (ATR) [3]
- the removal of H₂S from a gas stream (Claus reaction) [4-5]
- ammonia synthesis [6]
- oxy-fuel combustion [7]

From the literature review performed in Chapter 1, the CLAS process for producing oxygen was selected for further study, to enrich CO₂ gas streams for oxy-fuel combustion. The potential benefit of reducing the cost of oxygen production is significant in making this process cost-effective [8-9], as oxy-fuel combustion has been demonstrated to have significant potential as a CO₂ capture technology [10-12].

The major advantages of YBaCo₄O₇ for oxygen enrichment were seen in chapter 5, namely, a low temperature of operation, high efficiency of oxygen use, and a large amount of oxygen released per °C temperature swing compared to other oxygen carriers.

This chapter aims to determine the feasibility of using the interesting thermodynamic properties highlighted in Chapter 6 for oxygen enrichment. Firstly, the stability of the material will be investigated by TPR studies. After this analysis, cycling schemes to take advantage of the thermodynamics of YBaCo₄O₇ will be explored over multiple redox cycles. Finally, the kinetics of the system will be examined. Through all this work, it is important to note that a pO₂ of between 0.31 and 0.42 bar is essential for oxyfuel combustion, otherwise, the flame will be snuffed [13-14].

7.2 Results and discussion

7.2.1 Material stability

During oxygen enrichment processes, high concentrations of different reducing gases may be present, and it is important to ensure any materials that may be in contact with them are stable enough to prevent degradation. Of interest is CO₂ and CO which are produced in large quantities from any carbon-based combustion. However, combustion often produces water vapour, which in several important processes such as steel production using blast furnaces, can be reduced to H₂ due to the water having its oxygen stripped by the iron [15]. Stability in

water vapour will also be examined, as several oxy-fuel combustion systems see a benefit in having high moisture content [16-17]

The results of several TPRs of $\text{YBaCo}_4\text{O}_{7+\delta}$ in these reactive gases potentially found in an exhaust stream from potential oxy-fuel combustion processes are shown in Figure 7.1.

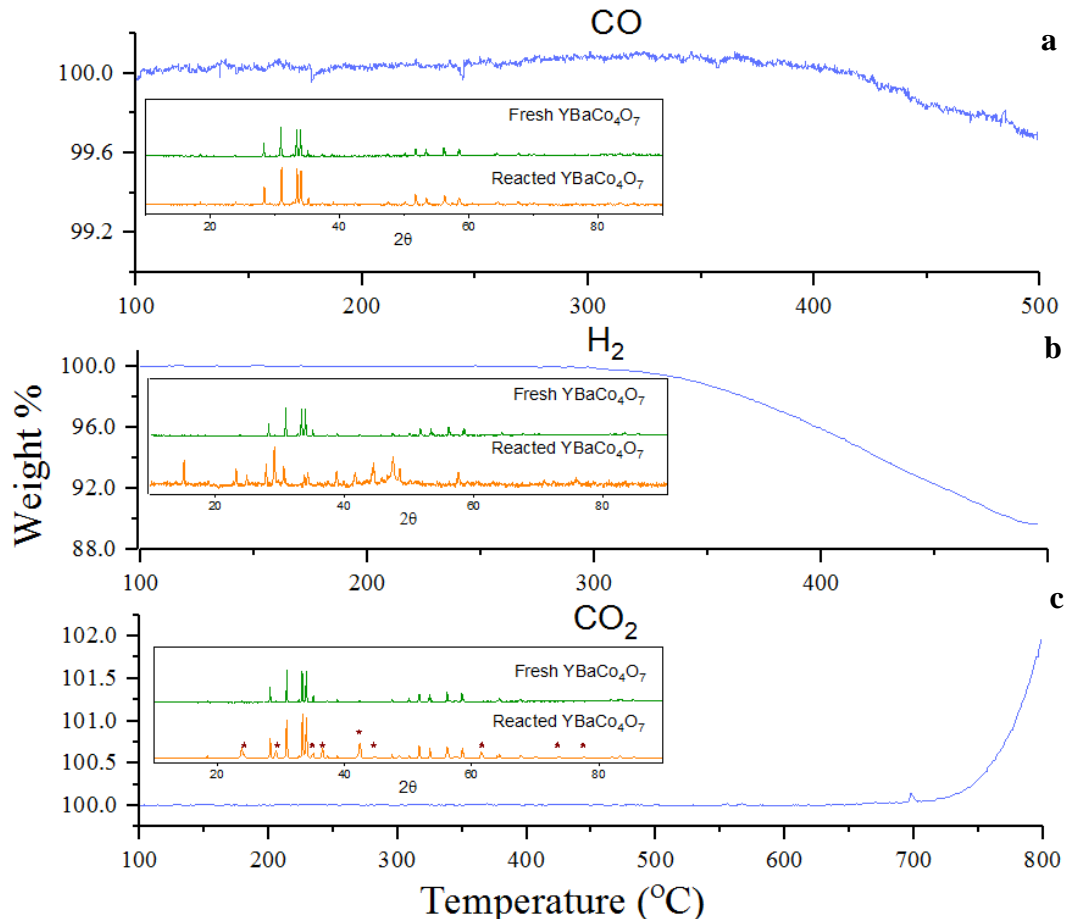


Figure 7.1 – Dynamic TG curves showing the mass change versus temperature of $\text{YBaCo}_4\text{O}_{7+\delta}$ heated at a ramp rate of 1 °C/min in (a), $p_{\text{CO}} = 0.05$ bar, (b), $p_{\text{H}_2} = 0.05$ bar, (c), $p_{\text{CO}_2} = 0.5$ bar (balance He). Inserts show XRD results of fresh powder and powder after each treatment. Peaks corresponding to barium carbonate are identified by a ★

Figure 7.1(a) shows that upon heating in a $p_{\text{CO}} = 0.05$ bar, the sample mass of $\text{YBaCo}_4\text{O}_{7+\delta}$ was constant until approximately 250°C. Upon further heating, a small weight gain of approximately 0.1% was observed. This weight gain was attributed to the deposition of carbon on the surface of the material via the Boudouard reaction [18] which was confirmed by EDX measurements which showed increased carbon loading on the treated sample when compared to fresh powder. Further heating of the sample between 350°C and 500°C caused the sample mass to decrease slightly to 99.6% of the initial mass, likely due to the reduction of the material by CO. The insert in Figure 7.1(a) compares the XRD patterns of a sample treated in helium only and the sample after the treatment in CO with no new phases detected.

This suggests that the material has good stability in relatively high concentrations of CO, although longer-term testing may be needed.

Figure 7.1 (b) shows the weight change of YBaCo_4O_7 upon heating in a $p\text{H}_2 = 0.05$ bar, the sample mass of $\text{YBaCo}_4\text{O}_{7+\delta}$ was stable until approximately 300 °C. Upon heating the sample above 300°C, a decrease in the sample mass at a constant rate was observed, until the sample mass stabilised at approximately 480°C. At this point, approximately 10% of the sample mass was lost. The insert in Figure 7.1(b) shows multiple new phases forming, along with the loss of the initial peaks associated with $\text{YBaCo}_4\text{O}_{7+\delta}$, indicating significant phase changes have occurred upon reduction. The full phase fitting can be found in Appendix A, however, all peaks were not identifiable. It is believed this is due to a reduced complex phase and thus has lattice parameters significantly different from those in known structural databases, and therefore isn't easily matched. From those that were found a mixture of reduced cobalt, barium and yttria phases were found.

In Figure 7.1(c), the weight change of $\text{YBaCo}_4\text{O}_{7+\delta}$ heated at a rate of 1 °C/min in a $p\text{CO}_2$ of 0.5 bar is shown. It can be seen, that the sample mass was stable upon heating until approximately 650°C, 250°C higher than the likely operating temperature of the material. Further heating caused the sample mass to increase by 2%, due to the formation of barium carbonate shown by the XRD patterns in the insert in Figure 7.1(c).

Additionally, the material's stability in water vapour was tested by exposing approximately 1 g of the material in a packed bed (internal diameter 5 mm) to a $p\text{H}_2\text{O}$ of 0.05 bar, balanced in Ar (99.995% purity) at 450°C for 3 hours, with a flow rate of 2×10^{-3} mol/min. Post-treatment, the sample was cooled in argon and underwent XRD analysis, where no new phases were detected. For many oxygen production processes, high-temperature steam is used as a sweep gas for a process, as it is easy to separate later, so stability in water to these temperatures is important.

7.2.2 Isothermal oxygen incorporation/release experiments

The rate of oxygen incorporation and release for $\text{YBaCo}_4\text{O}_{7+\delta}$ was investigated by gas switching experiments. Isothermal gas switching experiments were conducted in a TGA at temperatures between 270 to 330°C. After a helium pre-treatment described in Chapter 4, a sample was allowed to dwell for 1 hour in an air flow of 200ml/min ($p\text{O}_2 = 0.21$ bar) to allow oxygen incorporation, before the $p\text{O}_2$ was lowered by switching the gas environment to helium to release this oxygen. The results of this gas switching experiment can be seen in Figure 7.2, with Figure 7.2(a) showing the mass change during the oxidising isotherm, and

Figure 7.2 (b) showing the oxygen loss after this oxidising step when the gas environment was switched to helium.

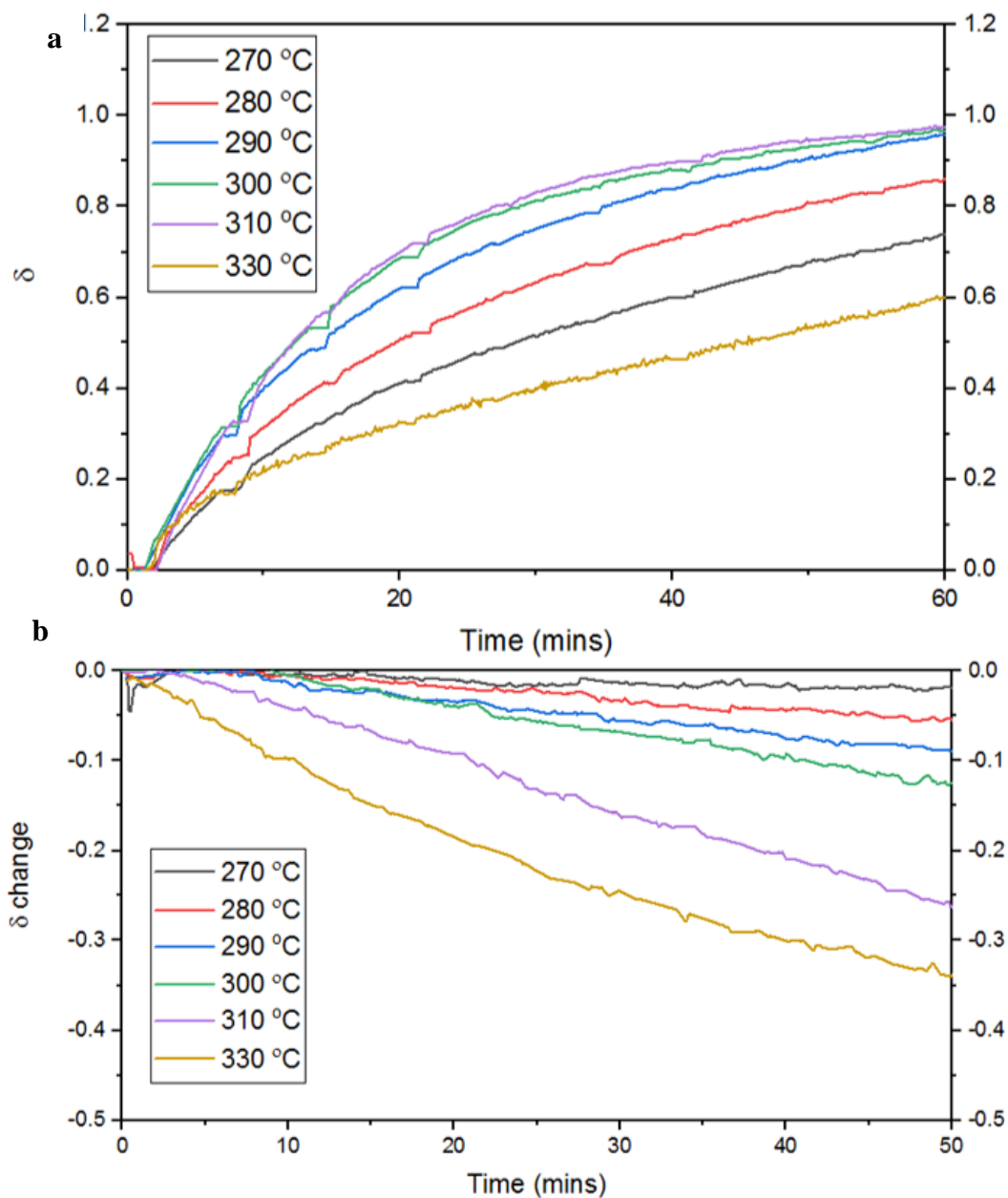


Figure 7.2 (a) - TG curves showing δ versus time for isothermal holds of $\text{YBaCo}_4\text{O}_{7+\delta}$ held in a $p\text{O}_2$ of 0.21 bar between 270 and 330 °C, (b) – TG curves showing δ change versus time for isothermal holds of $\text{YBaCo}_4\text{O}_{7+\delta}$ held in helium at temperatures between 270 and 330 °C after oxygen incorporation shown in Figure 7.2(a)

Figure 7.2 (a) shows how the rate of oxygen incorporation of $\text{YBaCo}_4\text{O}_{7+\delta}$ in a $p\text{O}_2$ of 0.21 bar changes with temperature. The fastest oxygen incorporation rate occurred at temperatures between 290 and 310°C, with the δ increasing to between 0.96 and 0.98 after 1 hour. An increase of the temperature by 20°C to 330°C decreased the rate of oxygen incorporation significantly, with 40% less oxygen incorporated during the hour dwell. Likewise, with temperatures below 290°C, the rate of oxygen incorporation slowed with a decrease of 20°C

reducing the incorporation rate by 25%. Figure 7.2 (b) shows how the rate of oxygen release from $\text{YBaCo}_4\text{O}_{7+\delta}$ changes with temperature. The rate of oxygen release appeared linear during each temperature. The rate of oxygen loss was slow at temperatures below 280°C , with an equivalent change in δ less than 0.02 over 1 hour. The amount of oxygen released increased upon heating, with the rate of oxygen release at 330°C being significantly faster than lower temperatures. The faster oxygen incorporation rates at 310°C are likely due to a mixture of kinetics and thermodynamics. From chapter 6, it was seen that at lower temperatures, the material has a greater chemical potential driving oxygen incorporation, likely speeding up diffusion. Conversely, at higher temperatures, there will be more energy, so chemical changes generally occur faster. Therefore, this intermediate temperature incorporating oxygen more quickly is likely a combination of the two effects. Conversely, the faster oxygen release rates at higher temperatures are likely a mixture of both thermodynamic and kinetics. Higher temperatures will provide more energy for oxygen release and create a greater driving force to release oxygen from the material. Similar behaviour is seen in metal oxide systems, where oxidation is favoured at lower temperatures, and reduction at higher temperatures [19-20].

7.2.3 Investigation into the effect of $p\text{O}_2$ on the useful oxygen release of $\text{YBaCo}_4\text{O}_{7+\delta}$

Due to the hysteresis of the oxygen content, it will be necessary to use the rapid oxygen feature of $\text{YBaCo}_4\text{O}_{7+\delta}$ to obtain the high $p\text{O}_2$ s required to allow oxy-fuel combustion and isothermal oxygen. It is therefore important to know the lower temperature limit to obtain the $p\text{O}_2$ s required. To determine the effect of $p\text{O}_2$ on the temperature of the material's oxygen release, a sample of $\text{YBaCo}_4\text{O}_{7+\delta}$ was held at 300°C for 10 hours in $p\text{O}_2$ s ranging from 0.05 to 0.42 bar, before being heated in the same $p\text{O}_2$ in 5°C steps, each lasting 1 hour. The results of this experiment can be seen in Figure 7.3 and shows how the temperature of rapid oxygen release changes with $p\text{O}_2$. Heating the sample above this oxygen release temperature for a given $p\text{O}_2$ causes the material to release oxygen into the gas environment, increasing the $p\text{O}_2$ of the gas stream.

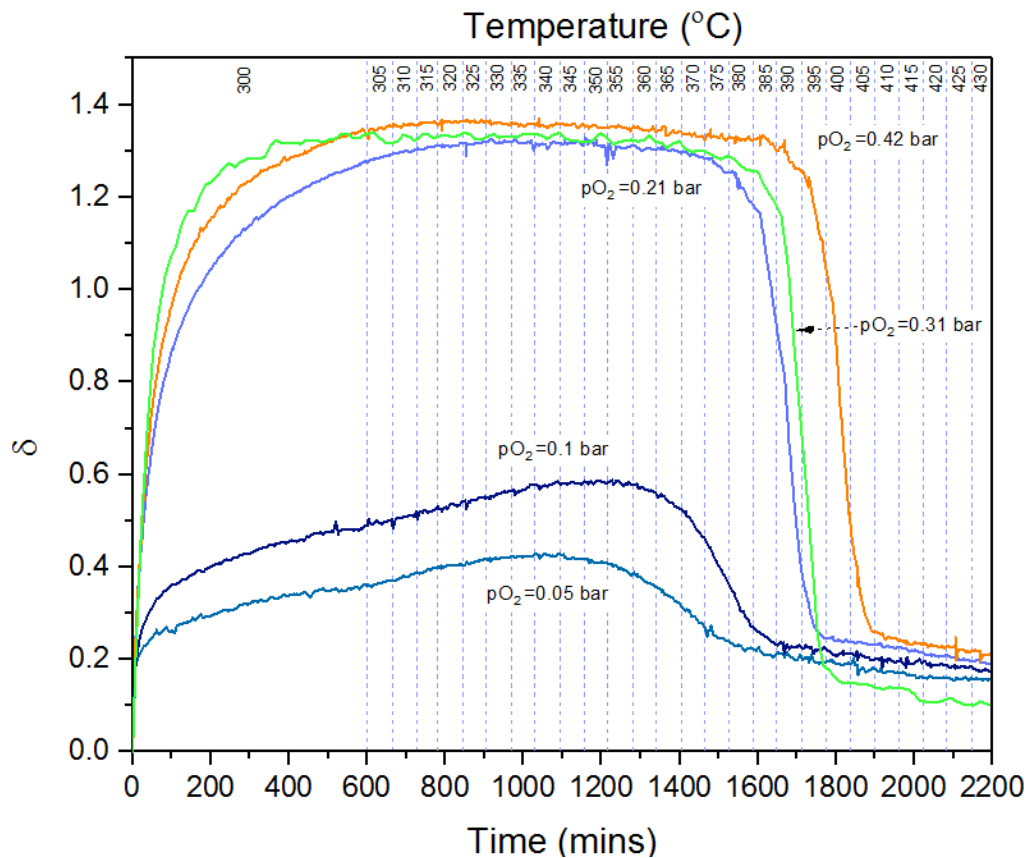


Figure 7.3 –TG curves showing δ versus time for $\text{YBaCo}_4\text{O}_{7+\delta}$ heated in hour-long 5°C steps from 300°C to 430°C with $p\text{O}_2$ s ranging from 0.05 to 0.42 bar after an initial 10 hour oxygen annealing in the same $p\text{O}_2$. The oxygen incorporation and release behaviour of the sample in each $p\text{O}_2$ behaves similarly. In each $p\text{O}_2$, large amounts of O_2 were incorporated at low temperatures (between 300 and 320°C). The sample maintains this δ upon heating until the rapid oxygen loss temperature is reached. From this experiment, it appears that this temperature is 370°C in a $p\text{O}_2$ of 0.21 bar, and 380°C for 0.3 bar (the minimum for oxy-fuel combustion). These temperatures of oxygen release match those seen in Chapter 6. Oxygen release temperatures increase with increased $p\text{O}_2$, again matching what was seen in Chapter 6. This figure clearly shows that oxygen release into the higher $p\text{O}_2$ s required for oxy-fuel combustion are accessible by use of a temperature swing in practical timescales if the material is heated above approximately 390°C during the oxygen release step.

7.2.4 Method of using YBaCo_4O_7 for oxygen enrichment processes

The effects of $p\text{O}_2$ and temperature on the oxygen incorporation/release behaviour of $\text{YBaCo}_4\text{O}_{7+\delta}$ have been investigated and show clear potential for $\text{YBaCo}_4\text{O}_{7+\delta}$ to be used for oxy-fuel combustion. From the data shown in Figure 7.2 and 7.3, a temperature swing, incorporating oxygen at 310°C and releasing this incorporated oxygen above 380°C would be able to inject oxygen not a gas stream with $p\text{O}_2 = 0.31$ bar, however, faster rates of oxygen

release would be found at higher reduction temperatures. To demonstrate a working cycle, a sample was cycled between an oxidising step at 310 °C in a pO_2 of 0.21 bar before heating to 430°C in a pO_2 of 0.31 bar to release this incorporated oxygen, shown in Figure 7.4.

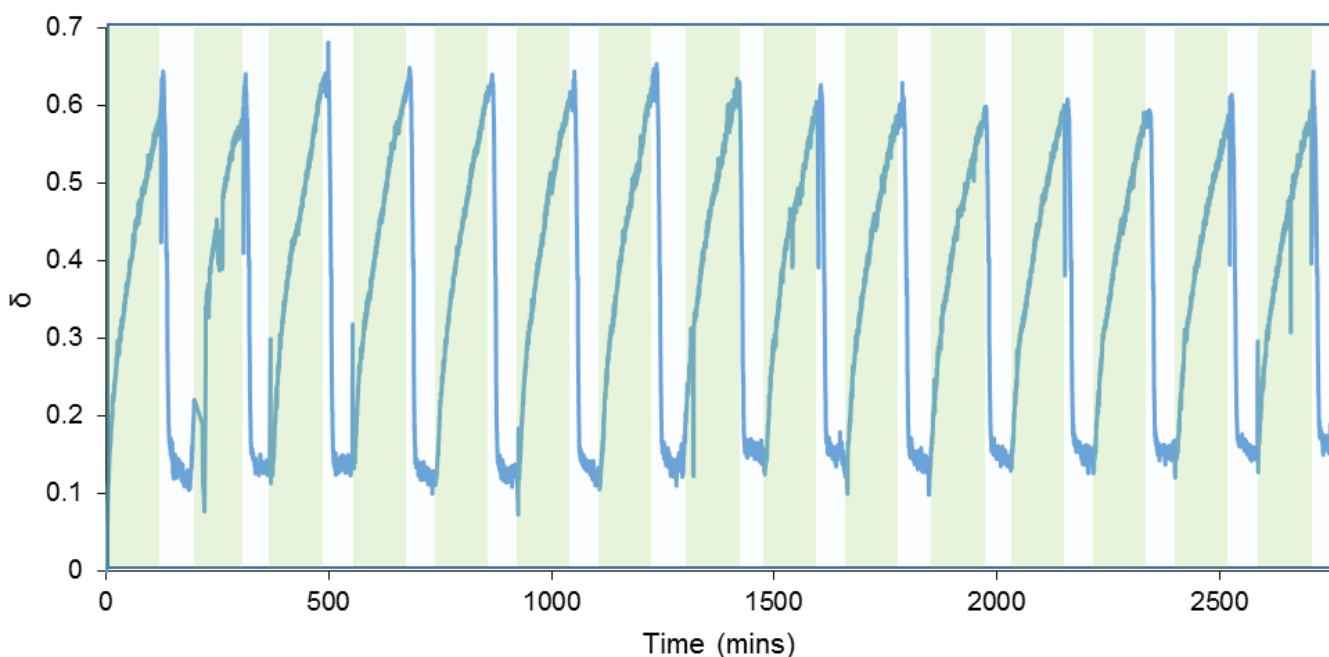


Figure 7.4 - TG curves showing δ versus time for $YBaCo_4O_{7+\delta}$ cycling between 120 minutes long holds in a pO_2 of 0.21 bar at 310 °C (pale green rectangles) before being heated at a rate of 20°C/min to 430°C in a pO_2 of 0.31 bar (pale blue rectangles)

During this cycling, the sample was oxidised to a δ of approximately 0.6 in a pO_2 of 0.21 bar, before releasing the oxygen during the heating phase in a pO_2 of 0.31 bar to give a final δ of 0.17. This change in mass is equal to approximately 1.5%, clearly demonstrating $YBaCo_4O_{7+\delta}$ is suitable for use for oxygen enrichment processes such as oxy-fuel combustion.

Figure 7.4 shows a drop in the amount of oxygen incorporated and released, and the amount of oxygen cycled decreasing over the 15 cycles (45 operational hours). Table 7.3 compares the maximum and minimum δ values obtained during the 3rd and 11th cycles. These cycles were chosen as the 3rd cycle incorporated and released the most oxygen during the experiment and the 11th cycle showed the greatest drop in capacity compared to the previous cycles. The 11th cycle also appears representative of the subsequent cycles which do not show further loss of performance.

Table 7.3 – List of δ 's obtained during the 3rd and 11th incorporation and release cycles shown in Figure 7.4

Parameter	Cycle 3	Cycle 11
δ Max	0.64	0.57
δ Min	0.12	0.15
Change in δ	0.52	0.42

The decrease in the amount of oxygen transferred during the first 10 cycles suggests there may be potential issues with the long-term stability of the material which required further investigation. This loss of activity was unexpected due to the low operating temperatures of the material and further investigations into the cause are required.

7.2.5 Reducing the temperature swing required for redox cycling

Figure 7.4 of this work showed clearly a potential operational scheme for the use of YBaCo_4O_7 for oxygen enrichment processes. This method however requires a temperature swing of approximately 100°C , reducing the efficiency of this material for oxygen enrichment processes. From Chapter 6, it was shown that thermodynamically a cycle of approximately 30°C could give a change in oxygen capacity equivalent to over 2% w/w. Unfortunately, due to low rates of oxygen incorporations at 350°C , this has seemed unfeasible. Figure 6.3 demonstrated that at higher $p\text{O}_2$'s, the rate of oxygen incorporation increased at higher temperatures, and this is investigated further in Figure 7.5 by isothermal oxygen incorporation experiments.

A sample was held isothermally at temperatures ranging between 330 and 370°C in a $p\text{O}_2$ of either 0.21 or 0.42 bar, after helium pre-treatment to allow oxygen incorporation.

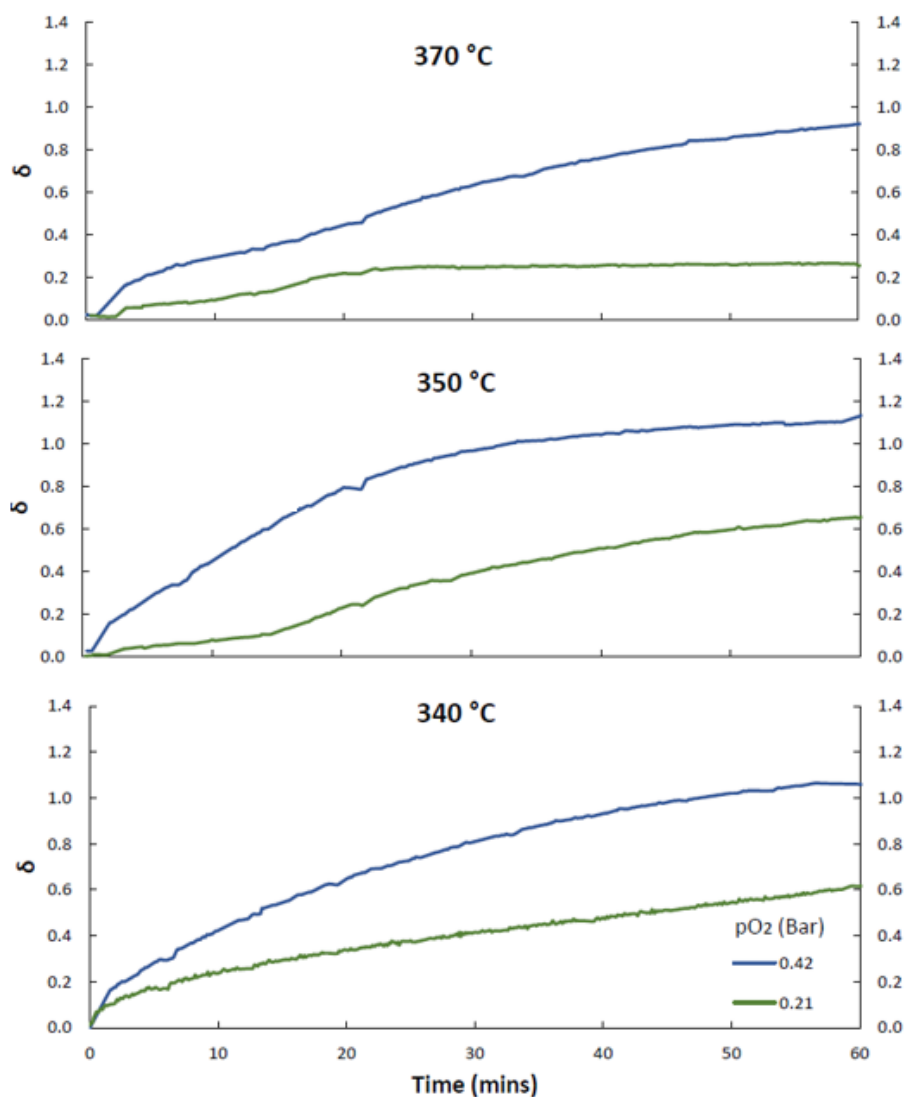


Figure 7.5 - TG curves showing δ versus time for isothermal holds of $YBaCo_4O_{7+\delta}$ held in a pO_2 of 0.21 or 0.42 bar between 340 and 370°C

As seen previously in Figure 7.2, oxygen incorporation in a pO_2 of 0.21 at these temperatures was seen to be slow. An increase of the pO_2 to 0.42 was seen to double the oxygen incorporation rate of the material at each temperature, giving equivalent δ 's to those seen at 310°C at 0.21 bar in Figure 7.2, with a minimal increase in the operating pressure.

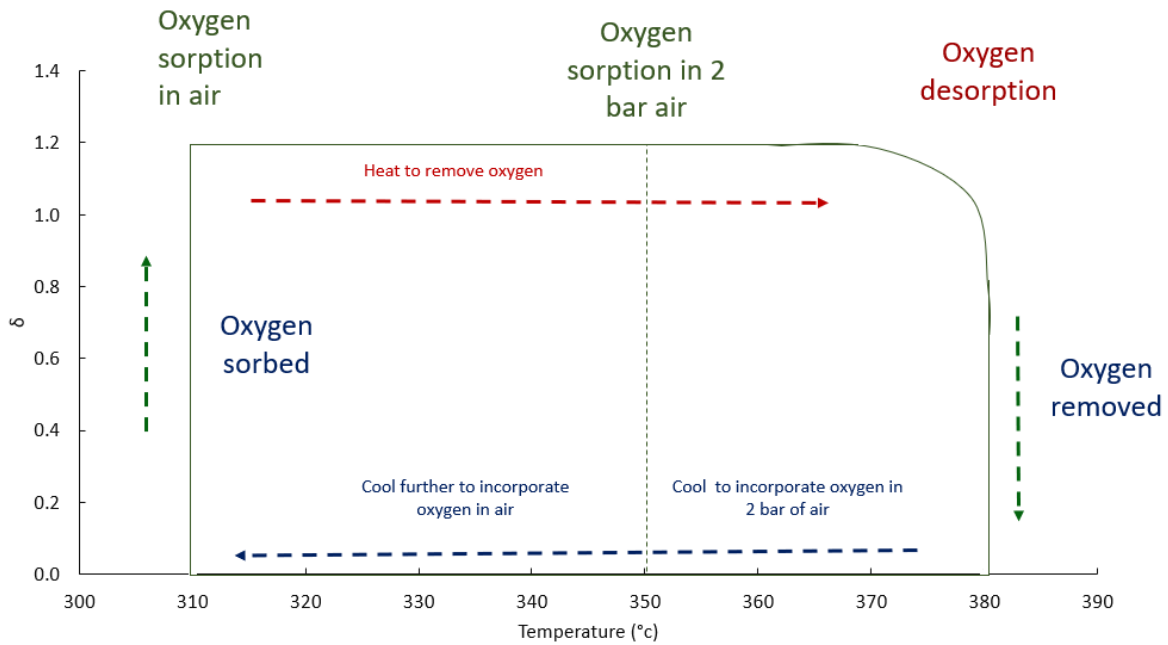


Figure 7.6 – Schematic show idealised methods for oxygen cycling using YBaCo₄O₇

As shown, a narrower temperature swing can be afforded if a higher oxygen incorporation pO_2 is used. The possible advantages of this reduced temperature swing are multiple, including lower energy costs and potential increased material stability, due to smaller temperature changes. This will however reduce the efficiency of the oxygen incorporation, and a higher pO_2 gas will exit the reactor, which will impact efficiency [21]. To demonstrate, two redox cycling methods were performed with YBaCo₄O₇, and these are shown in Figure 7.7. The first method incorporated oxygen at 0.21 bar at 310°C, the second allowed incorporation to occur at 0.42 bar at 350°C. The incorporated oxygen was then released by a temperature swing in inert, heating the sample at 20°C/min to 370°C.

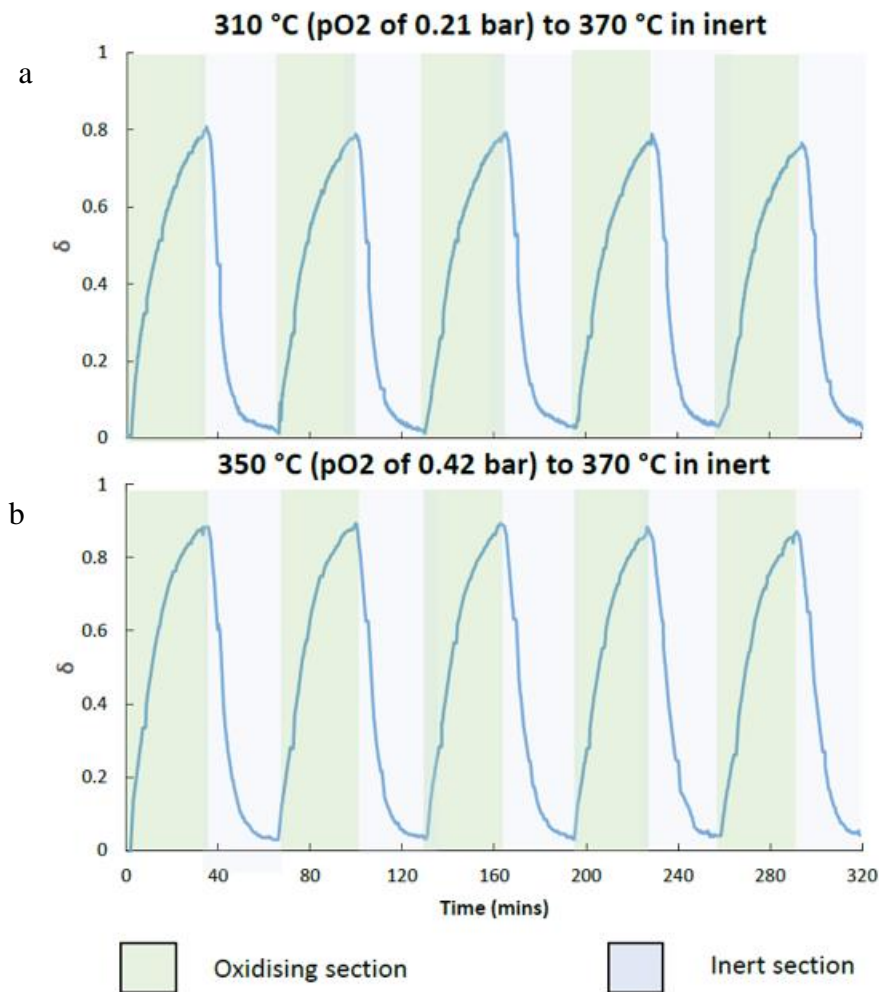


Figure 7.7 (a) - TG curves showing δ versus time for $\text{YBaCo}_4\text{O}_{7+\delta}$ cycling between 30 minutes long holds in a pO_2 of 0.21 bar at 310 °C (pale green rectangles) before being heated at a rate of 20 °C/min to 370 °C in an inert (pale blue rectangles), **(b)** TG curves showing δ versus time for $\text{YBaCo}_4\text{O}_{7+\delta}$ cycling between 30 minute long holds in a pO_2 of 0.42 bar at 350 °C (pale green rectangles) before being heated at a rate of 20 °C/min to 370 °C in inert (pale blue rectangles)

Figure 7.7 (a) and (b) shows similar oxygen uptake and release behaviour over cycling, with the oxidative cycles of 350 °C and 0.42 bar incorporating slightly more oxygen. With a combined pressure/temperature swing as shown, the required temperature swing can be significantly reduced.

7.2.6 Stability of $\text{YBaCo}_4\text{O}_{7+\delta}$ over multiple redox cycles

Figure 7.4 showed a drop in the amount of oxygen incorporated and released over 15 redox cycles, between a $p\text{O}_2$ of 0.21 bar at 310°C, and 430°C in a $p\text{O}_2$ of 0.31 bar, simulating the oxy-fuel combustion process conditions.

To investigate this loss of performance, 30 redox cycles were performed using helium pre-treated $\text{YBaCo}_4\text{O}_{7+\delta}$. A sample was heated from 310 to 430°C in argon, after which it was allowed to dwell isothermally for 54 minutes to release oxygen. The sample was subsequently cooled from 430 to 310°C, after which the sample was allowed to dwell isothermally for 105 minutes in a $p\text{O}_2$ of 0.21 bar, to re-incorporate the oxygen. The results of this cycling are shown in Figure 7.8.

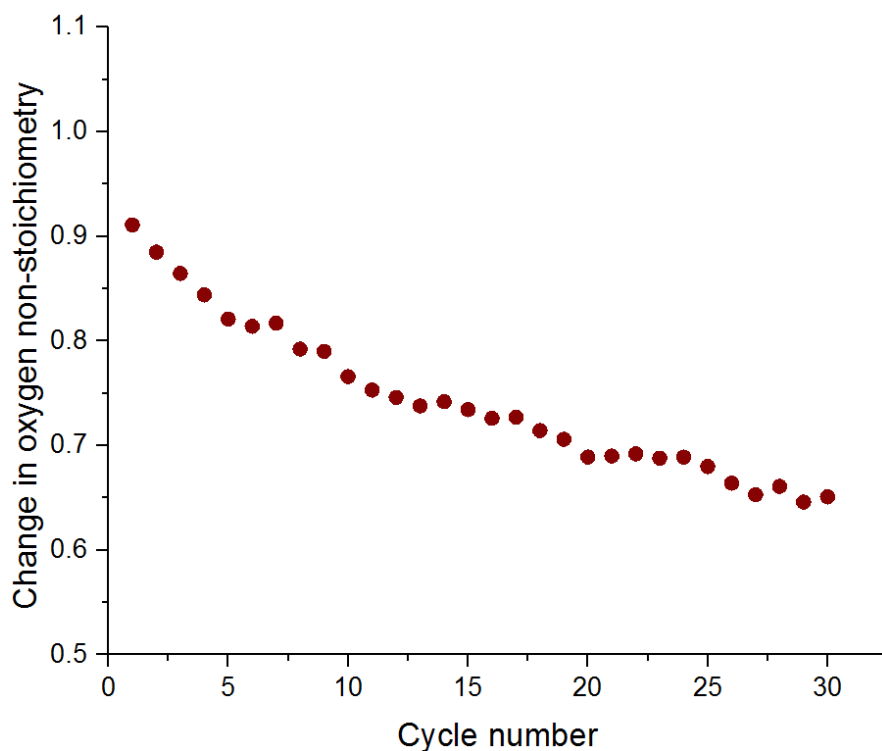


Figure 7.8 – Change in the oxygen non-stoichiometry ($\Delta\delta$) per cycle versus the cycle number, for $\text{YBaCo}_4\text{O}_{7+\delta}$ cycling between a $p\text{O}_2$ of 0.21 bar at 310°C and argon at 430°C. The sample was heated from 310°C at a rate of 20°C/min in argon until 430°C, at which point the sample was held isothermally for 54 minutes to remove the incorporated oxygen. The sample was subsequently cooled in a $p\text{O}_2$ of 0.21 bar to 310°C taking approximately 15 minutes, at which point the sample was held isothermally for 105 minutes.

Figure 7.8 shows a decrease in oxygen cycled over the experiment. During the initial cycle, the sample incorporated oxygen equal to a change of $\delta = 0.92$. This amount decreased rapidly over further cycling, with the material achieving a change in δ of 0.69 after 30 cycles, a drop of 29%.

To investigate whether isothermal oxygen incorporation could prevent this performance loss, 30 redox cycles were performed using pre-treated $\text{YBaCo}_4\text{O}_{7+\delta}$, heating a sample from 310 to 430°C in argon after which it was allowed to dwell for 54 minutes to release oxygen. The sample was then cooled in argon to 310°C, different from that shown in Figure 7.8, where the sample was cooled in a $p\text{O}_2$ of 0.21 bar. The gas environment was subsequently switched to a $p\text{O}_2$ of 0.21 bar at 310°C where the sample was allowed to incorporate oxygen isothermally for 120 minutes. The results of this cycling can be seen in Figure 7.9.

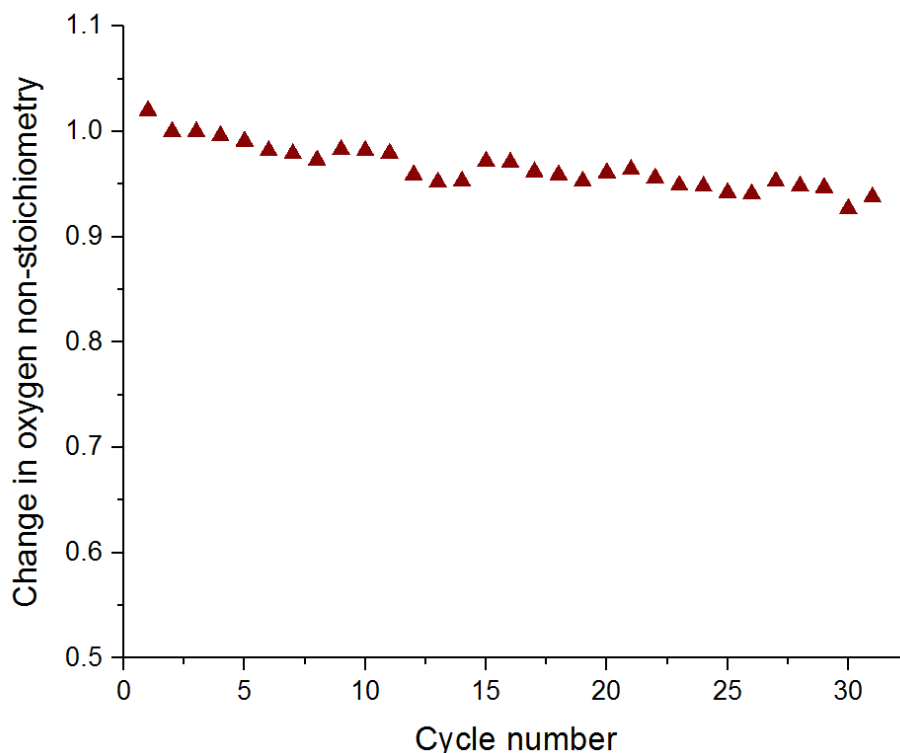


Figure 7.9 – Change in the oxygen non-stoichiometry ($\Delta\delta$) per cycle versus the cycle number, for $\text{YBaCo}_4\text{O}_{7+\delta}$ cycling between a $p\text{O}_2$ of 0.21 bar at 310°C and argon at 430°C. The sample was heated from 310°C at a rate of 20°C/min in argon until 430°C, at which point the sample was held isothermally for 54 minutes to remove the incorporated oxygen. The sample was subsequently cooled in argon for 60 minutes until it reached 310°C. The gas environment was then switched from argon to a $p\text{O}_2$ of 0.21 bar where the sample was held isothermally for 120 minutes

The cycling scheme shown in Figure 7.9 shows improved cycling stability relative to Figure 7.8, however, a 9% decrease in performance over the 30 cycles was still. To show the repeatability of this behaviour, 20 redox cycles were performed. The first ten of these cycles were performed using the cycling scheme seen in Figure 7.9, where oxygen incorporation occurred isothermally and cooling was performed in inert. The final ten cycles were performed using the cycling scheme shown in Figure 7.8, where the material was cooled in oxygen.

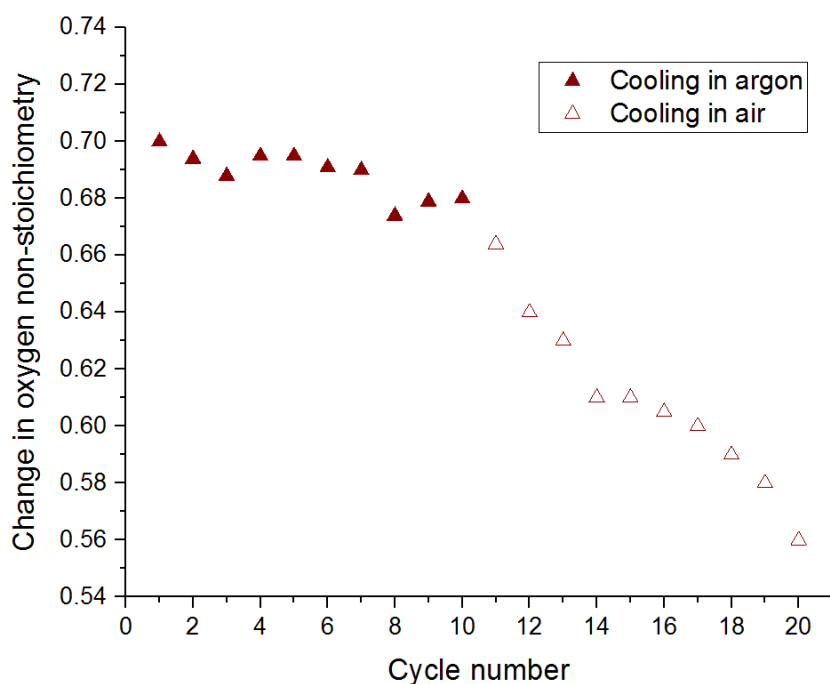


Figure 7.10 - Change in the oxygen non-stoichiometry ($\Delta\delta$) per cycle versus the cycle number, for $\text{YBaCo}_4\text{O}_{7+\delta}$ cycling between a $p\text{O}_2$ of 0.21 bar at 310°C and argon at 430°C . For the first ten cycles, the sample was heated from 310°C at a rate of $20^\circ\text{C}/\text{min}$ in argon until 430°C , at which point the sample was held isothermally for 54 minutes to remove the incorporated oxygen. The sample was subsequently cooled in argon for 60 minutes until it reached 310°C . The gas environment was then switched from argon to a $p\text{O}_2$ of 0.21 bar where the sample was held isothermally for 120 minutes. For the final ten cycles the sample was heated from 310°C at a rate of $20^\circ\text{C}/\text{min}$ in argon until 430°C , at which point the sample was held isothermally for 54 minutes to remove the incorporated oxygen. The sample was subsequently cooled in a $p\text{O}_2$ of 0.21 bar to 310°C taking approximately 15 minutes, at which point the sample was held isothermally for 105 minutes.

During the first ten cycles of Figure 7.10, there was a steady decrease in the amount of oxygen cycled, with a change in the oxygen content of 0.02, consistent with the data shown in Figure 7.9. When the cycling method was changed to cool the material in a $p\text{O}_2$ of 0.21 bar, the rate of degradation increased, and the amount of oxygen cycled dropped by a δ of over 0.1 during the subsequent 10 cycles, five times faster than previously. This result supports the results shown in Figures 7.8 and 7.9 that a difference between the cycling schemes was responsible for this increased rate of degradation.

A large driver for the use of YBaCo_4O_7 is the potential improvement to stability due to the low operating temperature. The current results to this point do not show this desired behaviour. Additionally, if an inert gas is required for steady cycling, there will be significant additional costs and complications of the process scheme. It is therefore necessary to examine the differences between Figures 7.8 and 7.9 to determine the cause of this drop-in performance. From the experiments there are several key differences, namely:

1. Oxygen incorporation occurred isothermally in Figure 7.8, rather than partially during cooling in Figure 7.9.
2. The length of time the material stayed isothermally at 310°C was shorter in Figure 7.8 compared to Figure 7.9.
3. The length of time the material stayed in an argon environment was longer during the experiment shown in Figure 7.8, compared to Figure 7.9
4. The maximum δ achieved during cycling was 0.92 and 1.04 for Figures 7.8 and 7.9 respectively.

These 4 factors will be examined, to find a more suitable cycling scheme.

7.2.7 Effect of reducing the oxygen incorporation time during cycling upon sample stability

To examine whether the length of time the material remained at 310°C in a pO_2 of 0.21 bar or the oxygen content had an impact on the cycling stability of the material, a sample was heated from 310 to 430°C in argon after which it was allowed to dwell for 54 minutes to release oxygen. The sample was then cooled in argon to 310°C. The gas environment was then changed to a pO_2 of 0.21 bar, and oxygen incorporation was allowed for 60 minutes. This is similar to Figure 7.9, but a decrease in the time the material was held isothermally for oxygen incorporation from 120 minutes to 60 minutes. The results of this cycling can be seen in Figure 7.11.

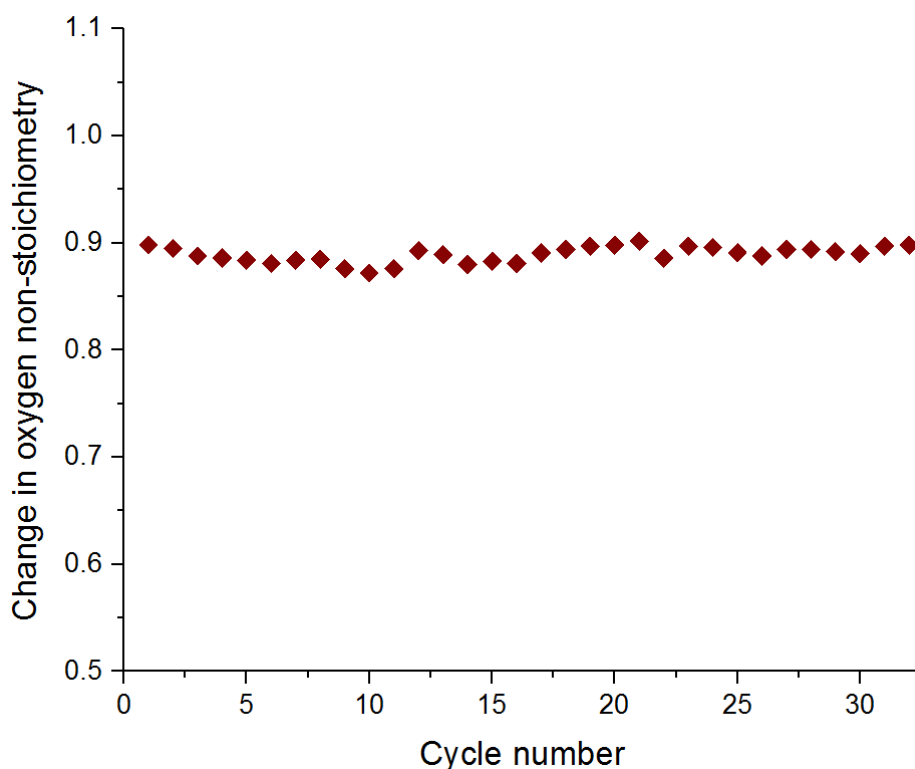


Figure 7.11 – Change in the oxygen non-stoichiometry ($\Delta\delta$) per cycle versus the cycle number, for $\text{YBaCo}_4\text{O}_{7+\delta}$ cycling between a $p\text{O}_2$ of 0.21 bar at 310°C and argon at 430°C . The sample was heated from 310°C at a rate of $20^\circ\text{C}/\text{min}$ in argon until 430°C , at which point the sample was held isothermally for 54 minutes to remove the incorporated oxygen. The sample was subsequently cooled in argon for 60 minutes until it reached 310°C . The gas environment was then switched from argon to a $p\text{O}_2$ of 0.21 bar where the sample was held isothermally for 60 minutes

Figure 7.11 shows that the amount of oxygen incorporated and released over the cycles stayed consistent throughout the experiment, with a fluctuation in the amount of oxygen exchanged of 0.02 through the cycles. During this cycling, there is no steady loss in the amount of oxygen incorporated and released like in Figure 7.9. This result makes it unlikely that the length of time the material was held isothermally at 310°C in a $p\text{O}_2$ of 0.21 bar, or the oxygen content had an impact on the stability.

7.2.8 The effect of increasing the duration of the argon reduction step during redox cycling upon sample stability

To examine whether the duration of the argon treatment step had an impact on the stability of the material over cycling, 20 redox cycles similar to the method used for Figure 7.8 were performed, using pre-treated $\text{YBaCo}_4\text{O}_{7+\delta}$. A sample was heated from 310 to 430°C in argon after which it was allowed to dwell for 116 minutes to release oxygen. The sample was then cooled to 310°C in a $p\text{O}_2$ of 0.21 bar (taking approximately 15 minutes), after which isothermal oxygen incorporation was allowed for 105 minutes. Ten of these cycles were

performed, before the sample underwent a helium pre-treatment after which a further ten cycles were performed. The results can be seen in Figure 7.12.

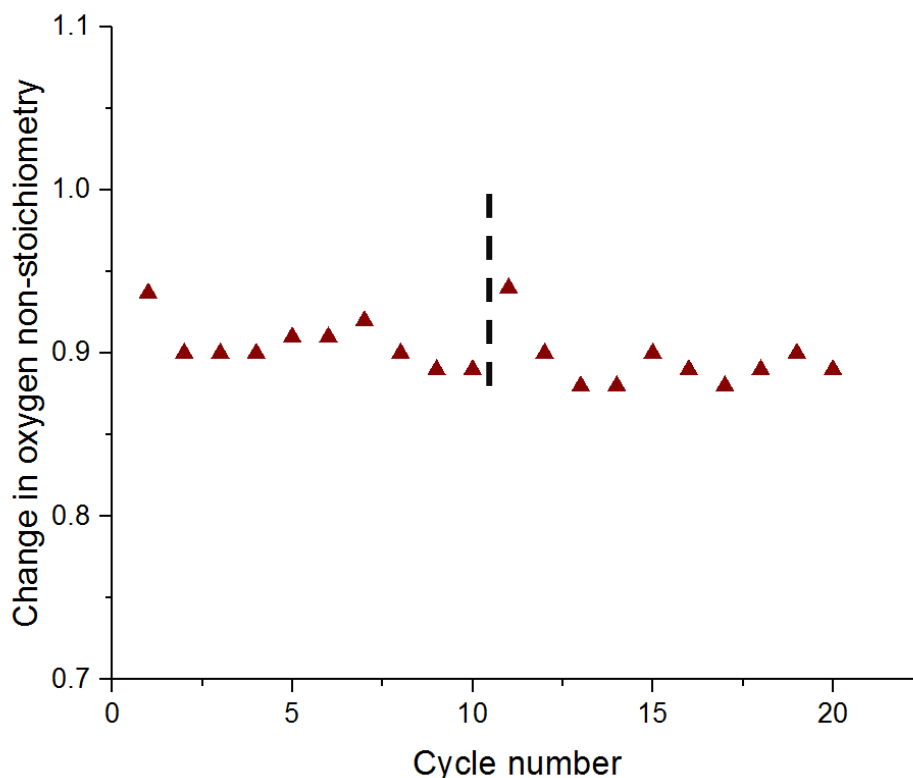


Figure 7.12 – Change in the oxygen non-stoichiometry ($\Delta\delta$) per cycle versus the cycle number, for $\text{YBaCo}_4\text{O}_{7+\delta}$ cycling between a $p\text{O}_2$ of 0.21 bar at 310°C and argon at 430°C . The sample was heated from 310°C at a rate of $20^\circ\text{C}/\text{min}$ in argon until 430°C , at which point the sample was held isothermally for 114 minutes to remove the incorporated oxygen. The sample was subsequently cooled in a $p\text{O}_2$ of 0.21 bar to 310°C taking approximately 15 minutes, at which point the sample was held isothermally for 105 minutes. The black dashed line shows at which point the material underwent the helium pre-treatment.

Figure 7.12 shows increased stability in cycling compared to Figure 7.8, which had shown a decrease in the amount of oxygen incorporated and released of 15% over 10 cycles, compared to a drop of $<5\%$ in Figure 7.12. The data shown in Figure 7.12 also has improved stability over that of Figure 7.9, where oxygen incorporation occurred isothermally and there was a decrease in the amount of oxygen incorporated and released of 9%.

In all figures in which improved stability has been seen, the material had longer contact with argon, either at the reduction temperature or upon cooling. This suggests that the reduction of the material plays a key role in the stability of the material. To demonstrate the reduction step is responsible for the improved stability, a sample underwent redox cycling between a $p\text{O}_2$ of 0.21 bar at 310°C and inert. During the first 15 cycles, the inert step was 60 minutes at 500°C ,

and during the remaining 14 cycles the reduction step occurred at 430°C for 60 minutes. The oxygen incorporation step lasted 120 minutes, inclusive of cooling.

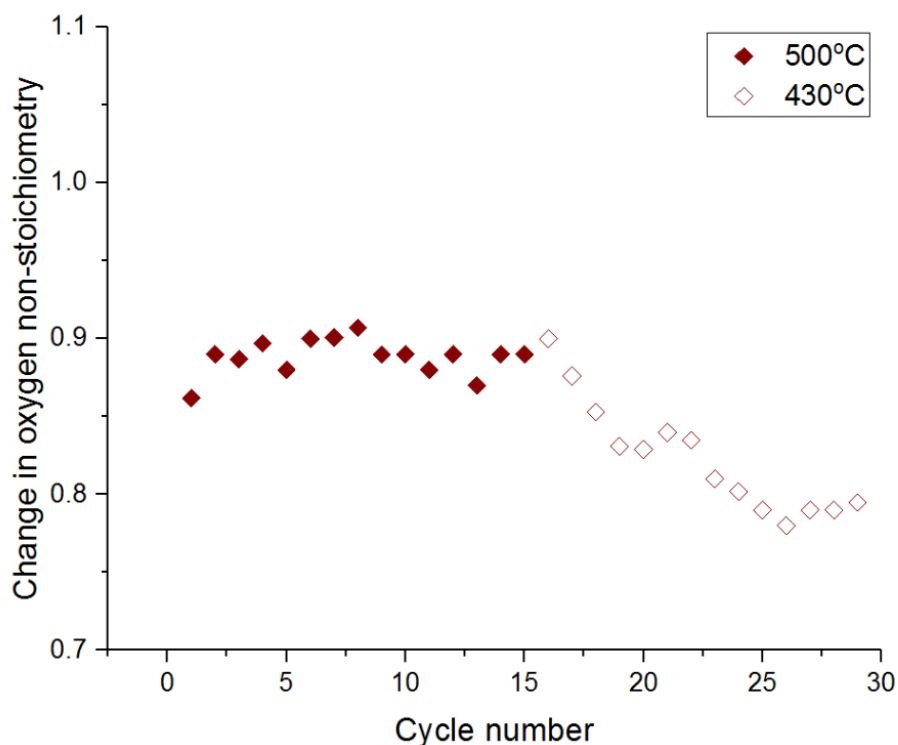


Figure 7.13 – Change in the oxygen non-stoichiometry ($\Delta\delta$) per cycle versus the cycle number, for $\text{YBaCo}_4\text{O}_{7+\delta}$ cycling between a $p\text{O}_2$ of 0.21 bar at 310°C and argon. During the first 15 cycles the argon reduction step occurred at 500°C, and the subsequent 14 cycles the reduction step occurred at 430°C. The sample was heated from 310°C at a rate of 20°C/min in argon until the reduction temperature, at which point the sample was held isothermally to remove the incorporated oxygen. The sample was subsequently cooled in a $p\text{O}_2$ of 0.21 bar to 310°C taking approximately 20 or 15 minutes respectively for 500 and 430°C, after which point the sample was held isothermally for a total duration of 120 minutes.

Figure 7.13 shows the amount of oxygen incorporated and released during the first 15 cycles had significantly improved stability compared to the final 14 reduced at 430°C. From both Figures 7.12 and 7.13, it is shown that increasing the effectiveness of the reduction, increased the cycling stability. During cycles with a significant reduction in performance, EDX, S.E.M., and XRD scans were performed and no clear reason for this drop-in performance has yet been found, however, results from the literature [22] found some agglomeration of YBaCo_4O_7 particles after cycling, potentially suggesting some drop in the surface area is responsible for the drop in performance. In the author's opinion, however, it is unlikely that over such short times at 400°C any significant drop in surface area would occur. A more likely option to the author is that when a sample is not completely reduced an oxygen-rich layer may sit at the surface of the material, preventing diffusion into the bulk. It is also possible that small amounts of the orthorhombic phase have not decomposed due to slow

kinetics, which forms a surface layer, inhibiting the oxygen incorporation into the hexagonal phase. This is however speculation, and no strong evidence is available to support this. It is clear, however, that the reduction step is of vital importance for the continued cyclability of the material.

In ref. [23-24] it was suggested that particle cracking may occur over multiple redox cycles, and S.E.M. evidence was provided in [24] showing this phenomenon. To investigate this, S.E.M. images of fresh and cycled material were taken. The cycled material was taken TGA samples used in Figure 5.2.

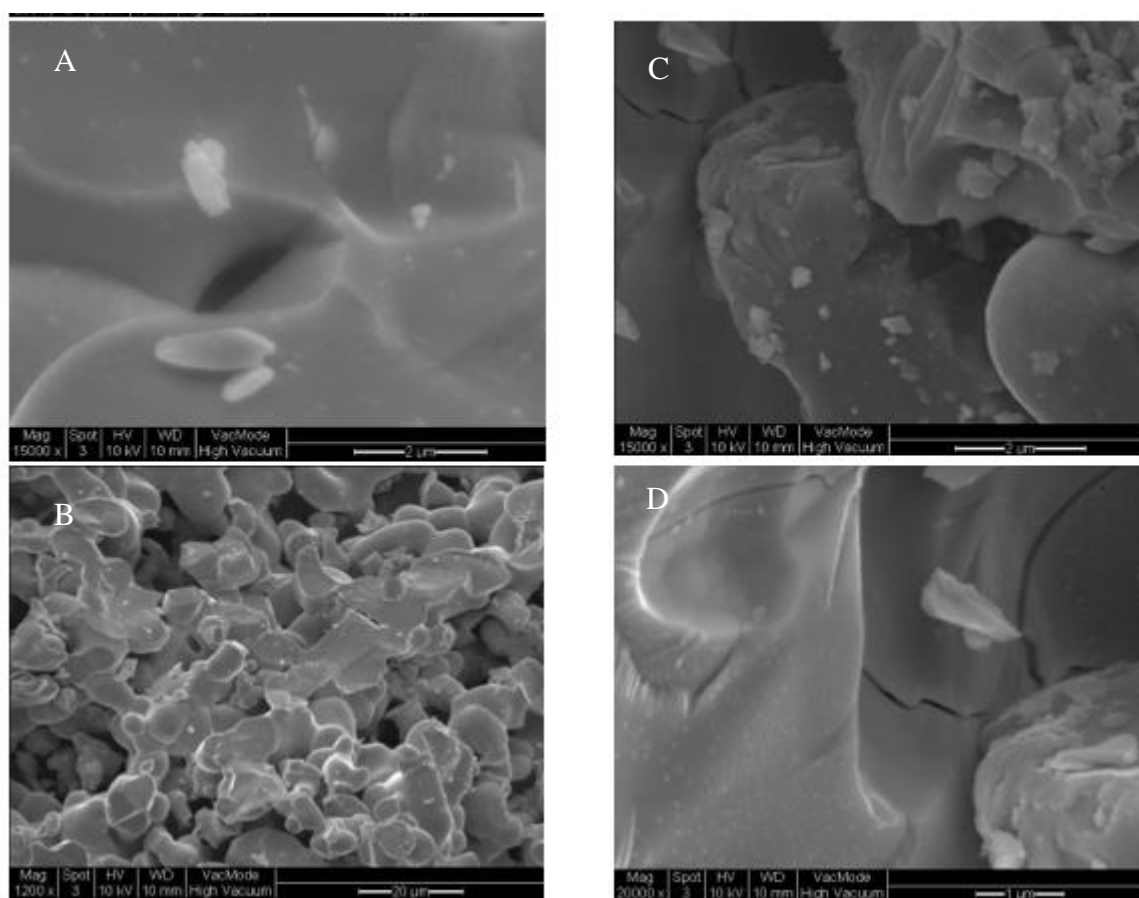


Figure 7.14 – S.E.M. images of fresh (a-b) and cycled (c-d) powder

In the images of Figure 7.14, cracks can be seen on the surface of the cycled samples like those matching those seen in ref [24]. In 7.14 (a-b) no such damage is seen on the fresh material. Such damage may have caused a loss of performance. In this work however it has been shown that redox cycling can be performed with no drop in performance if a suitable reduction step is used. This reduction step is unlikely to prevent this cracking, suggesting this is not the cause.

7.4 - Model of oxygen enrichment using $\text{YBaCo}_4\text{O}_{7+\delta}$

To effectively evaluate the potential of YBaCo_4O_7 for oxy-fuel combustion processes, a model of oxygen enrichment using the material was required. The information required for this was:

- Kinetics of oxygen released into the gas phase from the material
- Size of gas stream requiring treatment
- Reactor conditions (Speed of gas, bed voidage, etc.)

This work will focus on the oxygen release from the material, as the rate of oxygen incorporation was seen to be significantly slower than that of other oxygen storage materials which operate at higher temperatures [25-29]. The major advantage of this material is the rapid release of oxygen over a narrow temperature range, and if the rates for this are not suitable for an industrial process, then further investigation of the incorporation rate is not valuable.

7.4.1 – Kinetics of oxygen release from $\text{YBaCo}_4\text{O}_{7+\delta}$

To assess how the material may function as an oxygen carrier for oxy-fuel combustion it was necessary to first obtain kinetic information on the oxygen release. This information is needed to show how the material could release oxygen into different $p\text{O}_2$ s at different temperatures. This information is the groundwork to examine how the rate of oxygen release changes through the bed, due to the increase in the oxygen content of the gas stream.

To this end, a set of thermogravimetric experiments were conducted, allowing the material to dwell for one hour in a $p\text{O}_2$ of 0.21 bar after the helium pre-treatment pre-described, before being rapidly heated at a rate of $20^\circ\text{C}/\text{min}$ up to temperatures ranging between 370 and 430°C , at $p\text{O}_2$ s ranging from 0 (helium gas flow) to 0.42 bar. The rate of oxygen loss was constant during each run above a $\delta = 0.2$, after which point the rate of oxygen loss decreased. Therefore, any model will be limited to reducing the bed to this δ . This also gives a proportion of the oxygen content available to sacrificially combust to protect the material from reducing gases, such as H_2 is present in the gas stream, which is a potential problem at higher temperatures. The rate values obtained for this experiment are shown in Figure 7.15.

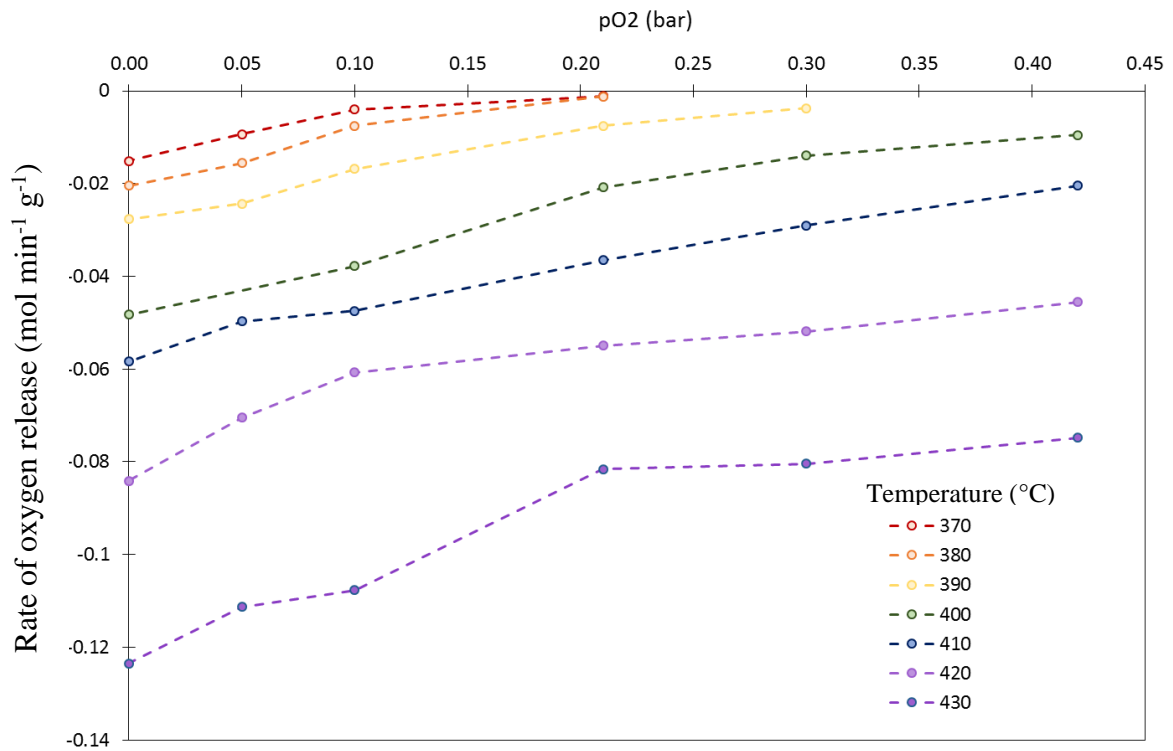


Figure 7.15 – Rate of oxygen release from YBaCo_4O_7 versus $p\text{O}_2$ for temperatures ranging from 370 to 430°C. As expected from the work shown in Chapter 6, the rate of oxygen release increased with temperature but decreased with increased $p\text{O}_2$ decreasing the driving force from the material. During use in the model, it is assumed that a linear relationship between rate and $p\text{O}_2$ exists at each temperature using a line of best fit through the 6 experimental points. It is believed that although this may have some error due to mass transfer limitations discussed in Chapter 5, this data should be accurate enough to give an estimate of the viability of the system.

7.4.2 – Size of exhaust gas stream

The size of the exhaust stream that requires oxygenation is varied, with larger power plants operating at up to 600 MW/h, and smaller more local stations operating at 10Mw/h. In this work three power stations will be compared, a small local station [30] (10 Mw/h), a medium station [31] (50 MW/h), and a large station [32] (600 MW/h). Smaller power stations are the most likely to benefit from this technology, as these are often in more remote regions, that may not have easy access to cryogenic distillation. An assumption made for these stations is that they will combust bituminous coal as a fuel source, with a fixed calorific value of 8.1MW/h [33].

From these assumptions, the amount of fuel required can be estimated by dividing the required power output by the calorific value. With the assumption that the carbon is completely combusted to CO_2 , with negligible production of CO , a one-to-one molar ratio

between the amount of fuel combusted and the amount of CO₂ produced can be made. During calculation, it is assumed 40% of the gas produced is captured, while 60% is recycled, in keeping with standard practice for oxy-fuel combustion systems. An assumption that the gas behaves ideally allows the change in volume at different temperatures to be assumed by the use of the perfect gas law. Table 7.4 shows the size of the gas streams assumed in this work for each sized power station.

Table 7.4 – Table of values showing the amount of CO₂ produced

Power output (MW/hr)	The calorific value of fuel (MW/h)	Mass of coal required (kg/h)	Moles of CO₂ produced (Kmoles/h)	Moles of CO₂ recycled (Kmoles/min)
600	0.0081	74074.07	6172.84	61.73
100	0.0081	12345.68	1028.807	10.29
10	0.0081	1234.57	102.8807	1.03

7.4.3 - Sizing of the reactor dimensions

To determine the width of the reactor required, the voidage of the bed was fixed at a value of 0.7 and the width of the bed was set to give a gas velocity of approximately 30 m/s, as recommended in the Chemical Engineering Handbook by Coulson and Richardson [34]. Because the volume of gas traveling through the reactor will be dependent on the temperature, the gas velocities of different temperatures compared will have some variation. However, keeping this value fixed was thought preferable to changing the size of the reactor for comparative purposes. Additionally, the pressure of the gas stream has been set to 5 bar and pressure drop through the reactor has not been considered. The diameter of the reactor used for a power output of 600, 100, and 10 MW plants were 15, 50, and 120 cm respectively.

7.4.4 – Model results

This model was created using an iterative approach. The bed was divided into 5 cm segments, or plugs, with a known pO₂ entering. The rate of oxygen release was assumed constant during this duration, and the amount of oxygen leaving the YBaCo₄O₇ bed was calculated. The assumed voidage of the bed was 0,7, and with an assumed density of the material equal to that of cobalt oxide, the amount of YBaCo₄O₇ in each 5cm plug was estimated. From the data shown in Figure 7.15, a rate of oxygen release of the material was estimated. This data was

input into a first-order rate equation, shown in Eq. 7.8, where R is the rate of oxygen release, t is the residence time of the gas plug in the 5cm section, and W is the weight of the oxygen carrier.

$$Mol_{o_2} = RtW \quad \text{Eq.7.8}$$

The moles of oxygen released from each section were assumed to be split evenly among the gas plug, and evenly from the reactant bed. The new pO₂ of the gas stream was then calculated by adding the new moles of oxygen after the 5cm plug to that which entered and dividing by the new total volume of gas. From this new volume of gas, a new gas velocity was calculated, assuming the system remained isobaric using Eq.7.9, where V is the gas velocity, Vol is the volume of the gas stream, and A is the cross-sectional area of the reactor

$$V = Vol/A \quad \text{Eq.7.9}$$

From the amount of oxygen released, a new pO₂ was calculated, which was taken as the entrance pO₂ of the next segment, and with this new pO₂ and residence time, the amount of oxygen released into the gas stream in this section was calculated. A segment length of 5cm was chosen, as performing the calculations with a step size of 1, 5, or 10 cm gave no notable difference to the results. This is shown in Figure 7.16, which shows the change in pO₂ versus length using the model with 1, 5, and 10 cm step size.

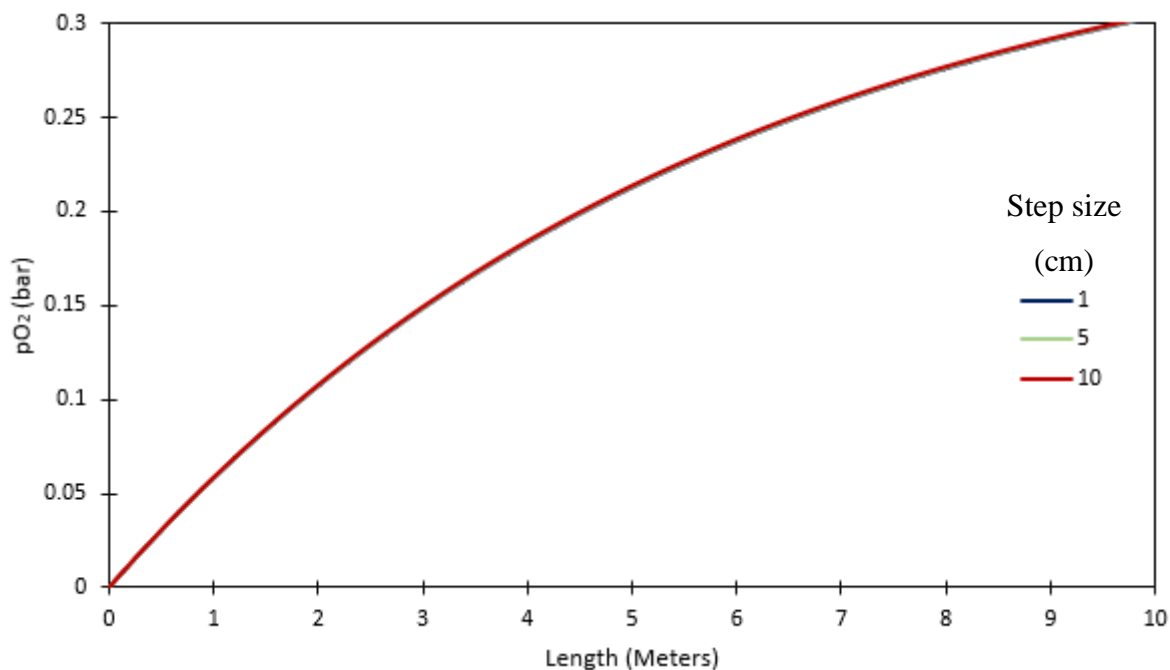


Figure 7.16 – Plot showing pO₂ versus length as calculated using the model using step sizes of 1, 5 and 10 cm. As shown in Figure 7.15, there is no notable difference between the values obtained at any step size. As such, 5 cm was used for each calculation

7.4.5– Required bed length for oxy-fuel combustion

To accurately evaluate the cost of the use of YBaCo_4O_7 for oxy-fuel combustion, it is necessary to calculate the bed length required to achieve the high $p\text{O}_2$ s necessary for oxy-fuel combustion. Using three reactor diameters of 15, 50 and 120 cm for the 10, 100 and 600 MW cases described previously, the treatment of the gas flow from each condition was modelled, and the results can be seen in Figure 7.17.

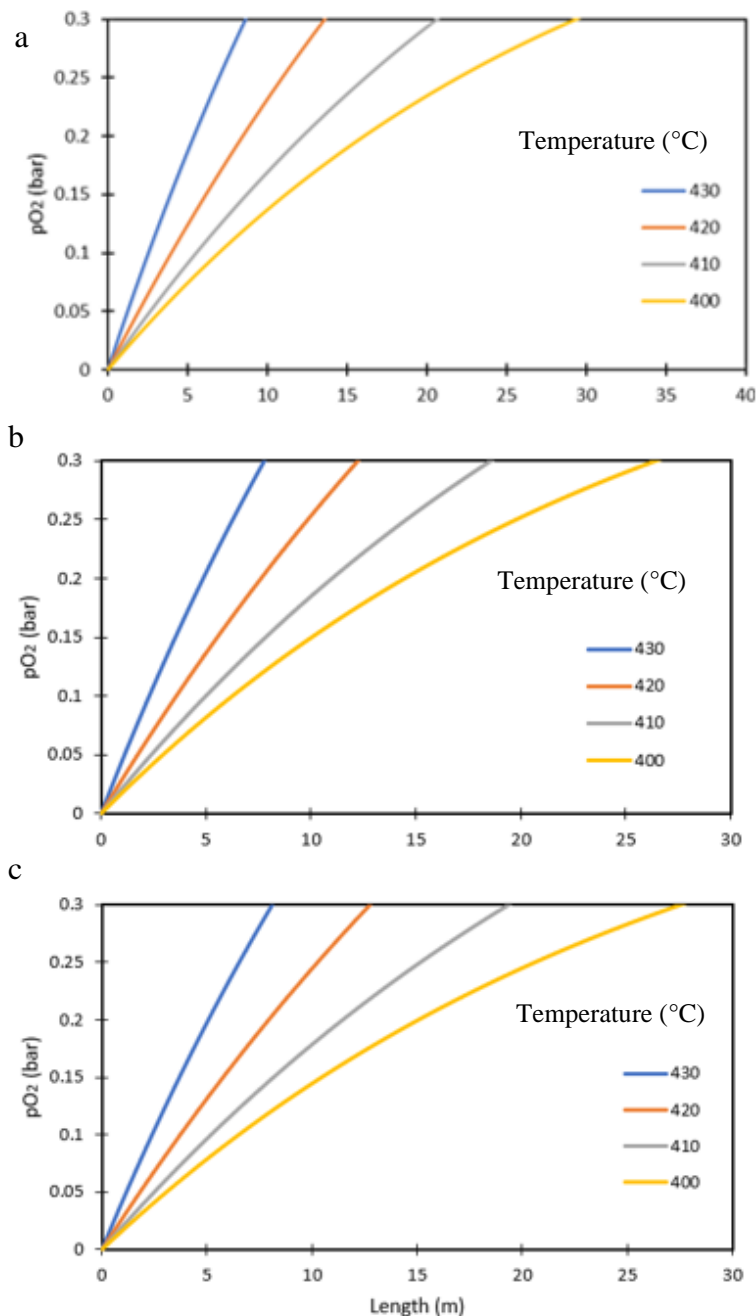


Figure 7.17 – Plot of calculated data showing the change in $p\text{O}_2$ versus length of exhaust gas of an (a) 10 Mw, (b) 100 Mw, (c) 600 Mw powerplant exhaust stream traveling through a reactor bed of YBaCo_4O_7 , operating at temperatures between 400 – 430°C

For all three cases, it is seen that at 400°C, the required reactor length was significantly larger than that of the higher temperatures. An increase from 400 to 410°C was enough to decrease the required length of the 10 Mw example from 29.4 to 20.6 m, a decrease of the required length by 30% over a 10°C window. This decrease in the required reactor volume with rising temperatures continued, however, the magnitude of the improvement decreased, and increasing the temperature from 420 to 430°C reduced the reactor size by 5 m, half the improvement was seen between 400 and 410 °C and so it is believed limited benefit would be gained from working at a higher temperature than this.

7.4.6 – Operational time of the material

It is important to know how long each bed of non-stoichiometric $\text{YBaCo}_4\text{O}_{7+\delta}$ could be operated in a redox cycling scheme before requiring regeneration. Figure 7.18 shows the change in δ through the bed during a reduction cycle, of $\text{YBaCo}_4\text{O}_{7+\delta}$ during operation for the 10, 100, and 600 MW examples, operating at 430 °C and assuming a gas inlet with a $p\text{O}_2$ of 0 bar.

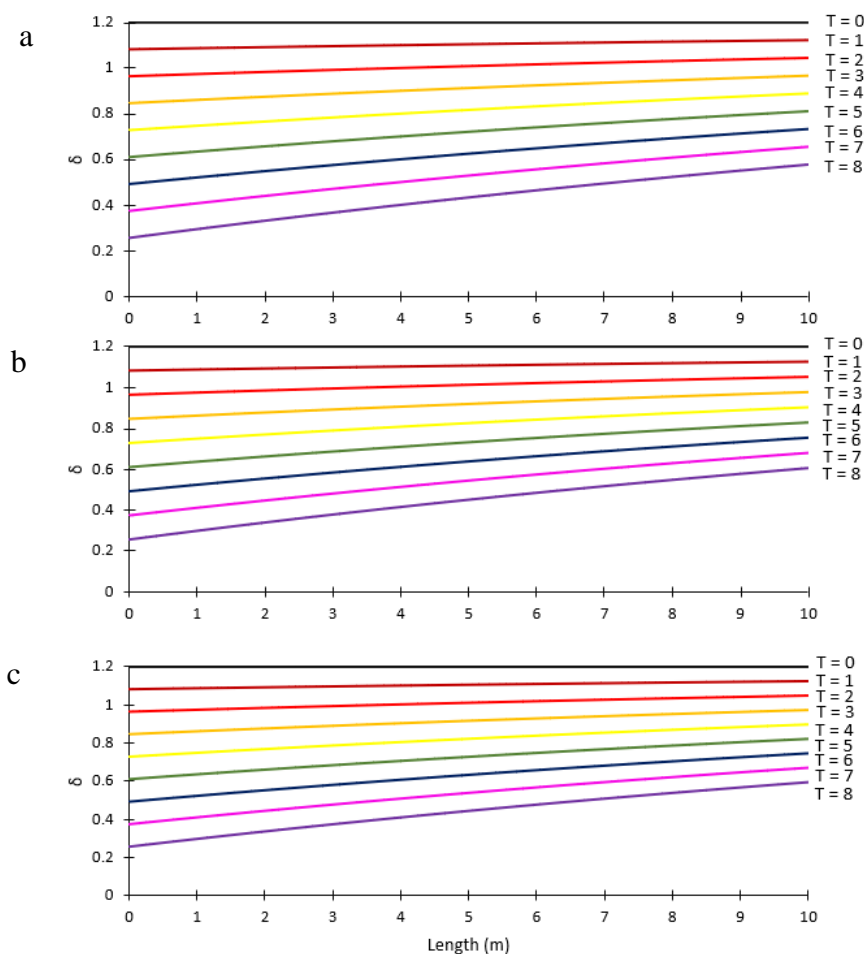


Figure 7.18 – Plot of calculated data showing the change in δ versus length of a reactor bed of YBaCo_4O_7 treating a (a) 10 Mw, (b) 100 Mw, and (c) a 600 Mw power plant exhaust stream operating at 430 °C

As seen in Figure 7.18, all three beds operating at 430°C would require to be regenerated after approximately 8 minutes, before reaching a $\delta = 0.2$, the cut-off point due to slow kinetics of oxygen release. From oxygen incorporation experiments conducted in Chapters 5 and 6, it was seen that it would take at a minimum an hour to regenerate a bed, but this value is likely underestimated in such a large system. This means that in the ideal scenario, a minimum of 8 beds would be needed for continuous operation, assuming the oxygen incorporation occurred as quickly in a reactor set-up compared to a TGA. It appears that the kinetics of $\text{YBaCo}_4\text{O}_{7+\delta}$ have the potential for oxygen enrichment processes. However, the major saving could be made by increasing the rate of oxygen incorporation, reducing the number of active beds needed. This may be suitable for smaller power stations, where the transport of oxygen produced by cryogenic distillation may be more difficult.

7.4 Discussion

In this chapter, the feasibility of $\text{YBaCo}_4\text{O}_{7+\delta}$ for oxy-fuel combustion was investigated. Three major sections were looked at, material stability in reducing gases, stability over redox cycling, and the kinetics and applicability to a usable system.

Previous literature reported no degradation of $\text{YBaCo}_4\text{O}_{7+\delta}$ in CO_2 . This testing was performed isothermally at 400°C [22] – which is lower than the recommended temperatures of oxygen release discussed through this work, therefore CO_2 stability at the higher reduction temperatures needed to be studied. In this work, this result was expanded, and stability was shown to approximately 700°C, approximately 300°C higher than the suggested operating temperatures. Barium-containing compounds are often prone to degradation in CO_2 environments at high temperatures [35-36], so this stability is reassuring for potential operational schemes. Similarly, water vapour was seen to have no negative impact at 500°C.

While good stability was seen in CO_2 , carbon deposition was found in the presence of CO , and a small decomposition equal to 0.4% of the unoxxygenated mass of the material was seen upon heating between 400 and 500°C. Carbon deposition on catalysts significantly reduces performance, and this would likely occur in this process [37-38]. Hydrogen was also seen to decompose the sample at temperatures above 300°C.

H_2 and CO should be in small quantities in a well-designed furnace system, and therefore should not pose too significant an issue in terms of material degradation. Additionally, in the schemes suggested, these gases will contact the oxygen-rich phases during the reduction step. Therefore, it is likely that the incorporated oxygen will be consumed sacrificially, protecting the samples. The carbon deposition seen is a greater concern, and likely needs further

investigation – although as furnaces are designed to minimise CO production, this may be a minor concern and potentially manageable through altering the furnace operation [39].

In this work, multiple redox cycling schemes of $\text{YBaCo}_4\text{O}_{7+\delta}$ have been investigated. 15 redox cycles were shown in Figure 7.4, incorporating oxygen from a lower $p\text{O}_2$, and enriching a gas suitable for oxy-fuel combustion. This was performed by incorporating oxygen upon cooling from 430 to 310°C in a $p\text{O}_2 = 0.21\text{bar}$, and releasing into a gas stream of $p\text{O}_2 = 0.31\text{bar}$, upon heating from 310 to 430°C. This was seen to be successful, with the sample releasing oxygen equal to approximately 1.5% of its mass.

Worryingly, a significant drop in the cycling performance of approximately 20% was found. Similar performance drops are seen upon redox cycling of the RMnO_3 [40] and $\text{Ca}_2\text{AlMnO}_5$ [41] families (albeit – not at this magnitude). The literature however did not explain this drop in performance. In ref [41], it was seen that for $\text{Ca}_2\text{AlMnO}_5$ the final state oxygen content after redox cycling remained consistent, it was however the amount of oxygen released which differed. In Figure 7.4, it is shown that the oxygen content after reduction was steadier than oxygen content after oxidation (although a decrease in both was seen). Due to this, and the lower operating temperatures compared to $\text{Ca}_2\text{AlMnO}_5$, the degradation mechanisms are likely different between these two materials. The results of $\text{YBaCo}_4\text{O}_{7+\delta}$ cycling are more similar to that seen in ref [40], suggesting the lower reaction rates due to low temperature are responsible. This cyclability must be improved, as the drop in performance is more like that seen for a transition metal oxide [42-43]. Additionally, other materials such as SrFeO_3 have shown significantly better cyclability [44].

Further work was performed to attempt to explain this phenomenon, and it was seen that the reduction step was important for maintaining stability. If the reduction was not aggressive enough, significant drops in performance were seen. This is demonstrated in Figure 7.13. It was also shown in Figure 7.12 that this degradation was reversible by a more aggressive reduction.

The simplest explanation is that upon oxygen release, oxygen is rapidly released from the sample surface region. As further oxygen release occurs, oxygen travels from the bulk of the particle to the surface, creating a gradient of non-stoichiometry through the sample. If the system is changed to prevent oxygen release, the gradient within the particle may stay, so oxygen incorporation into the particle must wait for the bulk diffusion, which is likely to be slower at low temperatures. Such gradients have been reported in fuel cells [45] and cathode

materials [46], and the stresses caused within crystals due to these gradients are seen to lower diffusion rates [47].

In this work, it was shown end that $\text{YBaCo}_4\text{O}_{7+\delta}$ can be repeatedly cycled to release oxygen, with no degradation in performance over 30 cycles. However, as the cycling scheme required almost complete removal of oxygen from the sample, there are likely to be additional concerns. Firstly, while technically possible to cycle significant amounts of oxygen over 40°C cycles as discussed in Chapter 6, the results do not favour this scheme. Slow oxygen incorporation rates are likely to be the limiting factor in the use of this material, and this is seen to be fastest at 310°C. Additionally, reduction will likely require higher temperatures to ensure that the oxygen content of the sample is reduced enough to allow for steady cycling of the sample. Therefore, the temperature swings used are more likely to be 150-200°C, rather than the 40°C discussed in Table 6.2. This would reduce the efficiency of the oxygen cycles by approximately 25% - although this is still seen to be more efficient than the other non-stoichiometric materials studied [48-58].

There are potential strategies to reduce this. Higher $p\text{O}_2$'s for the oxygen incorporation step could increase the useful oxidation temperature, as demonstrated in Figure 7.7. Additionally, it was shown in Figure 7.12 that a regeneration cycle could reset the performance of a working bed of YBaCo_4O_7 , so incorporating periodic regenerations may improve the performance.

In S.E.M. images of cycled material, particle cracking such as discussed in ref [23-24] was seen. This is likely due to the distortion of the crystal structure upon oxygen incorporation seen in ref [59] and Figure 6.13. This cracking is likely unpreventable and may cause issues over multiple cycles.

Kinetics were obtained from TGA to estimate oxidation and reduction rate, and these are shown in Figure 7.14. As seen in chapter 6 and literature, oxygen incorporation was favoured at 310°C, and oxygen loss was favoured at higher temperatures [60-61]. It was found that oxygen release was slower in higher $p\text{O}_2$'s, likely due to the change in chemical potential in the system. In chapter 5, it was suggested that oxygen could be released in a $p\text{O}_2$ of 0.31 bar at 390°C, and this is shown. It is clear however having that small temperature swing is likely to give extremely slow oxygen release rates. It is clear from this plot, however, that the schemes suggested in ref [22] are not feasible, and oxygen release must be performed upon heating from the oxidation temperature, not cooling as suggested in the reference, if the correct $p\text{O}_2$'s are to be achieved.

An iterative model was produced, and it was seen that increasing the temperature of reduction from 400 to 430°C reduced the required lengths of reacting beds by approximately 1/3, which would give significant energy reduction required. This was due to the faster rate of oxygen release from the samples. It was seen however that a gradient of non-stoichiometry may be formed in the bed. However, no variation in the gas profile was calculated, suggesting this material may avoid inconsistent gas production which can be an issue with the use of non-stoichiometric materials [62].

It is clear though that after the reduction step, a gradient of oxygen content will be present in the bed. This gradient could have an impact upon the re-oxidation of the sample, and the stability of the redox cycling. To fill this gradient in fastest, a counter-current flow should be used, to make the most efficient use of the oxygen, as oxygen incorporation will be slowest where the sample has almost equilibrated, where it, therefore, needs the greatest driving force.

The biggest issue with the potential use of the material is the length of time beds last. It was found that each bed would last approximately 8 minutes before requiring oxidation. Oxidation times in TGA can be between 1 and 2 hours, suggesting a series of between 7 and 15 beds would be required. The greatest step to make this more feasible would be to increase the oxygen incorporation rate. This may be achieved potentially by increasing the surface area by ball milling [63-34] or perhaps the use of a catalyst to increase oxygen incorporation rates[65]. Regardless, improvements in the oxidation rate would be required for useful operation.

7.5 Conclusions and further work

During this work, YBaCo_4O_7 has been investigated for oxygen cycling processes. Initially, the stability of the material was tested in different reducing conditions, and it was seen that the material was suitable for use in a flue gas setting. Redox cycles with the material were performed and it was seen that the material can easily be used to inject oxygen into a gas stream. The stability of the material over repeated cycling was investigated and it was seen that the material degraded over cycling if a high enough temperature or a low enough $p\text{O}_2$ was used during the reduction step. The cause of this is unknown, however, it is suspected to be due to an oxide-rich layer forming at the surface of the material preventing oxygen diffusion. Regardless of the cause, it was repeatedly seen that if the reduction step of the material was not of long enough duration, loss of performance over cycling occurred.

Finally, a model of a working bed of YBaCo_4O_7 was created, and slow oxygen incorporation kinetics were found to be the major issue with using this material for oxygen enrichment

processes. For this material to become viable for industrial applications, more work on improving the oxygen release kinetics is needed. Additionally, a cycling scheme that does not require expensive inert gases for the continued stability of the material will need to be found.

7.6 References

- [1] J. Kugaia, J. T. Miller, N. Guob, C. Song - Oxygen-enhanced water gas shift on ceria-supported Pd–Cu and Pt–Cu bimetallic catalysts, *Journal of Catalysis*, 277, 1, 2011, 46-53
- [2] J. Kugaia, E. B. Fox, C. Song - Kinetic characteristics of oxygen-enhanced water gas shift on CeO₂-supported Pt–Cu and Pd–Cu bimetallic catalysts, *Applied Catalysis A: General*, 497, 2015, 31–41
- [3] R.Horn, K.A.Willams, N.J.Degenstein, A.Bitsch-Larsen, D.Dalle Nogare, S.A. Tupy, L.D.Schmidt - Methane catalytic partial oxidation on autothermal Rh and Pt foam catalysts: Oxidation and reforming zones, transport effects, and approach to thermodynamic equilibrium, *Journal of Catalysis*, 249, 2007, 380–393
- [4] B.M.Khudenko, G.M.Gitman, T.E.P.Wechesler - Oxygen Based Claus Process for Recovery of Sulfur from H₂S Gases, *J. Environ. Eng.* 119, 6,1993, 1233-1251
- [5] M.Sassi, A.K.Gupta - Sulfur Recovery from Acid Gas Using the Claus Process and High Temperature Air Combustion (HiTAC) Technology, *American Journal of Environmental Sciences* 4, 5, 2008, 502-511
- [6] A.Bensakhira, M.Leturia - Natural gas oxy-combustion with flue gas recycling for CO₂ capture *Chemical Engineering Transactions*, 21, 2010, 637-642
- [7] A.Kontopoulos, J.Koenig - Oxygen and nitrogen injection for increasing ammonia production, U.S. Patent application no WO1998045211 A1
- [8] D. Singh, E. Croiset, P.L. Douglas, M.A. Douglas - Economics of CO₂ capture from a coal-fired power plant — a sensitivity analysis, *Proceedings of the 6th international conference on greenhouse gas control technologies*, Kyoto, Japan, October 1–4, 2002.
- [9] D. Singh, E. Croiset, P.L. Douglas, M.A. Douglas - Techno-economic study of CO₂ capture from an existing coal-fired power plant: MEA scrubbing Vs. O₂/CO₂ recycle combustion, *Energy Convers Manage*, 44, 2003, 3073–3091.
- [10] K. Kimura , K. Omata , T. Kiga , S. Takano , S. Shikisima - Characteristics of pulverized coal combustion in O₂/CO₂ mixtures for CO₂ recovery. *Energy Convers Manage* 36, 1995, 805–808.
- [11] F. Horn, M. Steinberg M. - Control of carbon dioxide emissions from a power plant (and use in enhanced oil recovery), *Fuel*, 61, 1982, 415 - 422.
- [12] D. Singh, E. Croiset, P.L. Douglas, M.A. Douglas. - Techno-economic study of CO₂ capture from an existing coal-fired power plant: MEA scrubbing Vs. O₂/CO₂ recycle combustion, *Energy Convers Manage*, 44, 2003, 3073–3091.
- [13] T. Nozaki, S. Takano, T. Kiga, K. Omata, K. Kimura - Analysis of the flame formed During oxidation of pulverised coal by an O₂– CO₂ mixture. *Energy*, 22, 1997, 199–206.
- [14] T. Kiga, S. Takano, N. Kimura, K. Omata, M. Okawa, T. Mori - Characteristics of Pulverised-coal combustion in the system of oxygen/recycled flue gas combustion, *Energy Convers Manage*, 38, 1997, 129–134.
- [15] P.Grammelis, N.Margaritis, E.Karampinis - Solid fuel types for energy generation: Coal and fossil carbon-derivative solid fuels, *Fuel Flexible Energy Generation Solid, Liquid and Gaseous Fuels*, 2016, 29-58

- [16] G.Bagheri, E.Ranzi, M.Pelucchi, A.Parente, A.Frassoldati, T.Faravelli - Comprehensive kinetic study of combustion technologies for low environmental impact: MILD and OXY-fuel combustion of methane, *Combustion and Flame*, 212, 2020, 142-155
- [17] H.Chi, S.Su, H.Li, K.Xu, H.Leong, J.Xu, L.Jiang, Y.Wang, S.Hu, J.Xiang - Effects of CO₂ and H₂O on oxy-fuel combustion characteristics and structural evolutions of Zhundong coal pellet at fast heating rate, *Fuel*, 294, 2021, 120525
- [18] D. L. Trimm - The formation and removal of coke from nickel catalyst, *Catalysis Reviews: Science and Engineering*, 16, 1997, 155–189
- [19] K.Wang, Q.Yu, Q.Qin, Z.Zuo, T.Wu - Evaluation of Cu-based oxygen carrier for chemical looping air separation in a fixed-bed reactor, *Chemical Engineering Journal*, 287, 2016, 292-301
- [20] H.Song, K.Shah, E.Doroodchi, T.Wall, B.Moghtaderi - Analysis on Chemical Reaction Kinetics of CuO/SiO₂ Oxygen Carriers for Chemical Looping Air Separation, *Energy Fuels* 28, 1, 2014, 173–182
- [21] J. Vietena, B. Bulfina, F. Calla, M. Langea, M. Schmückerb, M. Schmückerb, A. Franckeb, M. Roeba, C.Sattler - Perovskite oxides for application in thermochemical air separation and oxygen storage, *Journal of the royal society of chemistry*, 00, 2016, 1-3
- [22] Z.Rui, J.Ding, L.Fang, Y.S.Lin, Y.Li - YBaCo₄O_{7+δ} sorbent for oxygen-enriched carbon dioxide stream production at a low-temperature, *Fuel*, 94, 2012 191-196
- [23] A. V. Alekseev, M. Yu. Kameneva, L. P. Kozeeva, A. N. Lavrov, N. V. Podberezskaya, A. I. Smolentsev, A. N. Shmakov - Structural Phase Transitions in YBaCo₄O₇ + x Cobaltate upon Variations in Oxygen Content, According to XRay Diffraction Data Obtained Using Synchrotron Radiation, *Bulletin of the Russian Academy of Sciences. Physics*, 77, 2013, 151–15
- [24] N. V. Podberezskaya, N. B. Bolotina, V. Yu. Komarova, M. Yu. Kamenevaa, L. P. Kozeevaa, A. N. Lavrova, A. I. Smolentseva - Orthorhombic YBaCo₄O_{8.4} Crystals As a Result of Saturation of Hexagonal YBaCo₄O₇ Crystals with Oxygen, *Crystallography Reports*, 60, 2015, 484–492
- [25] T.Nomura, C.Zhu, N.Sheng, R.Muraia, T.Akiyama - Solution combustion synthesis of Brownmillerite-type Ca₂AlMnO₅ as an oxygen storage material, *Journal of Alloys and Compounds*, 646, 2015, 900-905
- [26] H. Falco, J. A. Barbero, J. A. Alonso, M. J. Martí'nez-Lope, J. L. G. Fierro - SrFeO_{3-δ} Perovskite Oxides: Chemical Features and Performance for Methane Combustion, *Chem. Mater*, 14, 2002, 2325-2333
- [27] B.Bulfin, J.Vieten, D.E.Starr, C.Sattler - Redox chemistry of CaMnO₃ and Ca_{0.8}Sr_{0.2}MnO₃ oxygen storage perovskites, *Journal of Materials Chemistry A* , 2017, *Journal of Materials Chemistry A* , 5, 2017, 7912-7919
- [28] T.Motohashi, T.Ueda, Y.Masubuchi, M.Takiguchi, T.Setoyama, K.Oshima, S.Kikkawa- Remarkable Oxygen Intake/Release Capability of BaYMn₂O_{5+δ}: Applications to Oxygen Storage Technologies, *Chem. Mater.*, 2010, 22, 3192–3196

- [29] O.V.Merkulov, A.A.Markov, M.V.Patrakeev, I.A.Leonidov, E.V.Shalaeva, A.P.Tyutyunnik, V.L.Kozhevnikov - Structural features and high-temperature transport in SrFe_{0.7}Mo_{0.3}O_{3-δ}, *Journal of Solid State Chemistry*, 2018, 258, 447-452
- [30] Lewis Berger - 10MW power plant Liberia, power.louisberger.com/our-work/project/10-mw-power-plant-liberia, accessed 19/02/2019
- [31] BWSC - 55 MW Pacora Power Station, www.bwsc.com/55-MWPacora-Power-Station.aspx?ID=155, Accessed 19/02/2019
- [32] Financial tribune - Belgians to Build 600 MW Power Plant in Tabriz, www.financialtribune.com/articles/energy/44698/belgians-to-build-600-mw-power-plant-in-tabriz, published 01/07/2016, accessed 19/02/19
- [33] The engineering toolbox, Fuels - Higher and Lower Calorific Values www.engineeringtoolbox.com/fuels-higher-calorific-values-d_169.html, Accessed 19/02/2019
- [34] R.K.Sinnot - Coulson and Richardson's Chemical Engineering Volume 6 - Chemical Engineering Design (4th Edition), Elsevier, 10/05/2010
- [35] M.J. Scholten, J. Schoonman, J.C. van Miltenburg, H.A.J. Onk - Synthesis of strontium and barium cerate and their reaction with carbon dioxide, *Solid State Ionics*, 61, 1–3, 1993, 83-91
- [36] E.Stavarakakis, M.West, S.R.W.Johnston, R.McIllwaine, D.Poulidi - Hydration, CO₂ stability and wireless electrochemical promotion studies on yttria-doped Ba (Ce, Zr) O₃ perovskites, *Solid state ionics*, 25, 2019, 1243–1257
- [37] K.Han, W.Yu, L.Xu, Z.Deng, H.Yu, F.Wang - Reducing carbon deposition and enhancing reaction stability by ceria for methane dry reforming over Ni@SiO₂@CeO₂ catalyst, *Fuel*, 291, 2021, 120182
- [38] D.Pashchenko, I.Makarov - Carbon deposition in steam methane reforming over a Ni-based catalyst: Experimental and thermodynamic analysis, *Energy*, 222, 2021, 119993
- [39] F.Alobaid, J.Peters, B.Epple -Experimental measurements for Polish lignite combustion in a 1 MWth circulating fluidized bed during load changes, *Energy*, 228, 2021, 120585
- [40] K.Cichy, K.Świerczek, K.Jarosz, A.Klimkowicz, M.Marzec, M.Gajewska, B.Dabrowski -Towards efficient oxygen separation from air: Influence of the mean rare-earth radius on thermodynamics and kinetics of reactivity with oxygen in hexagonal Y_{1-x}R_xMnO_{3+δ}, *Acta Materialia*, 205, 2021, 116544
- [41] K.Tanahashi, Y.Omura, H.Naya, K.Miyazaki, G.Saito, Y.Kunisada, N.Sakaguchi, T.Nomura - Sr-Doped Ca₂AlMnO₅ + δ for Energy-Saving Oxygen Separation Process, *ACS Sustainable Chemistry and engineering*, 9, 2021, 9317–9326
- [42] H.Song, K.Shah, E.Doroodchi, T.Wall, B.Moghtaderi - Reactivity of Al₂O₃- or SiO₂-Supported Cu-, Mn-, and Co-Based Oxygen Carriers for Chemical Looping Air Separation, *Energy Fuels* 28, 2, 2014, 1284–1294

- [43] H.Song, K.Shah, E.Doroodchi, B.Moghtaderi - Development of a Cu–Mg-Based Oxygen Carrier with SiO₂ as a Support for Chemical Looping Air Separation, *Energy and Fuels*, 28, 1, 2014, 163–172
- [44] E.Krzystowczyk, X.Wang, J.Dou, V.Haribala L.Fanxing - Substituted SrFeO₃ as robust oxygen sorbents for thermochemical air separation: correlating redox performance with compositional and structural properties, *Physical Chemistry Chemical Physics*, 22, 2020, 8924
- [45] R.Krishnamurthy, B.W.Sheldon, - Stresses due to oxygen potential gradients in non-stoichiometric oxides, *Acta Materialia*, 52, 7, 2004, 1807-1822
- [46] F.Lin, D.Nordlund, I.M.Markus, T.Weng, H.L.Xin, M. M.Doeff - Profiling the nanoscale gradient in stoichiometric layered cathode particles for lithium-ion batteries, *Energy and Environmental Science*, 7, 2014, 3077-3085
- [47] W.C. Johnson, H. Schmalzried - Phenomenological thermodynamic treatment of elastically stressed ionic crystals, *Journal of the American Ceramic Society*, 76, 7, 1993, 1713-1719
- [48] T.Matthers, K.T. Jacob - Variation of the Partial Thermodynamic Properties of Oxygen with Composition in YBa₂Cu₃O₇, *metallurgical transactions A*, 23, 1992, 3325-3335
- [49] K.Jeanjumnunja, W.Gong, T.Makerenko, A.J.Jacobson – A determination of the oxygen non-stoichiometry of oxygen storage material YBaMn₂O₅, *Journal of solid state chemistry*, 230, 2015, 397-403
- [50] X.Jin, T.Yang, K.Huang - Defect structure, thermodynamic and transport properties of SrCo_{0.9}Nb_{0.1}O_{2.5+δ}: A combined experimental and defect chemistry approach, *Solid State Ionics*, 320, 2018 159–171
- [51] O.V.Merkulov, E.N.Naumovich, M.V.Patrakeev, A.A.Markov, H. J.M.Bouwmeester, I.A.Leonidov, V.L.Kozhevnikova - Oxygen non-stoichiometry and defect chemistry of perovskite-structured SrFe_{1-x}MoxO_{3-δ} solid solutions, *Solid State Ionics*, 292, 2016 116-121
- [52] J. Vietena, B. Bulfina, F. Calla, M. Langea, M. Schmückerb, M. Schmückerb, A. Franckeb, M. Roeba, C.Sattler - Perovskite oxides for application in thermochemical air separation and oxygen storage, *JRSC*, 00, 2016, 1-3
- [53] A.Y.Suntsov, B.V.Politov, L.A.Leonidov, M.V.Patrakeev, V.J.Kozhevnikov - Improved stability and defect structure of yttrium doped cobalite PrBaCo₂O_{6-δ}, *Solid state ionics*, 295, 2016, 90-95
- [54] J.Mizusaki, N.Mori, H.Takai, Y.Yonemura, H.Minamiue, H.Tagawa, M.Dokiya, H.Inaba, K.Naraya, T.Sasamoto, T.Hashimoto - Oxygen nonstoichiometry and defect equilibrium in the perovskite-type oxides La Sr MnO, *Solid State Ionics*, 129, 2000, 163–177
- [55] M.B.Choi, D.-K.Lim, E.D.Wachsman, S.J.Song - Oxygen nonstoichiometry and chemical expansion of mixed conducting La_{0.1}Sr_{0.9}Co_{0.8}Fe_{0.2}O_{3-δ}, *Solid State Ionics*, 221, 2012 22-27
- [56] O.V.Murkulov, E.N.Naumovich, A.A.Markov, L.A.Leonidov, M.V.Patrakeev – Oxygen non-stoichiometry and defect structure of perovskite type Ca_{0.25}Sr_{0.75}Fe_{0.75}Mo_{0.25}O_{3-δ}, *Materials letters*, 236, 2019, 719-722
- [57] E.V.Tsipis, M.V.Patrakeev, J.C.Waerenborgh, Y.V.Pivak, A.A.Markov, P.Gaczyński, E.N.Naumovich, V.V.Kharton - Oxygen non-stoichiometry of Ln₄Ni_{2.7}Fe_{0.3}O_{10-δ} (Ln=La, Pr), *Journal of Solid State Chemistry*, 180, 2007 1902-1910
- [58] M.B.Choi, S.Y.Jeon, H..N.Im, S.J.Song - Thermodynamic quantities and oxygen non-stoichiometry of undoped BaTiO_{3-δ} by thermogravimetric analysis, *Journal of Alloys and Compounds*, 513, 2012, 487-494
- [59] J.Kim, A.Manthiram - Low Thermal Expansion RBa(Co,M)4O₇ Cathode Materials Based on Tetrahedral-Site Cobalt Ions for Solid Oxide Fuel Cells, *Chem. Mater*, 22, 3, 2010, 822–831

- [60] L.Hou, Q.Yu, K.Wang, F.Yang, T.Wu - Oxidation and reduction kinetic of $\text{YBaCo}_4\text{O}_{7+\delta}$ and substituted oxygen carriers, *Journal of Thermal Analysis and Calorimetry*, 134, 2018, 2213–2221
- [61] L.Hou, Q.Yu, K.Wang, S.Zhang, Q.Qin - Reduction Kinetics of $\text{YBaCo}_4\text{O}_{7+\delta}$ Oxygen Carrier for Chemical Looping Air Separation, *IOP Conference Series: Earth and Environmental Science*, 237, 3, 2019
- [62] G.Luongo, F.Donat, C.R.Müller - Structural and thermodynamic study of Ca A- or Co B-site substituted $\text{SrFeO}_3-\delta$ perovskites for low temperature chemical looping applications, *Physical Chemistry Chemical Physics*, 22, 2020, 9272-9282
- [63] T.Chen, Y.Asakura, T.Hasegawa, T.Motohashi, S.Yin - A simple and novel effective strategy using mechanical treatment to improve the oxygen uptake/release rate of $\text{YBaCo}_4\text{O}_{7+\delta}$ for thermochemical cycles, *Journal of Materials Science & Technology*, 68, 2021, 8-15
- [64] A. Klimkiewicz, K. Świerczek, S. Kobayashi, A. Takasaki, W. Allahyani, B. Dabrowski - Improvement of oxygen storage properties of hexagonal $\text{YMnO}_3+\delta$ by microstructural modifications, *Journal of Solid State Chemistry*, 258, 2018, 471-476
- [65] W.Yang, Z.Wang, Z.Wang, Z.Yang, C.Xia, R.Peng, X.Wu, Y.Lu - Enhanced Catalytic Activity toward O_2 Reduction on Pt-Modified $\text{La}_{1-x}\text{Sr}_x\text{Co}_{1-y}\text{Fe}_y\text{O}_{3-\delta}$ Cathode: A Combination Study of First-Principles Calculation and Experiment, *Applied material interfaces*, 6, 23, 2014, 21051–21059

Chapter 8 - Conclusions

This work aimed to identify potentially useful non-stoichiometric materials for oxygen enrichment processes and characterize them. To do these four objectives were set. In this section, each objective will be looked at independently to ascertain the success of the project.

8.1 Review of the initial objectives

8.1.1 Creation of a useful technique to characterise oxygen diffusion coefficients and non-stoichiometry

During this work, a novel technique to measure diffusion and non-stoichiometry of a sample using a single gas was created to reduce mass transfer limitations during diffusion measurement techniques. However, due to experimental issues, the benefit of calculating oxygen diffusion using this technique was not demonstrated. This technique was shown to be very powerful at characterising the oxygen capacity of the material, however, giving a user fine control over pO_2 changes in the reactor. It is believed that the poor results may be from issues with the temperature control and has much potential for further improvement.

8.1.2 Detailed investigation into the thermodynamics of selected oxygen carrier

During this work, the oxygen capacity upon heating and cooling of $YBaCo_4O_{7+\delta}$ was investigated and two useful plots were created, namely a δ versus pO_2 plot and a δ versus temperature plot at fixed pO_2 s. These plots were then used to compare the oxygen capacity and cyclability of the material versus alternative materials.

Additionally, crystallographic studies were performed, linking the change in δ to the percentage of the material in the orthorhombic phase. This information was then further linked to a changing temperature of oxygen release, where it was found that sudden oxygen release occurred at notably different temperatures if less than 50% of the material had converted to the orthorhombic phase. This behaviour was linked to a jump in the partial molar entropy and enthalpy of the sample, which appeared to act as an activation barrier between the oxidised and reduced states.

Finally, a change in the chemical potential was linked to the behaviour of the incorporation and release of the material, giving a thermodynamic explanation of the hysteresis behaviour.

8.1.3 Investigation into the stability of the non-stoichiometric material

The material was found to be stable in potentially reductive gas streams such as CO₂ and CO past the operational temperature of the material.

Repeated oxygen release and incorporation cycles were performed on the material, incorporating oxygen at a pO₂ of 0.21 bar, and releasing it into a pO₂ of 0.31 bar. Over this cycling, the performance of the material was seen to degrade. This was corrected by increasing the intensity of the reductive step. This corrective method is likely expensive and reduces the thermodynamic advantages of using the material.

8.1.4 Investigation into the kinetics of the oxygen incorporation and release of the selected material

As the novel technique for characterising diffusion coefficients was unsuccessful, TGA methods were used to estimate the rates of oxygen transfer from the material. While not ideal, it was useful to give estimates of the rates of oxygen transfer from the material. These rates were then used to calculate bed lengths and output for a working bed to supply oxygen to an oxy-fuel combustion plant. It was seen that the rates of oxygen transfer were likely too slow for useful application.

8.2 Further work

YBaCo₄O_{7+δ} has interesting structural and thermodynamic behaviour which would lend itself very efficiently for oxygen enrichment processes. However, the slow kinetics of the material are not offset by the beneficial thermodynamics and must be addressed before the material could be suitable for use in an industrial setting. There are several potential methods of doing this, including:

- **Microstructural modifications** - Ball milling and longer preparation time has improved the oxygen incorporation of low-temperature YBaCo₄O_{7+δ} and YMnO_{3+δ} [1-2]. Such improvements may be able to improve on the rates of oxygen incorporation
- **Modifications to the surface chemistry** – The treatment of the surface of a non-stoichiometric material may have significant effects on the rate of oxygen exchange. Silver coating of non-stoichiometric materials has long been seen to improve oxygen diffusion in the material and reduce the activation energy for oxygen exchange [3-4] and this may have a beneficial effect on the YBaCo₄O_{7+δ}. Another more recent method is exsolution, which has shown to stability improve the catalytic activity of a material [5-6]

- **High-pressure oxygen incorporation** – It was seen during this work, that higher oxygen incorporation pressures increased the rate of oxygen incorporation. If the pressure in the system, and the equivalent pO_2 was high enough, it may be that the rate of oxygen incorporation would be suitably high.
- **Use of chemical dopants** – Doping a material can have significant effects on the oxygen uptake and transport of the material. In literature, only one successful doping of $YBaCo_4O_7$ has improved the material's oxygen exchange properties, and this doping occurred with terbium, a rare expensive metal that is unlikely to be available for widespread use [7]. However, several common dopants such as silver have not been tried, and these may improve the oxygen exchange rate [8].

It is hoped that in the future, one of these strategies to improve the rates would be successful, allowing $YBaCo_4O_{7+\delta}$ to be competitive against the transition metal oxides.

8.3 References

- [1] A.Klimkowicz, K.Świerczek, S.Kobayashi, A.Takasaki, W.Allahyani, B.Dabrowski -Improvement of oxygen storage properties of hexagonal $\text{YMnO}_{3+\delta}$ by microstructural modifications, *Journal of Solid State Chemistry*, 258, 2018 471-476
- [2] T.Chen, Y.Asakura, T.Hasegawa, T.Motohashi, S.Yin - A simple and novel effective strategy using mechanical treatment to improve the oxygen uptake/release rate of $\text{YBaCo}_4\text{O}_{7+\delta}$ for thermochemical cycles, *Journal of Materials Science & Technology*, 68, 2021, 8-15
- [3] P.F.Haworth, S.Smart, J.M.Serrab J.C.Diniz da Costa - Combined investigation of bulk diffusion and surface exchange parameters of silver catalyst coated yttrium-doped BSCF membranes, *Phys. Chem. Chem. Phys.*, 14, 2012 9104-9111
- [4] Y.Hori, H.Ito, K.Okano, K.Nagasu, S.Sato - Silver-coated ion exchange membrane electrode applied to electrochemical reduction of carbon dioxide, 48, 2003 2651-2657
- [5] W.Zhang, W.Zheng - Exsolution-Mimic Heterogeneous Surfaces: Towards Unlimited Catalyst Design, *Chem.Cat* 7, 2015, 48-50
- [6] L.Thommy, O.Joubert, J.Hamon, M.Caldes - Impregnation versus exsolution: Using metal catalysts to improve electrocatalytic properties of LSCM-based anodes operating at 600 °C, *International Journal of Hydrogen Energy*, 41, 2016 14207-14216
- [7] H.Song, J.Jia, S.Zhang, D.Yang, H.Sun, X.Hu - Remarkable oxygen adsorption/desorption capability of $\text{Y}_{0.5}\text{Tb}_{0.5}\text{BaCo}_4\text{O}_{7+\delta}$ under temperature cycles, *Materials Research Bulletin* 47, 3, 2012, 518-520
- [8] Z.Zhang, X.Xu, J.Zhang, D.Chen, D.Zeng, S.Liu, W.Zhou, Z.Shao - Silver-doped strontium niobium cobaltite as a new perovskite-type ceramic membrane for oxygen separation, *Journal of Membrane Science*, 563, 2018, 617-624

Appendix A – Reduced XRD profiles

The XRD profile for the hydrogen reduced samples seen in Figure 7.1 (b) contained a mixture of new phases – however good agreement with reference XRD profiles was not found.

The best combination of phases found were yttrium oxide, barium and cobalt. This is shown in Figure A1.

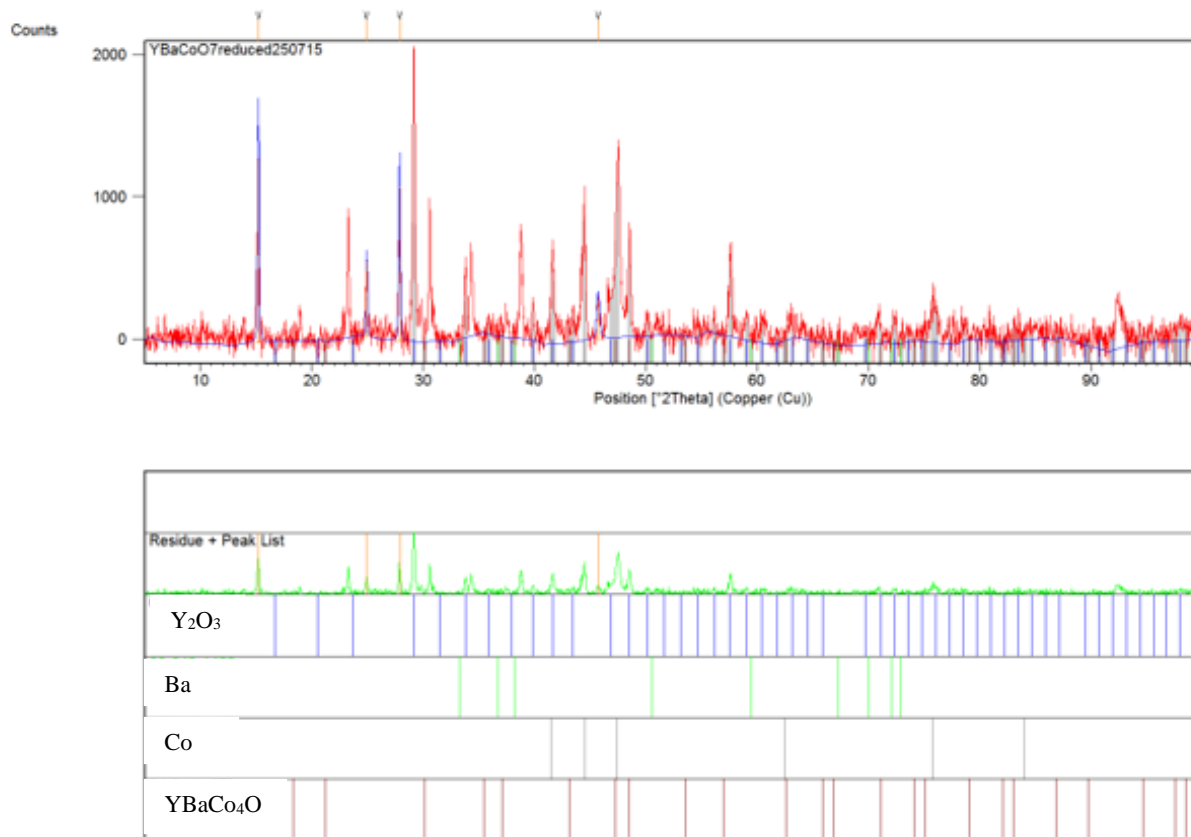


Figure A1 – Peak list from H₂ reduction of YBaCo₄O₇ shown in Figure 7.1

Unfortunately, several unidentified plots were present, shown in Figure A2.

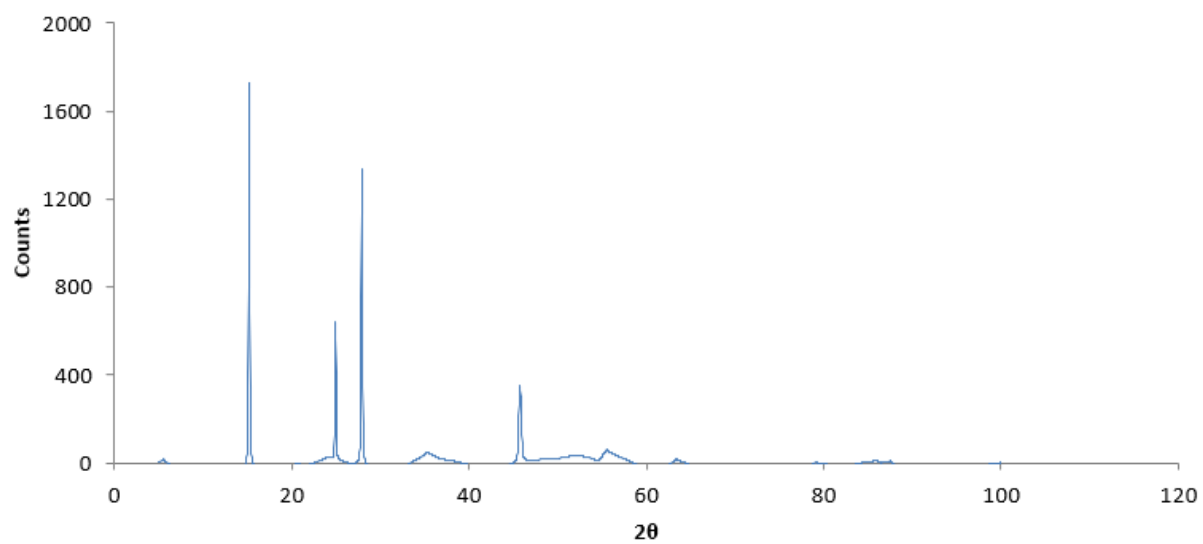


Figure A2 – Unidentified spectra from H₂ reduction of YBaCo₄O₇ shown in Figure 7.1